To IMAGE or to IMAGINE: visualization of parasite migration as a means to support (malaria) parasite vaccine development

Korne, C.M. de

Citation

Korne, C. M. de. (2023, November 2). *To IMAGE or to IMAGINE: visualization of parasite migration as a means to support (malaria) parasite vaccine development*. Retrieved from https://hdl.handle.net/1887/3655877

To IMAGE or To IMAGINE

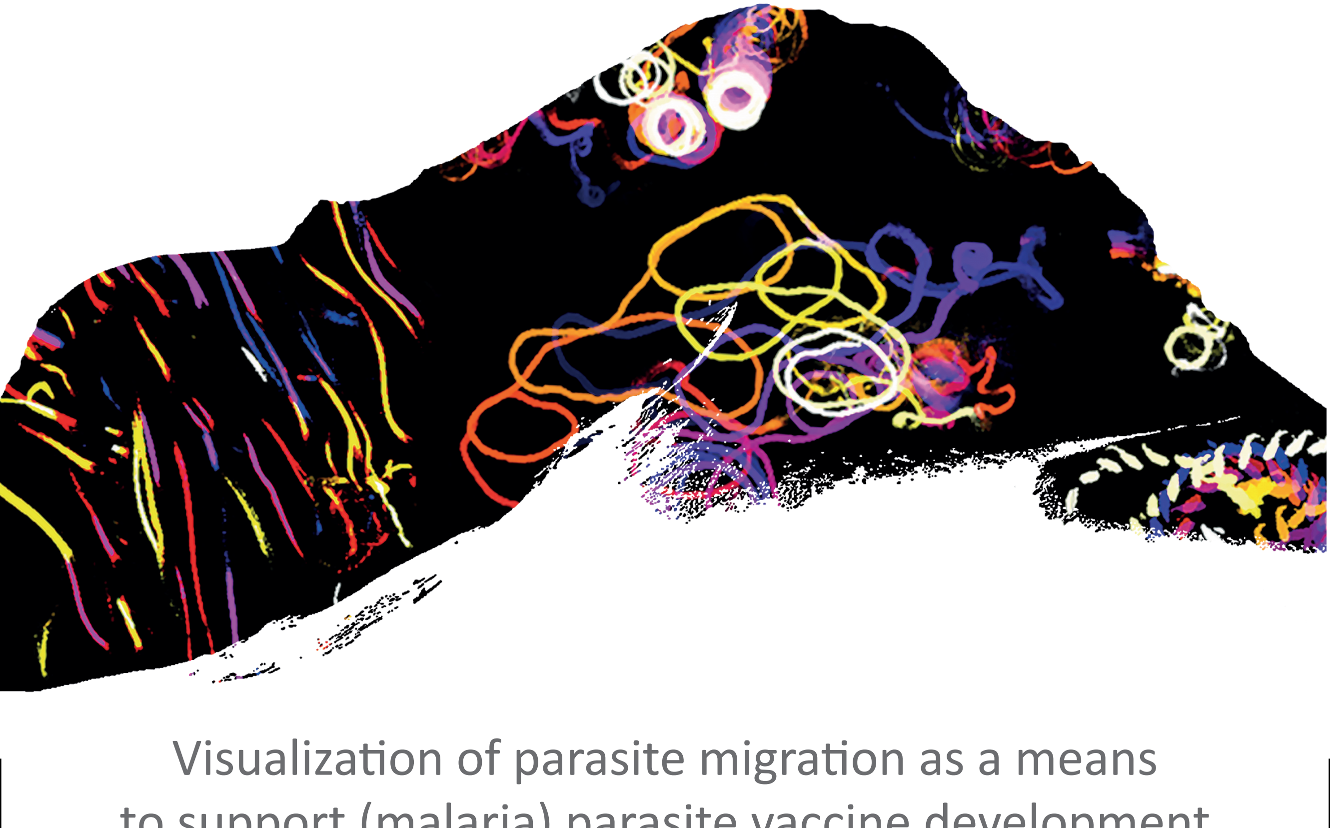

Visualization of parasite migration as a means to support (malaria) parasite vaccine development

Clarize de Korne

Colophon
Design and layout: Clarize de Korne
Printing: Ridderprint | www.ridderprint.nl

To IMAGE or to IMAGINE

Visualization of parasite migration as a means to support (malaria) parasite vaccine development

Proefschrift

ter verkrijging van
de graad van doctor aan de Universiteit Leiden,
op gezag van rector magnificus prof.dr.ir. H. Bijl,
volgens besluit van het college voor promoties
te verdedigen op donderdag 2 november 2023
klokke 13.45 uur

door
Clasina Maria de Korne
geboren te Rilland
in 1995

Promotores:
Prof. dr. F.W.B. van Leeuwen
Prof. dr. M. Roestenberg

Leden promotiecommissie:
Prof. dr. A.C.M. Kroes
Prof. dr. H.H. Smits
Ir. M.N. van Oosterom
Prof. dr. A.H. Velders (Wageningen University & Research, Wageningen)
Dr. J.J. van Hellemond (Erasmus Medisch Centrum, Rotterdam)

TABLE OF CONTENTS

GENERAL INTRODUCTION

The parasitic infections malaria, schistosomiasis and hookworm disease, have a devastating impact on global health, with children bearing the greatest burden. Malaria is the deadliest of these infections, causing acute illness and leading to the loss of 31 million life years and 2.5 million years of healthy life annually. Schistosomiasis and hookworm infections, on the other hand, gradually impair health resulting in the loss of 0.4 million life years and 2.2 million years of healthy life annually[1]. These infections disproportionally affect people living in low-income countries and perpetuate a vicious cycle of poverty and disease[2]. To combat these infections, preventive measures such as the use of bed nets, insecticide spraying and improved sanitation have been implemented and several drugs have been developed and administered to patients or whole populations at risk (mass drug administration)[3-5]. These therapeutic and preventative strategies have substantially reduced morbidity and mortality, however, the gains have levelled off while parasitic infections remain far from eradication.

Vaccination has been essential for the protection from infectious diseases, as evidenced by the global eradication of smallpox and the 99% reduction of polio[6]. Currently, only one vaccine against a parasitic disease is available; in 2021 the malaria vaccine RTS,S/AS01 has been accepted for widespread use among children in regions with moderate to high malaria transmission. RTS,S/AS01 is a subunit vaccine designed to elicit a protective immune response against the circumsporozoite protein, which is the major surface protein of malaria parasites. With a 36% protective efficacy that wanes over time, RTS,S/AS01 is not the ideal malaria vaccine yet[7, 8]. An alternative vaccine approach involves using live malaria parasites which are attenuated by radiation or genetic modification. Mice studies showed that these attenuated parasites can induce a protective immune response, but do not establish a full blown infection[9, 10]. In the 90s, the first clinical trial was performed that proved the potency of radiation attenuated malaria parasites, delivered via mosquito bites, to protect humans against malaria[11]. In following studies, attenuated malaria parasite vaccines have been administered by needle, a more amenable method for large-scale vaccine administration. Attenuated malaria parasite vaccines have provided up to 100% protection to malaria-naive adults in controlled human malaria infection trials, however the efficacy drops to around 50% in adult field trials in endemic settings and a recent field trial in infants failed to demonstrate significant efficacy[12-14]. Subunit and attenuated whole parasite vaccine approaches have also been used for the development of schistosomiasis and hookworm vaccines. However, currently only a few candidates are in, mainly early-stage, clinical development[15-18]. There is a pressing need for research that generates

> For combating parasitic infections, vaccines are considered a promising strategy

insights necessary to further fill the parasite vaccine pipeline and to support optimization of currently available vaccine candidates.

The ability to migrate is a prerequisite for parasites to continue their life cycle and establish an infection, making migratory mechanisms a potential target for new vaccines. Additionally, the efficacy of attenuated whole parasite vaccine approaches is likely to be impacted by the preservation of the migratory capacity of the attenuated parasites as for example dead sporozoites are unable to induce protection[19]. Following this reasoning, investigating parasite migration can deepen our understanding of the parasite biology and provide insights that can guide the rational design of new vaccines.

Comprehension of parasite migration is important for vaccine development

So far, parasite motility is mainly studied in an *in vitro* environment. Malaria sporozoites display (circular) gliding motility on a flat surface[20, 21]. The presence of an actin-myosin motor, a polarized arrangement of microtubules in sporozoites and adhesion proteins on their surface provide an ultrastructural basis for their movement patterns[22, 23]. Albumin is required for inducing sporozoite motility and physical constraints can induce a shift from circular to more linear movement[24, 25]. However, other factors regulating sporozoite motility are yet to be determined. Only recently, migration of malaria sporozoites has been monitored in real-time in their natural *in vivo* environment; in the skin and in the liver of mice. These initial mice studies have shown that, directly following inoculation by mosquitoes, sporozoites start migrating through the skin in complex, tortuous patterns until they either exit the skin site after a few minutes to several hours via a blood or lymph vessel, or get stuck in the skin[26-28]. Regarding schistosomal and hookworm larvae, *in vitro* motility studies have characterized their movement patterns and have revealed how schistosomal larvae beat their forked tail to swim and how hookworm larvae propagate sinusoidal waves along their bodies for forward locomotion[29, 30]. Infective larvae are able to respond to various cues for finding their human host, such as chemical cues, water turbulence or air flow, touch, temperature and light[31-33]. However, skin invasion and migration of these larvae inside their host has not been characterized yet. Given the importance of understanding parasite migration for vaccine development, this thesis aims to provide new insights into parasite migration.

Imaging technology provides a means to literally shed light on parasites and study their migration. Antonie van Leeuwenhoek, acknowledged as the father of microbiology, was the first to imagine and possess the tools to image the world of protozoa in the 17th century.

Ever since the introduction of light microscopy, imaging has played an important role in studying parasites. For a long time, brightfield microscopy was the only imaging technology available for detecting parasites and was used to unravel most of the parasitic life cycles known to date[34, 35]. Brightfield microscopy is still commonly used for characterizing parasite behavior *in vitro*. However, currently, a broad range of imaging modalities is available for biomedical applications, and some have been applied in the field of parasitology. Most *in vivo* imaging studies investigating malaria sporozoite behavior use fluorescent parasites (transgenic lines expressing fluorophores), allowing real-time monitoring of individual sporozoite behavior in tissue such as skin[26-28, 36]. Building on these findings, this thesis aims to expand the availability and application of quantitative imaging-based tools to study parasite migration both *in vitro* and *in vivo*.

> Imaging technology provides a means to literally shed light on parasites and study their migration

THESIS OUTLINE

This thesis describes the development of quantitative imaging-based tools that enable assessment of parasite migration under different conditions and how these tools can be used to deepen our understanding of parasite motility and to explore research questions arising during the development of malaria vaccines.

In **chapter 1** we describe the development of SMOOT (Sporozoite Motility Orienting and Organizing Tool), an image analysis tool suitable to quantitatively assess sporozoite motility *in vitro.* With this tool we show that different (macro)molecules act as regulators of sporozoite motility. In **chapter 2** we adapt SMOOT to quantify sporozoite migration in human skin explant and reveal that radiation attenuation impairs the migratory capacity of sporozoites. In **chapter 3** we microscopically examine the dermal site after sporozoite administration by syringe injection and mosquito inoculation to unravel the factors underlying the differential protective efficacy of mosquito-inoculated and intradermal syringe-injected attenuated sporozoite vaccines. While migrating through the skin, sporozoites are vulnerable to antibodies induced by active immunization or delivered by passive immunization. In **chapter 4** we develop a novel imaging-based assay and combine it with existing techniques to examine the coherence between antibody-antigen binding affinity and their functional effects on sporozoite motility and infectivity. In **chapter 5** we expand sporozoite tracking beyond the skin. Using a hybrid tracer (contains both a fluorophore and a radioisotope) we assess the biodistribution of intravenously injected sporozoites in a mouse model and investigate the role of sporozoite viability in their dissemination throughout the body.

Chapter 6 shows that the hybrid tracer labelling approach is also suitable for schistosomal and hookworm larvae. We monitor human skin invasion behavior of these larvae in real-time and quantitatively assess the amount of invasion. **Chapter 7** reviews the role that imaging plays in parasitology and how it can be applied to advance the development of high-standard diagnostic methods, efficacious drugs and vaccines and new transmission-blocking strategies. Finally, **chapter 8** summarizes the novel concepts presented in this thesis and discusses them in the broader context of the current literature.

REFERENCES

1. Organization, W.H., World Health Statistics 2021. 2021.
2. Ngonghala, C.N., et al., Poverty, disease, and the ecology of complex systems. PLoS biology, 2014. 12(4): p. e1001827.
3. Haldeman, M.S., M.S. Nolan, and K.R. Ng'habi, Human hookworm infection: is effective control possible? A review of hookworm control efforts and future directions. Acta tropica, 2020. 201: p. 105214.
4. Inobaya, M.T., et al., Prevention and control of schistosomiasis: a current perspective. Research and reports in tropical medicine, 2014: p. 65-75.
5. Wangdi, K., et al., Comparative effectiveness of malaria prevention measures: a systematic review and network meta-analysis. Parasites & vectors, 2018. 11(1): p. 1-13.
6. Henderson, D.A., The eradication of smallpox–an overview of the past, present, and future. Vaccine, 2011. 29: p. D7-D9.
7. Olotu, A., et al., Seven-year efficacy of RTS, S/AS01 malaria vaccine among young African children. New England Journal of Medicine, 2016. 374(26): p. 2519-2529.
8. Rts, S., Efficacy and safety of RTS, S/AS01 malaria vaccine with or without a booster dose in infants and children in Africa: final results of a phase 3, individually randomised, controlled trial. The Lancet, 2015. 386(9988): p. 31-45.
9. Nussenzweig, R.S., et al., Protective Immunity Produced by Injection of X-Irradiated Sporozoites of Plasmodium Berghei. Nature, 1967. 216(5111): p. 160-+.
10. Vaughan, A.M., et al., A Plasmodium parasite with complete late liver stage arrest protects against preerythrocytic and erythrocytic stage infection in mice. Infection and immunity, 2018. 86(5): p. e00088-18.
11. Hoffman, S.L., et al., Protection of humans against malaria by immunization with radiation-attenuated Plasmodium falciparum sporozoites. J Infect Dis, 2002. 185(8): p. 1155-64.
12. Oneko, M., et al., Safety, immunogenicity and efficacy of PfSPZ Vaccine against malaria in infants in western Kenya: a double-blind, randomized, placebo-controlled phase 2 trial. Nature Medicine, 2021. 27(9): p. 1636-1645.
13. Richie, T.L., et al., Progress with Plasmodium falciparum sporozoite (PfSPZ)-based malaria vaccines. Vaccine, 2015. 33(52): p. 7452-61.
14. Sissoko, M.S., et al., Safety and efficacy of a three-dose regimen of Plasmodium falciparum sporozoite vaccine in adults during an intense malaria transmission season in Mali: a randomised, controlled phase 1 trial. The Lancet Infectious Diseases, 2022. 22(3): p. 377-389.
15. Chapman, P.R., et al., Vaccination of human participants with attenuated Necator americanus hookworm larvae and human challenge in Australia: a dose-finding study and randomised, placebo-controlled, phase 1 trial. The Lancet Infectious Diseases, 2021. 21(12): p. 1725-1736.
16. Hewitson, J.P. and R.M. Maizels, Vaccination against helminth parasite infections. Expert review of vaccines, 2014. 13(4): p. 473-487.
17. Molehin, A.J., Schistosomiasis vaccine development: update on human clinical trials. Journal of biomedical science, 2020. 27(1): p. 28.
18. Shalash, A.O., et al., Oral peptide vaccine against hookworm infection: correlation of antibody titers with protective efficacy. Vaccines, 2021. 9(9): p. 1034.
19. Haeberlein, S., et al., Protective immunity differs between routes of administration of attenuated malaria parasites independent of parasite liver load. Scientific reports, 2017. 7(1): p. 10372.
20. Hegge, S., et al., Automated classification of Plasmodium sporozoite movement patterns reveals a shift towards productive motility during salivary gland infection. Biotechnol J, 2009. 4(6): p. 903-13.
21. Stewart, M.J. and J.P. Vanderberg, Malaria sporozoites leave behind trails of circumsporozoite protein during gliding motility. J Protozool, 1988. 35(3): p. 389-93.
22. Kappe, S.H., C.A. Buscaglia, and V. Nussenzweig, Plasmodium sporozoite molecular cell biology. Annu. Rev. Cell Dev. Biol., 2004. 20: p. 29-59.
23. Kudryashev, M., et al., Structural basis for chirality and directional motility of Plasmodium sporozoites. Cell Microbiol, 2012. 14(11): p. 1757-68.
24. Muthinja, M.J., et al., Microstructured Blood Vessel Surrogates Reveal Structural Tropism of Motile Malaria Parasites. Adv Healthc Mater, 2017. 6(6).

25. Vanderberg, J.P., Studies on the motility of Plasmodium sporozoites. J Protozool, 1974. 21(4): p. 527-37.
26. Hellmann, J.K., et al., Environmental constraints guide migration of malaria parasites during transmission. PLoS pathogens, 2011. 7(6): p. e1002080.
27. Hopp, C.S., et al., Longitudinal analysis of Plasmodium sporozoite motility in the dermis reveals component of blood vessel recognition. Elife, 2015. 4.
28. Amino, R., et al., Quantitative imaging of Plasmodium transmission from mosquito to mammal. Nat Med, 2006. 12(2): p. 220-4.
29. Chauhan, V.M., et al., The physicochemical fingerprint of Necator americanus. PLoS neglected tropical diseases, 2017. 11(12): p. e0005971.
30. Krishnamurthy, D., et al., Schistosoma mansoni cercariae swim efficiently by exploiting an elastohydrodynamic coupling. Nature Physics, 2017. 13(3): p. 266-271.
31. Castelletto, M.L., et al., Diverse host-seeking behaviors of skin-penetrating nematodes. PLoS pathogens, 2014. 10(8): p. e1004305.
32. Chaisson, K.E. and E.A. Hallem, Chemosensory behaviors of parasites. Trends in Parasitology, 2012. 28(10): p. 427-436.
33. Haas, W., Parasitic worms: strategies of host finding, recognition and invasion. Zoology, 2003. 106(4): p. 349-364.
34. Grove, D.I., History of human helminthology. 1990: CAB International.
35. Mahmud, R., Y.A.L. Lim, and A. Amir, Medical parasitology. Cham, Switzerland: Springer International Publishing. doi: https://doi.org/10.1007/978-3-319-68795-7, 2017.
36. De Niz, M., et al., Progress in imaging methods: insights gained into Plasmodium biology. Nature Reviews Microbiology, 2017. 15(1): p. 37-54.

To IMAGE

Part I

“

Joy in looking and comprehending is nature’s most beautiful gift.

- Albert Einstein

1

Regulation of *Plasmodium* sporozoite motility by formulation components

Clarize M. de Korne, Luuk T. Lageschaar, Matthias N. van Oosterom, Els Baalbergen, Beatrice M.F. Winkel, Severine C. Chevalley-Maurel, Aldrik H. Velders, Blandine M.D. Franke-Fayard, Fijs W.B. van Leeuwen, Meta Roestenberg

Malaria Journal 2019. DOI: 10.1186/s12936-019-2794-y

ABSTRACT

The protective efficacy of the most promising malaria whole-parasite based vaccine candidates critically depends on the parasite's potential to migrate in the human host. Key components of the parasite motility machinery (e.g. adhesive proteins, actin/myosin-based motor, geometrical properties) have been identified, however the regulation of this machinery is an unknown process. *In vitro* microscopic live imaging of parasites in different formulations was performed. We analyzed, with the quantitative analysis software SMOOT$_{\textit{in vitro}}$, their motility; their adherence capacity, movement pattern and velocity during forward locomotion. SMOOT$_{\textit{in vitro}}$ enabled the detailed analysis of the regulation of the motility machinery of *Plasmodium berghei* in response to specific (macro-)molecules in the formulation. Albumin acted as an essential supplement to induce parasite attachment and movement. Glucose, salts and other whole serum components further increased the attachment rate and regulated the velocity of the movement. Based on the findings can be concluded that a complex interplay of albumin, glucose and certain salts and amino acids regulates parasite motility. Insights in parasite motility regulation by supplements in solution potentially provide a way to optimize the whole-parasite malaria vaccine formulation.

INTRODUCTION

In 2017, an estimated 219 million cases of malaria occurred worldwide leading to nearly half a million deaths, which makes malaria the most deadly parasitic disease worldwide[1]. Infection with malaria is initiated when *Plasmodium* parasites are injected into the skin by a probing *Anopheles* mosquito in the highly motile sporozoite (SPZ) stage[2]. Motility enables SPZ to exit the skin site, enter the bloodstream and reach and infect the liver, which makes SPZ motility a target for anti-malarial drugs and vaccines[3]. In addition, the potency of malaria vaccine candidates based on live attenuated SPZ depends on their potential to migrate in the human host, infect hepatocytes and induce an immune response, which cannot be replicated by dead SPZ[4]. Nevertheless, the regulation of this migratory behavior is still an unknown process.

After intradermal deposition, SPZ rely on their own adhesion capacity and actin/myosin-based motility machinery to migrate. Their adhesion capacity relies on proteins, e.g. the circumsporozoite protein (CSP) and the thrombospondin-related adhesive protein (TRAP), which can form adhesion sites[5, 6]. The establishment of new adhesion sites and the release of the old, enabled by the actin/myosin motor, provides the forward locomotion at a speed linked to the turnover rate[7]. The subsequent direction of this movement is related to the geometrical properties (the crescent shape and the presence of polar rings) of the SPZ which induce chirality[8, 9]. SPZ motility is required to move out of the dermal tissue and to reach the bloodstream. At that point the blood flow will transport SPZ to the liver where they can invade hepatocytes[10, 11]. As a result, the migration process of SPZ and possibly thereby also their infectivity is directly influenced by their motility[12, 13]. Although the presence and importance of the elements of the SPZ motility machinery are confirmed, the regulation of e.g. adhesive protein secretion, actin/myosin motor activity and SPZ chirality is still poorly understood[10, 14, 15]. Given the importance of SPZ motility, a better understanding of stimuli that promote and inhibit SPZ motility is needed[12, 13].

To shed light on SPZ motility, transgenic SPZ e.g. *Plasmodium berghei* and *Plasmodium yoelii* expressing fluorescent proteins (e.g. green fluorescent protein; GFP)[16] have been generated for intravital studies[17, 18]. These studies showed that SPZ display complex motility in their natural environment[19-21], possibly due to tissue morphology and the availability of nutrients in the extracellular matrix. In order to dissect the role of these factors separately, more simplified *in vitro* models are needed[14, 22]. Studies using 3D *in vitro* environments revealed that physical confinement plays an important role in regulating the direction and velocity of SPZ movement[23, 24]. However, when physical confinement is taken out of the equation, the availability of chemical stimuli is revealed as a crucial regulator of SPZ motility. So far, reports on *in vitro* SPZ motility have shown that albumin and calcium act as essential stimuli of SPZ motility[25-27]. More research is needed to characterize other stimuli of SPZ motility.

Classically, gliding assays are used as the gold standard for assessing SPZ motility *in vitro*[28, 29], but this assay is not ideal for exploring SPZ motility regulation, because it only provides indirect analysis of SPZ motility performed through post hoc assessment of SPZ trails[6, 30]. What is lacking to date, is a quantitative *in vitro* analysis tool that allows real time detailed SPZ motility characterization.

In vitro microscopic imaging studies with fluorescent *Plasmodium berghei* when augmented with a quantitative analysis tool have the potential to provide a means to assess the regulation of *P. berghei's* adhesion and locomotion by formulation composition. To illustrate the potential of this concept, the custom image analysis software called SMOOT$_{in\ vitro}$ (Sporozoite Motility Orienting and Organizing Tool) has been developed and used to study the effect of a systematic variation in formulations: PBS, HBSS and RPMI, enriched with either albumin or whole serum.

METHODS

Preparation of sporozoites

Mosquitoes were infected by feeding on infected mice (female OF1 mice, 6-7 weeks old; Charles River, Leiden, The Netherlands) as described previously[31]. The animal experiments of this study were performed in compliance with Dutch welfare regulations and were approved by the institutional Animal Ethics Committee of the Leiden University Medical Center (DEC PE.18.005.001). *Plasmodium berghei* SPZ (*Pb*ANKA-mCherry$_{hsp70}$+Luc$_{eef1\alpha}$; line RMgm-1320, www.pberghei.eu) which contain the fusion gene *mcherry* under control of the strong *hsp70* promoter integrated into the neutral *230p* gene locus (PBANKA_0306000) were obtained by microsurgical dissection of the salivary glands of infected female *Anopheles stephensi* mosquitoes. To allow the SPZ to mature dissections were performed 21-24 days following infection of the mosquitoes. During this period mosquitoes were kept at a temperature of 21 °C and 80% humidity. The salivary glands were collected and crushed in the different formulations mentioned in the next section. The free SPZ were counted in a Bürker counting chamber using phase-contrast microscopy. On average, dissection yielded 55k SPZ/mosquito. The mosquitoes and the SPZ were kept on ice (0-4 ^{o}C) for a maximum of 3 hr until use.

Sporozoite motility analysis set-up

To investigate which components are needed to induce motility of SPZ, the mosquitoes were dissected and the obtained salivary glands were crushed in eleven different formulations: 1) Phosphate buffered saline which contains potassium, sodium, chloride and phosphate (PBS; Life Technologies Inc.), 2) Hanks' balanced salt solution which contains besides the salts present in PBS also glucose, calcium, magnesium, sulphate and bicarbonate (HBSS; Life Technologies Inc.), 3) Roswell Park Memorial Institute medium (RPMI; Life Technologies Inc.) which contains besides the components of HBSS also amino acids and vitamins, 4) PBS enriched with 3.5 mg/ml bovine serum albumin (BSA; Sigma-Aldrich), 5) HBSS + 3.5 mg/ml BSA, 6) RPMI + 3.5 mg/ml BSA, 7) PBS enriched with 10% fetal bovine serum (FBS; Life Technologies Inc.), 8) HBSS + 10% FBS, 9) RPMI + 10% FBS, 10) RPMI without amino acids (Caisson Labs) + 3.5 mg/ml BSA and 11) RPMI without glucose (Life Technologies Inc.) + 3 mg/ml BSA. All eleven formulations had a physiological pH of 7.0-7.5 and a viscosity of <1.1 cP. For imaging of the SPZ, 10 µl of the SPZ solution was pipetted on the cover slip of a confocal dish without any precoating (ø14mm; MatTek Corporation), covered with another cover slip (ø12mm; VWR Avantor) and imaged within 45 minutes. The set-up is schematically depicted in Sup. Figure S1.

Confocal imaging

Images of the SPZ were taken on a Leica TCS (true confocal scanning) SP5 or SP8X WLL (white light laser) microscope (Leica Microsystems). The SPZ expressed mCherry which was excited at 587 nm and the emission was collected between 600-650 nm. The movies were recorded with a frame rate of 35 frames per minute, 400 frames per movie, three movies per condition. The resolution of the images was set at 1024x1024 pixels. For imaging of the SPZ a 40x objective (Leica HCX PL APO CS 40x/1.25-0.75na OIL) was used and the experiments were performed at room temperature, unless otherwise stated. The movies were recorded using the Leica software (LAS X version 1.1.0.12420; Leica Microsystems).

Movie analysis

Maximum projections of the recorded microscopy movies were generated using Fiji software[32]. The movies were further processed using SMOOT$_{in\ vitro}$, an in-house developed graphical user interface (GUI), written in the MATLAB programming environment (version r2017b, The MathWorks Inc.). Via SMOOT$_{in\ vitro}$ analysis the SPZ could be segmented per movie frame, based on their fluorescence signal intensity, size and crescent shape by applying a binary threshold, a median filter, skeleton adjustment and spot removal. Colliding SPZ and SPZ circling on the edge of the field of view were excluded, since the locations of these SPZ on the consecutive frames cannot be stitched together in a reliable way. The value of these segmentation parameters can be set in the GUI. The direct visual feedback provided by the GUI during the setting of the parameters was used to find the optimal segmentation settings. Over time the median pixel locations of segmented SPZ visible on different frames could be connected into full SPZ tracks, which were subsequently separated in segments based on changes in movement pattern. The movement pattern of the SPZ was classified per segment as floating, stationary or circling. The velocity and turn angle at frame level, the turn direction (clockwise (CW) or counter-CW (CCW)) at segment level and the length of the travelled path (expressed as number of frames and displacement per frame) at track level of the circling SPZ were determined. On average ~100 SPZ were analyzed per condition.

Statistics

Statistical analysis consisted of the One-way ANOVA, the Mann-Whitney U test and the independent sample t-test depending on the nature of the variables tested (pre-test of normality: Shapiro-Wilk test; pre-test of variance homogeneity: Levene-test). p-values < 0.05 were considered significant. All statistical tests were performed by SPSS Statistics (version 23; IBM Nederland B.V.).

RESULTS

Sporozoite movement patterns

$\text{SMOOT}_{\textit{in vitro}}$ was able to discern three main SPZ movement patterns in the microscopic SPZ movies: floating (red), stationary (green) and circling (blue; Figure 1). The floating SPZ could not attach to the surface and as such displayed random movement based on fluidics (Figure 1A). Overall, 3% of the total number of SPZ imaged were considered to be stationary, either by full length or partial surface attachment. Uniquely the latter results in a “waving” phenomenon (47% of stationary SPZ, Figure 1B). Furthermore, motile SPZ were observed which attached to the surface and turned in circles (Figure 1C). The majority of circling SPZ moved in a CCW direction, only 2% of them turned CW. Whilst the CCW movement was often sustained during the whole movie, CW-turning SPZ only turned on average 1.5 circles (range: 1-7 circles) before detaching from the surface. The different formulations did not influence the ratio between CCW and CW movement (Sup. Figure S2).

Movement pattern quantification

Using automated $\text{SMOOT}_{\textit{in vitro}}$ movement pattern classification, a matrix of nine different formulations (f1-9) was studied: PBS, HBSS and RPMI (f1-3), which were enriched with either 3.5 mg/ml purified BSA (f4-6) or 10% FBS which contains amongst other things ~3.5 mg/ml BSA (f7-9). Changes in the formulation yielded a direct effect on the SPZ movement patterns. Typically, in formulations without BSA or FBS (f1-3) and also in the condition PBS+BSA (f4), most SPZ were floating. An example of such an effect is shown in Figure 2A. In the formulation HBSS+BSA both floating and circling SPZ were seen (f5, Figure 2B), whereas in the other conditions with BSA and FBS the majority of SPZ were circling (f6-9, Figure 2C).

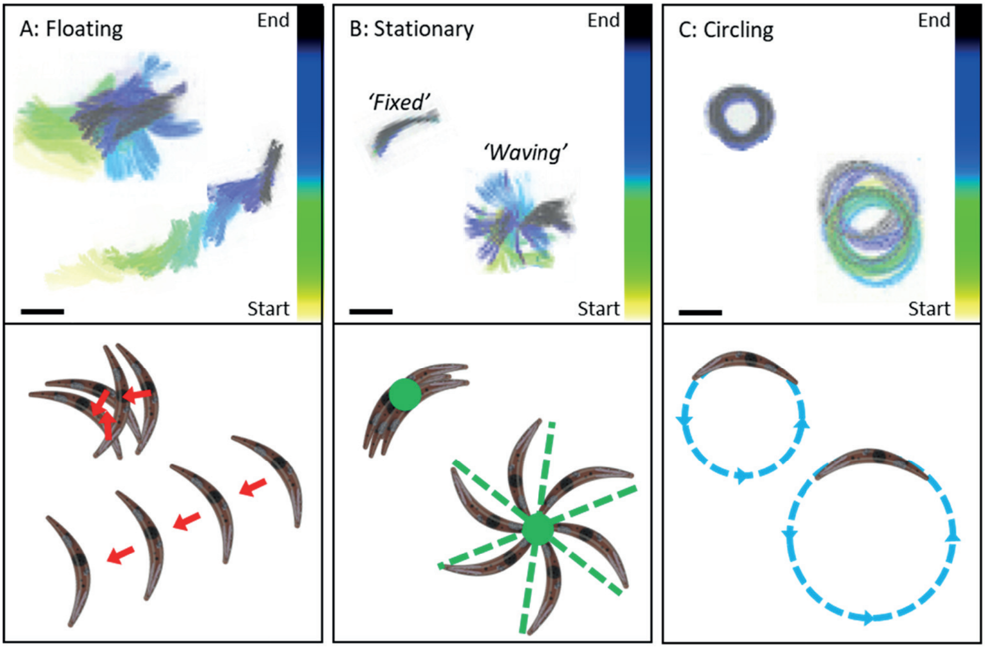

Figure 1 Sporozoite movement patterns. A-C) Maximum projections of movies showing the different movement patterns of SPZ on a glass surface: SPZ floated within the solution (A), SPZ fully attached to the surface 'fixed' or with one tip attached to the surface 'waving' (B), and SPZ were turning in circles with varying diameters (C). The moving patterns seen at the maximum projections are also schematically depicted. Scalebar: 10 µm.

Quantitative analysis confirmed that the movement behavior of SPZ was significantly different between the conditions with and without BSA and FBS ($p=0.007$; One-way ANOVA; Figure 3). Without FBS or BSA, 92% of the SPZ were floating, only a 7% minority of the SPZ could attach to the surface and were stationary (Figure 3:1-3). These stationary SPZ were either fully attached (41%) or were waving (59%). Interestingly, waving SPZ were observed significantly more in the formulations which did not induce circling (Figure 3:1-4) than in the formulations which could (Figure 3:5-9; resp. 94% and 6%, $p=0.026$; independent sample t=test), suggesting that waving and circling are mutually exclusive. It thus seems that SPZ which are unable to circle can (partially) adhere, but then cannot progress to the next movement phase and as a consequence start waving.

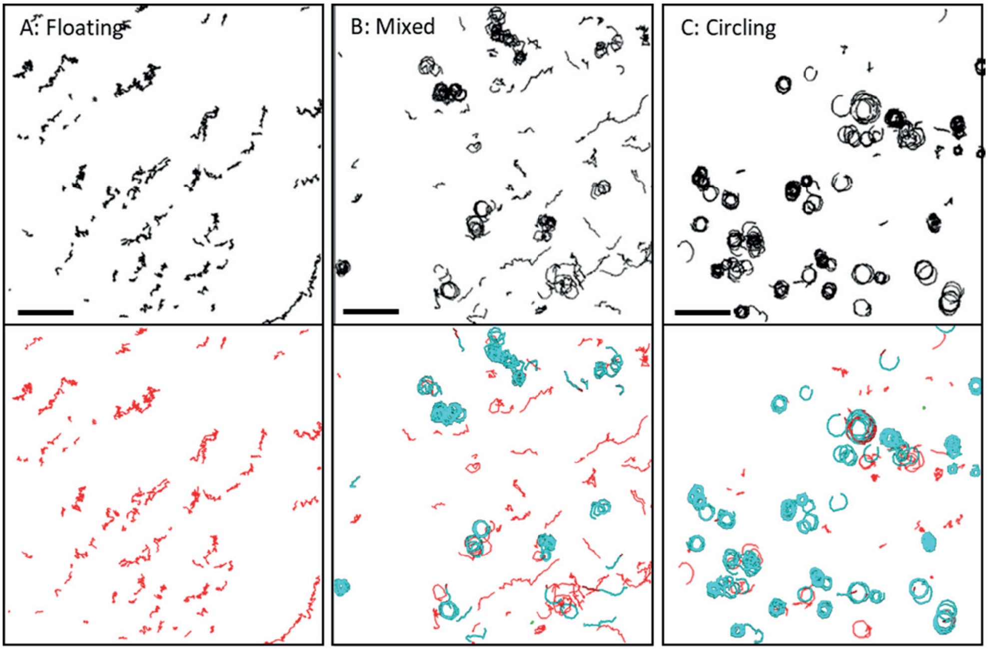

Figure 2 Effect of formulation on sporozoite movement. A-C) Overview of tracks of SPZ under three different conditions: without FBS or BSA only floating SPZ were seen (A), HBSS+BSA resulted in a mix of both floating and circling SPZ (B) and other conditions with BSA and FBS showed primarily circling SPZ (C). The tracks of the lower row are color-coded; floating tracks are depicted in red, circling tracks are depicted in blue and stationary tracks are depicted in green. Scalebar: 50 µm.

Conforming previous data, BSA proved to be an essential supplement[25] since HBSS and RPMI enriched with 3.5 mg/ml BSA induced circling (Figure 3:5-6). However, BSA was not the only essential supplement since PBS+BSA was not able to induce circling (Figure 3:4). The following trend was seen for the three formulations enriched with BSA: PBS, a phosphate-buffered sodium chloride solution, did not induce circling, HBSS which contains additional ions (e.g. calcium, magnesium and bicarbonate) and glucose induced 41% circling SPZ and RPMI, which contains salts, glucose, amino acids and vitamins increased the percentage of circling SPZ to 76% (Figure 3:4-6). This trend revealed that besides BSA, also salts, glucose and certain amino acids and/or vitamins were essential supplements to induce attachment and circling. The role of glucose and amino acids was dissected in more detail by removing these components from the RPMI+BSA formulation (f6). Both depletion of amino acids and glucose resulted in a significant decrease of SPZ adherence capacity: 22% of the SPZ were floating in RPMI+BSA, 55% of the SPZ were floating in the solution without amino acids (Figure 4:1; p=0.002; independent sample t-test) and 63% of the SPZ were floating in the solution without glucose (Figure 4:2; p=0.005; independent sample t=test).

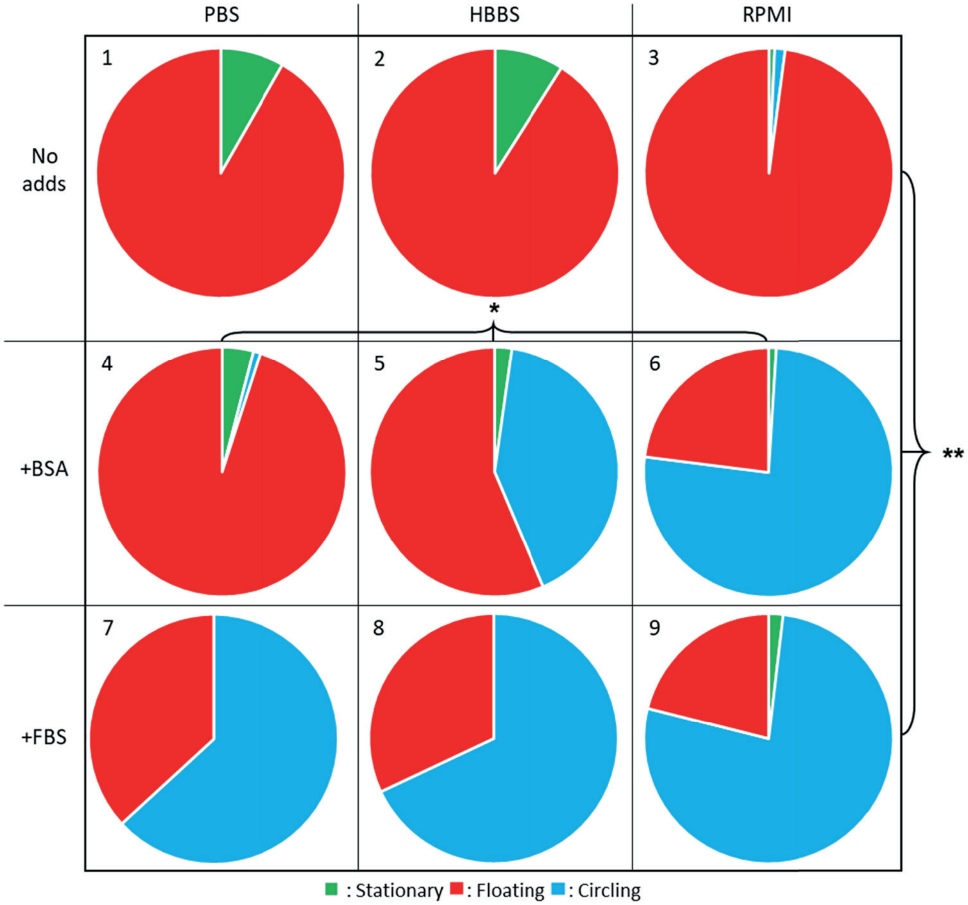

Figure 3 Movement pattern distribution. The movement pattern distribution for SPZ in the 9 different solutions. More SPZ were circling in the solutions enriched with BSA (4-6) and FBS (7-9) compared to the non-enriched solutions (1-3) ($p=0.007$; One-Way ANOVA). In RPMI enriched with BSA or FBS (6, 9), the SPZ circled more compared to PBS (4,7) and HBSS (5,8) enriched with BSA or FBS ($p=0.014$; One-Way ANOVA).No significant difference was found between RPMI enriched with BSA or FBS ($p=0.823$; independent sample t-test). *: $p<0.05$, **: $p<0.01$.

FBS contains, in addition to its major component BSA (~35 mg/ml), many other components like salts, glucose, vitamins and cholesterol. Enrichment of any of the formulations with FBS induced circling of 60-80% of the SPZ. Significantly more SPZ were circling in the presence of FBS compared to BSA when it was added to PBS or HBSS (Figure 3:4,5,7,8; $p=0.005$; independent sample t-test). In contrast, addition of FBS instead of BSA to RPMI did not further increase the amount of circling SPZ (Figure 3:6,9; $p=0.816$; independent sample t-test). Thus, the supplements present in FBS enhanced the percentage of circling SPZ, however they did not add value on top of RPMI+BSA: albumin, salts, glucose, amino acids and vitamins.

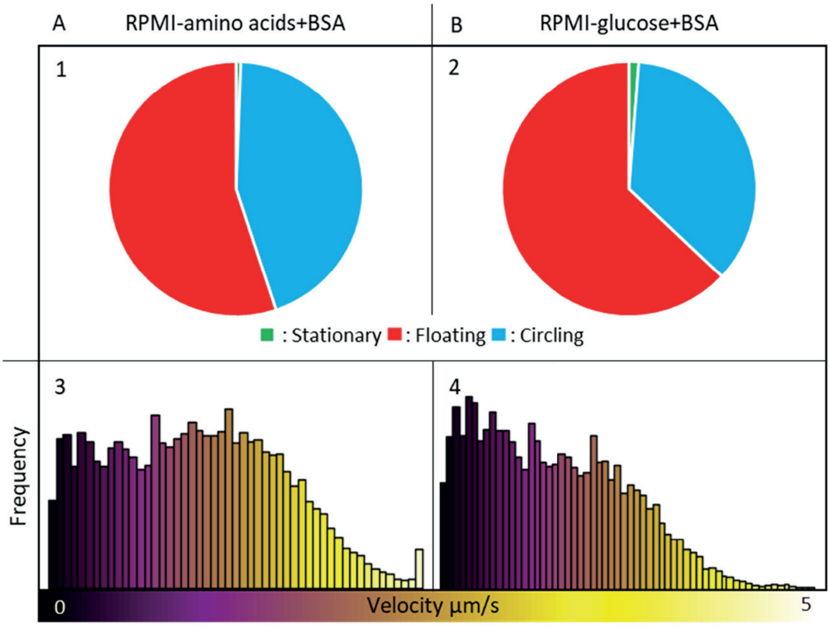

Figure 4 Effect of amino acids and glucose. A-B) The movement pattern distribution for SPZ in RPMI without amino acids (A1) and without glucose (B1) both enriched with BSA and the velocity distribution for SPZ in RPMI without amino acids (A3) and without glucose (B4) both enriched with BSA are plotted. Under the condition without amino acids and without the glucose, the SPZ circled on average with a velocity of 2.0 µm/s and 1.7 µm/s respectively.

Sporozoite velocity during circling

When studying the velocity of SPZ in the five different formulations that induced circling (Figure 3:5-9), overall, SPZ displayed circular movement with a median velocity of 2.0 ± 1.0 µm/s. When comparing the different formulations, the median velocity was 1.4 and 1.7 µm/s for SPZ supplemented with BSA (HBSS and RPMI respectively), whereas SPZ supplemented with FBS exhibited higher velocities; 2.1, 2.5 and 2.7 µm/s (RPMI, HBSS and PBS respectively). This velocity difference persisted over time (Figure 5A). Besides the components available in solution, also temperature influenced the velocity of the SPZ. The velocity of SPZ in RPMI supplemented with FBS nearly doubled after increasing the temperature from room temperature to 37 °C (Figure 5B; median velocity: 3.8 µm/s at 37 °C versus 2.1 µm/s at room temperature). The SPZ did not move at a constant speed, their velocity fluctuated along the track which was visualized by color-coding (Figure 6A-B). Yellow sections, corresponding to a high velocity, alternated with purple sections, corresponding to a lower velocity. Given these velocity fluctuations along the track, the velocity of the SPZ was analyzed per frame instead of analyzing average track velocities.

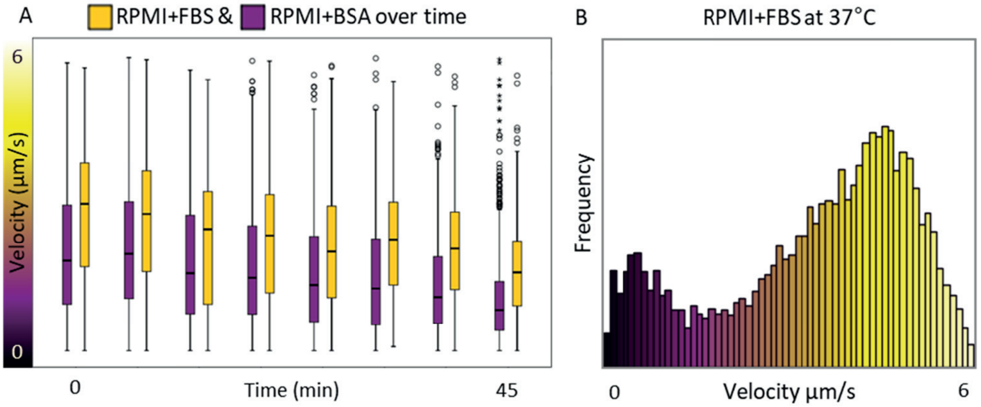

Figure 5 Effect of time and temperature on sporozoite velocity. A) The velocity of SPZ in RPMI enriched with FBS (depicted in yellow) or BSA (depicted in purple) is plotted over time. B) The velocity distribution of the SPZ circling on a glass surface in RPMI enriched with FBS at 37 °C. On average the SPZ circled with a velocity of 3.8 µm/s.

Although the range of velocities was similar for SPZ in the five different solutions (~1% of the SPZ could reach a velocity of 4.0 µm/s under all conditions), between these formulations striking variations could be observed in the distribution of the velocities measured (Figure 6C:5-9). Clearly the velocity of the SPZ was not normally distributed ($p<0.001$; Shapiro-Wilk test). Two different trends were seen. First, the SPZ in medium enriched with FBS moved significantly faster than the SPZ enriched with BSA ($p=0.002$; Mann-Whitney U test). Second, within the three formulations enriched with FBS, SPZ in PBS moved faster than SPZ in RPMI ($p=0.050$; Mann-Whitney U test). Although less SPZ started circling in RPMI without amino acids compared to complete RPMI, for the SPZ which started circling a shift to higher velocities was observed (Figure 4:3). Interestingly, this shift was related to a significant decrease in the diameter of the circles (Sup. Figure S3; 12.3 µm in complete RPMI, 10.3 µm in RPMI without amino acids; $p<0.001$; independent sample t-test). Hence, the availability of specific (macro-)molecules in the formulation seemed to determine not only SPZ adherence and their capacity of forward locomotion but also the velocity at which SPZ were able to move.

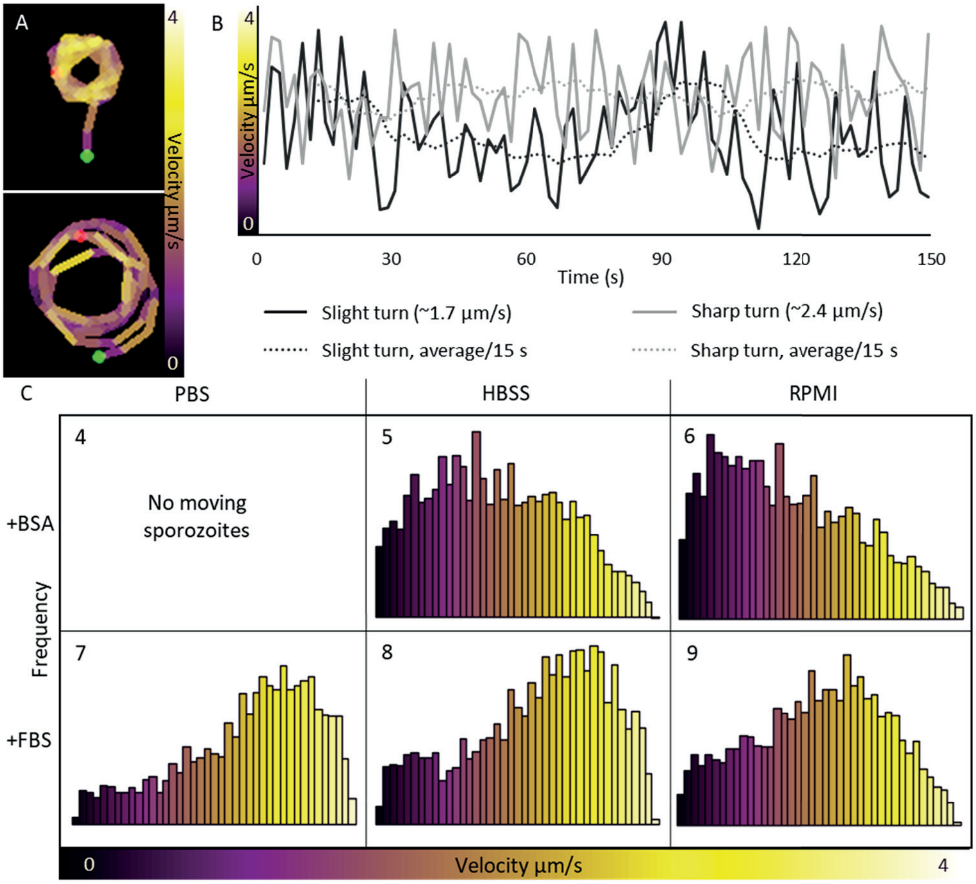

Figure 6 Sporozoite velocity during circling. A) Velocity heatmaps of a sharp (top) and slight turn (bottom). The start of the tracks is marked with a green dot and the end with a red dot. The velocity of the SPZ fluctuated along the tracks. B) The velocity of the SPZ tracks depicted in A are plotted over time, including a line for the average velocity per 15 s. C) The velocity distribution of the SPZ circling on a glass surface in the different formulations. In PBS enriched with BSA, the SPZ did not circle. In HBSS and RPMI enriched with BSA, the SPZ circled on average with a velocity of 1.6 μm/s. In the solutions enriched with FBS, the SPZ circled faster, on average: 2.5 μm/s ($p=0.002$; Mann-Whitney U test). Although the median velocity differed between the solutions enriched with BSA and FBS, the velocity ranges were the same ($p=0.796$; Mann-Whitney U test).

DISCUSSION

The availability of a dedicated analysis tool (SMOOT$_{in\ vitro}$) enabled a quantitative analysis of SPZ motility by describing their 1) attachment rate, 2) movement pattern distribution and 3) velocity distribution. Because SMOOT$_{in\ vitro}$ enabled to tease apart SPZ motility in tracks, segments and frames, the different motility parameters could be individually dissected and subtle differences could be quantified. In this way has been confirmed that albumin is essential to induce SPZ attachment and movement. Glucose, salts, amino acids and vitamins, components in RPMI, further increased the attachment rate and the percentage of moving SPZ, whereas the supplements present in whole serum regulated the velocity of the SPZ movement. Combined, these findings indicate that the regulation of SPZ motility is a complex interplay of SPZ with different (macro-)molecules and salts.

The three *in vitro* movement patterns, floating, stationary (fully attached and waving) and circling (>95% CCW), which were observed for *P. berghei* are in line with previous reports[9, 29, 33]. These same reports have also shown that SPZ could only sustain CW circling for a short period of time. In this study, SMOOT$_{in\ vitro}$ facilitated the analysis of the circular movement patterns at a level of detail beyond what has previously been performed[26, 34]. Particularly, the image processing tool enabled the assessment of unique but subtle alterations in SPZ velocity along the tracks, which might reflect the turnover rate of SPZ adhesion sites[7]. The remarkable differences in velocity distribution between the formulations suggested that this level of detail is needed to do justice to the complex interplay between the available (macro-)molecules and the SPZ motility machinery. Since SMOOT$_{in\ vitro}$ allowed for detailed analysis of SPZ motility at frame level, the tool can be used to further study the action of (novel) motility inhibiting drugs at different concentrations. Potentially, motility analysis with SMOOT$_{in\ vitro}$ could be performed as an additional assay to previously described high-throughput screening methods[3].

SPZ attachment and movement are two distinguishable, but likely related steps in SPZ motility. Both appear to be initiated by external stimuli transferred by internal signaling cascades. Hegge *et al.* have described SPZ adherence and movement as a four step procedure[35]: step 1 is the initial adhesion with one tip, step 2 the formation of secondary adhesion site, step 3 full body attachment, step 4 the initiation of gliding. According to literature, step 2-4 of this adhesion model should be dependent on the secretion of adhesive proteins triggered by albumin and the turnover of these adhesion sites by the actin/myosin-based molecular motor[7, 25, 36]. The latter requires a considerable sustained internal energy production. In accordance with the proposed model, without the presence of albumin and glucose only a few SPZ (7%) could achieve full body attachment (step 3) and none of the SPZ started gliding (step 4). Albumin strongly promoted full body attachment and glucose further increased it (step 3), however in these conditions also gliding was initiated (step 4). In conclusion, our data supports the notion that SPZ attachment and movement are related steps in SPZ motility.

Interestingly, albumin and glucose do not seem to be the sole supplements regulating SPZ motility. In addition, supplements present in RPMI (which, besides salts and glucose also contains amino acids and vitamins) act as stimuli for SPZ attachment and subsequent moving. As SPZ can also use glutamate or glutamine to enter the Krebs cycle to produce

energy and the availability of these compounds influences SPZ motility[11, 34], this could explain why depletion of the amino acid content of RPMI decreased the percentage of attached and moving SPZ compared to PBS and HBSS.
The available (macro-)molecules did not only regulate the occurrence of SPZ adherence and moving, but also the velocity of their forward locomotion. Besides attachment to the surface via adhesive proteins, also detachment by the turnover of the adhesion sites is essential to allow the SPZ to move forwards at a certain speed[7, 37]. This attachment-detachment process could have caused the fluctuating velocity we measured at frame level. Strikingly, whole serum induced a distribution shift to higher velocities of SPZ compared to albumin without changing the maximum reached velocity. It is still unclear which of the >30 components that whole serum consists of is responsible for this shift. Nevertheless, the change in velocity distribution induced by whole serum reveals that besides the attachment rate and the initiation of movement, the velocity of SPZ movement is clearly also regulated by the formulation composition.

The comparison between the attachment rate, movement pattern distribution and velocity distribution induced by the different formulations suggested two different trends: 1) whole serum both increased the attachment rate, the percentage of circling SPZ and their velocity compared to albumin and 2) RPMI increased the attachment rate and the percentage of circling SPZ, but decreased their velocity compared to PBS and HBSS. Combined these trends indicate that SPZ motility is dependent on regulators inducing the right balance between strong attachment and fast detachment. The $\mathrm{SMOOT}_{\textit{in vitro}}$ analysis of the effect of different potential stimuli and inhibitors has the potential to provide insight in the biological mechanisms behind SPZ motility. A recently developed fluorescent labelling approach for non-fluorescent parasites provides the opportunity to study the motility of SPZ in vaccine preparations or isolated in the field[38]. Potentially, $\mathrm{SMOOT}_{\textit{in vitro}}$ can be adapted to study the motility of malaria parasites in other developmental stages (e.g. ookinetes) if the segmentation and stitching parameters were adjusted and validated to select the parasite.

Despite the regulating role of the different supplements on SPZ motility, PfSPZ vaccines currently are formulated in PBS with albumin only[39]. It is not yet clear to what extent the observed *in vitro* formulation effects can impact the *in vivo* situation where proteins, glucose, salts and amino acids are in supply from the surrounding blood/tissue. However, this should be the subject of further research, as the addition of glucose, salts and amino acids will potentially improve SPZ motility after deposition in the human skin and thereby may enhance the potency of whole-parasite malaria vaccines.

In conclusion, this initial *in vitro* study indicated that (macro-)molecules effect SPZ motility by acting as regulators of adherence to the surface, induction of forward locomotion and the velocity of this movement. SMOOT$_{in\ vitro}$ allowed for a quantitative assessment of the different conditions studied and with that helped isolate the supplements that were key for SPZ motility. This SPZ motility analysis tool can be of future use to gain insight in the mechanisms behind SPZ migratory behavior, to determine the most optimal vaccine formulation, to study the effect of radiation and chemical attenuation of SPZ and to screen potential SPZ motility inhibiting drugs.

Acknowledgments: The authors are grateful to ing. J. Ramesar and dr. C.J. Janse for support with the mosquito infection. The research leading to these results has received funding from the European Research Council under the European Union's Seventh Framework Programme (FP7/2007-2013) (2012-306890), a ZONMW VENI grant (016.156.076) financed by the Netherlands Organization for Scientific Research (NWO) and a Gisela Thier fellowship of the LUMC.

REFERENCES

1. Organization, W.H., World malaria report 2018. World Health Organization: Geneva, 2018.
2. Sinnis, P. and F. Zavala, The skin: where malaria infection and the host immune response begin. Seminars in Immunopathology, 2012. 34(6): p. 787-792.
3. Douglas, R.G., et al., Screening for potential prophylactics targeting sporozoite motility through the skin. Malaria Journal, 2018. 17.
4. Hafalla, J.C.R., et al., Priming of CD8(+) T cell responses following immunization with heat-killed Plasmodium sporozoites. European Journal of Immunology, 2006. 36(5): p. 1179-1186.
5. Coppi, A., et al., The Plasmodium circumsporozoite protein is proteolytically processed during cell invasion. J Exp Med, 2005. 201(1): p. 27-33.
6. Ejigiri, I., et al., Shedding of TRAP by a rhomboid protease from the malaria sporozoite surface is essential for gliding motility and sporozoite infectivity. PLoS Pathog, 2012. 8(7): p. e1002725.
7. Munter, S., et al., Plasmodium sporozoite motility is modulated by the turnover of discrete adhesion sites. Cell Host Microbe, 2009. 6(6): p. 551-62.
8. Battista, A., F. Frischknecht, and U.S. Schwarz, Geometrical model for malaria parasite migration in structured environments. Phys Rev E Stat Nonlin Soft Matter Phys, 2014. 90(4): p. 042720.
9. Kudryashev, M., et al., Structural basis for chirality and directional motility of Plasmodium sporozoites. Cell Microbiol, 2012. 14(11): p. 1757-68.
10. Boucher, L.E. and J. Bosch, The apicomplexan glideosome and adhesins - Structures and function. J Struct Biol, 2015. 190(2): p. 93-114.
11. Daher, W. and D. Soldati-Favre, Mechanisms controlling glideosome function in apicomplexans. Curr Opin Microbiol, 2009. 12(4): p. 408-14.
12. Aly, A.S., A.M. Vaughan, and S.H. Kappe, Malaria parasite development in the mosquito and infection of the mammalian host. Annu Rev Microbiol, 2009. 63: p. 195-221.
13. Douglas, R.G., et al., Active migration and passive transport of malaria parasites. Trends Parasitol, 2015. 31(8): p. 357-62.
14. Montagna, G.N., K. Matuschewski, and C.A. Buscaglia, Plasmodium sporozoite motility: an update. Front Biosci (Landmark Ed), 2012. 17: p. 726-44.
15. Moreau, C.A., et al., A unique profilin-actin interface is important for malaria parasite motility. PLoS Pathog, 2017. 13(5): p. e1006412.
16. Natarajan, R., et al., Fluorescent Plasmodium berghei sporozoites and pre-erythrocytic stages: a new tool to study mosquito and mammalian host interactions with malaria parasites. Cellular microbiology, 2001. 3(6): p. 371-379.
17. Frischknecht, F., et al., Imaging movement of malaria parasites during transmission by Anopheles mosquitoes. Cell Microbiol, 2004. 6(7): p. 687-94.
18. Vanderberg, J.P. and U. Frevert, Intravital microscopy demonstrating antibody-mediated immobilisation of Plasmodium berghei sporozoites injected into skin by mosquitoes. Int J Parasitol, 2004. 34(9): p. 991-6.
19. Amino, R., et al., Quantitative imaging of Plasmodium transmission from mosquito to mammal. Nat Med, 2006. 12(2): p. 220-4.
20. Formaglio, P., et al., Loss of host cell plasma membrane integrity following cell traversal by Plasmodium sporozoites in the skin. Parasitol Int, 2014. 63(1): p. 237-44.
21. Hopp, C.S., et al., Longitudinal analysis of Plasmodium sporozoite motility in the dermis reveals component of blood vessel recognition. Elife, 2015. 4.
22. Vanderberg, J.P., Imaging mosquito transmission of Plasmodium sporozoites into the mammalian host: immunological implications. Parasitol Int, 2014. 63(1): p. 150-64.
23. Muthinja, M.J., et al., Microstructured Blood Vessel Surrogates Reveal Structural Tropism of Motile Malaria Parasites. Adv Healthc Mater, 2017. 6(6).
24. Perschmann, N., et al., Induction of malaria parasite migration by synthetically tunable microenvironments. Nano Lett, 2011. 11(10): p. 4468-74.
25. Kebaier, C. and J.P. Vanderberg, Initiation of Plasmodium sporozoite motility by albumin is associated with induction of intracellular signalling. Int J Parasitol, 2010. 40(1): p. 25-33.
26. Vanderberg, J.P., Studies on the motility of Plasmodium sporozoites. J Protozool, 1974. 21(4): p. 527-37.

27. Carey, A.F., et al., Calcium dynamics of Plasmodium berghei sporozoite motility. Cell Microbiol, 2014. 16(5): p. 768-83.
28. Carey, A.F., R. Menard, and D.Y. Bargieri, Scoring sporozoite motility. Methods Mol Biol, 2013. 923: p. 371-83.
29. Stewart, M.J. and J.P. Vanderberg, Malaria sporozoites leave behind trails of circumsporozoite protein during gliding motility. J Protozool, 1988. 35(3): p. 389-93.
30. Bane, K.S., et al., The Actin Filament-Binding Protein Coronin Regulates Motility in Plasmodium Sporozoites. PLoS Pathog, 2016. 12(7): p. e1005710.
31. Haeberlein, S., et al., Protective immunity differs between routes of administration of attenuated malaria parasites independent of parasite liver load. Scientific reports, 2017. 7(1): p. 10372.
32. Schindelin, J., et al., Fiji: an open-source platform for biological-image analysis. Nat Methods, 2012. 9(7): p. 676-82.
33. Hegge, S., et al., Automated classification of Plasmodium sporozoite movement patterns reveals a shift towards productive motility during salivary gland infection. Biotechnol J, 2009. 4(6): p. 903-13.
34. Mack, S.R. and J.P. Vanderberg, Plasmodium berghei: energy metabolism of sporozoites. Exp Parasitol, 1978. 46(2): p. 317-22.
35. Hegge, S., et al., Multistep adhesion of Plasmodium sporozoites. FASEB J, 2010. 24(7): p. 2222-34.
36. Heintzelman, M.B., Gliding motility in apicomplexan parasites. Semin Cell Dev Biol, 2015. 46: p. 135-42.
37. Baum, J., et al., Host-cell invasion by malaria parasites: insights from Plasmodium and Toxoplasma. Trends Parasitol, 2008. 24(12): p. 557-63.
38. Winkel, B.M.F., et al., A tracer-based method enables tracking of Plasmodium falciparum malaria parasites during human skin infection Theranostics, 2019. 9(10): p. 2768-2778.
39. Lyke, K.E., et al., Attenuated PfSPZ Vaccine induces strain-transcending T cells and durable protection against heterologous controlled human malaria infection. Proc Natl Acad Sci U S A, 2017. 114(10): p. 2711-2716.

SUPPLEMENTARY INFORMATION

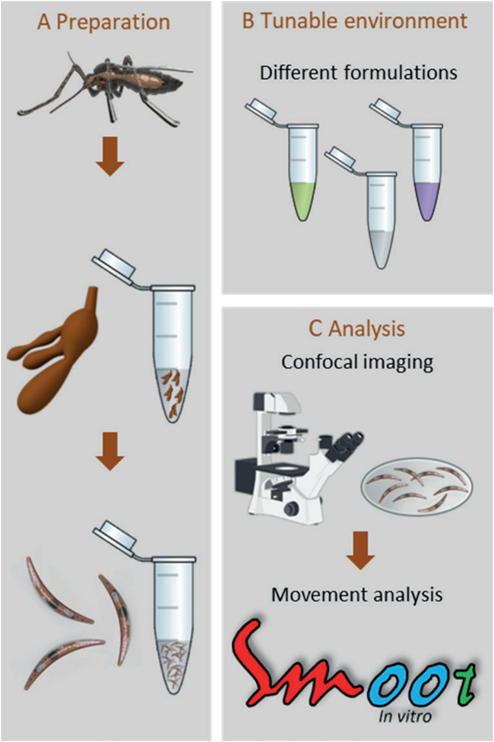

Sup. Figure S1 Sporozoite motility analysis tool. A) The *Plasmodium berghei* SPZ were obtained by manual dissection and crushing of the salivary glands of infected *Anopheles stephensi* mosquitoes. B) The behavior of SPZ in different types of media was studied. C) The SPZ were imaged by confocal microscopy and analyzed using the software SMOOT.

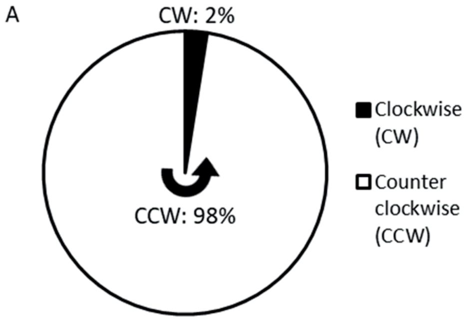

B

Condition	CW (%)	CCW (%)
PBS+BSA	n.a.	n.a.
HBSS+BSA	4	96
RPMI+BSA	6	94
PBS+FBS	2	98
HBSS+FBS	2	98
RPMI+FBS	0	100

Sup. Figure S2 (Counter) clockwise movement. A) Distribution of clockwise (CW) and counter-clockwise (CCW) turning SPZ for the pooled dataset. B) Distribution of CW and CCW turning SPZ per condition.

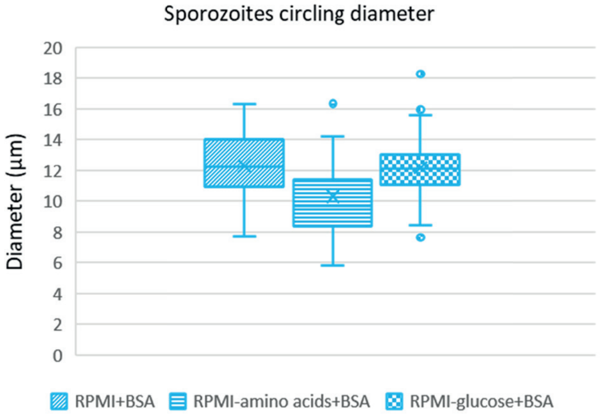

Sup. Figure S3 Sporozoites circling diameter. The average diameter of the circles of turning SPZ in RPMI and RPMI without glucose (both enriched with BSA) were 12.3 µm and 12.2 µm respectively. The average diameter of the circles of turning SPZ in RPMI without amino acids and enriched with BSA was significantly smaller: 10.3 µm ($p<0.001$; independent sample t-test).

2

Quantification of wild-type and radiation attenuated *Plasmodium falciparum* sporozoite motility in human skin

Béatrice M.F. Winkel*, Clarize M. de Korne*, Matthias N. van Oosterom, Diego Staphorst, Mark Meijhuis, Els Baalbergen, Munisha S. Ganesh, Koen J. Dechering, Martijn W. Vos, Séverine C. Chevalley-Maurel, Blandine Franke-Fayard, Fijs W.B. van Leeuwen, Meta Roestenberg

*These authors contributed equally to this work

Scientific Reports 2019. DOI: 10.1038/s41598-019-49895-3

ABSTRACT

Given the number of global malaria cases and deaths, the need for a vaccine against *Plasmodium falciparum* (*Pf*) remains pressing. Administration of live, radiation-attenuated *Pf* sporozoites can fully protect malaria-naïve individuals. Despite the fact that motility of these attenuated parasites is key to their infectivity and ultimately protective efficacy, sporozoite motility in human tissue (e.g. skin) remains wholly uncharacterized to date. We show that the ability to quantitatively address the complexity of sporozoite motility in human tissue provides an additional tool in the development of attenuated sporozoite vaccines. We imaged *Pf* movement in the skin of its natural host and compared wild-type and radiation-attenuated GFP-expressing *Pf* sporozoites. Using custom image analysis software and human skin explants we were able to quantitatively study their key motility features. This head-to-head comparison revealed that radiation attenuation impaired the capacity of sporozoites to vary their turn angle, velocity and direction, promoting less refined movement patterns. Understanding and overcoming these changes in motility will contribute to the development of an efficacious attenuated parasite malaria vaccine.

INTRODUCTION

Nearly half the human population lives in areas with an increased risk of malaria transmission, resulting in more than 200 million cases each year[1], illustrating the urgent need for a highly effective malaria vaccine. Vaccines based on live attenuated *Plasmodium falciparum* (*Pf*) parasites obtained from the mosquito salivary gland, so-called sporozoites (SPZ), are currently most promising. Clinical trials that used mosquitoes to transmit SPZ into human subjects yielded 100% protection in non-endemic settings[2-4]. When translating the seminal mosquito bite studies into a needle-based cryopreserved vaccine formulation[3], intradermal (ID) injection of isolated live attenuated SPZ were found to induce inferior protective immunity in humans[5]. Further research showed that an impractical intravenous (IV) route of attenuated SPZ injection was more effective, because IV administration promotes transportation of SPZ to the liver[3, 4, 6], which is key to the induction of protection[7, 8]. To date, the factors which affect the motility of *Pf* SPZ on their journey from human skin to liver have not been studied.

Imaging studies using genetically modified fluorescent *Plasmodium berghei (Pb*) or yoelii *(Py*) SPZ in mouse skin yielded insight into the migration patterns of SPZ, with contrasting differences between *in vitro* and *in vivo* motility or the site of injection (tail or ear)[9-14]. Because the anatomical structure of murine skin differs from human skin, with respect to thickness, muscle layers, dermal papillae and hair follicle density[15, 16], a human skin model would provide a valuable contribution. Despite differences such as the lack of blood flow, *ex vivo* skin explant models have shown excellent viability of dermal cells over long periods of time[17, 18]. Analysis of *Pf* SPZ migration in human tissue is an important first step to understanding *Pf* transmission and attenuated SPZ vaccine delivery. In addition, a human skin model could also allow for future evaluation of subunit vaccines[14].

Attenuated SPZ vaccines have been produced using radiation attenuation (RA), gene modification or concomitant drug administration[19]. RA is the most commonly used method, whereby RA SPZ vaccines are currently entering phase 3 clinical trials[20, 21]. RA introduces double strand breaks in DNA[22] and has been shown to impact the SPZ gene expression and ultrastructure[23-25]. In both ways, SPZ motility might be influenced. At present, preservation of motility following RA can only be validated using an *in vitro* gliding assay[26], where the SPZ are allowed to glide on a glass surface. However, this assay does not mimic the complexity of environmental interactions that are observed in tissue (e.g. physical confinement)[10, 27]. Therefore, *ex vivo* imaging technologies that make use of human tissue are required.

The pioneering literature that presents image analysis of rodent SPZ (*Pb*) movement in murine tissue, has focused on an often used measure of random diffusion of particles, the mean squared displacement (MSD)[9, 10, 28]. This measurement separates anomalous diffusion (with a non-linear relation to time) from the classic linear diffusion process. This has supported quantitative investigations toward motility changes over time and in relation to dermal structures[9, 10]. As SPZ movement through tissue suits a specific purpose, it makes sense for motility analyses to include quantitative parameters for directionality rather than limit the analysis to parameters that present random diffusion. Analysis of directional movement, referred to as tortuosity, is a common approach to study e.g. animal migration through the desert[29] and analysis of disease severity in cognitively impaired patients[30], but has also been applied during cell tracking studies[31]. The tortuosity of movement indicates whether it is directional or random. We reasoned that the concept of directional movement could complement the diffusion-based in skin SPZ analysis and could provide more detailed insight in SPZ motility in complex environments such as human skin tissue.

The aim of this study was to image and quantitatively assess motility of wild-type, GFP-expressing *Pf* SPZ (*Pf*^{WT}) in human skin (Figure 1). For image analysis we developed a software tool for in skin analysis called SMOOT$_{\text{human skin}}$ (Sporozoite Motility Orienting and Organizing Tool) that can output tortuosity and velocity related motility parameters of individual *Pf* SPZ. In order to assess the effect of RA on SPZ migration, we subsequently compared the motility of *Pf*^{WT} and RA SPZ (*Pf*^{RA}) populations in human skin explants.

METHODS

Study design

In order to explore movement characteristics of *Pf* sporozoites (SPZ) in human skin explants, we performed a controlled laboratory experiment, in which we compared motility parameters (assessed using our custom software tool SMOOT$_{\text{human skin}}$) of 352 unattenuated *Pf* SPZ (*Pf*^{WT}; 14 movie sections) with those of 350 radiation attenuated *Pf* SPZ (*Pf*^{RA}; 18 movie sections). The movies were made of SPZ injected in human skin explants of two donors (in two independent experiments), comparing *Pf*^{WT} with *Pf*^{RA} in both donors at two different locations in the skin ending up with four unique locations for both *Pf*^{WT} and *Pf*^{RA}. The experiments were evaluated individually (Sup. Figure S1), thereafter the data was pooled (Sup. Figure S2) and the final analysis of the motility of *Pf*^{WT} vs *Pf*^{RA} was performed on the pooled dataset. The study was not randomized or blinded.

Parasites

Anopheles stephensi mosquitoes infected with a transgenic *Pf* line that constitutively expresses fluorescent reporter protein GFP under the *pf*CS promotor (NF54-ΔPf47-5'*csp*-GFP-Luc, kindly provided by dr. Koen Dechering; TropIQ Health Sciences), were killed using ethanol spray and rinsed in RPMI 1640 (Invitrogen). Salivary glands were dissected manually at day 14-21 post infection, incubated in RPMI 1640 and kept on ice. Radiation attenuation of SPZ was performed by irradiating intact salivary glands to a total dose of 20 krad using a Cesium radiation source (total of 28 minutes) on ice. During this time control SPZ were also kept on ice. Within 1 hr, glands were homogenized to release *Pf* SPZ. SPZ were then counted using a Bürker counting chamber, brought to a concentration of 20 x 10^6/ml in RPMI 1640 containing 10% Fetal Calf Serum (FCS; Bodinco) and used for imaging experiments immediately.

Skin explants

We obtained human skin explants from collaborating hospitals immediately after abdominal skin reduction surgery. The use of human skin explants for this research was approved by the Commission Medical Ethics (CME) of the LUMC (CME: B18-009). The methods were carried out in accordance with the relevant guidelines and regulations, and informed consent was obtained from all participants. The skin explants were kept at 4°C for 3 hr until use. Subcutaneous fat was removed and the epidermal side was cleaned with 70% ethanol. One million SPZ were injected intradermally in a 50 µl injection using a 0.3 ml insulin syringe (30G; BD). In order to facilitate quick localization of the injection site by confocal microscopy the injection formulation contained Yellow-Green fluorescent 500 nm Latex nanoparticles (Sigma Aldrich). Immediately after injection, the injection site was biopsied using a 6 mm biopsy punch, sliced longitudinally through the center and mounted on a microscopy slide with a 1 mm depression in RPMI 10% FCS. Slides were imaged within 30 minutes post injection.

Confocal imaging

Skin biopsy slides were imaged using the time-lapse function of the Leica TSC (true confocal scanning) SP8 microscope (Leica Microsystems). 2D images (no z-stacks) were obtained using an exposure time of 1.7 seconds per frame (400 frames per movie section, 11 minutes) and a 40x objective. Microscopy videos were rendered using accompanying Leica LASX software and were analyzed using custom software $\text{SMOOT}_{\text{human skin}}$.

Movie analysis with $\text{SMOOT}_{\text{human skin}}$

MATLAB (The MathWorks Inc. Natick, MA, USA) software was created for in skin SPZ analysis, which we called Sporozoite Motility Orienting and Organizing Tool ($\text{SMOOT}_{\text{human skin}}$). This tool is an extended version compared to the $\text{SMOOT}_{\text{human skin}}$ tool previously used to determine the velocity and movement pattern distribution of Cy5M_2 labeled *Pf* SPZ[32]. Similar to our recently published *in vitro* tool $\text{SMOOT}_{\textit{in vitro}}$[33], the upgraded $\text{SMOOT}_{\text{human skin}}$ software now also includes turn angle and displacement. In addition, $\text{SMOOT}_{\text{human skin}}$ takes into account the directionality by computing the angular dispersion, straightness index and the direction of SPZ tracks. Firstly, SPZ tracks were characterized as motile or stationary based on their displacement. Subsequently, motile tracks were subdivided into movement patterns: sharp turn, slight turn and linear.

To investigate the influence of RA on SPZ motility, we compared SMOOT$_{\text{human skin}}$ parameter outcomes of 14 *Pf*^{WT} motility movie files (11 minutes/movie, 154 minutes total, 352 SPZ tracks consisting of 511 segments and 26932 frames; Sup. Movie S1) with 18 *Pf*^{RA} motility files (11 minutes/ movie, 198 minutes total, 350 SPZ tracks consisting of 563 segments and 25804 frames; Sup. Movie S2). Software output was manually validated.

Velocity was determined by measuring the displacement between frames. We defined step number in the track *i* to measure velocity *v* using formula (1), with *x as* the median pixel location of the segmented structure and *t* as the time passed in seconds.

(1) $$v(i) = \frac{x_i - x_{i-1}}{t_i - t_{i-1}} = \frac{dx}{dt}$$

The mean squared displacement (MSD) is a common measure to distinguish random versus non-random motion for moving particles and was previously used to analyze SPZ motility[9, 10]. The squared displacement (SD) is a measure of the displacement per time point of an individual track, which can be calculated with formula (2):

(2) $$SD(i) = \left(x_n(i) - x_n(0)\right)^2$$

The MSD was derived from the SD of all linear tracks using formula (3):

(3) $$MSD(i) = \langle (x(i) - x_0)^2 \rangle = \frac{1}{N}\sum_{n=1}^{N}\left(x_n(i) - x_n(0)\right)^2$$

The turn angle (θ) of the SPZ was defined by the angle difference between path directions in consecutive frames. If we start calculating the turn angle from location x_0 then the SPZ reaches x_i after *i* steps. The angle of x_i is the angle δ_i between point x_i and the horizontal. The turn angle was then defined as described in formula (4).

(4) $$\theta_i = \delta_i - \delta_{i-1}$$

The straightness index (SI) is the most basic approach to quantify tortuosity and is defined as the ratio of distance between track end points (*C*) and track length (*L*), as calculated using formula (5). This parameter quantifies deviation from a straight line, e.g. SI = 1 means a perfect linear path, SI = 0 means circular motion.

(5)
$$SI = \frac{C_{track}}{L_{track}} = \frac{x(i) - x(0)}{\sum_{k=1}^{i}\big(x(k) - x(k-1)\big)}$$

Angular dispersion (AD) quantifies the number of turning angles diverging from the main angle of movement. It describes tortuosity by quantifying changes in direction. It is calculated using the turn angles (formula (4)) according to the following formula:

(6)
$$AD = \frac{1}{I}\sqrt{C^2 + S^2}$$

Where I is the last step of the track and C and S are defined as:

(7)
$$C = \sum_{i=1}^{I} \cos\theta_i \; S = \sum_{i=1}^{I} \sin\theta_i$$

Statistics

Data extracted from $\mathrm{SMOOT}_{\text{human skin}}$ was analyzed in IBM (Armonk, NY, USA) SPSS version 23 or GraphPad Prism (La Jolla, CA, USA) version 7. Comparisons between two or more independent categorical data groups were made by Chi-squared test, continuous nonparametric parameters were compared by Mann-Whitney U test. $P<0.05$ was considered statistically significant. Bonferroni correction was applied for post hoc analysis after Chi-squared testing.

RESULTS

Generation of a semi-automated sporozoite migration analysis tool

Firstly, we generated confocal microscopy movies of *Pf*$^{\mathrm{WT}}$ and *Pf*$^{\mathrm{RA}}$ migrating through human skin explants by a trans sectional skin setup (fourteen 11 min movie sections of *Pf*$^{\mathrm{WT}}$ and eighteen 11 min movie sections of *Pf*$^{\mathrm{RA},}$ yielding a total of 352 and 350 analyzed SPZ, respectively). Experiments were performed in two independent donor samples and while splitting the batch of SPZ in a *Pf*$^{\mathrm{WT}}$ and *Pf*$^{\mathrm{RA}}$ group. Using our semi-automated software tool $\mathrm{SMOOT}_{\text{human skin}}$, we were able to track SPZ movement (Figure 1) by identifying SPZ based on their shape and fluorescence intensity (Figure 1B) and connecting their location over time (see Sup. Figure S1 for an overview of the data per individual location and supplementary movie S1 and S2 for examples). SPZ locations per frame were stitched together in order to generate track segments, where multiple segments in the same 2D plane build up a full track (Figure 1B-C). Depending on the straightness index (SI) of the individual segments, their movement patterns (sharp turn, slight turn and linear) were determined and color-coded (Figure 1C). Slight turns were defined as the turns which resulted from the natural curvature of the SPZ (0.21-0.23 μm^{-1})[34].

Sharper turns, requiring extra bending of the SPZ, were defined as sharp turns[34]. Furthermore, the following movement parameters were calculated at track level: straightness index (SI) and angular dispersion (AD), at segment level: turn direction (clockwise or counter clockwise) and at frame level: mean squared displacement (MSD) and velocity. Using the unique ID allocated to each individual SPZ track, all computed parameters were extracted for the individual SPZ and, where relevant, analyzed over time. In the experiments 81% of the SPZ were characterized as motile, which surpasses the 66% reported earlier for *Pb* SPZ in murine skin[9].

Mean Squared Displacement (MSD) data alone does not reflect individual sporozoite movement heterogeneity

In analogy to previous protocols for *Pb* SPZ[10], we evaluated the MSD of linear Pf^{WT} tracks (37% of tracks). Comparing the MSD of Pf^{WT} with the Pf^{RA} population (containing 18.5% total linear tracks) yielded no significant difference (Figure 2A). This analysis, however, excluded a large fraction of SPZ that exhibited non-linear movement (slight and sharp turn; 81.5% for Pf^{RA} and 63% for Pf^{WT}). We thus concluded that this analysis methodology was not suitable to fully grasp the complexity of *Pf* motility in human skin. In addition, we found that squared displacement plots of SPZ revealed a high level of heterogeneity. A typical example of this heterogeneity is shown in Figure 2B-C, where we plotted the squared displacement (SD; where displacement is the difference in SPZ position between begin and endpoint of a track) of 4 very different individual SPZ tracks from the same movie file. In order to do justice to the sample heterogeneity, we aimed to include other parameters of movement, such as the tortuosity, in the motility analysis.

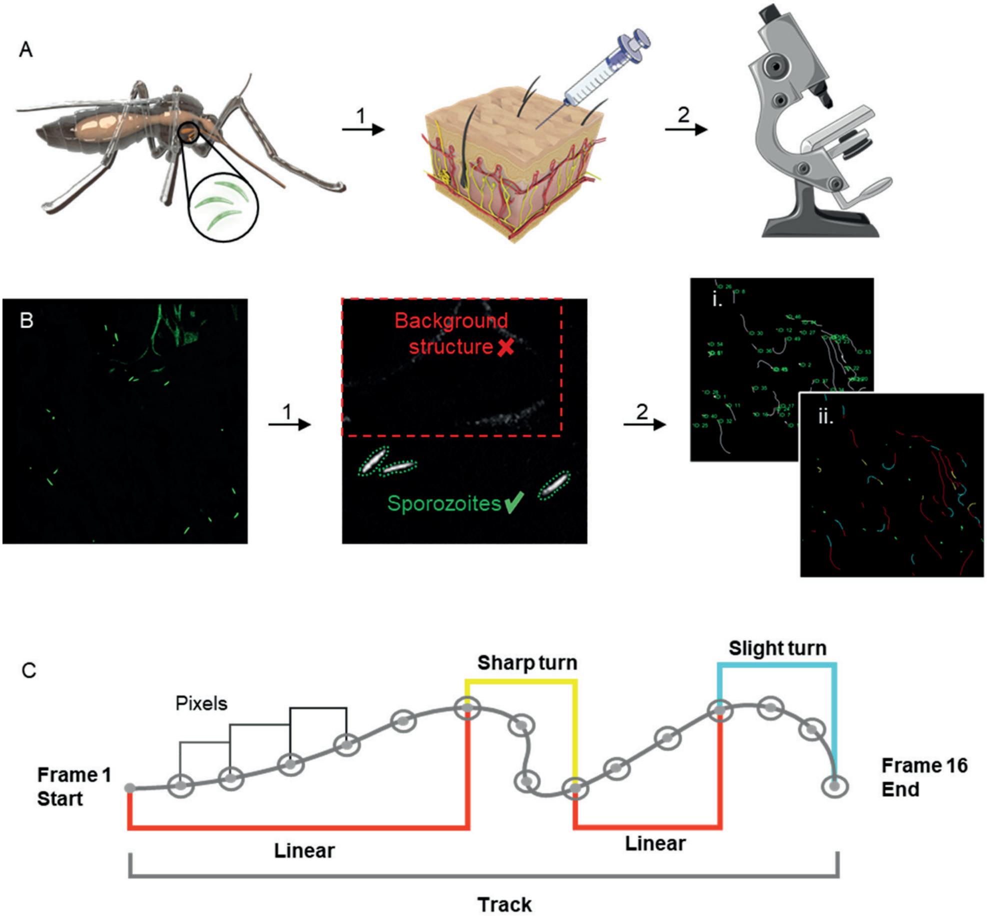

Figure 1 Schematic of experimental setup and SMOOT$_{\text{human skin}}$ analysis. A) Schematic of an *Anopheles* mosquito as the host of *Plasmodium* SPZ within its salivary glands. Isolated SPZ, *Pf*^{WT} or *Pf*^{RA}, were injected into human skin (1). The skin samples containing SPZ were filmed using a confocal microscope (2) (Images of needle and microscope were adapted from image copyright https://smart.servier.com, Creative Commons Attribution 3.0 Unported License, https://creativecommons.org/licenses/by/3.0/). B) Raw confocal video images were uploaded into SMOOT$_{\text{human skin}}$. Per video frame individual SPZ were semi-automatically segmented (1). Segmented SPZ in consecutive frames were stitched to generate tracks. Generated tracks have a unique SPZ ID (i) in order to extract measured parameters (for example movement pattern (ii)) per SPZ over time (2). C. SPZ tracks are divided into segments based on the underlying movement pattern.

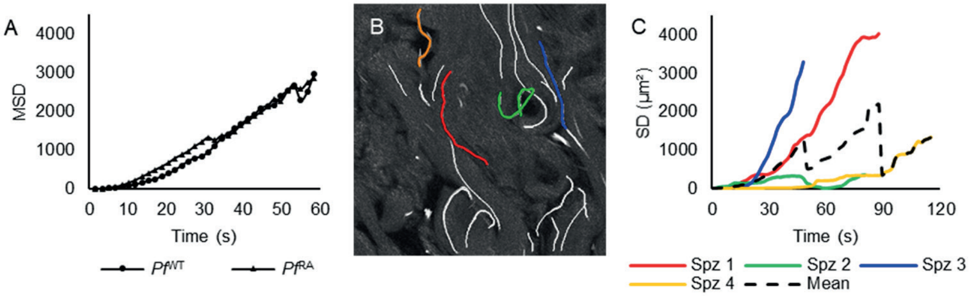

Figure 2 Mean squared displacement of sporozoites. A) Mean squared displacement (MSD in µm^2) of the SPZ plotted against time, only linear tracks are taken into account. B) Examples of individual SPZ tracks in a single movie file. C) The four differently colored individual tracks from B. are presented as squared displacement (SD in µm^2) over time and presented relative to the dotted line, which presents the MSD of all four lines.

Tortuosity analysis reveals differences in sporozoite motility after RA

Using tortuosity-based analysis we quantified pattern characteristics of SPZ tracks. First, the individual experiments were evaluated (Sup. Figure S1), thereafter the data of all *Pf*^{RA} and *Pf*^{WT} was pooled (Sup. Figure S2) and further analyzed. Automated pattern classification of SPZ tracks showed that 37% of *Pf*^{WT} tracks were linear, 42% classified as sharp turn and 21% as slight turn (Fig. 3A). *Pf*^{WT} tracks displayed a median SI of 0.86, indicating relatively straight tracks (SI close to 1 indicates a linear track; Figure 3B) and a balanced AD of 0.45 indicating random meandering of SPZ (AD close to 1 indicates a consistent track, AD close to 0 indicate random direction changes; Figure 3C).

In contrast, the *Pf*^{RA} population displayed significantly more slight and sharp turn segments (7.2% blue and 74.3% yellow color coding respectively), and a decrease in linear patterns (18.5%, red) as compared to the *Pf*^{WT} (Figure 3A). This difference was caused by continuous circular turning behavior of SPZ (arrowheads Figure 3A), as well as a back and forth motion (180° turn; hereafter termed 'reversal'). Although *in vitro* on circular movement of *Pf* is reported on coated surfaces, under the conditions studied, *Pf* did not show such movement (see Sup. Movie S4). This was confirmed by an increase in SI values close to 0, representing these turning tracks (Figure 3B; post hoc Chi squared test p=0.008 and p=<0.0001 respectively). In addition, *Pf*^{RA} showed significantly more persistent straight tracks compared to *Pf*^{WT} (increased indices close to 1; overall Chi squared test p=<0.0001; median SI 0.89). Similarly, *Pf*^{RA} showed more consistent tracks with fewer deviations from the mean angle of movement patterns compared to *Pf*^{WT} (Figure 3C; angular dispersion median 0.92; overall Chi squared test p=<0.001 post hoc Chi squared test AD >0.75 p=<0.0001). Taken together, the pattern analysis and tortuosity parameters indicate that *Pf*^{RA} exhibit reduced motility variation compared to *Pf*^{WT} and preferentially display continuous circling patterns.

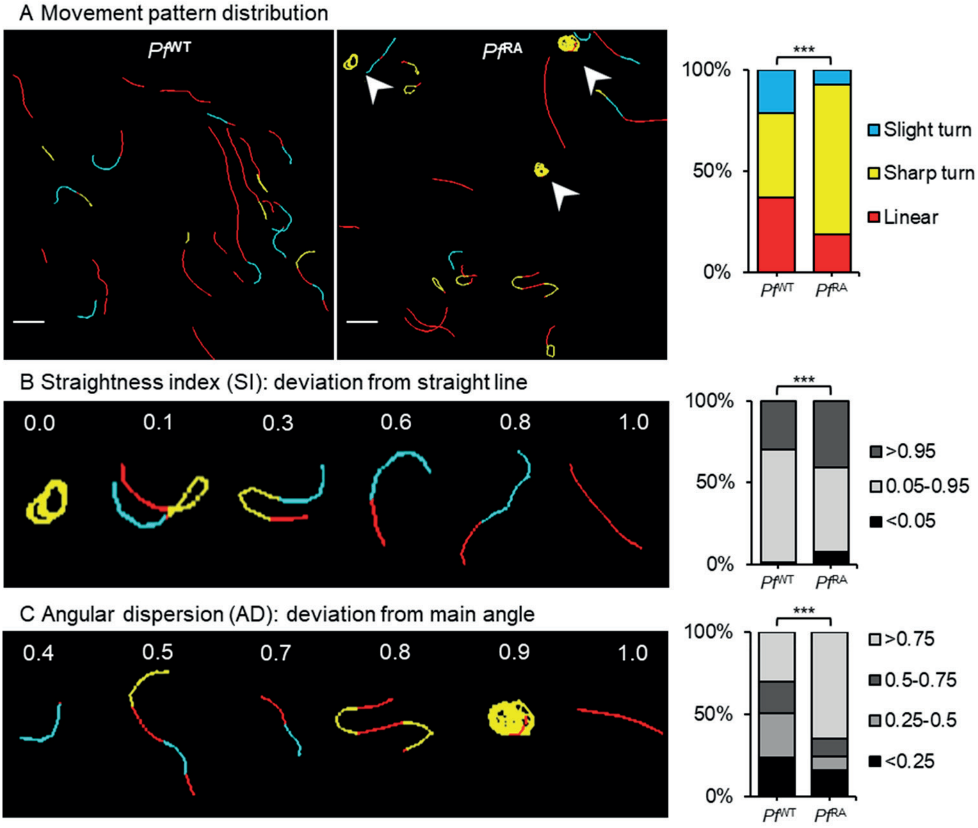

Figure 3 Tortuosity of sporozoite tracks. A) Two examples of movement pattern maps of tracked SPZ; *Pf*^{WT} in skin (left) and *Pf*^{RA} in skin (middle). Linear segments are depicted in red, slight turns in blue and sharp turns in yellow. Arrowheads indicate circular SPZ tracks comparable to *in vitro* movement. The movement pattern distribution of the *Pf*^{WT} and *Pf*^{RA} is quantified for all SPZ tracks based on frames (right). Scale bar: 20 µm. B) To illustrate the concept of straightness index (SI) in relation to SPZ tracks, 6 tracks are displayed out of the movement pattern maps shown in A. The SI distribution is quantified based on the SI values of total tracks (*Pf*^{WT} median: 0.89, IQR: 0.66-0.96; *Pf*^{RA} median: 0.90, IQR: 0.46-0.98). C) To illustrate the concept of angular dispersion (AD) in relation to SPZ tracks, 6 tracks are displayed out of the movement pattern maps shown in A. The AD distribution is quantified based on the AD values of total tracks (*Pf*^{WT} median: 0.47, IQR: 0.26-0.80; *Pf*^{RA} median: 0.93, IQR: 0.51-0.99). *** = p<0.0001 using Chi squared test.

RA causes sporozoites to circle consistently in a clockwise direction

Possibly due to the tilted arrangement of the SPZ polar-ring[35], circularly moving SPZ display a preferred clockwise (CW) turn direction *in vitro*[36]. In the three dimensional (3D) skin environment this preference was lost; SMOOT$_{\text{human skin}}$ analysis demonstrated that *Pf*^{WT} turned equally CW and counterclockwise (CCW; Figure 4A). Surprisingly, analysis of turn direction in the *Pf*^{RA} population yielded a preference for CW directionality (Figure 4A; 65.2% CW; p=0.013). Analysis of the duration of the turns (number of frames) revealed that *Pf*^{RA}

continued turning in circles when this pattern was initiated.

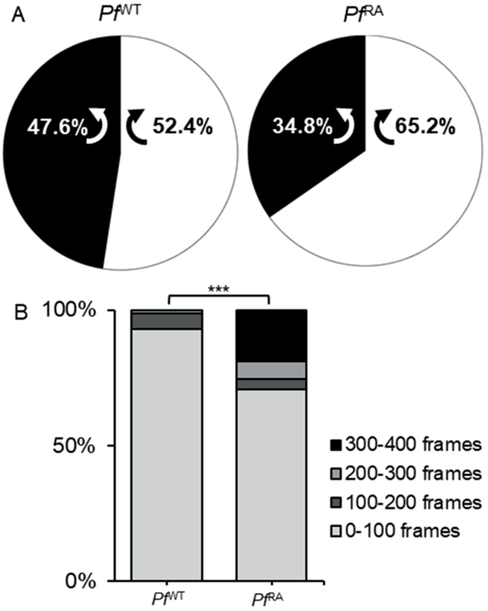

Figure 4 Direction of turning sporozoites. A) Turn direction of Pf^{WT} and Pf^{RA} in skin. Pf^{RA} turn significantly more CW than Pf^{WT}, p=0.013 using Chi-Squared test. B) The sharp turns of Pf^{RA} contain significantly more frames than the turns of Pf^{WT} (Pf^{WT} median: 32, IQR: 22-55; Pf^{RA} median: 33, IQR: 14-218; p>0.000 using Chi-Squared test). Indicating persistent circular motion.

Per frame analysis of velocity reveals decreased velocity alterations after RA

In line with previous findings[9, 10, 37], we recorded an average SPZ velocity per track of 1.1 µm/s (time did not seem to have an effect on the average velocity (Sup. Figure S3)). $\text{SMOOT}_{\text{human skin}}$ also allowed analysis of the velocity per captured frame within a track (Figure 5), revealing marked variations over time. Examples illustrate that a single SPZ could display non-parametric velocity changes between 0 and 3.5 µm/s over the course of one track (Figure 5A). While the velocity changes occurred within all movement patterns, the median velocity was highest in linear segments followed by slight turns and in sharp turns (Figure 5B). Pf^{RA} consistently showed higher velocity in all movement patterns (median 1.1 µm/s vs 0.85 µm/s for linear tracks, 0.6 vs 0.48 µm/s for slight turns and 0.34 vs 0.24 µm/s for sharp turns in Pf^{RA} vs Pf^{WT} respectively, p=<0.0001). Despite the fact that Pf^{RA} displayed more 'slow' sharp turns, in a per frame analysis their overall median velocity at 0.37 µm/s was higher than the median velocity of Pf^{WT} (0.35 µm/s; p=<0.0001). This difference was caused by a reduction in stop-and-go action (frames with velocity <0.5 µm/s were 56.8 % for Pf^{RA} and 59.6 % for Pf^{WT}, p=0.037). Furthermore, velocity variability was smaller in Pf^{RA}

(Figure 5B, range 0-4.1 µm/s) compared to *Pf*^{WT} (0-4.8 µm/s). Corroborating this finding, *Pf*^{RA} velocities of linear tracks were normally distributed compared to a nonparametric velocity distribution for *Pf*^{WT} (Figure 5B, p=<0.0001), whereas velocities in other movement patterns were nonparametrically distributed for both *Pf*^{RA} and *Pf*^{WT}. Taken together, *Pf*^{RA} less readily alternated their velocity.

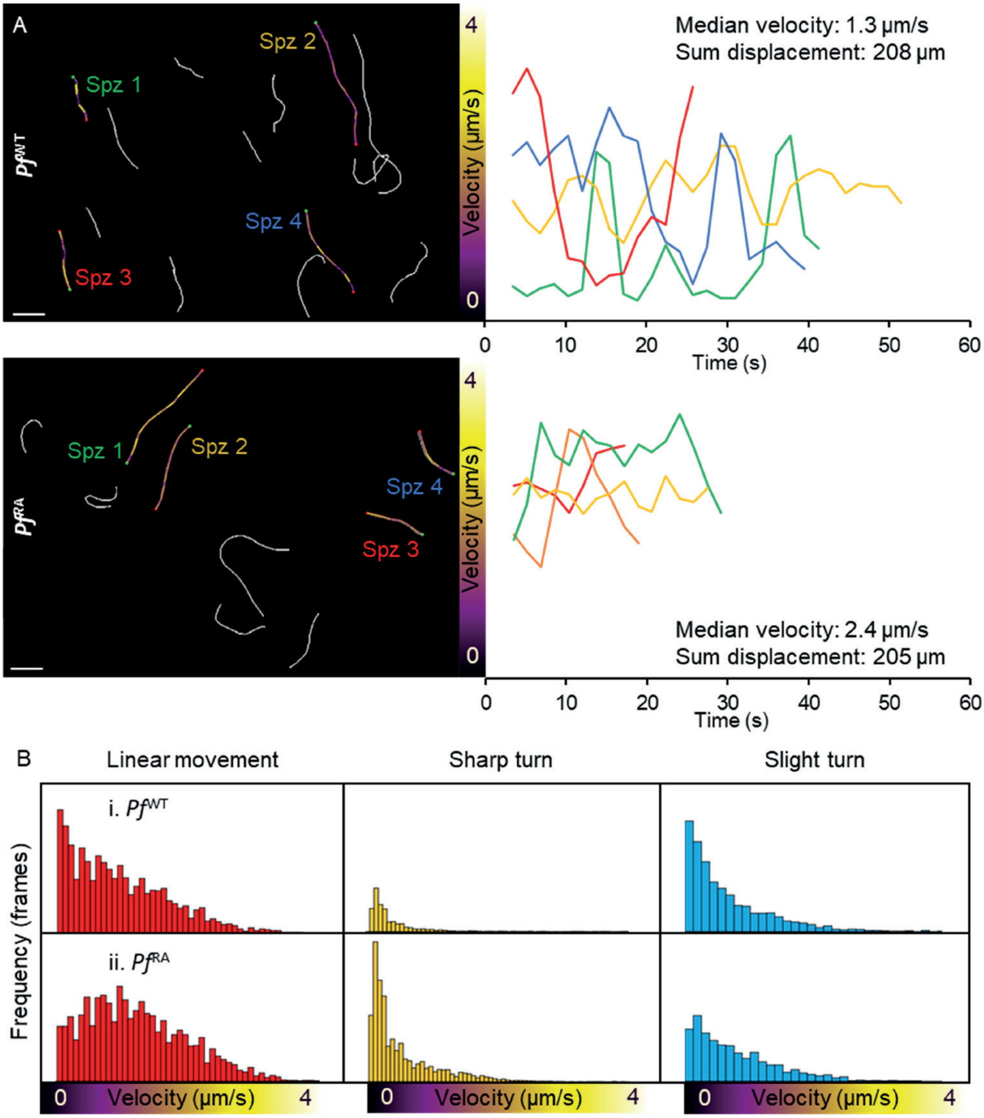

Figure 5 Velocity of sporozoites. A) Four *Pf*^{WT} (above) and four *Pf*^{RA} (below) tracks are color-coded based on velocity. Scalebar: 20 µm. Their individual velocity is plotted over time (right). B) Velocity distribution of *Pf*^{WT} and *Pf*^{RA} per movement pattern.

Pf^{RA} display a default motility pattern: reversal

Interestingly, some SPZ in the *Pf*^{RA} group (9% of motile *Pf*^{RA} tracks) revealed pendulum movement, whereby they reverse direction repeatedly moving up and down a short path (Figure 6; Sup. Movie S3). This is in line with earlier findings where SPZ moved in this particular fashion while residing in the mosquito[38-40]. Plotting this movement (over x and y axis) over time yielded a sinuous track (yellow) that is clearly distinct from the short linear track (red) observed in the same movie segment. Strikingly, this movement pattern was not observed in *Pf*^{WT}.

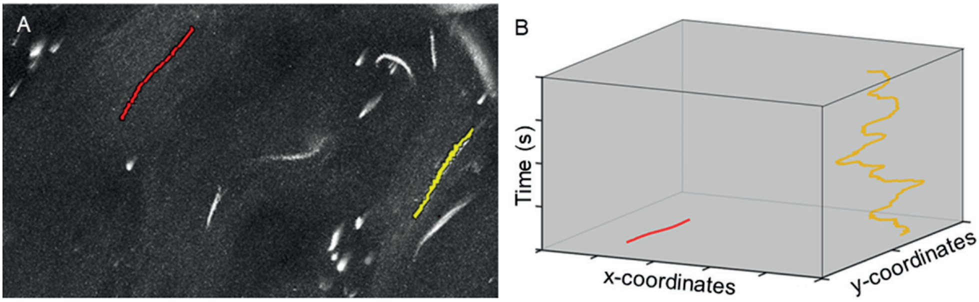

Figure 6 Reverse movement. A) In this example, one SPZ was moving in a linear direction and one SPZ was moving back and forth. The linear track is depicted in red, the reverse movement is classified as a sharp turn, thereby depicted in yellow. B) The coordinates of the linear and the reversal track are plotted in a xyt coordinate axis system.

DISCUSSION

In this study we compared movement of wild-type with irradiated *Pf* SPZ in a human skin explant using our semi-automated custom analysis tool for SPZ tracking. We found that *Pf*^{RA} display increased circular motility patterns, more extreme SI values and higher AD compared to *Pf*^{WT}. In addition, *Pf*^{RA} exhibited less variability in velocity over the course of their track and 'reversal' patterns were unique to this group. Combined, the data indicates that attenuation via radiation may alter SPZ motility.

In vitro, SPZ display very elementary circular movement with little variation in velocity, angle or direction[36, 41, 42]. Recently, we reported that for *Pb* SPZ, a complex interplay of various nutrients including albumin, glucose and certain amino acids and vitamins regulates parasite motility *in vitro*[33]. Under the conditions used to study the movement in human skin explants (uncoated glass; RPMI 160 + 10% FCS) *Pf* SPZ did not display this movement pattern *in vitro* (Sup. Movie S4). In skin, however, sharp turns (combination of circular and reversal movement) were observed in addition to linear and slight turn movement patterns. This indicates that the environment influences *Pf* SPZ movement and in particular their directionality. It was previously shown for *Pb* SPZ that an environment with artificial physical constraints in the form of pillars increases the movement directionality as function of interstitial space[27]. This trend is in line with the reported increase of tortuosity in porous materials that occurs when reducing the interstitial space[43]. An influence of tissue structure on directionality of *Pb* SPZ can also be extrapolated from the different motility patterns in the skin of mouse ears as compared to the skin of a mouse tail[10]. Our findings suggest that the highly complex heterogeneity of human skin composition, in combination with the mixed nutrient availability, may similarly impact motility patterns of individual SPZ, generating highly complex movement patterns which vary according to the local donor tissue structure.

Although *Pf* SPZ displayed average track velocities in line with previous reports (on average 1.1 µm/s as compared to previous studies reporting averages of 0.9-1.5 µm/s in mouse skin[9, 10, 37]), a per frame velocity analysis revealed ongoing stop-and-go actions. These heterogeneous patterns in combination with the high level of path tortuosity suggest that environmental cues and cellular interactions such as traversal[44] impact heterogeneity of direction and speed of the SPZ. Indeed, the SPZ surface displays many proteins such as CSP, SPECT1 and CelTOS which facilitate interaction with targets like heparan sulphate and αvβ3 integrin which are present in human skin[11, 45, 46]. Because these alterations in velocity resulted in a nonparametric velocity distribution, that differs between SPZ taking sharp or slight turns or moving straight, we reason that average velocity alone is insufficient to unravel complex migratory behavior.

Our findings suggest that radiation may not only effectively attenuate *Pf* SPZ at the liver stage, which has been described before[8], but could also influence their motility at the skin stage. Similar to what has been described before with respect to the effect of cryopreservation on *Pb* SPZ motility[47], RA also seems to induce small alterations in motility. The differences in motility between Pf^{WT} and Pf^{RA} (observed in samples from both donors), although minor, are indicative of a reduced complexity of the Pf^{RA} interaction with the tissue environment. Moreover, the increased AD of Pf^{RA}, and the increased duration of their turns seems to suggest that once a 'default' movement pattern has been initiated, the movement pattern persists. Since circling and reversal patterns result in Pf SPZ remaining in a single location, one could argue that this movement pattern would render SPZ at risk for elimination by phagocytic dermal immune cells, which could impact antigen presentation and vaccine efficacy.

Understanding how radiation attenuation interferes with these pathogen-host interactions could be important to identify novel vaccine targets or improve the efficacy of existing radiation attenuated SPZ vaccines. Here it should be noted that for our studies we solely used 20 krad attenuation dose as described previously in murine studies[48, 49], meaning we cannot state if a similar difference would be observed at lower radiation doses. However, increased radiation dosages result in reduced infectivity of *Plasmodium* species and reduced effectivity of attenuated parasite immunization[8, 50]. The altered motility induced by radiation may contribute to this reduced infectivity. It remains to be investigated whether similar effects also occur when using genetically modified SPZ vaccines[51-53].

Using viable human skin explants allowed us to analyze *Pf* SPZ movement in their natural skin environment thereby enhancing the possibilities to gain insight in their behavior. Obviously, also this model system has limitations. Although not per se relevant for the field of live attenuated *Pf* vaccines, intradermal syringe-based injections may not accurately represent the mosquito-based transmission of the disease[54]. The lack of blood and lymphatic circulation prevents *Pf* to migrate out of the skin, which means the motility of the total population of administered *Pf* is analyzed. Due to light attenuation in tissue, the analysis of SPZ movement was restricted to 2D, which shortened the length of the more linear tracks and thus biased circular and reversal movement patterns occurring in plane. Finally, the location in the dermis that was imaged seemed to affect SPZ movement patterns, even when the same batch of *Pf* was used. Nevertheless, we feel confident that the analysis performed in *ex vivo* human skin helps building a bridge between *in vitro* assays and *in vivo* assays of *Pb* SPZ in mouse skin[9, 10] and controlled human infection studies[21, 51].

In conclusion, we imaged *Pf* SPZ migration in the dermis of their natural host and performed an in-depth analysis of the motility of wild-type and irradiated *Pf* SPZ. We demonstrate loss of movement variability after radiation attenuation which might reflect reduced viability and ultimately decreased infectivity. Because of the ability of $\text{SMOOT}_{\text{human skin}}$ to analyze complex migration, it may contribute to the refinement of live SPZ vaccine formulations.

Acknowledgments: The authors would like to thank Sven van Leeuwen for his contribution to the images in this article. The research leading to these results has received funding from a ZONMW VENI grant (016.156.076) financed by the Netherlands Organization for Scientific Research (NWO) and a Gisela Thier fellowship of the LUMC.

REFERENCES

1. Organization, W.H., World malaria report 2018. World Health Organization: Geneva, 2018.
2. Roestenberg, M., et al., Protection against a malaria challenge by sporozoite inoculation. N Engl J Med, 2009. 361(5): p. 468-77.
3. Seder, R.A., et al., Protection against malaria by intravenous immunization with a nonreplicating sporozoite vaccine. Science, 2013. 341(6152): p. 1359-65.
4. Ishizuka, A.S., et al., Protection against malaria at 1 year and immune correlates following PfSPZ vaccination. Nat Med, 2016. 22(6): p. 614-23.
5. Epstein, J.E., et al., Live attenuated malaria vaccine designed to protect through hepatic CD8(+) T cell immunity. Science, 2011. 334(6055): p. 475-80.
6. Mordmuller, B., et al., Sterile protection against human malaria by chemoattenuated PfSPZ vaccine. Nature, 2017. 542(7642): p. 445-449.
7. Cochrane, A.H., R.S. Nussenzweig, and E.H. Nardin, Immunization against sporozoites. Malaria in Man and Experimental Animals, 1980: p. Academic Press, New York, Editor: Kreier, J.P. Pages 163-202.
8. Silvie, O., et al., Effects of irradiation on Plasmodium falciparum sporozoite hepatic development: implications for the design of pre-erythrocytic malaria vaccines. Parasite Immunol, 2002. 24(4): p. 221-3.
9. Hopp, C.S., et al., Longitudinal analysis of Plasmodium sporozoite motility in the dermis reveals component of blood vessel recognition. Elife, 2015. 4.
10. Hellmann, J.K., et al., Environmental constraints guide migration of malaria parasites during transmission. PLoS Pathog, 2011. 7(6): p. e1002080.
11. Amino, R., et al., Quantitative imaging of Plasmodium transmission from mosquito to mammal. Nat Med, 2006. 12(2): p. 220-4.
12. Vanderberg, J.P. and U. Frevert, Intravital microscopy demonstrating antibody-mediated immobilisation of Plasmodium berghei sporozoites injected into skin by mosquitoes. Int J Parasitol, 2004. 34(9): p. 991-6.
13. Douglas, R.G., et al., Screening for potential prophylactics targeting sporozoite motility through the skin. Malar J, 2018. 17(1): p. 319.
14. Aliprandini, E., et al., Cytotoxic anti-circumsporozoite antibodies target malaria sporozoites in the host skin. Nature Microbiology, 2018. 3(11): p. 1224-1233.
15. Pasparakis, M., I. Haase, and F.O. Nestle, Mechanisms regulating skin immunity and inflammation. Nat Rev Immunol, 2014. 14(5): p. 289-301.
16. Treuting, P.M., S.M. Dintzis, and K.S. Montine, Comparative Anatomy and Histology: A Mouse and Human Atlas. Academic Press, Elsevier, 2017. Chapter 24: p. 433-441.
17. Frade, M.A., et al., Prolonged viability of human organotypic skin explant in culture method (hOSEC). An Bras Dermatol, 2015. 90(3): p. 347-50.
18. Gunawan, M., L. Jardine, and M. Haniffa, Isolation of Human Skin Dendritic Cell Subsets. Methods Mol Biol, 2016. 1423: p. 119-28.
19. Menard, R., et al., Looking under the skin: the first steps in malarial infection and immunity. Nat Rev Microbiol, 2013. 11(10): p. 701-12.
20. Richie, T.L., et al., Progress with Plasmodium falciparum sporozoite (PfSPZ)-based malaria vaccines. Vaccine, 2015. 33(52): p. 7452-61.
21. Hoffman, S.L., et al., Protection of humans against malaria by immunization with radiation-attenuated Plasmodium falciparum sporozoites. J Infect Dis, 2002. 185(8): p. 1155-64.
22. Jeggo, P.A. and M. Lobrich, DNA double-strand breaks: their cellular and clinical impact? Oncogene, 2007. 26(56): p. 7717-9.
23. Oakley, M.S., et al., Molecular Markers of Radiation Induced Attenuation in Intrahepatic Plasmodium falciparum Parasites. PLoS One, 2016. 11(12): p. e0166814.
24. Hoffman, B.U. and R. Chattopadhyay, Plasmodium falciparum: effect of radiation on levels of gene transcripts in sporozoites. Exp Parasitol, 2008. 118(2): p. 247-52.
25. Singer, M., et al., Zinc finger nuclease-based double-strand breaks attenuate malaria parasites and reveal rare microhomology-mediated end joining. Genome Biol, 2015. 16: p. 249.
26. Prinz, H.L., J.M. Sattler, and F. Frischknecht, Plasmodium Sporozoite Motility on Flat Substrates. .

Bio-protocol, 2017. 7(14): p. e2395.
27. Battista, A., F. Frischknecht, and U.S. Schwarz, Geometrical model for malaria parasite migration in structured environments. Phys Rev E Stat Nonlin Soft Matter Phys, 2014. 90(4): p. 042720.
28. Beltman, J.B., A.F. Maree, and R.J. de Boer, Analysing immune cell migration. Nat Rev Immunol, 2009. 9(11): p. 789-98.
29. Miller, C., M.C. Christman, and I. Estevez, Movement in a condifed space: Estrimating path tortuosity. Applied Animal Behaviour Science, 2011(135): p. 13-23.
30. Kearns, W.D., J.L. Fozard, and V.O. Nams, Movement Path Tortuosity in Free Ambulation: Relationships to Age and Brain Disease. IEEE J Biomed Health Inform, 2017. 21(2): p. 539-548.
31. Loosley, A.J., et al., Describing directional cell migration with a characteristic directionality time. PLoS One, 2015. 10(5): p. e0127425.
32. Winkel, B.M.F., et al., A tracer-based method enables tracking of Plasmodium falciparum malaria parasites during human skin infection. Theranostics, 2019. 9(10): p. 2768-2778.
33. de Korne, C.M., et al., Regulation of Plasmodium sporozoite motility by formulation components. Malar J, 2019. 18(1): p. 155.
34. Muthinja, M.J., et al., Microstructured Blood Vessel Surrogates Reveal Structural Tropism of Motile Malaria Parasites. Adv Healthc Mater, 2017. 6(6).
35. Kudryashev, M., et al., Structural basis for chirality and directional motility of Plasmodium sporozoites. Cell Microbiol, 2012. 14(11): p. 1757-68.
36. Vanderberg, J.P., Studies on the motility of Plasmodium sporozoites. J Protozool, 1974. 21(4): p. 527-37.
37. Amino, R., et al., Imaging malaria sporozoites in the dermis of the mammalian host. Nat Protoc, 2007. 2(7): p. 1705-12.
38. Quadt, K.A., et al., Coupling of Retrograde Flow to Force Production During Malaria Parasite Migration. ACS Nano, 2016. 10(2): p. 2091-102.
39. Frischknecht, F., et al., Imaging movement of malaria parasites during transmission by Anopheles mosquitoes. Cell Microbiol, 2004. 6(7): p. 687-94.
40. Munter, S., et al., Plasmodium sporozoite motility is modulated by the turnover of discrete adhesion sites. Cell Host Microbe, 2009. 6(6): p. 551-62.
41. Yoeli, M., Movement of the Sporozoites of Plasmodium Berghei (Vincke Et Lips, 1948). Nature, 1964. 201: p. 1344-5.
42. Stewart, M.J. and J.P. Vanderberg, Malaria sporozoites leave behind trails of circumsporozoite protein during gliding motility. J Protozool, 1988. 35(3): p. 389-93.
43. Pisani, L., Simple Expression for the Tortuosity of Porous Media. Transp Porous Med, 2011(88): p. 193-203.
44. Amino, R., et al., Host cell traversal is important for progression of the malaria parasite through the dermis to the liver. Cell Host Microbe, 2008. 3(2): p. 88-96.
45. Coppi, A., et al., The malaria circumsporozoite protein has two functional domains, each with distinct roles as sporozoites journey from mosquito to mammalian host. J Exp Med, 2011. 208(2): p. 341-56.
46. Dundas, K., et al., Alpha-v-containing integrins are host receptors for the Plasmodium falciparum sporozoite surface protein, TRAP. Proc Natl Acad Sci U S A, 2018. 115(17): p. 4477-4482.
47. Prinz, H., et al., Immunization efficacy of cryopreserved genetically attenuated Plasmodium berghei sporozoites. Parasitology Research, 2018. 117(8): p. 2487-2497.
48. Hafalla, J.C., et al., Short-term antigen presentation and single clonal burst limit the magnitude of the CD8(+) T cell responses to malaria liver stages. Proc Natl Acad Sci U S A, 2002. 99(18): p. 11819-24.
49. Ocana-Morgner, C., M.M. Mota, and A. Rodriguez, Malaria blood stage suppression of liver stage immunity by dendritic cells. J Exp Med, 2003. 197(2): p. 143-51.
50. Mellouk, S., et al., Protection against malaria induced by irradiated sporozoites. Lancet, 1990. 335(8691): p. 721.
51. Roestenberg, M., et al., Controlled human malaria infections by intradermal injection of cryopreserved Plasmodium falciparum sporozoites. Am J Trop Med Hyg, 2013. 88(1): p. 5-13.
52. Belnoue, E., et al., Protective T cell immunity against malaria liver stage after vaccination with live sporozoites under chloroquine treatment. J Immunol, 2004. 172(4): p. 2487-95.

53. Mueller, A.K., et al., Genetically modified Plasmodium parasites as a protective experimental malaria vaccine. Nature, 2005. 433(7022): p. 164-7.
54. Haeberlein, S., et al., Protective immunity differs between routes of administration of attenuated malaria parasites independent of parasite liver load. Sci Rep, 2017. 7(1): p. 10372.

SUPPLEMENTARY INFORMATION

Evaluation and pooling of individual experiments

Two independent experiments were performed to investigate the effect of radiation attenuation on SPZ motility. During each experiment SPZ were obtained by dissection and half of them were radiated to obtain a *Pf*^{WT} and *Pf*^{RA} sample. One million *Pf*^{WT} and *Pf*^{RA} were injected intradermally in a skin explant from the same donor and imaged by confocal microscopy, both samples at two different locations. The movies made at the 4 different locations per donor were divided in sections of 400 frames, because the length of the movies varied from 800-2000 frames and SMOOT$_{\text{human skin}}$ is optimized to process movies of 400 frames.

The color-coded track overviews of the movies made at the eight different locations are shown in Sup. Figure S1. Linear segments are depicted in red, slight turns in blue and sharp turns in yellow. The latter consisted of both SPZ moving forward while turning sharply and SPZ moving back and forth (pendulum movement) making a 180° turn (see also Figure 6 for more detailed explanation of this movement pattern). In the overviews, these tracks seem linear but are coded “yellow”, because of their 180° sharp turn. The movement pattern distribution of the *Pf*^{WT} and *Pf*^{RA} was quantified at frame level. In both donors more sharp turns were found in the *Pf*^{RA} sample. In donor 1, *Pf*^{WT} did make some sharp turns and one SPZ started circling, while *Pf*^{RA} made more sharp turns in the form of reversal movement (Sup. Figure S1A-D). In donor 2, the *Pf*^{RA} exhibited the circling movement, which is observed *in vitro* (Sup. Figure S1G-H). The difference in movement pattern distribution seen for the *Pf*^{RA} in donor 2 (Sup. Figure S1G-H) revealed the effect of location on movement pattern and underlined that the location needs to be standardized as much as possible by using the same part of the skin and imaging at the same depth.

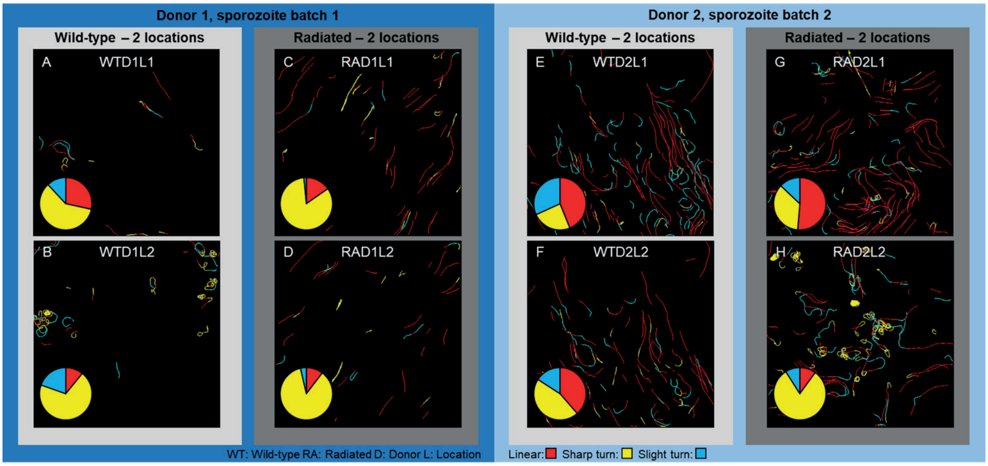

Sup. Figure S1 Overview sporozoite tracks for individual locations. A-B) Track overview and movement pattern distribution for *Pf*^{WT} injected into the skin explant from donor 1 and imaged at two different location. C-D) Track overview and movement pattern distribution for *Pf*^{RA} injected into the skin explant from donor 1 and imaged at two different location. E-F) Track overview and movement pattern distribution for *Pf*^{WT} injected into the skin explant from donor 2 and imaged at two different location. G-H) Track overview and movement pattern distribution for *Pf*^{RA} injected into the skin explant from donor 2 and imaged at two different location. The field of view was 290x290 µm for all movies.

Pooling of individual experiments

The data from the eight different locations was pooled before the detailed motility analysis was performed, which is reported in the main manuscript. Sup. Figure S2 shows the effect of pooling per donor and the effect of pooling the data from both donors. The same trend is visible when comparing the movement pattern distribution of *Pf*^{WT} and *Pf*^{RA} per donor or after pooling the data from both donors.

In vitro assay with *Plasmodium falciparum*

For the *in vitro* assay, the SPZ were obtained in the same way as for the experiments in human skin explants. For imaging of the SPZ, 10 µl of the SPZ solution was pipetted on the cover slip of a confocal dish without any precoating (ø14mm; MatTek Corporation), covered with another cover slip (ø12mm; VWR Avantor) and imaged within half an hour (Sup. Movie 4).

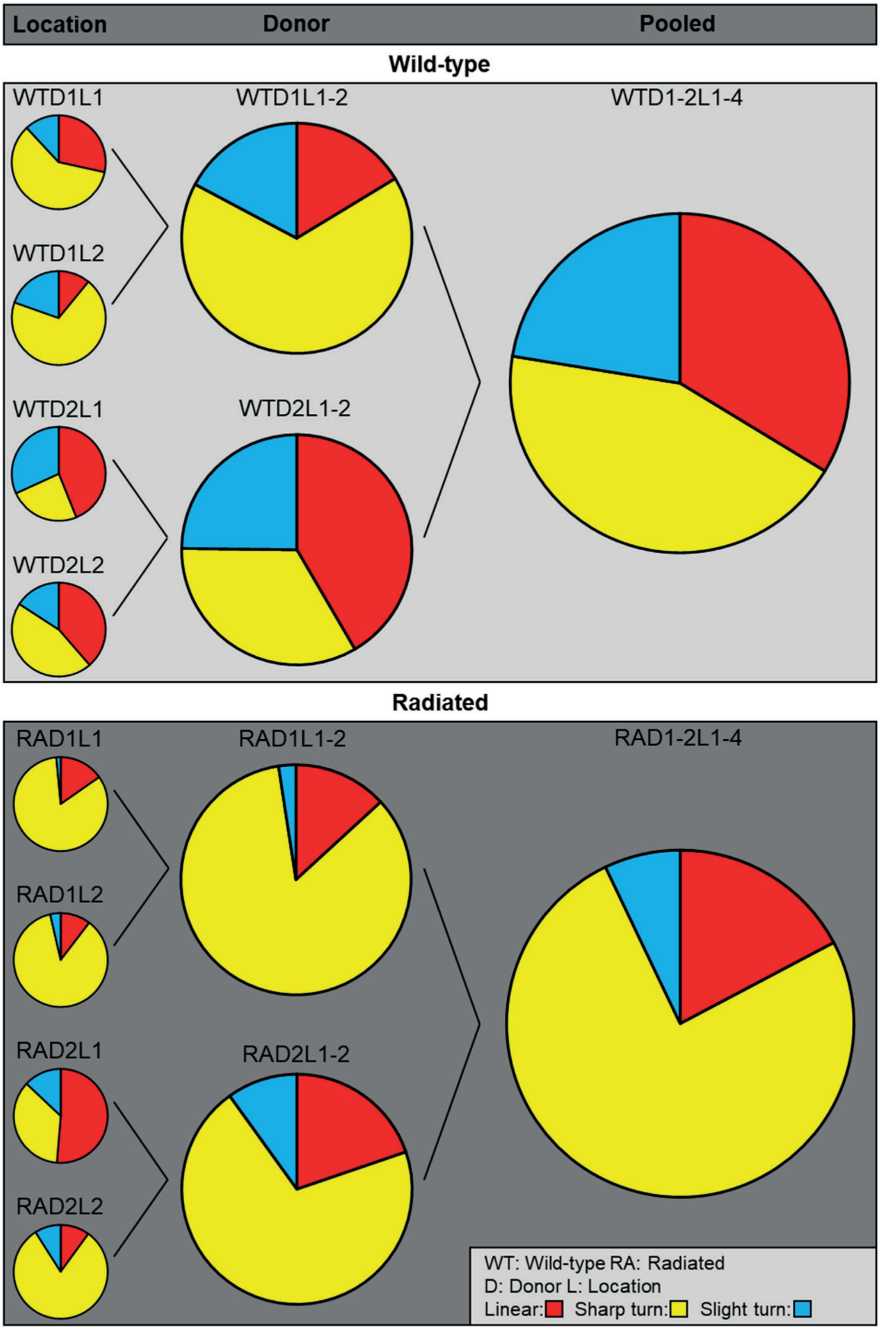

Sup. Figure S2 Pooling process of sporozoite motility data. The movement pattern distribution is shown for wild-type and radiation attenuated SPZ (*Pf*^{WT} and *Pf*^{RA}) per individual location (L), per donor (D) and after pooling. The movement pattern distribution of *Pf*^{RA} was significantly different from the movement pattern distribution of *Pf*^{WT}, both per donor and after pooling ($p<0.0001$; Chi-Squared test).

Sporozoite velocity and movement pattern distribution over time

To assess the influence of the time on SPZ velocity we longitudinally sampled 1 movie file over a 2 hr time period, see Sup. Figure S3. This data suggested that in the current setting time had little influence on the velocity of *Plasmodium falciparum* (trendline slope: decrease of 0.0023 µm/sec per minute; R^2: 0.3). In the same movie we assessed the influence of time on the turning behavior of SPZ and again, there seem to be little to no influence (trendline slope: decrease of 0.09 percent per min; R^2: 0.4).

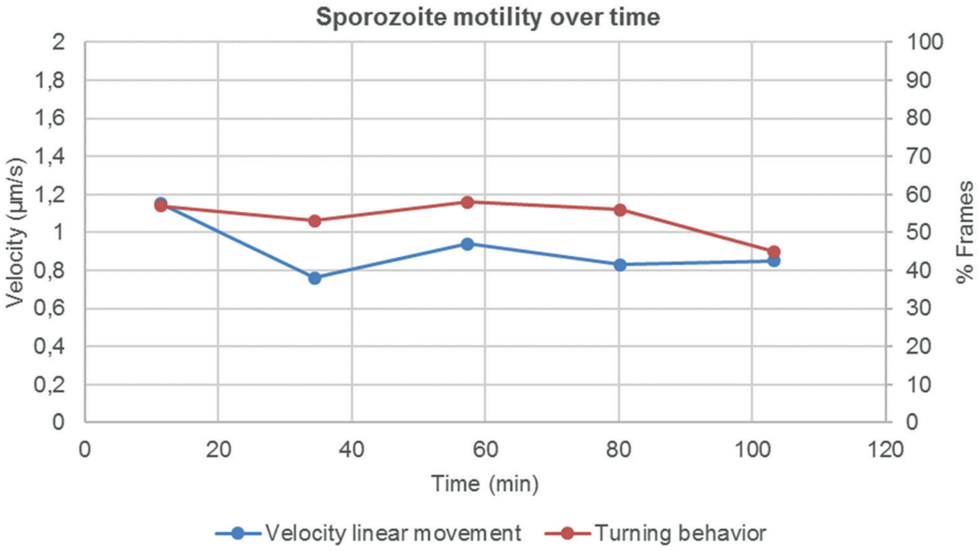

Sup. Figure S3 Sporozoite motility over time. A 4000 frames movie file was longitudinally sampled in 5 sections of 800 frames (23 min). The velocity of the SPZ during linear movement is depicted in blue and the percentage of turns (calculated at frame level) is depicted in red.

Supplementary movies

Movie S1 Example of a confocal microscopy movie showing *Pf*^{WT} migrating through human skin explant tissue.

Movie S2 Example of a confocal microscopy movie showing *Pf*^{RA} migrating through human skin explant tissue.

Movie S3 Example of reversal movement exhibited by *Pf*^{RA}.

Movie S4 Example of *Pf*^{WT} motility on uncoated glass surfaces.

These movies are available online:
http://dx.doi.org/10.1038/s41598-019-49895-3

3

Clustering and erratic movement patterns of syringe-injected versus mosquito-inoculated malaria sporozoites underlie decreased infectivity

Clarize M. de Korne, Béatrice M.F. Winkel, Matthias N. van Oosterom, Severine C. Chevalley-Maurel, Krijn M. Houwing, Jeroen C. Sijtsma, Samaneh Azargoshasb, Els Baalbergen, Blandine M.D. Franke-Fayard, Fijs W.B. van Leeuwen, Meta Roestenberg

mSphere 2021. DOI: 10.1128/mSphere.00218-21

ABSTRACT

Malaria vaccine candidates based on live attenuated sporozoites have led to high levels of protection. However, their efficacy critically depends on the sporozoites' capability to reach and infect the host liver. Administration via mosquito inoculation is by far the most potent method for inducing immunity, but highly impractical. Here, we observed that intradermal syringe-injected *Plasmodium berghei* sporozoites (^{syr}SPZ) were three-fold less efficient in migrating to and infecting mouse liver compared to mosquito-inoculated sporozoites (^{msq}SPZ). This was related to a clustered dermal distribution (2-fold decreased median distance between ^{syr}SPZ vs ^{msq}SPZ) and, more importantly, a significantly 1.4-fold slower and more erratic movement pattern. These erratic movement patterns were likely caused by alteration of dermal tissue morphology (>15 µm intercellular gaps) due to injection of fluid and may critically decrease sporozoite infectivity. These results suggest that novel microvolume-based administration technologies hold promise for replicating the success of mosquito-inoculated live attenuated sporozoite vaccines.

INTRODUCTION

Since 2014, the number of cases of malaria worldwide has remained at 200 million annually leading to more than 400 thousand deaths every year, with children in sub-Saharan Africa bearing the greatest burden[1]. This high morbidity and mortality underline the pressing need for an effective vaccine to support control programs. Live attenuated *Plasmodium falciparum (Pf)* sporozoite (SPZ) based vaccine strategies currently are in clinical development (PfSPZ Vaccine, PfSPZ CVac, PfSPZ-GA1[2]) and have the potential of inducing up to 100% sterile immunity[3, 4].

In order to make live attenuated SPZ amenable for large scale immunization, the US-based biotech Sanaria has developed tools to isolate, purify and cryopreserve SPZ for injection. Unfortunately, the dermal or subcutaneous injection of SPZ provided suboptimal protective efficacy[5]. Although much better efficacy was obtained when injecting high numbers of SPZ intravenously[6], the intradermal, intramuscular or subcutaneous administration routes of low numbers of SPZ are preferred to facilitate global administration to infants in endemic countries at a low cost-of-goods. Better understanding of the differences between the potent mosquito-inoculated SPZ and the unsuccessful syringe-injected SPZ is needed to boost the development of practical and efficacious attenuated SPZ vaccines.

The potency of attenuated SPZ vaccines critically depends on the ability of the SPZ to migrate to and infect the host liver. Transgenic luciferase-expressing SPZ and bioluminescence-based visualization of parasites in mice provide a macroscopic imaging platform to study the liver stage parasite burden after different routes of administration[7]. These studies indicated that mosquito-inoculated SPZ migrate to the liver much more efficiently than intradermally injected SPZ[8-11]. The subsequent development of fluorophore-expressing SPZ and a SPZ fluorescent labelling approach has allowed for more detailed microscopic studies on the motility of individual SPZ, both *in vitro* and in skin[12-14]. Moreover, automated analysis of SPZ motility now provides a platform to quantitatively study SPZ motility under different conditions[15-18].

We aimed to unravel the factors underlying the difference in potency and infectivity between mosquito-inoculated and intradermal syringe-injected SPZ (Scheme 1). For this we microscopically examined the dermal site, quantitatively assessed the distribution of SPZ and their motility patterns after inoculation by mosquito bite (^{msq}SPZ) and injection by needle and syringe (^{syr}SPZ) through automated image analysis. We assessed liver stage parasite burden through bioluminescence assays.

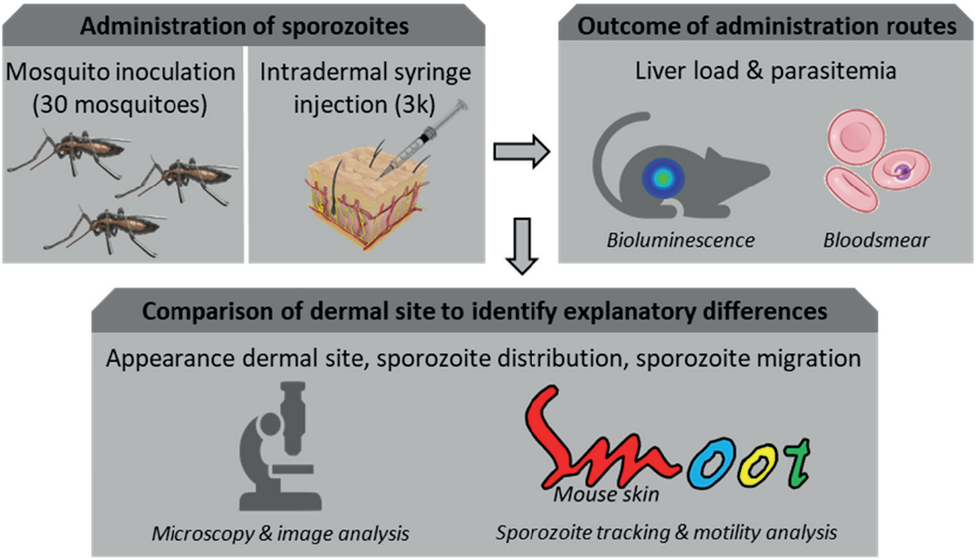

Scheme 1 Study design. SPZ were administered via mosquito inoculation or intradermal syringe injection. Liver load was subsequently assessed by bioluminescence and blood smear patency. Detailed analysis of 1) the appearance of the dermal site, 2) the SPZ distribution and 3) SPZ migration behavior was performed to reveal underlying mechanisms of decreased infectivity.

METHODS

Rodent experiments

Mouse experiments were performed with Female Swiss OF1 mice (6-7 weeks old; Charles River). All animal experiments were granted a license by the Competent Authority after advice on the ethical evaluation by the Animal Experiments Committee Leiden (AVD1160020173304). All experiments were performed in accordance with the Experiments on Animals Act (Wod, 2014), the applicable legislation in the Netherlands and in accordance with the European guidelines (EU directive no. 2010/63/EU) regarding the protection of animals used for scientific purposes. All experiments were performed in a licensed establishment for the use of experimental animals (LUMC). Mice were housed in individually ventilated cages furnished with autoclaved aspen woodchips, fun tunnel, wood chew block and nestlets at 21 ± 2°C under a 12:12 hr light-dark cycle at a relative humidity of 55 ± 10%.

Sporozoite production

Naive mice were infected with the rodent malaria species *P. berghei* as described previously[8]. The transgenic line 1868cl1 expressing mCherry and luciferase under the constitutive HSP70 and eef1a promotors respectively (*Pb*ANKA-mCherry$_{hsp70}$+Luc$_{eef1\alpha}$; line RMgm-1320, www.pberghei.eu) was used. The infected mice were anesthetized and *Anopheles stephensi* female mosquitoes were infected by feeding on the gametocytemic mice as described previously[19]. The mosquitoes were kept at a temperature of 21 °C and 80% humidity until use.

Sporozoite administration

After anesthetizing mice, *P. berghei* 1868cl1 SPZ were administered using two different methods:

1. ^{msq}SPZ were delivered by shaving the abdomen of the mice and 1 cm^2 skin was exposed for 15 minutes to around 30 infected mosquitoes (exact numbers are specified per experiment). Blood-fed mosquitoes were counted and the presence of SPZ in their salivary glands was confirmed using the quantitative analysis of the luciferase activity after putting the mosquitoes in a 20 µl drop D-luciferin (8 mg/ml in phosphate-buffered saline (PBS)).
2. ^{syr}SPZ were obtained by manual dissection of the salivary glands of infected female *Anopheles stephensi* mosquitoes 20-24 days post infection. The salivary glands were collected and homogenized to release SPZ in Roswell Park Memorial Institute medium (RPMI; Thermo Fisher Scientific) enriched with 10% fetal bovine serum (Life Technologies Inc.). The free SPZ were counted in a Bürker counting chamber using phase-contrast microscopy to prepare the injection samples. Directly after counting (within 45 minutes after crushing), 10 µl sample containing 3000 SPZ was administered by injection into the abdominal skin (within the same region as defined for exposure to mosquitoes) using an insulin syringe (Becton Dickinson, Micro-Fine+, 0.5 ml; 0.30 x 8.0 mm, 30G). The number of SPZ delivered by exposure to 30 infected mosquitoes was considered consistent with intradermal delivery of 3000 SPZ via syringe injection based on available literature (mean number of SPZ inoculated per mosquito: 116 ± 28[20]).

Quantification of parasite liver load and prepatent period

The liver stage of the *P. berghei* infection in 11 mice (6 mice challenged by 33 (IQR: 30-33) mosquito bites of which 25 (IQR: 22-28) contained blood and 5 mice challenged by syringe injection of SPZ) was visualized and quantified by measuring the luciferase activity in the liver at 44 hr after the challenge with SPZ using the IVIS Lumina II Imaging System (Perkin Elmer Life Sciences). Before imaging, the mice were shaved and anesthetized. IVIS measurements (exposure time: 120 seconds, binning factor: 16, aperture: f/1.2) were performed 8 minutes after subcutaneous injection of D-luciferin in the neck (100 mg/kg in PBS; Caliper Life Sciences). The liver load was quantified measuring total flux (p/s) of an ROI covering the liver (same ROI for all mice). Image analysis was performed using the Living Image® 4.4 software (Perkin Elmer Life Sciences). Infected mice were monitored for blood stage infections by Giemsa-stained blood smear until day 9 post infection. The prepatent period (measured in days after SPZ challenge) was defined as the first day at which blood stage infection with a parasitemia of >0.5% was observed.

Quantification of sporozoites by PCR

Directly after SPZ delivery by 32 (IQR: 32-33) mosquito bites of which 18 (IQR: 17-19) contained blood, the skin of 4 exposed mice was cut out, snap-frozen and stored at -20 °C until further use. Parasite burden was measured by quantitative real-time reverse transcription polymerase chain reactions (qRT-PCR). The DNA was extracted from the frozen skin using the QIAamp DNA Micro Kit (Qiagen) following the manufacturer's instruction. Amplification reactions of each DNA sample were performed in PCR plates (hard-shell PCR plate, #HSP9645; Bio-Rad), in a volume of 25 µl containing 12.5 µl PCR buffer (HotstarTaq mastermix; Qiagen), 0.5 µl $MgCl_2$ (25mM), Plasmodium-specific forward and reverse primer (12.5 pmol; Plas-7F 5'-GTTAAGGGAGTGAAGACGATCAGA-3' and Plas-171R 5'-AACCCAAAGACTTTGATTTCTCATAA-3'; Sigma-Aldrich), PhHV-specific forward and reverse primer (15 pmol; PhHV-267S 5'-GGGCGAATCACAGATTGAATC -3' and PhHV-337AS 5'-GCGGTTCCAAACGTACCAA -3'; Biolegio), Plasmodium-specific FAM10 labelled detection probe (2.5 pmol; PP FAM 5'-ACCGTCGTAATCTTAACC-3'; Biolegio), PhHV-specific Cy5 double-labelled detection probe (1.25 pmol; PhHV-305TQ Cy5 5'-TTTTTATGTGTCCGCCACCATCTGGATC-3'-BHQ2; Biolegio) and 5 µl of the DNA sample (dilution factor: 10x). Amplification consisted of 15 min at 95°C followed by 50 cycles of 15 s at 95°C, 30 s at 60°C, and 30 s at 72°C. Amplification, detection, and analysis were performed with the CFX96TM real-time PCR detection system (Bio-Rad). A calibration curve to assess the SPZ numbers in the mosquito inoculation samples was generated by analyzing skin samples injected with a dilution range of SPZ (2-step dilution, start: 20.000 SPZ, 10 samples, n=3 performed *in duplo*, Figure 1C).

Ex vivo (fluorescent) imaging of the dermal site

Immediately after SPZ delivery, the exposed skin of 8 mice (4 ^{msq}SPZ and 4 ^{syr}SPZ samples) was excised, covered with a cover slip and imaged using an Andor Dragonfly 500 spinning disk confocal on a Leica DMi8 microscope (Oxford Instruments) or a Leica True Confocal Scanning SP8 microscope (Leica Microsystems). The mCherry expressed by SPZ was excited with the 561nm laser. A 20x objective (HC PL APO 20x/0.75 IMM CORR CS2) was used, resulting in images of 617 x 617 µm. The experiments were performed within 1.5 h after tissue excision at room temperature.

To create overview images of the dermal site, up to 570 fields of views were stitched using the Andor imaging software Fusion (Oxford Instruments). Z-slices were imaged covering an average total depth of 124 µm (IQR: 103-131). Using the Fiji package for the open source software ImageJ[21], the three-dimensional z-stack was reduced into a two-dimensional image using maximum intensity projection (retrieves the level of maximum intensity along the z axis for each x,y position) and was converted into a binary image only showing the SPZ. This image was further processed in two different ways: 1) The Gaussian blur filter was applied and a pseudo color image was created by applying the inferno color lookup table in Fiji to visualize the location and density of the SPZ, 2) The coordinates of the individual SPZ in the ^{msq}SPZ and ^{syr}SPZ samples were determined and the nearest neighbor distance (distance between the center points of neighboring SPZ) was calculated using the ImageJ Nnd plugin. The blood vessels visible at the brightfield overview image of the dermal site were segmented using the Image Segmenter app available within MATLAB (MathWorks) and the distance from the SPZ center to the nearest blood vessel was calculated. The number of SPZ residing within or in close proximity to hematomas was determined using circular ROIs with a diameter of 650 µm and around the center of the hematoma. The shape of the cells visible at the zoom-in brightfield images (after mosquito inoculation n=164, after syringe injection n=203) was described by two shape descriptors available within ImageJ, namely roundness: with a value of 1.0 indicating a perfect circle and the Feret's diameter: the longest distance between any two points along the cell membrane.

Sporozoite motility

To analyze SPZ motility, movies were recorded with a frame rate of 35-40 frames per minute, 200 frames per movie. Recording ^{msq}SPZ samples (n=6) yielded a total of 3400 frames. Recording ^{syr}SPZ samples (n=8) yielded a total of 3600 frames. Maximum intensity projections of the recorded microscopy movies were generated using ImageJ. The motility of the SPZ was analyzed using SMOOT$_{\text{mouse skin}}$, an in-house developed software program, written in the MATLAB programming environment (MathWorks). This tool is an adapted version of the SMOOT$_{\text{human skin}}$[13, 18] and SMOOT$_{\textit{in vitro}}$[15] tools previously described. Via SMOOT$_{\text{mouse skin}}$, the SPZ could be segmented per movie frame, based on their fluorescence signal intensity, size and crescent shape. The median pixel locations of the segmented SPZ were connected into full SPZ tracks.

First, the SPZ tracks were characterized as motile or stationary based on their displacement, using a displacement cut-off of 21 pixels which corresponds to the length of a SPZ. Subsequently, the tracks of the motile SPZ were subdivided into defined movement patterns: sharp turn, slight turn and linear segments. Third, for the motile SPZ the mean squared displacement at frame level, the average velocity of their tracks and the nearest neighbor distance per track was calculated and the tortuosity of the tracks was described via the straightness index (the ratio between the total length of the direct path between the start and the end of a track and the total length of the travelled path) and the angular dispersion (the deviation from the mean angle of the track). Finally, the interplay between the angular dispersion, straightness index, velocity and nearest neighbor distance was analyzed, for which the number of ^{msq}SPZ and ^{syr}SPZ tracks within the dataset was equated using random sampling. Twelve subsets of SPZ tracks were defined based on the angular dispersion (<0.5 and >0.5), straightness index (<0.5 and >0.5) and velocity, (<1 µm/s, 1-2 µm/s, >2 µm/s).

Statistical analysis

The average and variability of the data was summarized using the mean and standard deviation (SD) for parametric data or the median and interquartile range (IQR) for nonparametric data. For the comparison of groups, the difference between means or medians was assessed using respectively the independent sample T test and the Mann-Whitney U test. For the comparison of a group with a set value the one sample T test was used. For the comparison of the distribution of categorical data the Chi-squared test was used, including a post hoc analysis based on residuals. A univariate general linear model was used to examine the relationship between a continuous and categorical variable. p-values < 0.05 were considered significant, in case of multiple testing the Bonferroni correction was applied to adjust the p-value. All statistical tests were performed by SPSS Statistics (IBM Nederland BV). To compare the velocity distributions of both groups, the distribution was described performing Expectation-Maximization based fitting. The probability density function that could describe the SPZ velocity distribution consisted of a mixture of 2 normal distributions. The package mixR[22] within the open source R environment[23] was used to define the distribution parameters yielding the best fit.

RESULTS

Infectivity of ^{msq}SPZ and ^{syr}SPZ

At roughly equal numbers of administered ^{msq}SPZ and ^{syr}SPZ, the parasite liver loads of infected mice, assessed by bioluminescence imaging, were 3.5-fold higher in ^{msq}SPZ mice (median: $2.7*10^5$ RLU, IQR: $1.8*10^5$-$3.7*10^5$) as compared to ^{syr}SPZ mice (median: $7.9*10^4$ RLU, IQR: $5.9*10^4$-$8.5*10^4$; p: 0.011; Mann-Whitney U test) (Figure 1). These results were in line with previous reports[8]. The prepatent period of blood stage infection was on average 7 days after infection by mosquito bites. After syringe injection 3/5 mice were still blood slide negative at day 9 after infection, the remaining two mice became positive at day 7 after injection.

Attempts to quantify the number of ^{msq}SPZ by qRT-PCR (Figure 1) showed high variability in estimates (median: 6060, range 2203-13,481), which was at least partly caused by technical variability inherent to DNA extraction from skin lysis samples. The estimated average number of ^{msq}SPZ delivered did not significantly differ from the targeted 3000 (p: 0.205; one-sample t test).

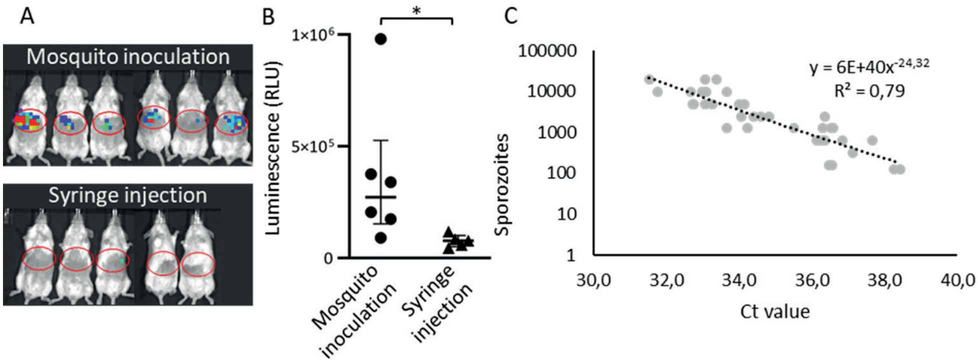

Figure 1 Outcome different administration routes. A) *In vivo* images which show the liver load 44 hr post infection via 33 (IQR: 30-33) mosquito bites or intradermal syringe injection of 3000 SPZ. (B) Average of the luciferase activity in the liver 44 hr after challenge by mosquito inoculation (median: $2.7*10^5$ RLU, IQR: $1.8*10^5$-$3.7*10^5$) or intradermal syringe injection (median: $7.9*10^4$ RLU, IQR: $5.9*10^4$-$8.5*10^4$)(*p=0.011; Mann-Whitney U test). (C) A calibration curve was generated based on a syringe injected concentration range of SPZ in skin (n=3 *in duplo*) to estimate the number of SPZ delivered by 30 mosquito bites (median: 6060 (2203-13,481) SPZ).

Dermal site appearance

The dermal ^{msq}SPZ and ^{syr}SPZ sites were imaged over an average total depth of 124 µm (IQR: 103-131) by confocal microscopy in order to visualize the SPZ distribution. In general, ^{msq}SPZ were distributed both individually and in clusters dispersed throughout the dermal tissue (Figure 2A). We found that ^{msq}SPZ dermal tissue contained multiple hematomas (median number per sample: 6.5). Interestingly we also found hematomas and ^{msq}SPZ in the mouse peritoneum (Sup. Figure S1). Of the ^{msq}SPZ identified, 9% was found within or in close proximity to the hematomas (example is shown in Figure 2Aiv), which represented roughly 23% of the hematomas (6/26). Three quarters of ^{msq}SPZ were found within a 255 µm radius of a blood vessel (Sup. Figure S2).

In contrast, dermal sites containing ^{syr}SPZ showed that the injected medium diffused throughout skin, with a single cluster of ^{syr}SPZ in the centre of this injection site (Figure 2B). Zooming in on the ^{syr}SPZ cluster showed that the ^{syr}SPZ did not agglutinate (Figure 2Bi-iv). We did not find hematomas in the ^{syr}SPZ dermal tissue, nor ^{syr}SPZ in the peritoneum. On average ^{syr}SPZ were located further away from blood vessels, three quarters were found within a 504 µm radius of a blood vessel (Sup. Figure S2; p<0.001, Mann Whitney U test). The SPZ distribution was quantified according to their nearest neighbor distance (NND) confirming the dispersed nature of ^{msq}SPZ with a median NND of 55 µm (IQR: 18-132), 5% of the ^{msq}SPZ were further than 376 µm apart (Figure 2C). In contrast, ^{syr}SPZ were clustered at a median NND of 23 µm (IQR: 13-43), 5% of the ^{syr}SPZ were further than 112 µm apart.

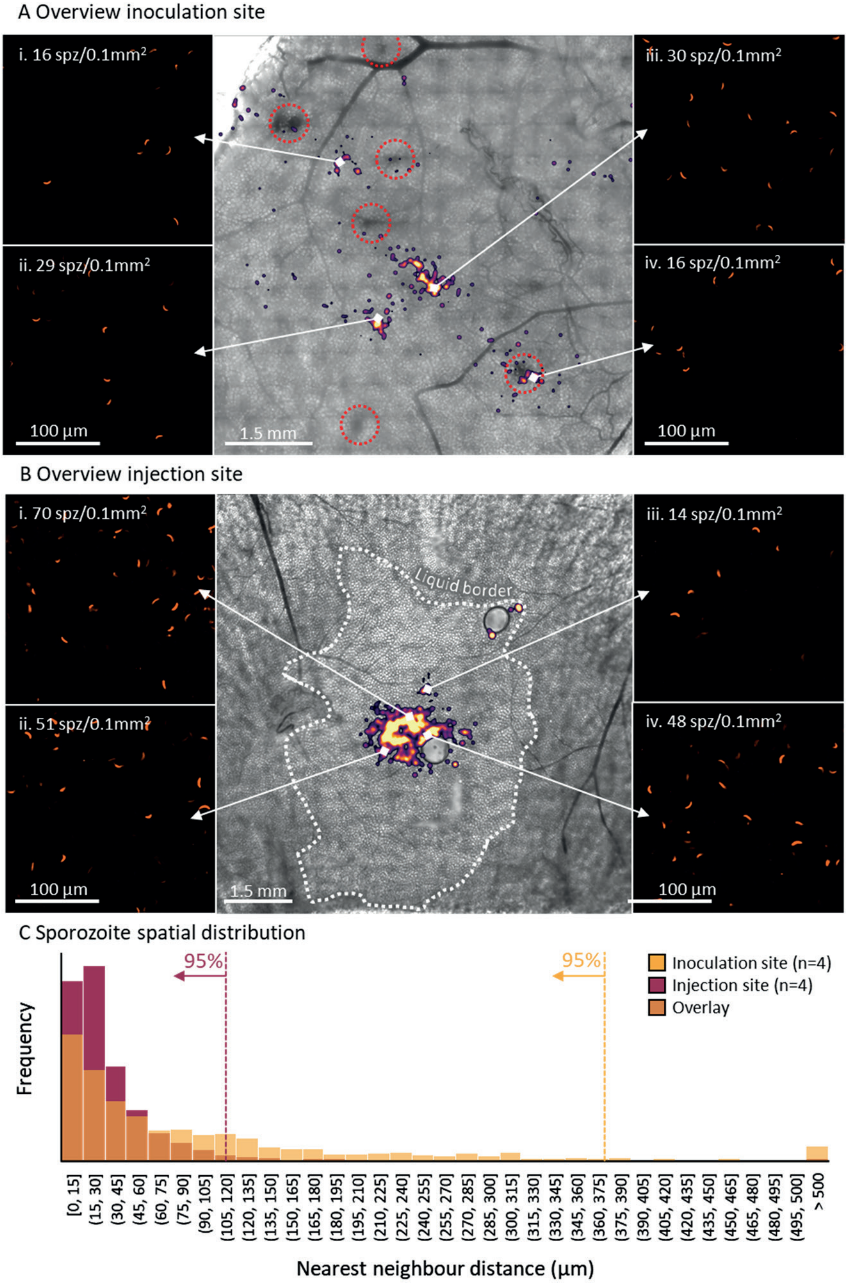

Figure 2 Overview dermal site appearance. A-B) Overview of the inoculation site after SPZ delivery by mosquito (A) and the injection site after SPZ delivery by intradermal syringe injection (B), shown as an overlay of a brightfield image and the SPZ distribution (pseudo-colored, blurred fluorescent image) accompanied by zoom-in images showing the individual SPZ (i-iv). C) Plot of the nearest neighbor distance for ^{msq}SPZ (yellow, median: 55 µm, IQR: 18-132) or ^{syr}SPZ (purple, median: 23 µm, IQR: 13-43), the overlap of both distributions is plotted in orange.

Zooming in on the morphology of the skin tissue, we found that after mosquito inoculation, cells remained densely packed resulting in polygonal shaped cells (mean roundness: 0.75 ± 0.11; Feret's diameter: 82 ± 13 µm) (Figure 3AB). Conversely, after the syringe injection the interstitial space between the cells was enlarged, leading to >15 µm gaps between cells and a change in cell shape towards significantly more rounded cells (mean roundness: 0.87 ± 0.07, $p<0.001$, independent sample T test; Feret's diameter: 68 ± 10 µm, $p<0.001$, independent sample T test) (Figure 3AB). The projection of ^{msq}SPZ and ^{syr}SPZ tracks on top of brightfield images showing tissue morphology revealed that the altered tissue morphology was accompanied by altered movement patterns (Figure 3C).

Intradermal sporozoite motility

After delivery, the majority of SPZ displayed tortuous movement through the dermal tissue, representative examples are shown in Figure 4A. In total, the movement of 566 ^{msq}SPZ and 1079 ^{syr}SPZ could be captured and analyzed. Both ^{msq}SPZ and ^{syr}SPZ were equally motile (respectively 89% and 88%). Following both administration routes, the tracks of the SPZ were highly curved. Traditional motility measures such as the mean squared displacement were thus unsuitable to accurately describe the migration behavior of both groups of SPZ (Sup. Figure S3). Therefore, we included other parameters to investigate the tortuous migration behavior. Tracks were color-coded for movement pattern, e.g. straight in red, slight turns in blue, sharp turns in yellow. Both ^{msq}SPZ and ^{syr}SPZ showed equal numbers of turns as compared to straight paths with the percentage turns at frame level at 88% for both samples (Figure 4Bi). The percentage of sharp turns was somewhat decreased in ^{msq}SPZ as compared to ^{syr}SPZ (slight/sharp turns ^{msq}SPZ: 46/42%, ^{syr}SPZ: 34/54%; $p<0.001$, Chi-square test; Figure 4Bi). Analysis of straightness index (Figure 4Biii), revealed a similarly high level of tortuosity in both conditions (median straightness index ^{msq}SPZ: 0.24, IQR: 0.09-0.53; ^{syr}SPZ: 0.28, IQR: 0.14-0.56; $p=0.14$, Chi-square test). Turns were made both clockwise (CW) and counter CW (CCW), with a slight preference for CCW in the ^{msq}SPZ group (CW ^{msq}SPZ: 40%, ^{syr}SPZ: 51%; CCW ^{msq}SPZ: 60%, ^{syr}SPZ: 49%; $p<0.001$, Chi-square test) (Figure 4Bii). Interestingly, the turn angle of ^{msq}SPZ was much more consistent, described by angular dispersion (Figure 4Biv), as compared to ^{syr}SPZ (median angular dispersion ^{msq}SPZ: 0.74, IQR: 0.54-0.87; ^{syr}SPZ: 0.58, IQR: 0.32-0.77; $p<0.001$, Chi-square test). In conclusion, both ^{msq}SPZ and ^{syr}SPZ travelled highly tortuous paths, whereby ^{msq}SPZ showed less sharp turns, a more consistent turn angle and a predominance for the well-described preferred CCW turn angle.

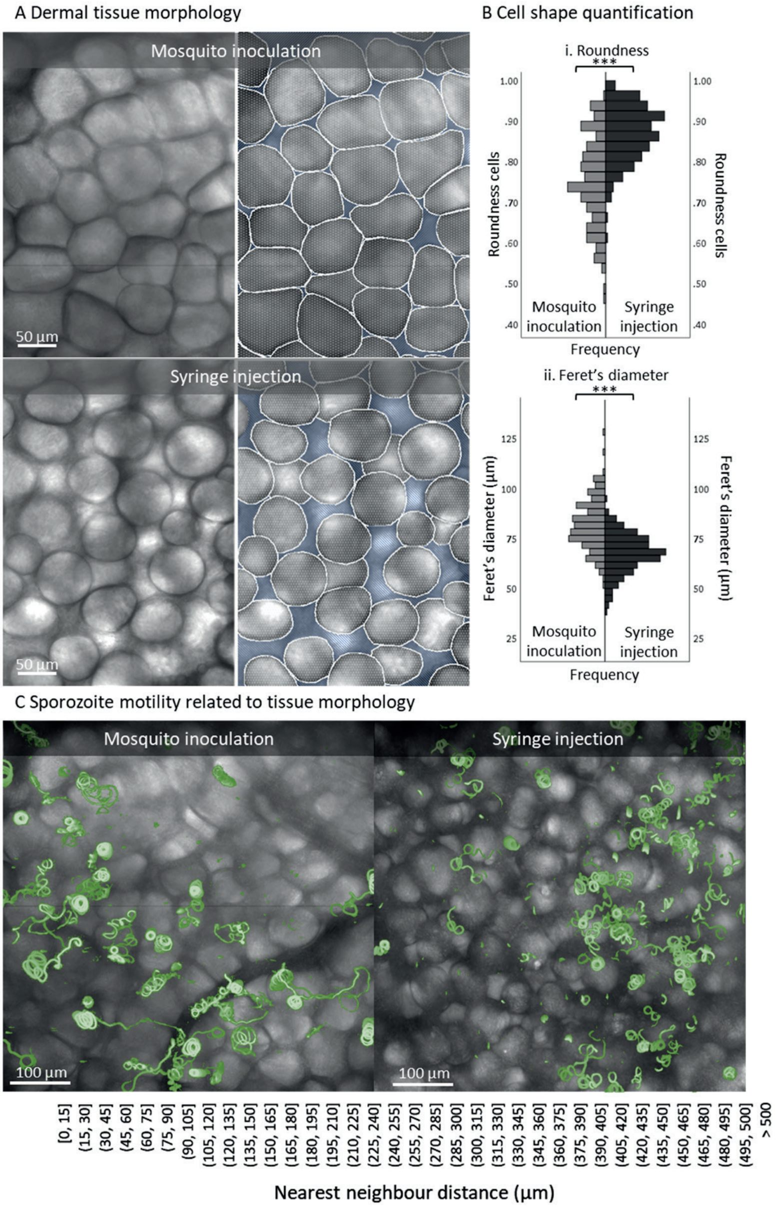

Figure 3 Zoom-in on dermal tissue morphology after sporozoite delivery. A) Zoom-in on the tissue morphology of the inoculation site after SPZ delivery by mosquito and the injection site after SPZ delivery by intradermal syringe injection. Based on the brightfield images, the cells (depicted in white) and the interstitial space (depicted in blue) were segmented. B) Quantification of the cell shapes found after mosquito inoculation (n=164) and syringe injection (n=203) using roundness (i) and the Feret's diameter (the longest distance between any two points along the cell membrane) (ii) as measures. ***p<0.001; independent sample T test. C) Overview of the dermal site shown as an overlay of a brightfield image and a map of mosquito-inoculated and syringe-injected SPZ tracks (depicted in green).

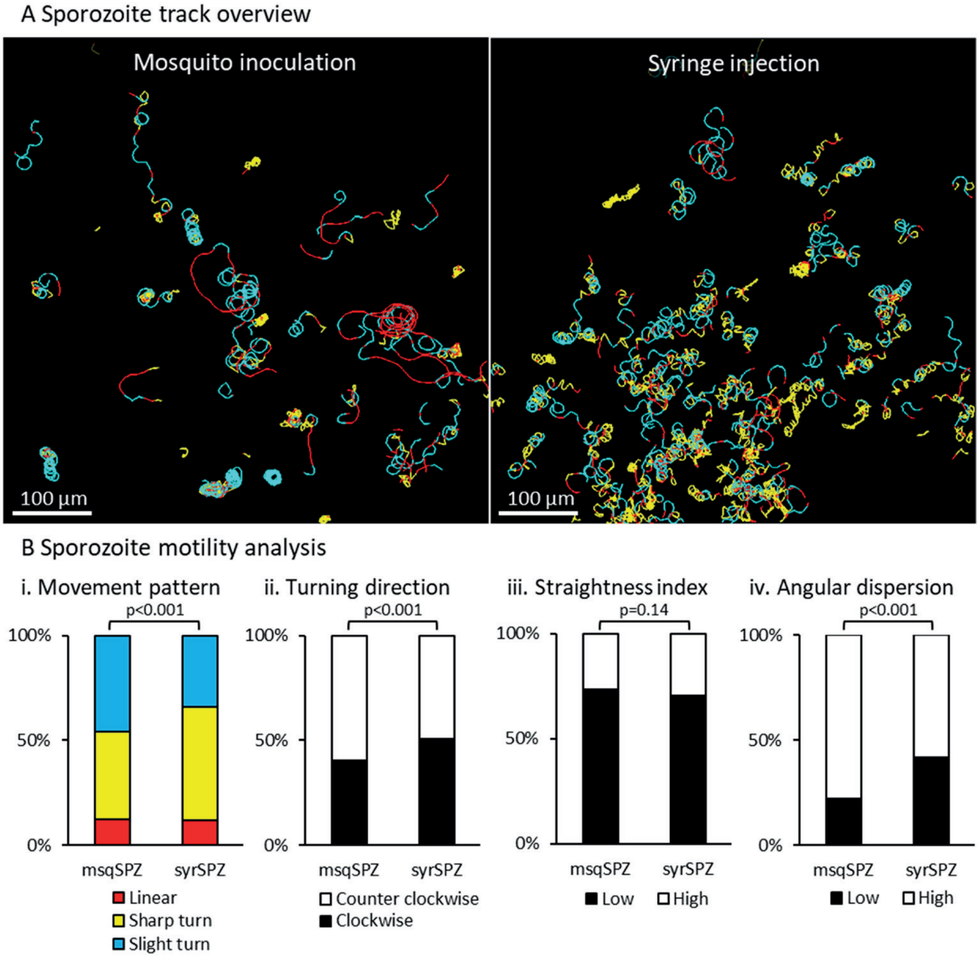

Figure 4 Movement pattern of sporozoites. A) Overview of the inoculation site after SPZ delivery by mosquito and the injection site after SPZ delivery by intradermal syringe injection, shown as a map of SPZ tracks, color-coded for movement pattern (sharp turns in yellow, slight turns in blue, linear movement in red). B) Quantification of the different aspects of SPZ motility after administration by mosquito or syringe: (i) The movement pattern distribution based at frames, (ii) the percentage of clockwise and counter clockwise segments (iii) the straightness index of the tracks (low: <0.5, high: >0.5) and (iv) the angular dispersion of the tracks (low: <0.5, high: >0.5). p-values obtained by Chi-square test.

SPZ velocity fluctuated along tracks (visualized by color-coding in Figure 5A), which was in line with earlier findings[15, 18, 24, 25]. Plotting the average track-velocities revealed a distribution that could be described with a mixture of two normal distributions (Figure 5B). The first peak was comparable for both administration routes and contained the slow moving $^{\mathrm{msq}}$SPZ and $^{\mathrm{syr}}$SPZ with a mean velocity of respectively 1.0 ± 0.4 and 0.9 ± 0.2 µm/s. The second peak, containing the highly viable and rapid $^{\mathrm{msq}}$SPZ and $^{\mathrm{syr}}$SPZ, differed between the administration routes at a mean of 2.4 ± 0.7 µm/s for $^{\mathrm{msq}}$SPZ and 1.7 ± 0.6 µm/s for $^{\mathrm{syr}}$SPZ. Thus, the rapid $^{\mathrm{msq}}$SPZ moved on average 1.4-fold faster than the $^{\mathrm{syr}}$SPZ.

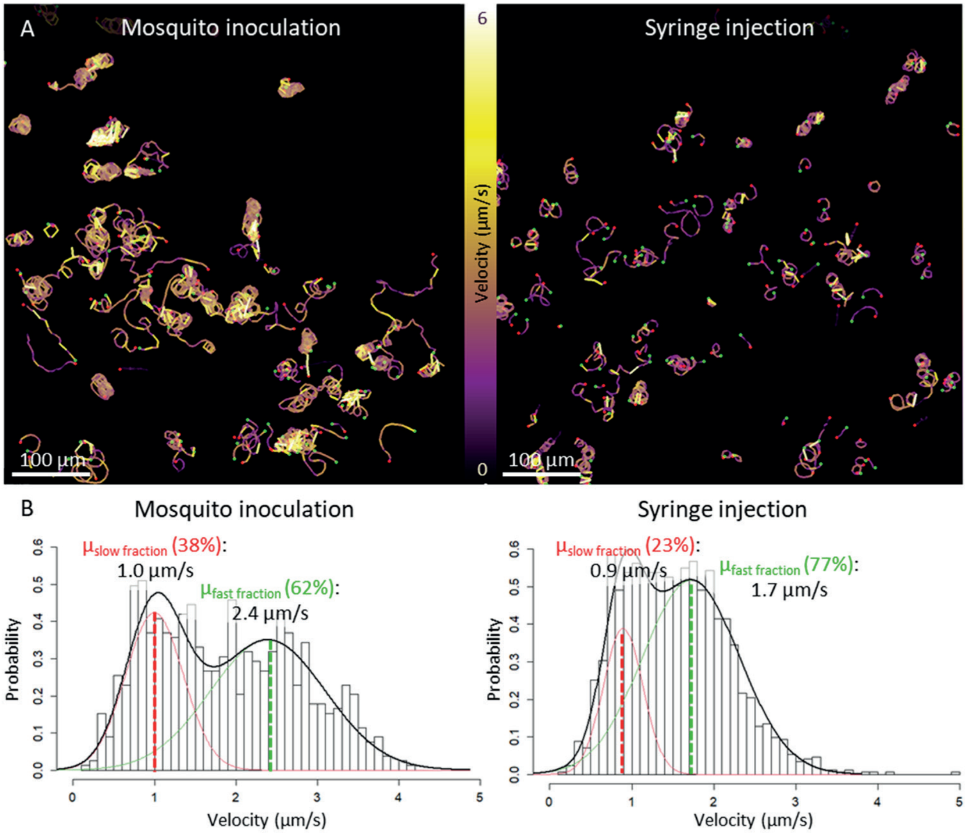

Figure 5 Velocity of sporozoites. A) Overview of the inoculation site after SPZ delivery by mosquito inoculation and the injection site after SPZ delivery by intradermal syringe injection, shown as a map of SPZ tracks, color-coded for velocity (yellow sections corresponded to a high velocity, purple sections, corresponded to a lower velocity) (B) The distribution of the average track velocity including a probability density function with its mean determined using expectation-maximization based fitting of a mixture of 2 normal distributions; one describing the slow moving SPZ fraction (depicted in red, accounting for 38% of the $^{\mathrm{msq}}$SPZ and 23% of the $^{\mathrm{syr}}$SPZ) and one describing the fast moving SPZ fraction (depicted in green, accounting for 62% of the $^{\mathrm{msq}}$SPZ and 77% of the $^{\mathrm{syr}}$SPZ).

Interplay between motility parameters

To obtain a multidimensional view of SPZ migration, we explored the relationship between tortuosity parameters. Based on high and low straightness index (SI) and angular dispersion (AD), the SPZ tracks could be divided into four typical movement patterns: short erratic tracks (low AD, high SI), short straight tracks (high AD, high SI), consistently turning tracks (high AD, low SI) and erratically turning tracks (low AD, low SI) (Figure 6A). Representative examples of tracks from these groups are shown in Figure 6B. The majority of the tracks (49%) were classified as consistently turning (49%), which typically is the 'default' movement pattern which SPZ display *in vitro* (Figure 6A).

We subsequently investigated the relationship between the four movement patterns and velocity. We found that consistently turning tracks were generally rapid SPZ (median 2.0 µm/s, IQR 1.5-2.6), whereas erratically turning SPZ were considerably slower (median: 1.2 µm/s, IQR 0.9-1.7; $p<0.001$, Mann-Whitney U test). Interestingly, these consistently turning rapid SPZ were overrepresented within the ^{msq}SPZ group as compared to the ^{syr}SPZ group (2.4-fold difference), which was offset by a reciprocal increase in slower erratically turning SPZ within the ^{syr}SPZ group (2.5-fold difference) ($p<0.001$, Chi-square test) (Figure 6D).

Lastly, we determined if the distribution of the SPZ as reflected by the nearest neighbor distance (NND) influenced the tortuosity and velocity of their tracks. In general, the average NND of ^{msq}SPZ was larger compared to ^{syr}SPZ as was observed by the analysis of the individual parameters (Figure 2, Sup. Figure S4). However, this difference was consistent among all different movement patterns ($p=0.52$; interaction term $^{msq/syr}$SPZ * subsets, univariate general linear model), which suggested that the movement pattern or velocity of SPZ was not dependent on their interindividual distance. Taken together, the ^{syr}SPZ group contained more SPZ that exhibited erratic movement at a slower speed, whereas the ^{msq}SPZ group contained more SPZ that circled consistently at high speed.

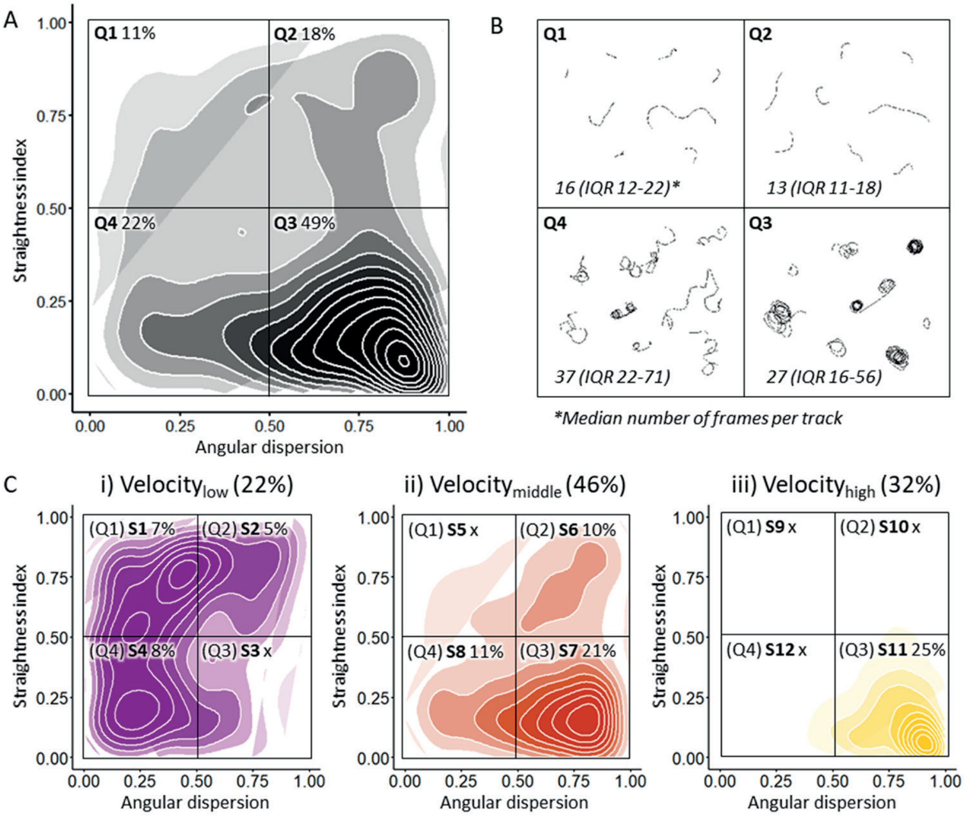

D

(%)	S1	S2	S3	S4	S5	S6	S7	S8	S9	S10	S11	S12
^{msq}SPZ	4.9	6.4	x	5.8	x	8.5	19.5	6.0	x	x	35.5	x
^{syr}SPZ	8.2	3.7	x	9.9	x	11.6	22.9	15.3	x	x	14.7	x

Figure 6 Interplay between motility parameters. A) Density plot of all SPZ tracks (including both ^{msq}SPZ (n=778) and ^{syr}SPZ (n=778) in a matrix of angular dispersion and the straightness index. B) Representative example movement patterns associated with every quarter of the density plot. Group Q1: low angular dispersion, high straightness index (short, erratic tracks); Q2: high angular dispersion, high straightness index (short, straight tracks); Q3: high angular dispersion, low straightness index (consistently turning tracks); Q4: low angular dispersion, low straightness index (erratically turning tracks). C) Density plot of all low (i), intermediate (ii) and high (iii) velocity tracks on the same matrix of angular dispersion and straightness index, resulting in twelve subsets (S1-12). Velocity categories are defined as: slow <1 µm/s (depicted in purple), intermediate 1-2 µm/s (depicted in orange) and fast >2 µm/s (depicted in yellow). Percentage of the overall number of SPZ tracks in every quarter of the density plots are given. D) Comparison of the distribution (as a percentage of total tracks) for ^{msq}SPZ and ^{syr}SPZ tracks across subsets S1-12, with significant differences between S8 and S11 (p<0.001, Chi-square test).

DISCUSSION

Using confocal microscopy and dedicated SPZ imaging software, we visualized SPZ deposited by mosquito inoculation or syringe injection and assessed quantitative differences. We found that delivery via syringe injection decreases infectivity of SPZ by roughly three-fold as compared to mosquito inoculation, which is related to 1) a clustered distribution of ^{syr}SPZ through the skin with larger distance to blood vessels, 2) a lack of hematomas, which are typically induced by mosquito bites, 3) enlarged interstitial space due to the syringe injection of fluid, 4) slower and more erratic migration patterns of ^{syr}SPZ as compared to ^{msq}SPZ. Each of these parameters could impact the efficiency of SPZ migration, blood vessel invasion and ultimate liver infectivity and thus provide important insights on how to critically improve delivery of SPZ-based vaccines.

The dispersed distribution of ^{msq}SPZ and the fact that a substantial proportion of ^{msq}SPZ is deposited close to hematomas created by mosquito probing[26, 27] provide them with better odds of finding blood stream access as compared to ^{syr}SPZ. This is in line with the consistent circular motility of ^{msq}SPZ, which has previously been associated with increased blood vessel engagement[14, 17]. However, in previous publications, this engagement was generally related to deceleration, while in our study consistent circular motility was related to high velocities[14, 17]. Conversely, the slower erratic movement of ^{syr}SPZ is most likely caused by the alteration of physical space as a consequence of fluid injection. SPZ movement is strongly guided by their three-dimensional environment; without any confinement, SPZ *in vitro* display a continuous, preferential counter-clockwise movement pattern[15, 24], while *in vivo*, skin structure redirects SPZ to display much more complex patterns[16, 18]. The role of physical confinement has been further supported by experiments whereby micropatterned *in vitro* environments were created that could induce specific movement patterns of SPZ[28]. We clearly found that the liquid co-injected with the ^{syr}SPZ widened the interstitial space, which allows ^{syr}SPZ to display erratic movement patterns.

Despite the fact that mouse skin does not fully replicate human skin regarding skin thickness (mouse skin <1 mm vs human skin >2 mm[29]), as underlined by ^{msq}SPZ deposition in the mouse peritoneum (length of mosquito proboscis: 1.5-2.0 mm[30]), the remarkable differences between the ^{msq}SPZ and ^{syr}SPZ dermal sites provide important clues on how to critically improve intradermal syringe injections of attenuated SPZ vaccines. Particularly, a microneedle (patch), tattoo device or Nanoliter Injector may be useful to not only create the relevant SPZ dispersion, but also to decrease injection volume to the nanoliter range[31-35]. In addition, laser-induced vascular damage can potentially mirror the hematomas induced by mosquito probing and enhance the blood vessel entrance of ^{syr}SPZ[36]. Recently, this concept was successfully applied to increase parasite loads in the liver after intradermal syringe injection[37].

Importantly, our study demonstrates that state-of-the-art imaging (analysis) techniques can provide valuable quantitative assessments of parameters affecting SPZ migration. Our *ex vivo* set-up combined with spinning-disk confocal microscopy and SPZ tracking software enabled 1) the visualization of (the SPZ distribution throughout) the whole inoculation and injection site (up to 100 mm^2), whereas up to now only one field of view (<0.5 mm^2) was visualized during *in vivo* live imaging[14, 17, 38], 2) the visualization of morphological tissue deformation as a result of the fluid injection, previously acknowledged as an important parameter regarding transdermal drug delivery[39-41], but not yet visualized at a micron level resolution and 3) a multidimensional analysis of SPZ motility unveiling an remarkable interplay between motility parameters which were up to now only studied independently[16-18]. Further research is needed to study the role of other potential contributors not accounted for in this imaging study, such as their pre-processing of ^{syr}SPZ (manual extraction from salivary glands in culture medium) and the effect of saliva inoculated by mosquitoes[15, 42, 43]. Our quantitative assessment of parameters affecting SPZ migration 1) indicates that engineering solutions should be explored that can better mimic mosquito inoculation as well as 2) provides a readout needed to assess the potential of the suggested engineering solutions. In conclusion, detailed microscopic imaging of the dermal site appearance and migration patterns of SPZ revealed important quantitative differences between SPZ administration via mosquito inoculation vs intradermal syringe injection. These findings open new avenues for intradermal delivery of attenuated SPZ vaccines with enhanced efficacy.

Acknowledgments: We would like to thank ing. J. Ramesar and dr. C.J. Janse for support with the mosquito infection. We also thank the light microscopy facility team of the LUMC for their support during image acquisition and analysis.

REFERENCES

1. Organization, W.H., World Malaria Report 2019. 2019.
2. Richie, T.L., et al., Progress with Plasmodium falciparum sporozoite (PfSPZ)-based malaria vaccines. Vaccine, 2015. 33(52): p. 7452-61.
3. Clyde, D.F., Immunity to Falciparum and Vivax Malaria Induced by Irradiated Sporozoites - a Review of the University-of-Maryland Studies, 1971-75. Bulletin of the World Health Organization, 1990. 68: p. 9-12.
4. Hoffman, S.L., et al., Protection of humans against malaria by immunization with radiation-attenuated Plasmodium falciparum sporozoites. J Infect Dis, 2002. 185(8): p. 1155-64.
5. Epstein, J.E., et al., Live attenuated malaria vaccine designed to protect through hepatic CD8(+) T cell immunity. Science, 2011. 334(6055): p. 475-80.
6. Seder, R.A., et al., Protection against malaria by intravenous immunization with a nonreplicating sporozoite vaccine. Science, 2013. 341(6152): p. 1359-65.
7. Ploemen, I.H.J., et al., Visualisation and Quantitative Analysis of the Rodent Malaria Liver Stage by Real Time Imaging. Plos One, 2009. 4(11).
8. Haeberlein, S., et al., Protective immunity differs between routes of administration of attenuated malaria parasites independent of parasite liver load. Sci Rep, 2017. 7(1): p. 10372.
9. Nganou-Makamdop, K., et al., Reduced Plasmodium berghei sporozoite liver load associates with low protective efficacy after intradermal immunization. Parasite Immunology, 2012. 34(12): p. 562-569.
10. Nussenzweig, R.S., et al., Protective Immunity Produced by Injection of X-Irradiated Sporozoites of Plasmodium Berghei. Nature, 1967. 216(5111): p. 160-+.
11. Ploemen, I.H., et al., Plasmodium liver load following parenteral sporozoite administration in rodents. Vaccine, 2013. 31(34): p. 3410-3416.
12. Natarajan, R., et al., Fluorescent Plasmodium berghei sporozoites and pre-erythrocytic stages: a new tool to study mosquito and mammalian host interactions with malaria parasites. Cellular microbiology, 2001. 3(6): p. 371-379.
13. Winkel, B.M.F., et al., A tracer-based method enables tracking of Plasmodium falciparum malaria parasites during human skin infection Theranostics, 2019. 9(10): p. 2768-2778.
14. Amino, R., et al., Quantitative imaging of Plasmodium transmission from mosquito to mammal. Nat Med, 2006. 12(2): p. 220-4.
15. de Korne, C.M., et al., Regulation of Plasmodium sporozoite motility by formulation components. Malaria Journal, 2019. 18.
16. Hellmann, J.K., et al., Environmental constraints guide migration of malaria parasites during transmission. PLoS Pathog, 2011. 7(6): p. e1002080.
17. Hopp, C.S., et al., Longitudinal analysis of Plasmodium sporozoite motility in the dermis reveals component of blood vessel recognition. Elife, 2015. 4.
18. Winkel, B.M.F., et al., Quantification of wild-type and radiation attenuated Plasmodium falciparum sporozoite motility in human skin. Scientific Reports, 2019. 9.
19. Sinden, R., Infection of mosquitoes with rodent malaria, in The Molecular Biology of Insect Disease Vectors, C.B.B.a.C.L. J. M. Crampton, Editor. 1997, Springer, Dordrecht. p. 67-91.
20. Kebaier, C., Y. Jin, and J. Vanderberg, Direct microscopic quantification of transmission dynamics of Plasmodium sporozoites from mosquitoes to mice. American Journal of Tropical Medicine and Hygiene, 2007. 77(5): p. 11-12.
21. Schindelin, J., et al., Fiji: an open-source platform for biological-image analysis. Nature Methods, 2012. 9(7): p. 676-682.
22. Yu, Y., mixR: Finite Mixture Modeling for Raw and Binned Data. 2018.
23. R Core Development Team, R: A language and environment for statistical computing. 2020, R Foundation for Statistical Computing: Vienna, Austria.
24. Hegge, S., et al., Automated classification of Plasmodium sporozoite movement patterns reveals a shift towards productive motility during salivary gland infection. Biotechnol J, 2009. 4(6): p. 903-13.
25. Munter, S., et al., Plasmodium sporozoite motility is modulated by the turnover of discrete adhesion sites. Cell Host Microbe, 2009. 6(6): p. 551-62.
26. Choumet, V., et al., Visualizing Non Infectious and Infectious Anopheles gambiae Blood Feedings

in Naive and Saliva-Immunized Mice. Plos One, 2012. 7(12).
27. Vanderberg, J.P., Imaging mosquito transmission of Plasmodium sporozoites into the mammalian host: Immunological implications. Parasitology International, 2014. 63(1): p. 150-164.
28. Muthinja, M.J., et al., Microstructured Blood Vessel Surrogates Reveal Structural Tropism of Motile Malaria Parasites. Adv Healthc Mater, 2017. 6(6).
29. Wei, J.C.J., et al., Allometric scaling of skin thickness, elasticity, viscoelasticity to mass for micro-medical device translation: from mice, rats, rabbits, pigs to humans. Scientific Reports, 2017. 7.
30. Ramasubramanian, M.K., O.M. Barham, and V. Swaminathan, Mechanics of a mosquito bite with applications to microneedle design. Bioinspiration & Biomimetics, 2008. 3(4).
31. Crichton, M.L., et al., The changing shape of vaccination: improving immune responses through geometrical variations of a microdevice for immunization (vol 6, 27217, 2016). Scientific Reports, 2016. 6.
32. Esser, E.S., et al., Microneedle patch delivery of influenza vaccine during pregnancy enhances maternal immune responses promoting survival and long-lasting passive immunity to offspring. Scientific Reports, 2017. 7.
33. Quinn, H.L., et al., The role of microneedles for drug and vaccine delivery. Expert Opinion on Drug Delivery, 2014. 11(11): p. 1769-1780.
34. Shio, M.T., et al., Drug Delivery by Tattooing to Treat Cutaneous Leishmaniasis. Scientific Reports, 2014. 4.
35. Atif, M., J.W. Lynch, and A. Keramidas, The effects of insecticides on two splice variants of the glutamate-gated chloride channel receptor of the major malaria vector, Anopheles gambiae. British Journal of Pharmacology, 2020. 177(1): p. 175-187.
36. Sklar, L.R., et al., Laser Assisted Drug Delivery: A Review of An Evolving Technology. Lasers in Surgery and Medicine, 2014. 46(4): p. 249-262.
37. Zhou, C., et al., Laser mimicking mosquito bites for skin delivery of malaria sporozoite vaccines. Journal of Controlled Release, 2015. 204: p. 30-37.
38. Vanderberg, J.P. and U. Frevert, Intravital microscopy demonstrating antibody-mediated immobilisation of Plasmodium berghei sporozoites injected into skin by mosquitoes. Int J Parasitol, 2004. 34(9): p. 991-6.
39. Gupta, J., et al., Infusion pressure and pain during microneedle injection into skin of human subjects. Biomaterials, 2011. 32(28): p. 6823-6831.
40. Mansoor, I., et al., A microneedle-based method for the characterization of diffusion in skin tissue using doxorubicin as a model drug. Biomedical Microdevices, 2015. 17(3).
41. Shrestha, P. and B. Stoeber, Fluid absorption by skin tissue during intradermal injections through hollow microneedles. Scientific Reports, 2018. 8.
42. Doolan, D.L., Malaria Methods and Protocols. 2002: Humana Press Inc.
43. Schleicher, T.R., et al., A mosquito salivary gland protein partially inhibits Plasmodium sporozoite cell traversal and transmission. Nature Communications, 2018. 9.

SUPPLEMENTARY INFORMATION

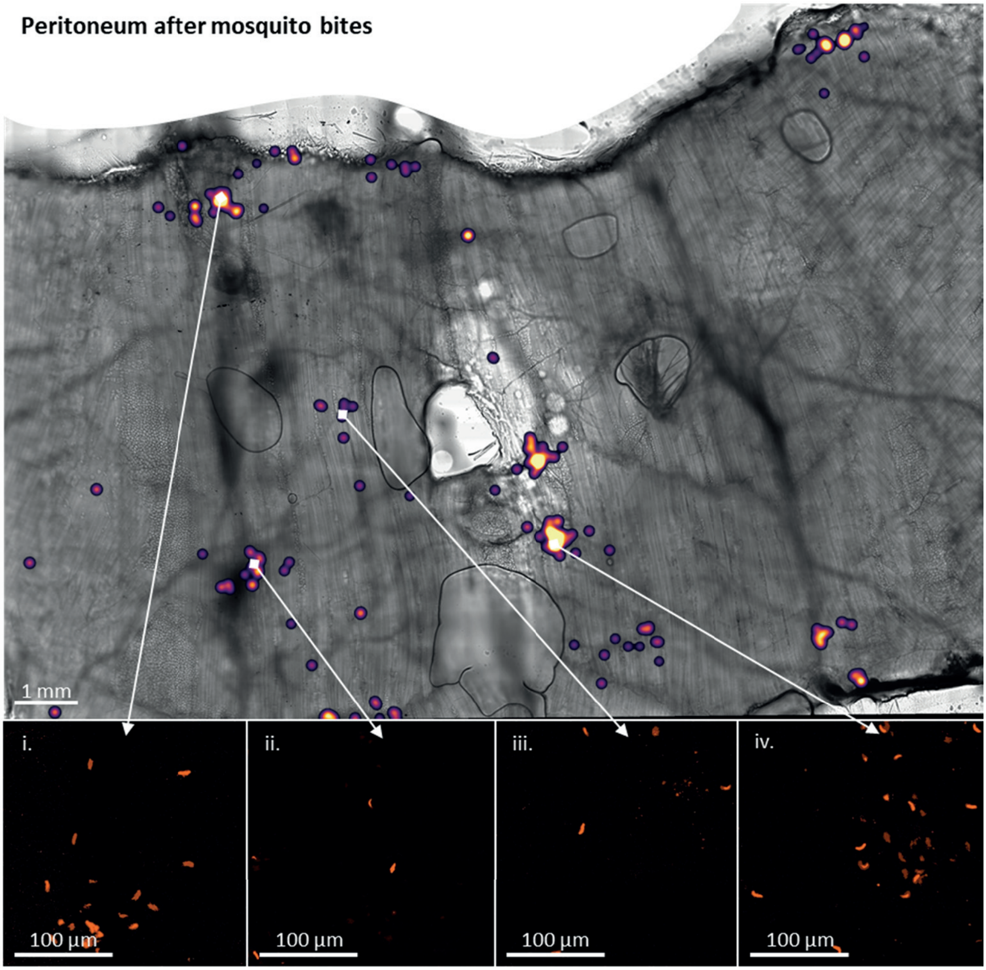

Sup. Figure S1 Peritoneum after mosquito bites. Overview of peritoneum after SPZ delivery by mosquito inoculation shown as an overlay of a brightfield image and the SPZ distribution accompanied by zoom-in images showing the individual SPZ (i-iv).

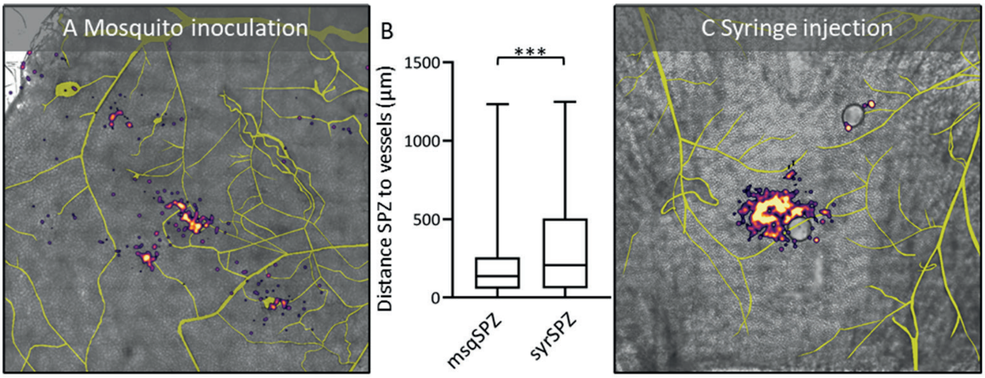

Sup. Figure S2 Sporozoite to blood vessel distance. A & C) Overview of the inoculation site after SPZ delivery by mosquito (A) and the injection site after SPZ delivery by intradermal syringe injection (C) shown as an overlay of a brightfield image, the SPZ distribution (pseudo-colored, blurred fluorescent image) and the segmented blood vessels (depicted in yellow). B) Quantification of the SPZ-to-blood vessel distance (n=2 per condition). ***p<0.001; Mann Whitney U test.

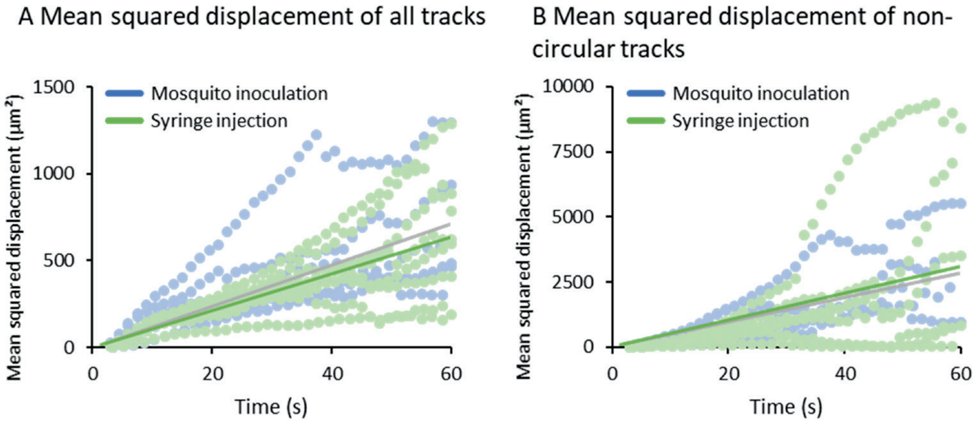

Sup. Figure S3 Mean squared displacement. A-B) The mean squared displacement of the SPZ after administration by mosquito inoculation or syringe injection is plotted. In A) all tracks are included, in B) the circular tracks are excluded (90% of mosquito inoculation frames, 95% of syringe injection frames). The mean squared displacement of the individual samples is plotted as a dotted line, a linear trendline is plotted as a solid line.

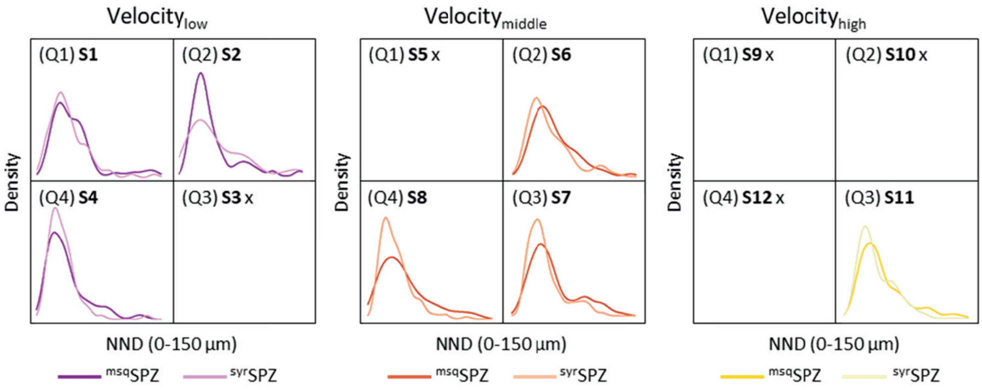

Sup. Figure S4 Relation between motility parameters and nearest neighbor distance. The nearest neighbor distance (NND) is plotted for the tracks split into 12 subsets (S1-12) based on four specific movement patterns (Q1-4, see Figure 6) and three velocity categories (1: <0.1 µm/s, depicted in purple; 2: 1-2 µm/s, depicted in orange; 3: >2 µm/s, depicted in yellow). The NND of the ^{msq}SPZ is depicted in the darker color and the NND of the ^{syr}SPZ in depicted in the lighter color.

4

Sporozoite motility as a quantitative readout for anti-CSP antibody inhibition

Clarize M. de Korne, Roos van Schuijlenburg, Jeroen C. Sijtsma, Laura M. de Bes, Els Baalbergen, Samaneh Azargoshasb, Matthias N. van Oosterom, Matthew B.B. McCall, Fijs W.B. van Leeuwen, Meta Roestenberg

Scientific Reports 2022. DOI: 10.1038/s41598-022-22154-8

ABSTRACT

Antibodies can prevent malaria by neutralizing the infectious *Plasmodium falciparum* sporozoites (SPZ) before they establish an infection in the liver. Circumsporozoite protein (CSP), the most abundant surface protein of SPZ, is the leading candidate for passive (and subunit) immunization approaches against malaria. Comprehensive assessment of the parasite-inhibitory capacity of anti-CSP monoclonal antibodies (mAbs) is an important step in advancing CSP-based immunization strategies. In this study, we employed a quantitative imaging-based motility assay to quantify the effect of anti-CSP mAbs on SPZ motility, both *in vitro* and in human skin. Our assay provided a quantitative measure of mAb parasite-inhibitory capacity through measurement of the half-maximal motility inhibitory concentration (IC_{50M}) value for anti-CSP mAbs (IC_{50M} 2A10: 24 nM, IC_{50M} 3SP2: 71 nM). We found a 7-fold discrepancy between the IC_{50M} and the binding saturation concentration measured by ELISA, possibly related to the observed shedding of CSP-mAb complexes during SPZ movement. In a subset of SPZ (5%), *in vitro* motility was unaffected by the presence of 2A10 while 3SP2 was able to completely block movement. In our *ex vivo* skin explant model, SPZ proved less susceptible to anti-CSP mAbs compared to SPZ *in vitro*. By quantitatively assessing motility, we created a valuable tool that can be used for comprehensive assessment of anti-CSP mAb potency, thereby providing insight that will help deepen our understanding of anti-CSP mAb potency and guide selection of the most promising anti-CSP mAbs for downstream clinical development.

INTRODUCTION

Since the gains of the current approaches have levelled off and malaria still causes more than 500,000 deaths annually, controlling and eventually eradicating malaria requires additional strategies[1]. Currently, the passive transfer of monoclonal antibodies (mAbs) as a prevention strategy for malaria infections is gaining traction. The concept of passive immunization against malaria is not new[2], but only recently it has been demonstrated that it can induce protection in humans against a controlled malaria infection and prevent onward transmission[3, 4]. Passive immunization can be a valuable approach to induce short-term protection (up to 6 months) against malaria for e.g. pregnant women, military personnel and residents of areas with highly seasonal transmission (e.g. the Sahel sub-region of Africa)[5].

So far, the target of these anti-malaria infection mAbs (and leading malaria vaccine candidates) is the circumsporozoite protein (CSP), abundantly presented at the sporozoite (SPZ) surface[6]. SPZ are considered an attractive vaccine target, since this early life cycle stage is the longest extracellular stage of the life cycle (ranging from minutes to hours[7, 8]). This stage also presents a bottleneck for the infection process as approximately only 1-500 SPZ are inoculated by a mosquito[9, 10]. CSP is thought to play a critical role in SPZ migration; an essential process which enables the SPZ to migrate from the inoculation site to the liver and invade hepatocytes to establish a full-blown infection[11, 12]. In line with this, *in vivo* studies suggest that the direct impact of anti-CSP mAbs on the motility of SPZ hampers their dermal exit, thus contributing to the protective effect of anti-CSP mAbs in preventing liver infection[13-16].

Despite the direct effect of anti-CSP mAbs on SPZ motility, a quantitative assay for this parameter is lacking. Currently, the binding capacity of anti-CSP mAbs for CSP is assessed by ELISA and some of their functional effects on SPZ have been assessed in gliding, cell traversal and hepatocyte invasion assays[17-19]. However, these assays are not sufficiently quantitative to rank the parasite-inhibitory capacity of the increasing number of anti-CSP mAbs being produced nowadays which is needed to select the most potent candidates for downstream (pre)clinical testing.

We hypothesize that an assay capable of more comprehensive quantitative assessment of anti-CSP mAb functionality (including not only binding capacity and hepatocyte invasion inhibition, but also *in vitro* and in skin motility interference) will aid the identification of efficacious anti-CSP mAbs. As such, we have employed SMOOT (Sporozoite Motility Orienting and Organizing Tool[20, 21]), which has been developed to detect subtle differences in SPZ motility, to quantitate the impact of anti-CSP mAbs in an *in vitro* and *ex vivo* human skin experimental model. As a proof-of-concept, we studied the functionality of two commonly used and known inhibitory anti-CSP mAbs 2A10[22] and 3SP2[23] and explored the coherence between mAb-antigen binding affinity and the mAb's functional effects on SPZ motility and hepatocyte invasion. Overall, this study established the quantification of SPZ motility as a valuable additional part of the assessment of anti-CSP mAb functionality needed to support the development of CSP-based passive immunization strategies for malaria.

METHODS

Sporozoite production

Plasmodium falciparum (NF54 strain) SPZ were obtained, both wildtype SPZ and transgenic SPZ that express the fluorescent reporter protein GFP under the CSP promoter (NF54-ΔPf47-5'*csp*-GFP-Luc, kindly provided by dr. Koen Dechering; TropIQ Health Sciences) or the fluorescent reporter protein mCherry under the Sui1 promotor (line Pf-Exp. 159 as described by Miyazaki *et al.*[24]). *Plasmodium falciparum* gametocyte cultures were generated using standard culture conditions in a semi-automated culture system and subsequently gametocytes were fed to *Anopheles stephensi* female mosquitoes by standard membrane feeding as described previously[25, 26]. SPZ were obtained by manual dissection of the salivary glands of mosquitoes 14-17 days post infection. The salivary glands were collected and homogenized to release SPZ in Roswell Park Memorial Institute medium (RPMI; Thermo Fisher Scientific) enriched with 10% fetal bovine serum (FBS; Thermo Fisher Scientific) and 1% penicillin-streptomycin (PS; Thermo Fisher Scientific) unless otherwise stated. The free SPZ were counted in a Bürker counting chamber using phase-contrast microscopy and used for experiments immediately or frozen down (> 1 week at -20 °C) to obtain SPZ lysate for ELISA.

Whole SPZ ELISA for mAb affinity measurements

Thawed SPZ lysate was suspended to a concentration of $0.2*10^6$ SPZ/ml in phosphate buffered saline (PBS; Thermo Fisher Scientific), plated at 50 µl/well in a flat bottom clear, half-area 96 well plate (Corning) and incubated overnight at 4 °C. The solution was gently removed from the wells and the plate was air dried for 30 min. Plates were then blocked with PBS + 1% FBS for 1 hr at room temperature (RT) and washed with PBS + 0.05% Tween 20 (Sigma-Aldrich). To assess the binding affinity of the anti-CSP mAbs 2A10 (obtained through BEI Resources, contributed by prof. E. Nardin) and 3SP2 ([23]; Radboudumc), these mAbs were titrated in 3-fold serial dilutions (concentration range: 1.0 µg/ml – 0.02 ng/ml, control: no mAb) in PBS + 1% FBS and allowed to bind to the SPZ lysate-coated surface for 1 hr at RT. After washing, the wells were incubated with a secondary antibody (HRP labelled goat anti-mouse IgG antibody, 1:1000 in PBS + 1% FBS; Invitrogen) for 1 hr at RT. After washing, a color reaction was induced using a substrate solution (TMB Microwell Peroxidase Substrate System; KPL) following the manufacturer's instructions and subsequently stopped by adding stop solution (1.8 M sulphuric acid in MilliQ; Merck). Plates were read on a Multiskan FC

Microplate Photometer (Thermo Scientific) at 450 nm absorption. All experiments were performed *in duplo*, containing two samples per concentration per experiment. Competition curves were obtained by plotting the obtained absorbance values against the log of the mAb concentration. Sigmoidal curves were fitted to a four-parameter logistic equation using GraphPad Prism (version 9.0.1; GraphPad Software), from which IC_{50} values (concentration at which binding of the mAbs to SPZ lysate was inhibited by 50%) were determined.

Elution procedure for mAb avidity measurements

To measure the avidity of the anti-CSP mAbs 2A10 and 3SP2, the whole SPZ ELISA was performed as described above with the addition of an elution procedure with ammonium thiocyanate (NH_4SCN; Sigma-Aldrich) performed between the incubation steps with the primary mAbs (2A10: 10 ng/ml, 3SP2: 100 ng/ml) and the secondary antibody. A concentration range of ammonium thiocyanate in 0.1 M sodium phosphate pH 6.0 was added to the wells (concentration range: 1.0 M – 1.0 mM, control: no sodium thiocyanate; Sigma-Aldrich) and incubated for 20 min at RT. The absorbance readings in the presence of increasing concentrations of ammonium thiocyanate were converted to the appropriate percentage of the total bound mAb in the absence of ammonium thiocyanate. For both 2A10 and 3SP2 the avidity index was estimated, representing the molar concentration of thiocyanate required to reduce the initial absorbance by 50%.

Sporozoite motility *in vitro*

To assess the effect of the anti-CSP mAbs (2A10 & 3SP2) on *in vitro* SPZ motility, SPZ expressing mCherry were pre-incubated with a concentration range (control: no antibody, 0.5, 1, 2.5, 5, 10, 25, 50, 100 µg/ml) of the anti-CSP antibodies 2A10 or 3SP2 in RPMI + 10% FBS for 30 min at RT and subsequently (without washing away mAbs) $0.5*10^5$ SPZ were pipetted on the coverslip of a non-coated confocal dish and covered. Movies were recorded on a Leica TCS (true confocal scanning) SP5 microscope (Leica Microsystems, Wetzlar) at 37 °C under 5% CO_2 conditions using a 561 nm laser to excite mCherry. The emission signal was collected between 600 and 650 nm and movies were recorded with a frame rate of 35 frames per minute, 200 frames per movie. The movies were further processed using $SMOOT_{in\ vitro}$; in-house developed motility analysis software written in the MATLAB programming environment (The MathWorks Inc.). The movement patterns of the SPZ were classified as floating, stationary or moving (circling) and the velocity of the moving SPZ was determined as previously described[20]. In total, movies from two independent experiments containing 2-3 samples per concentration were included in the analysis; a total number of 4227 SPZ were analyzed, on average 235 ± 95 per condition.

Localization anti-CSP mAbs

Immunohistochemistry was performed to visualize the localization of anti-CSP mAbs.

Wildtype SPZ were incubated with a concentration range (0.5, 1, 2.5, 5, 10, 25, 50 µg/ml) of the anti-CSP mAbs 2A10 or 3SP2 in RPMI + 10% FBS for 30 min at RT and subsequently $0.5*10^5$ SPZ were added to a confocal dish without any precoating (ø14 mm; MatTek Corporation) and covered with a coverslip (ø12 mm; VWR Avantor). Then, the secondary antibody (goat anti-mouse IgG Alexa Fluor 488, 1:500 in PBS; Invitrogen) was added and incubated for 45 min at RT. The SPZ were counterstained with Cy5-Methyl-Methyl (50 nm; whole body staining) and Hoechst (10 µg/ml; nucleus staining). Finally, the samples were mounted with Prolong Gold Dapi (Invitrogen) and examined using a Leica TCS (true confocal scanning) SP8X WLL (white light laser) microscope (Leica Microsystems) with a 100x objective (HCX PL APO 100x/1.40-0.70 OIL CS). The Alexa 488 dye conjugated to the secondary antibody was excited at 488 nm (emission: 500-550 nm), Cy5-Methyl-Methyl was excited at 633 nm (emission: 650-700 nm) and Hoechst was excited at 405 nm (emission: 420-470).

Sporozoite motility in human skin explant

To assess the effect of the anti-CSP mAbs (2A10 & 3SP2) on SPZ movement in human skin explant, SPZ expressing GFP were pre-incubated with a concentration range (control: no mAb, 10, 25, 50, µg/ml) of the anti-CSP mAbs 2A10 or 3SP2 in RPMI + 10% FBS for 30 min at RT. Following pre-incubation, 10 µl mAb solution containing $0.1*10^5$ SPZ (without washing away mAbs) was injected intradermally into human skin explant using a NanoFil needle and syringe (10 µl NanoFil syringe, MicroFil 28G needle; World precision instruments). Human skin explants from 4 different donors were obtained from collaborating surgical centers immediately after surgery. Anonymized human skin explants were obtained from donors undergoing mastectomy after informed consent, approval was obtained by the Commission Medical Ethics (CME) Leiden under number CME: B18-009. All research has been performed according to relevant guidelines/regulations. Immediately after SPZ injection, the injection site was biopsied using a 6 mm biopsy punch (Stiefel), sliced longitudinally through the center, mounted on a microscopy slide. Movies were recorded using an Andor Dragonfly 500 spinning disk confocal on a Leica DMi8 microscope (Oxford Instruments) with a 40x objective (HCX PL APO 40x/1.30 OIL). The GFP expressed by the SPZ was excited with the 488 nm laser. The movies were recorded with a frame rate of 40 frames per minute, 200 frames per movie. The motility of the moving SPZ was analyzed using $\text{SMOOT}_{\text{human skin}}$[21]. In total, 1047 SPZ were analyzed, on average 150 ± 41 per condition.

Sporozoite infection assay

HC-04.J7 cells (a human liver cell line kindly provided by prof. R. Dinglasan) were maintained in culture at 37°C and 5% CO_2 in culture medium (IMDM (Lonza) supplemented with 10% FBS and 1% PS). One day prior to infection, the cells were harvested in seeding medium (DMEM without glucose (Thermo Fisher Scientific) supplemented with 5% FBS and 1% PS) and seeded at a density of $4x10^4$ cells/well in collagen-coated (50 µg/ml, 30 min incubation at RT; Corning) 96-well plates (for PCR samples: plate with Nunclon Delta surface and for imaging samples: Nunc optical-bottom plate with cover glass base; both Thermo Scientific) which resulted in a confluent monolayer at the day of infection. 4-6 hr prior to infection, the seeding medium was replaced by infection medium (seeding medium supplemented with glucose (15 mM; Thermo Fisher Scientific) and Gibco insulin-transferrin-selenium solution (1:100; Thermo Fisher Scientific). Wildtype SPZ were collected as described above in infection medium and pre-incubated with a dilution range of anti-CSP mAbs 2A10 and 3SP2 (3-fold serial dilutions, concentration range: 50 µg/ml – 69 ng/ml in infection medium, control: no mAb) for 30 min at RT. Subsequently, $4x10^4$ pre-incubated SPZ were added to the HC-04.J7 cells by replacing the medium of the cells by 50 µl SPZ solution. Unbound mAb was not removed before addition of the SPZ to the hepatocyte culture. As a negative control, $4x10^4$ heat-killed SPZ (15 min at 100ºC) were added to the cells. The SPZ were spun down for 3 min at 1200 RPM and the plates were incubated for 3 hr at 37°C and 5% CO_2. After the incubation period, the cells were washed with culture medium to remove the non-invaded SPZ. The culture medium was refreshed at day 2. At day 4, the imaging samples were fixed with 4% formaldehyde for 20 min at RT and subsequently stained. The PCR-samples were lysed using 100 µl RLT buffer (25 min incubation; Qiagen). The lysed cells were stored at -80°C until further use.

Imaging-based analysis of hepatocyte infection

To assess SPZ infection by microscopy, the fixed HC-04.J7 cells were permeabilized with 0.5% Triton (Thermo Fisher Scientific) in PBS for 20 min and blocked with 10% FBS in PBS for 45 min. After blocking, the primary anti-Hsp70 (1:200; Thermo Fisher Scientific) and anti-GAPDH (1:1000; University of Edinburgh) antibodies were added to the control samples and incubated o/n at 4°C. Next, the secondary antibodies (anti-rabbit AF594, 1:500 in PBS & anti-mouse AF488, 1:500 in PBS; Invitrogen) were added to all dishes and incubated for 1 hr min at RT. Finally, Hoechst 33342 (1 mg/ml, 1:200; Sigma-Aldrich) was added to the cells and incubated for 30 min at RT. The samples were stored in PBS at 4°C until imaging. The samples were imaged using an Andor Dragonfly 500 spinning disk confocal on a Leica DMi8 microscope (Oxford Instruments) with a 40x objective (HCX PL APO 40x/1.30 OIL). Hoechst was excited with the 405 nm laser, AF488 with the 488 nm laser and AF594 with the 561 laser. The Andor imaging software Fusion (Oxford Instruments) and Fiji software were used to generate a single image from the z-stacks (10 Z-slices, total dept 30 µm) obtained with the different lasers.

PCR-based analysis of hepatocyte infection

To assess SPZ infection by PCR, the 18S ribosomal RNA (rRNA) levels were determined. To this end, RNA was isolated from the cell cultures using the RNeasy kit (Qiagen) and cDNA was generated using random hexamer primers (Promega) and Superscript™ III (Thermo Fisher) according to manufacturer's instructions. Amplification reactions of each cDNA sample were performed in PCR plates (hard-shell PCR plate; Bio-Rad), in a volume of 10 µl containing 5 µl PCR buffer (GoTaq qPCR master mix; Promega), 1 µl RNase-free milliQ water, 2 µl primer mix (forward primer: Plasmo Plu3F 5'-GCTCTTTCTTGATTTCTTGGATG-3' (0.2 µM; Integrated DNA Technologies, Inc.); reverse primer: Plasmo Plu3R 5'- AGCAGGTTAAGATCTCGTTCG-3' (0.2 µM; Integrated DNA Technologies, Inc.)) and 2 µl of the cDNA sample. Amplification was performed 10 min at 95°C followed by 50 cycles of 10 s at 94°C, 15 s at 60°C, and 30 s at 72°C. Amplification, detection, and analysis were performed with the CFX96TM real time PCR detection system (Bio-Rad).

Statistical analysis

Data were summarized using the mean and standard deviation (SD) for parametric data or the median and interquartile range (IQR) for nonparametric data. For the comparison of groups, the difference between means or medians was assessed using respectively the independent sample T test and the Mann-Whitney U test. All statistical tests were performed by SPSS Statistics (IBM Nederland BV). The probability distribution of SPZ velocity was obtained by calculating the probabilities of velocities between 0 and 5 µm/s using the probability density function available in the open source R environment[27].

RESULTS

Binding of anti-CSP mAbs to sporozoites

A whole SPZ ELISA was used to confirm the picomolar affinity of the anti-CSP monoclonal antibodies (mAbs) 2A10 and 3SP2 for SPZ. The equilibrium dissociation constant (K_D) of 2A10 was 8.4-fold lower than the K_D of 3SP2 (K_D 2A10: 0.086 nM, K_D 3SP2: 0.73 nM) (Figure 1A). These values are in line with those previously reported for anti-CSP mAbs[18]. Saturation of binding sites occurred around 1 nM for 2A10 and 10 nM for 3SP2. The mAbs avidity was determined using thiocyanate elution. The avidity index (IC_{50A}: amount of thiocyanate required to reduce antibody-antigen binding by 50%) of 2A10 was 26-fold higher than the avidity index of 3SP2 (IC_{50A} 2A10: 1.2 M, IC_{50A} 3SP2: 0.045 M) (Figure 1B).

Effect of anti-CSP mAbs on sporozoite behavior *in vitro*

To assess the functional effect of the anti-CSP mAbs 2A10 and 3SP2 on SPZ, SPZ were preincubated with the mAbs after which their motility was assessed *in vitro*. Three movement patterns were discerned: floating, stationary and moving. Roughly 50% of non-exposed control SPZ were moving, about 10% was attached to the surface but not moving and the remaining 40% were floating (Figure 2A). Interestingly, neither mAb had a detectable effect on SPZ motility at the concentration that fully saturated the available binding sites in a SPZ ELISA (1 nM for 2A10, 10 nM for 3SP2; Figure 2B). At higher concentrations, the anti-CSP mAbs interfered both with SPZ attachment and motility. Exposure to a concentration of 15 nM 2A10 or higher interfered with attachment of SPZ to the glass surface, which resulted in an increased number of floating SPZ (>70%) and a reciprocal decreased percentage of moving SPZ (±5%). In contrast, exposure to 65 nM or higher concentrations of 3SP2 resulted in attached, but non-moving SPZ (stationary: >80%, moving: 0%) (Figure 2B). This indicates that two different mechanisms are at play; 2A10 reduces movement mainly through a reduction in surface attachment, while 3SP2 reduces movement by increasing surface attachment and thereby blocking movement. To reduce the percentage of moving SPZ by 50%, 3-fold more 3SP2 was needed compared to 2A10 (half maximal motility inhibitory concentration (IC$_{50M}$) 2A10: 24 nM, IC$_{50M}$ 3SP2: 71 nM) (Figure 2B). That said, 3SP2 was able to completely block movement, while even at high concentrations of 2A10 (>100 nM) 5% of the SPZ continued to move (Figure 2B).

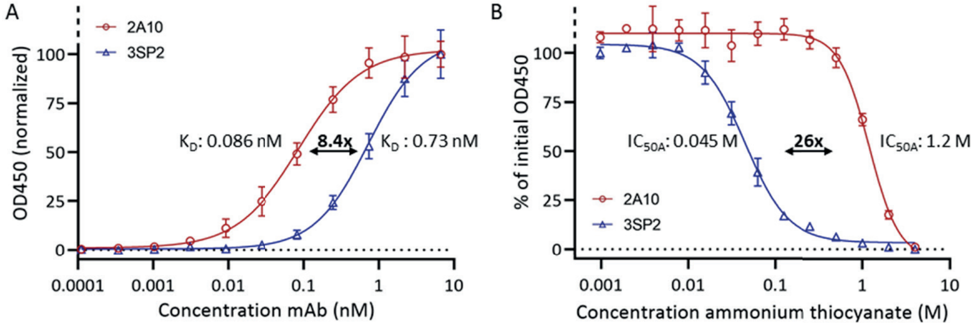

Figure 1 Anti-CSP mAb reactivity to whole sporozoite lysate. A) ELISA curve of anti-CSP mAb binding at different concentrations to whole SPZ lysate to determine mAb affinity (expressed as K$_D$). B) ELISA curve of the effect of a serial dilution of ammonium thiocyanate on anti-CSP mAbs binding to whole SPZ lysate to determine mAb avidity (expressed as IC$_{50A}$).

The impact of the mAbs on the median velocity of the moving SPZ was assessed next. At lower concentrations of mAbs (<10 nM), SPZ velocity was not reduced compared to untreated controls (2.0 (IQR 1.5-2.6) µm/s; Figure 2C+D). At concentrations around the IC$_{50M}$ (when roughly half of the SPZ still move; Figure 2B), both mAbs slowed down the SPZ that were still able to move (median velocity while exposed to 33 nM 2A10: 1.4 (IQR: 1.0-2.2) µm/s, median velocity while exposed to 66 nM 3SP2: 1.1 (IQR: 0.9-1.6) µm/s) (Figure 2D). At increasing concentrations of 2A10, the SPZ velocity distribution changed shape, indicative for a subpopulation of SPZ less susceptible to the effect of 2A10 (Figure 2D), which correlated with the abovementioned finding that a small percentage of SPZ continues moving at high concentrations of 2A10. In summary, the functional *in vitro* motility assessment of mAbs revealed that mAb concentrations above the saturating concentration (as determined by ELISA) are needed to inhibit SPZ motility, mAb motility inhibition mechanisms may vary and that subsets of SPZ may be refractory to the effect of mAbs.

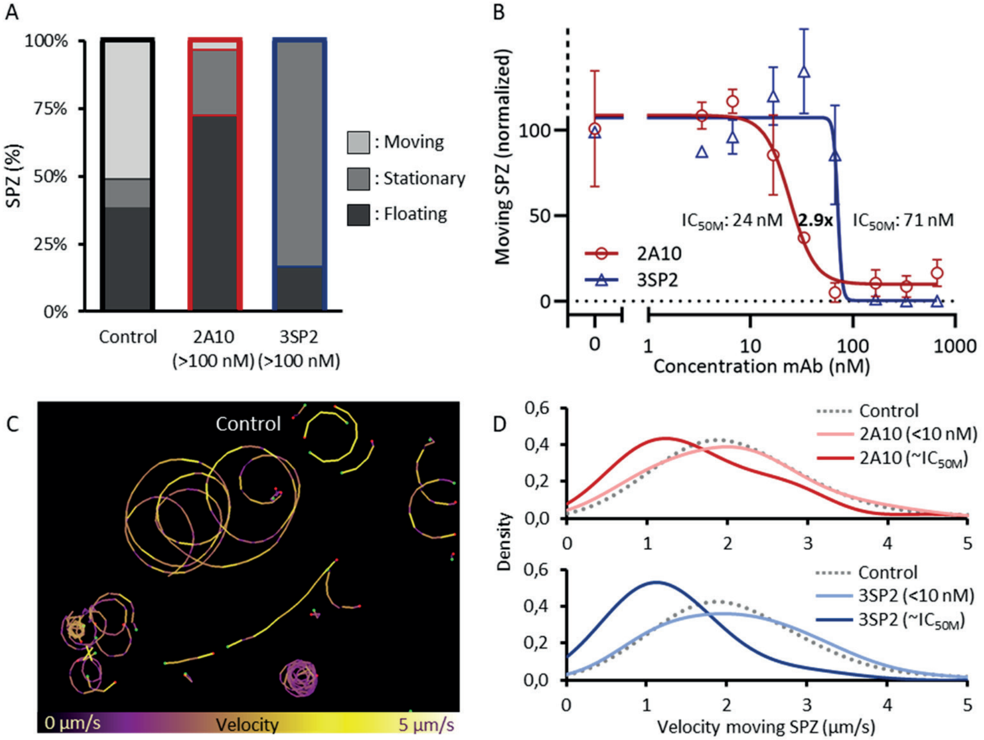

Figure 2 Effect of anti-CSP mAb on sporozoite movement and attachment. A) The movement pattern distribution for control SPZ and SPZ exposed to a high concentration (>100 nM) of the anti-CSP mAbs 2A10 and 3SP2. B) The normalized percentage of moving SPZ plotted against the concentration of mAb to determine the IC$_{50M}$ value at which movement of SPZ was 50% reduced. C) Tracks of SPZ moving *in vitro* on a glass surface, color-coded for velocity using color range: purple (low velocity) to yellow (high velocity). D) The probability distribution plotted of the velocity of control SPZ (median: 2.0 (IQR: 1.5-2.6) µm/s), SPZ exposed to low concentrations of 2A10 and 3SP2 (7nM) (median velocity 2A10: 2.1 (IQR: 1.4-2.6) µm/s, median velocity 3SP2: 2.1 (IQR: 1.4-2.8) µm/s) and SPZ exposed to approximately their IC$_{50M}$ concentration (median velocity while exposed to 33 nM 2A10: 1.4 (IQR: 1.0-2.2) µm/s, median velocity while exposed to 66 nM 3SP2: 1.1 (IQR: 0.9-1.6) µm/s).

Localization of anti-CSP mAbs

The discrepancy between the mAb concentrations needed to interfere with movement and those saturating available binding sites based on SPZ ELISA, suggests that mAbs detach from the SPZ during kinematic analysis. To investigate this, we visualized anti-CSP mAbs using fluorescent secondary Ab staining (Figure 3A). At all concentrations, the mAbs were located on the SPZ surface (Figure 3B). At the lower concentrations of mAbs at which the SPZ were still able to move (Figure 2B), fluorescent spots/trails were visible, indicative of mAbs shedding (Figure 3B). At concentrations of mAbs that interfered with SPZ attachment and motility, 2A10 (≥33 nM) and 3SP2 (≥67 nM) were located on protrusions that seemed distinctive for the two mAbs (2A10: elongated, tubular shaped; 3SP2: short, irregularly shaped) (Figure 3BC). This indicates that viable SPZ can shed mAbs off their surface.

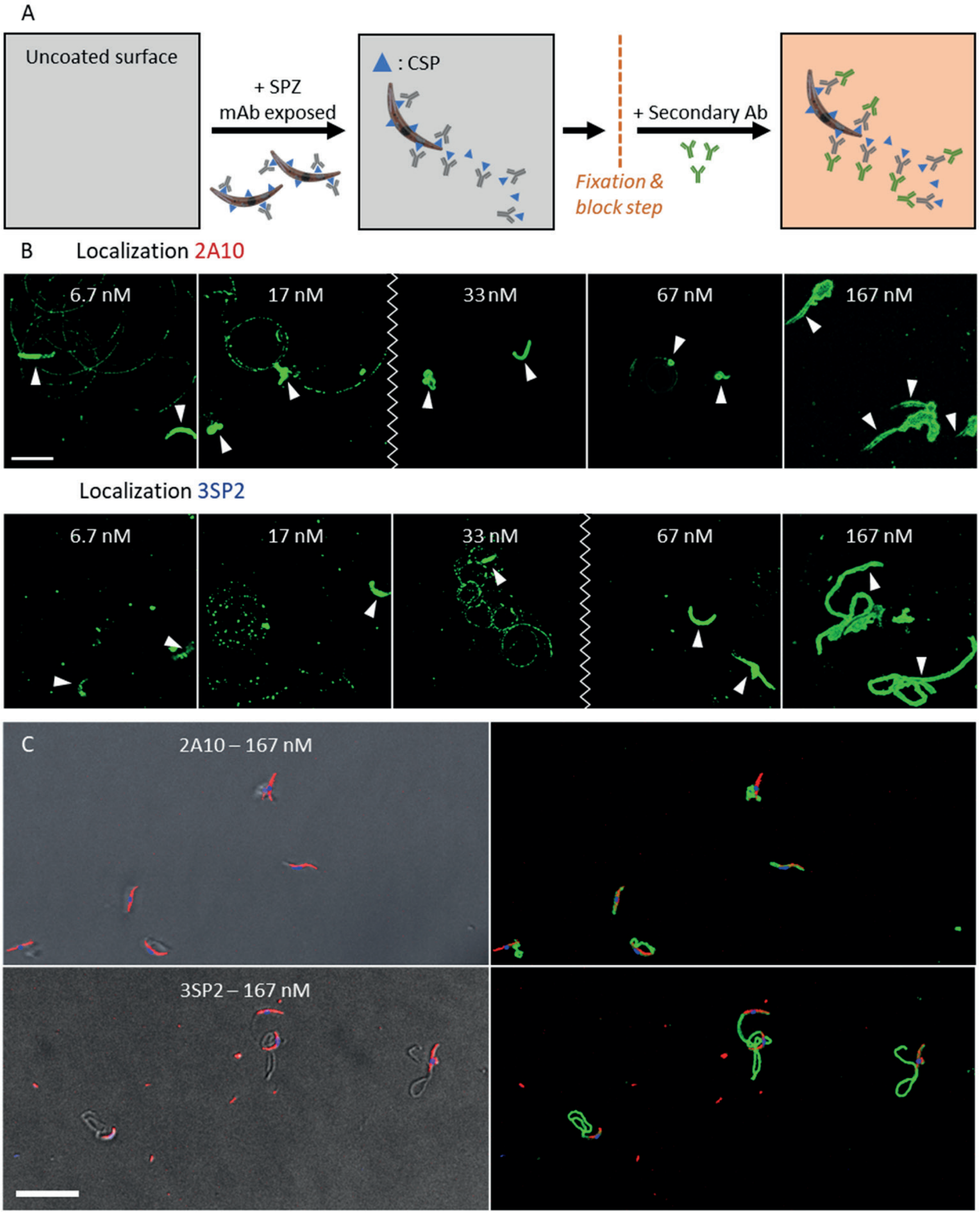

Figure 3 Localization of anti-CSP mAb. A) Schematic overview of the localization of bound anti-CSP mAbs using a fluorescent secondary Ab. B) Visualization of the presence of the anti-CSP mAbs 2A10 and 3SP2; the mAbs staining is shown in green, the location of the SPZ is depicted with an arrow and the zigzag line indicates at which concentration the mAbs started to induce protrusions. Scalebar: 10 µm. C) Visualization of the presence and the effect of 2A10 and 3PS2 on SPZ; to the left an overlay of the brightfield image with the SPZ counterstained with Cy5-Methyl-Methyl (shown in red) and Hoechst (shown in blue) and to the right an overlay of the mAbs staining (shown in green) and the counterstained SPZ. Scalebar: 20 µm.

Effect of anti-CSP mAbs on sporozoite migration patterns in human skin explant

Next, we set out to compare the effect of 2A10 and 3SP2 on SPZ migration patterns in human skin explant. As reported, SPZ migration is markedly different in the 3D skin environment, with more 'directional' linear tracks, as compared to the 'default' circular movement which SPZ exhibit *in vitro*[21] (Figure 4A). In contrast to the mAb concentrations needed *in vitro* to impact SPZ motility described above, pre-incubation with 2A10 and 3SP2 up to concentrations of 333 nM for 30 minutes did not block SPZ motility as compared to untreated controls (median velocity of 1.8 (IQR: 1.1-2.4) µm/s (Figure 4BC)). Only at high concentrations (≥ 67 nM for 2A10 and 333 nM for 3SP2) the SPZ velocity significantly decreased to respectively 1.0 (IQR: 0.6-1.5) and 1.4 (IQR: 0.8-2.0) µm/s ($p<0.001$ and $p=0.002$, Mann-Whitney U test) (Figure 4BC). Increasing concentrations of 2A10 did not further reduce SPZ velocity (median velocity SPZ exposed to 333 nM 1.0 (IQR: 0.7-1.3) µm/s; $p=0.829$ when compared to 67 nM, Mann-Whitney U test) which corresponded with the abovementioned finding that a subset of SPZ is less susceptible to the effect of 2A10. Altogether, these results indicate that higher concentrations of mAbs are needed *ex vivo* to inhibit motility compared to the *in vitro* assay.

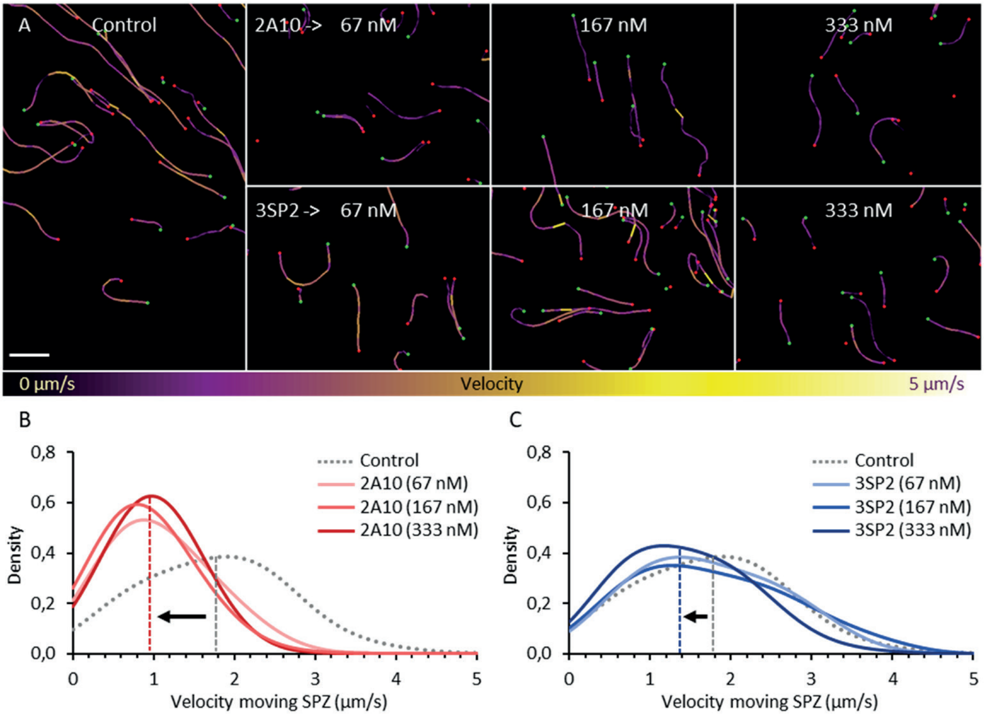

Figure 4 Sporozoite velocity in human skin explant. A) Tracks of SPZ moving in human skin explant, color-coded for velocity using color range: purple (low velocity) to yellow (high velocity). Scalebar: 100 µm. B) The probability distribution plotted of the velocity of control SPZ (median: 1.8 (IQR: 1.1-2.3) µm/s, median annotated with grey dashed line) and SPZ exposed to increasing concentrations

(67, 167, 333 nM) of 2A10 (median velocity SPZ exposed to 333 nM: 1.0 (IQR: 0.7-1.3) µm/s, median annotated with red dashed line). C) The probability distribution plotted of the velocity of control SPZ and SPZ exposed to increasing concentrations (67, 167, 333 nM) of 3SP2 (median velocity SPZ exposed to 333 nM: 1.4 (IQR: 0.8-2.0) µm/s, median annotated with blue dashed line).

Effect of anti-CSP mAbs on sporozoite infectivity

The functional effect of the anti-CSP mAbs on SPZ invasion of hepatocytes was assessed using the HC-04.J7 hepatocyte cell line. Control SPZ readily infected the hepatocytes, as confirmed by microscopy using an anti-Hsp70 staining (Figure 5A). Exposure to 2A10 and 3SP2 inhibited hepatocyte invasion (Figure 5B), which was quantified using RT-PCR. A dose-dependent reduction in invasion was found for both anti-CSP mAbs, despite high assay variability (Figure 5C). Exposure to low concentrations of 4.1 nM of both 2A10 and 3SP2 mAb reduced the hepatocyte infection by ≥50%. No difference in the potency of 2A10 and 3SP2 to inhibit hepatocyte infection was observed.

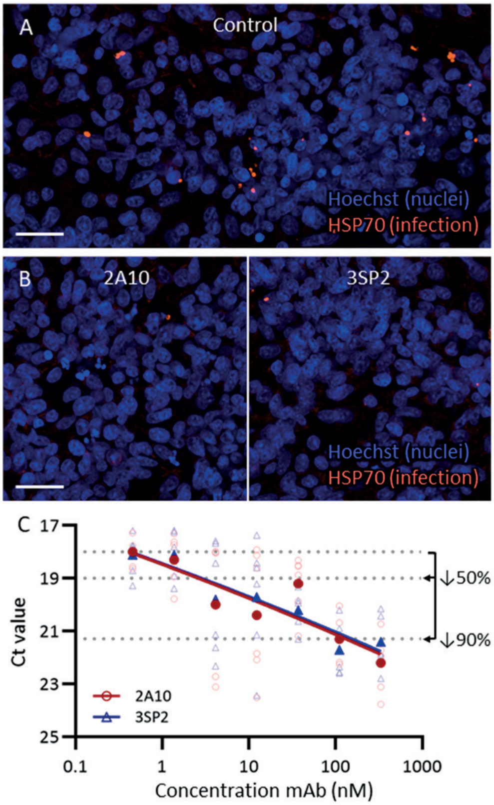

Figure 5 Effect of anti-CSP mAb on HC-04.J7 infection rate.
A) Immunofluorescent staining of schizonts in HC-04.J7 cells by anti-Hsp70 staining (orange) and counterstaining with Hoechst (blue). Scale bar: 30 µm. B) Images of the liver stage development assay representative for exposure to 333 nM 2A10 and 3SP2. Fluorescent anti-Hsp70 staining (orange) and counterstaining with Hoechst (blue). Scale bar: 30 µm. C) The Ct (cycle threshold) value of 6 wells (open symbols) and the median (closed symbols) obtained by RT-PCR plotted against the concentration of mAb. The Ct values that represent a decrease of 50% and 90% in liver stage development are annotated.

DISCUSSION

We were able to establish a quantitative motility assay that enables assessment of anti-CSP mAbs inhibitory capacity against *Plasmodium falciparum (Pf)* SPZ. Interestingly, anti-CSP mAb concentrations far above the saturating binding concentration (as determined by ELISA) were needed to inhibit SPZ motility *in vitro* and these values increased even further in human skin explants. In addition, we found that motility inhibition differs between anti-CSP mAbs and that subsets of SPZ can be refractory to the effect of mAbs. These findings underline that a comprehensive assessment of anti-CSP mAb functionality, including SPZ motility inhibition, is needed to characterize their parasite-inhibitory efficacy and predict potency.

Real-time tracking of SPZ combined with the SPZ motility analysis tool SMOOT enabled us to estimate a half-maximal motility inhibitory concentration (IC_{50M}) for both mAbs, providing a quantitative measure of mAb functionality. So far, *Pf* SPZ motility *in vitro* in the presence of a mixture of antibodies has only been assessed *post hoc* by staining and subsequent counting of the trails produced by gliding SPZ, a qualitative rather than quantitative analysis subject to considerable assay variability[17, 24]. SMOOT was able to pick up subtle differences in SPZ motility, ultimately deepening our understanding of anti-CSP mAb functionality. We found a remarkable discrepancy between the IC_{50M} and the binding saturation concentration measured by ELISA, which may be caused by shedding of mAbs by viable SPZ during shedding and replenishing CSP[28]. Exposure to anti-CSP mAbs has previously been suggested to enhance the secretion of CSP[13, 29, 30]. This could mean that the functionality of anti-CSP mAbs does not merely rely on their binding affinity and avidity, but also on their impact on the CSP shedding rate. This may explain why a direct correlation between the binding capacity of anti-CSP mAbs and their inhibitory activity in *in vitro* and *in vivo* models is lacking[31].

In this study, we are the first to assess anti-CSP mAb functionality in human skin. SPZ exhibit more directional movement in their natural skin environment compared to the mere circular movement on a 2D surface. Although mAbs reduced the velocity of SPZ migrating through skin, they did not block SPZ motility to the same extent as observed *in vitro*. This is in line with the reduced motility reported in studies investigating SPZ in the skin of passively immunized mice[13, 14, 16, 32]. It remains to be determined why SPZ are relatively refractory to the effects of anti-CSP mAbs in skin. Potentially, redundancy in binding sites for CSP or the molecular mechanisms regulating SPZ motility in their natural environment may be part of the explanation.

Hitherto, functional assays to investigate the effect of anti-CSP mAbs on SPZ have mainly focused on the liver stage of the infection by measuring the inhibition of hepatocyte traversal/invasion or liver stage development (ILSDA)[33-37]. Nevertheless, mice studies have suggested that immobilizing SPZ after intradermal inoculation would likely limit their chances to reach and infect the liver[38]. In our study, both the results from the motility analysis and the ILSDA showed a dose dependent inhibitory effect of anti-CSP mAbs on SPZ, however only the former revealed differences between anti-CSP mAbs. This incoherence may have arisen from different mechanisms involved in motility and hepatocyte invasion, which were unequally susceptible to anti-CSP mAb inhibition. The differences may also have been masked in the ILSDA due to the high assay variability[33, 36, 39]). Either way, these findings underline that a motility-based functional assay provides valuable complementary information about the parasite-inhibitory potency of anti-CSP mAbs.

The anti-CSP mAbs 2A10 and 3SP2 differed in how they interfered with motility *in vitro*, whereby 2A10 reduced attachment to the surface, while 3SP2 increased attachment. Remarkably, only 3SP2 was able to block motility completely. Other studies have also suggested that the direct effect of anti-CSP mAbs on SPZ is mediated by different mechanisms of action, dependent on their binding capacity[31], the recognized epitope(s) [13, 19, 40, 41] and the possibility to crosslink CSP or otherwise affect CSP conformation[30, 42, 43]. Assessing which epitope(s) are recognized by 2A10 and 3SP2 and how they affect CSP confirmation would help to further elucidate the mechanistic basis for the observed differences. Especially the finding that 2A10, despite its higher binding capacity, could not block SPZ movement may have consequences for the potency of mAbs targeting a similar CSP epitope.

Despite the technical challenges involved, extending assessment of anti-CSP mAbs potency by measuring their motility inhibitory capacity can help to select the most promising candidates for passive immunization against malaria[3, 44]. Passive transfer of mAbs is a strategy which bypasses obstacles encountered during active immunization strategies, such as immunoregulatory effects of previous malaria exposure and the influence of age on immune responses[5]. To extend the short-term protection (up to 6 months) possibly induced by passive immunization, mAbs could potentially be delivered via a viral vector; an approach that has shown potential for protecting against malaria and other infectious diseases in preclinical models[45, 46]. In addition, selection of high potential mAbs for epitope characterization can provide a means to support the rational design of subunit vaccines[6]. For example, an epitope within the junctional region of CSP was recently identified as a target of mAbs with protective efficacy and may become part of the sequence of next-generation CSP-based subunit vaccines[47]. Future research would be needed to develop a prediction model that includes the results, weighted based on their discriminative power, of different assays to score and rank anti-CSP mAbs potency which may aid more accurate identification of potential candidates for downstream (pre)clinical testing.

Taken together, our motility-based assay SMOOT can support comprehensive functionality assessment of anti-CSP mAbs which have recently become available and will continue to appear[18, 19, 31, 39, 44]. Thus deepening our understanding of anti-CSP mAb functionality and aiding the selection of lead candidates for passive immunization strategies against malaria.

Acknowledgments: We would like to thank dr. Koen Dechering from TropIQ Health Sciences for providing a transgenic fluorescent *Plasmodium falciparum* strain.

REFERENCES

1. WHO, World malaria report 2021. 2021.
2. Cohen, S., S. Carrington, and I.A. Mcgregor, Gamma-Globulin and Acquired Immunity to Human Malaria. Nature, 1961. 192(480): p. 733-&.
3. Gaudinski, M.R., et al., A Monoclonal Antibody for Malaria Prevention. New England Journal of Medicine, 2021. 385(9): p. 803-814.
4. van de Boor, S.C.e.a., Safety, tolerability and Plasmodium falciparum transmission-reducing activity of monoclonal antibody TB31F: an open-label, first-in-human, trial in healthy malaria-naïve adults. Lancet Infectious Diseases, 2022.
5. Cockburn, I.A. and R.A. Seder, Malaria prevention: from immunological concepts to effective vaccines and protective antibodies. Nature Immunology, 2018. 19(11): p. 1199-1211.
6. Chatterjee, D. and I.A. Cockburn, The challenges of a circumsporozoite protein-based malaria vaccine. Expert Review of Vaccines, 2021. 20(2): p. 113-125.
7. Amino, R., et al., Quantitative imaging of Plasmodium transmission from mosquito to mammal. Nature medicine, 2006. 12(2): p. 220-224.
8. Yamauchi, L.M., et al., Plasmodium sporozoites trickle out of the injection site (vol 9, pg 1215, 2007). Cellular Microbiology, 2007. 9(8): p. 2093-2093.
9. de Korne, C., et al., Clustering and erratic movement patterns of syringe-injected versus mosquito-inoculated malaria sporozoites underlie decreased infectivity. Msphere, 2021. 6(2): p. e00218-21.
10. Medica, D.L. and P. Sinnis, Quantitative dynamics of Plasmodium yoelii sporozoite transmission by infected anopheline mosquitoes. Infection and Immunity, 2005. 73(7): p. 4363-4369.
11. Coppi, A., et al., The malaria circumsporozoite protein has two functional domains, each with distinct roles as sporozoites journey from mosquito to mammalian host. Journal of Experimental Medicine, 2011. 208(2): p. 341-356.
12. Mishra, S., R.S. Nussenzweig, and V. Nussenzweig, Antibodies to Plasmodium circumsporozoite protein (CSP) inhibit sporozoite’s cell traversal activity. Journal of Immunological Methods, 2012. 377(1-2): p. 47-52.
13. Aliprandini, E., et al., Cytotoxic anti-circumsporozoite antibodies target malaria sporozoites in the host skin. Nat Microbiol, 2018. 3(11): p. 1224-1233.
14. Flores-Garcia, Y., et al., Antibody-Mediated Protection against Plasmodium Sporozoites Begins at the Dermal Inoculation Site. Mbio, 2018. 9(6).
15. Hopp, C.S., et al., Comparative intravital imaging of human and rodent malaria sporozoites reveals the skin is not a species-specific barrier. Embo Molecular Medicine, 2021. 13(4).
16. Vanderberg, J.P. and U. Frevert, Intravital microscopy demonstrating antibody-mediated immobilisation of Plasmodium berghei sporozoites injected into skin by mosquitoes. Int J Parasitol, 2004. 34(9): p. 991-6.
17. Behet, M.C., et al., Sporozoite immunization of human volunteers under chemoprophylaxis induces functional antibodies against pre-erythrocytic stages of Plasmodium falciparum. Malaria Journal, 2014. 13.
18. Livingstone, M.C., et al., In vitro and in vivo inhibition of malaria parasite infection by monoclonal antibodies against Plasmodium falciparum circumsporozoite protein (CSP). Scientific Reports, 2021. 11(1).
19. Scally, S.W., et al., Rare PfCSP C-terminal antibodies induced by live sporozoite vaccination are ineffective against malaria infection. Journal of Experimental Medicine, 2018. 215(1): p. 63-75.
20. de Korne, C.M., et al., Regulation of Plasmodium sporozoite motility by formulation components. Malar J, 2019. 18(1): p. 155.
21. Winkel, B.M.F., et al., Quantification of wild-type and radiation attenuated Plasmodium falciparum sporozoite motility in human skin. Scientific Reports, 2019. 9.
22. Zhang, M., et al., Monoclonal Antibodies against Plasmodium falciparum Circumsporozoite Protein. Antibodies, 2017. 6(3).
23. Verhave, J.P., et al., The Biotin-Streptavidin System in a 2-Site Elisa for the Detection of Plasmodial Sporozoite Antigen in Mosquitos. Parasite Immunology, 1988. 10(1): p. 17-31.
24. Miyazaki, Y., et al., Generation of a Genetically Modified Chimeric Plasmodium falciparum Parasite Expressing Plasmodium vivax Circumsporozoite Protein for Malaria Vaccine Development.

Frontiers in Cellular and Infection Microbiology, 2020. 10.
25. Mogollon, C.M., et al., Rapid Generation of Marker-Free P. falciparum Fluorescent Reporter Lines Using Modified CRISPR/Cas9 Constructs and Selection Protocol. Plos One, 2016. 11(12).
26. Ponnudurai, T., et al., Infectivity of Cultured Plasmodium-Falciparum Gametocytes to Mosquitos. Parasitology, 1989. 98: p. 165-173.
27. R Core Development Team, R: A language and environment for statistical computing. 2020, R Foundation for Statistical Computing: Vienna, Austria.
28. Stewart, M.J. and J.P. Vanderberg, Malaria Sporozoites Release Circumsporozoite Protein from Their Apical End and Translocate It Along Their Surface. Journal of Protozoology, 1991. 38(4): p. 411-421.
29. McCoy, M.E., et al., Mechanisms of protective immune responses induced by the Plasmodium falciparum circumsporozoite protein-based, self-assembling protein nanoparticle vaccine (vol 12, 136, 2013). Malaria Journal, 2013. 12.
30. Potocnjak, P., et al., Mono-Valent Fragments (Fab) of Monoclonal-Antibodies to a Sporozoite Surface-Antigen (Pb44) Protect Mice against Malarial Infection. Journal of Experimental Medicine, 1980. 151(6): p. 1504-1513.
31. Murugan, R., et al., Evolution of protective human antibodies against Plasmodium falciparum circumsporozoite protein repeat motifs. Nature Medicine, 2020. 26(7): p. 1135-+.
32. Hopp, C.S., et al., Plasmodium falciparum-specific IgM B cells dominate in children, expand with malaria, and produce functional IgM. Journal of Experimental Medicine, 2021. 218(4).
33. House, B.L., et al., Functional immunoassays using an in-vitro malaria liver-stage infection model: where do we go from here? Trends in Parasitology, 2009. 25(11): p. 525-533.
34. Rodriguez-Galan, A., et al., An in vitro assay to measure antibody-mediated inhibition of P. berghei sporozoite invasion against P. falciparum antigens. Scientific Reports, 2017. 7.
35. Sinnis, P., et al., Quantification of sporozoite invasion, migration, and development by microscopy and flow cytometry, in Malaria. 2012, Springer. p. 385-400.
36. Tweedell, R.E., et al., The Selection of a Hepatocyte Cell Line Susceptible to Plasmodium falciparum Sporozoite Invasion That Is Associated With Expression of Glypican-3. Frontiers in Microbiology, 2019. 10.
37. Zou, X.Y., et al., Towards an optimized inhibition of liver stage development assay (ILSDA) for Plasmodium falciparum. Malaria Journal, 2013. 12.
38. Sack, B.K., et al., Model for In Vivo Assessment of Humoral Protection against Malaria Sporozoite Challenge by Passive Transfer of Monoclonal Antibodies and Immune Serum. Infection and Immunity, 2014. 82(2): p. 808-817.
39. Tan, J., et al., A public antibody lineage that potently inhibits malaria infection through dual binding to the circumsporozoite protein. Nature Medicine, 2018. 24(4): p. 401-+.
40. Flores-Garcia, Y., et al., The P. falciparum CSP repeat region contains three distinct epitopes required for protection by antibodies in vivo. Plos Pathogens, 2021. 17(11).
41. Thai, E., et al., A high-affinity antibody against the CSP N-terminal domain lacks Plasmodium falciparum inhibitory activity. Journal of Experimental Medicine, 2020. 217(11).
42. Kucharska, I., et al., Structural ordering of the Plasmodium berghei circumsporozoite protein repeats by inhibitory antibody 3D11. Elife, 2020. 9.
43. Oyen, D., et al., Structural basis for antibody recognition of the NANP repeats in Plasmodium falciparum circumsporozoite protein (vol 114, pg E10438, 2017). Proceedings of the National Academy of Sciences of the United States of America, 2018. 115(25): p. E5838-E5839.
44. Kisalu, N.K., et al., A human monoclonal antibody prevents malaria infection by targeting a new site of vulnerability on the parasite. Nature Medicine, 2018. 24(4): p. 408-+.
45. Deal, C., et al., Vectored antibody gene delivery protects against Plasmodium falciparum sporozoite challenge in mice. Proceedings of the National Academy of Sciences of the United States of America, 2014. 111(34): p. 12528-12532.
46. Zhan, W., et al., Vectored Immunotherapeutics for Infectious Diseases: Can rAAVs Be The Game Changers for Fighting Transmissible Pathogens? Frontiers in Immunology, 2021. 12.
47. Wang, L.T., et al., A Potent Anti-Malarial Human Monoclonal Antibody Targets Circumsporozoite Protein Minor Repeats and Neutralizes Sporozoites in the Liver. Immunity, 2020. 53(4): p. 733-+.

5

A hybrid tracer approach reveals the in vivo dissemination kinetics of syringe-injected malaria sporozoites

Clarize M. de Korne, Mick M. Welling, Danny M. van Willigen, Fabian W. Hensbergen, Severine C. Chevalley-Maurel, Jeroen C. Sijtsma, Roos van Schuijlenburg, Els Baalbergen, Blandine M.D. Franke-Fayard, Meta Roestenberg, Fijs W.B. van Leeuwen

Unpublished

ABSTRACT

Malaria sporozoites (SPZ) present the first stage of a malaria infection. Following release during a mosquito bite, SPZ actively migrate from the skin to the liver to initiate the next stage of their life cycle. Currently, one of the leading vaccine candidates to prevent malaria are live-attenuated SPZ administered intravenously by syringe (PfSPZ Vaccine, Sanaria). Preclinical and clinical data indicate that the way of administration is essential to determine the overall potency of SPZ-based vaccine candidates. While it is known that accumulation of SPZ in the liver is key, little is known about the dissemination kinetics of these SPZ vaccines following injection and the role of SPZ motility in this process. To obtain such insights, SPZ need to be labeled to allow for whole-body tracking. Based on our previous experience with SPZ tracking in skin using a fluorescent tracer, we have now developed a radiolabeled analogue (^{99m}Tc-Cy5-AmineC4.MAS$_3$-Methyl) that was used to quantify SPZ dissemination in a murine model. The fluorescent signature of the tracer was used to confirm the labeling of the SPZ by microscopy and flow cytometry. We found that 2 hr post injection live SPZ mainly distributed towards the liver. This contrasted the biodistribution of non-viable and thus non-motile SPZ, which showed a lower liver-to-lungs distribution as compared to their live counterparts. These findings suggest that SPZ viability is critical for them to pass the lungs and migrate to the liver. Further research is needed to improve the specificity of the labeling and thereby reduce the background signal found in this study. Nevertheless, in this proof-of-concept study the first hybrid tracer-based labeling approach for SPZ has been developed and tested, enabling investigation of the spatial and temporal dynamics of (vaccine) SPZ throughout their host.

INTRODUCTION

The initial progress made in malaria control during the first two decades of the 21st century has come to a halt, and as a result malaria cases are resurging and malaria remains responsible for over 500.000 deaths every year[1]. A pressing need remains for novel control tools such as malaria vaccines. During the initial stage of a malaria infection, the mosquito-inoculated parasites called sporozoites (SPZ) are still low in number (1-500 per mosquito bite) and vulnerable to immune attack[2-5]. As a consequence, vaccine researchers have turned to exploiting the use of whole SPZ or SPZ proteins as vaccines. Live-attenuated whole SPZ vaccines have shown potential in providing 50-100% protection to adults in clinical trials and thus are currently leading vaccine candidates in the prevention of malaria[6-8].

Remarkably, the potency of vaccine SPZ is determined by the way they are administered, raising the hypothesis that SPZ biodistribution is of importance in the protection induced by SPZ. Dose-escalation studies showed that intradermal administration protected at best 2/16 (13%) volunteers against a controlled human malaria infection while intravenous administration induced protection in 12/15 (80%) volunteers at high doses[9, 10].

Despite the fact that the location of SPZ and their interactions with immune cells at these different locations seem to be critical for the vaccine-induced protective immune response[11], only a little is known about the migration patterns of live, attenuated vaccine SPZ. After intradermal mosquito-inoculation in rodents, SPZ aim to enter the circulatory system to get transported to the liver where they invade hepatocytes and multiply[12]. Initial studies into the migration patterns of mosquito-inoculated SPZ revealed that the majority of SPZ remain for at least several hours in the skin and some are trapped in lymphatic vessels[13, 14]. However, studies into the distribution of vaccine SPZ administered by injection have not been performed. A better understanding of the distribution of SPZ throughout the host following injection would help to understand where immune interactions can take place and thus aid the development of an efficacious malaria vaccine.

Investigations into the biodistribution of SPZ is hampered by the lack of a method that enables whole-body, longitudinal tracking of SPZ. SPZ migration has been extensively studied in murine and human skin using fluorescence-based tracking. This method is sensitive enough to track single SPZ under the condition of a micrometer-scale field of view[13, 15-17], but this sensitivity is lost when zooming out to whole-body scale due to the limited penetration depth of fluorescence signal in tissue. Longitudinal tracking of malaria parasites has so far only been done using the parasite's blood stages in mice. To make this possible, bioluminescence imaging is used, which will detect parasites provided that their numbers are high enough to reach the detection threshold[18, 19]. However, this method is not sensitive enough to track the low numbers of parasites during the SPZ stage.

Although not applied in the field of parasitology yet, tracking of low numbers of cells, e.g. T cells and stem cells, migrating throughout the body is achieved in other research fields using the sensitivity, quantifiability and tissue penetration capacity of radioactivity[20-22]. For example, a clinical standard for detecting inflammatory lesions makes use of radiolabeled white blood cells[23]. Recently, we have developed a fluorescent cyanine dye-based tracer suitable to label SPZ by targeting their mitochondrion and subsequently track them in skin[24].

In this study, we report a preliminary assessment of SPZ dissemination following intravenous injection using the mitochondrial tracer ^{99m}Tc-Cy5-Methyl-AmineC4.MAS$_3$ (^{99m}Cy5-MAS$_3$). We performed biodistribution studies of radiolabeled viable and non-viable SPZ using a murine model. Hereby we exploit both the fluorescent and radioactive signature of the tracer. As far as we are aware, this is the first study that provides a proof of concept for the radiolabeling of SPZ that enables whole-body *in vivo* tracking. We were able to gain insights in the role of SPZ viability in their dissemination throughout the host, especially regarding lung passage.

METHODS

Tracer synthesis

Cy5-AmineC4.MAS$_3$-Methyl was synthesized and characterized as described in the Supplementary Information. In brief, the chelate mercaptoacetyltriserine (MAS$_3$) was coupled to Cy5-Methyl-AmineC4 by forming an amide bond, yielding the tracer Cy5- AmineC4.MAS$_3$-Methyl (from now abbreviated as Cy5-MAS$_3$). The crude compound was purified using preparative-scale prep-HPLC (high-performance liquid chromatography) and the product structure was confirmed by NMR (nuclear magnetic resonance) spectroscopy. Subsequently, the (photo)physical properties of the tracer were assessed; the molar extinction coefficient (ε) and quantum yield (ΦF) were assessed to calculate the brightness (ε*ΦF) and the lipophilicity (log P) and serum binding were determined as previously described[25].

Radiolabeling of Cy5-MAS$_3$

Radiolabeling of Cy5-MAS$_3$ with technetium-99m was performed according to a previously described protocol with some minor amendments[26]. To Cy5-MAS$_3$, 80 or 250 MBq technetium-99m (80 Mbq for biodistribution of free tracer, 250 Mbq for radiolabeling of SPZ) freshly eluted from a generator (~1 GBq/ml; Ultra-Technekow™, Mallinckrodt Medical B.V.) was added to a mixture containing 0.5 nmol of the tracer (992 µM stock in H_2O) and the following buffer solutions: 10.5 µl of phosphate buffer (0.5 M, pH 8), 15.6 µl of phosphate buffer (0.25 M, pH 8), 12.5 µl disodium tartrate dihydrate (50 mg/mL in phosphate buffer (0.5 M, pH 8)) and 3.1 µl of Tin(II) chloride dihydrate (4 mg/ml in L-ascorbic acid solution (3 mg/ml in 0.1 M HCl)) (Sigma-Aldrich). The Tin(II) chloride dihydrate solution was freshly prepared and N_2 degassed for 20 minutes, all other buffers were prepared and stored at 4°C for maximally 1 month. After heating to 100°C for 20 minutes, the reaction mixture was cooled down to room temperature and diluted with 10 ml Milli-Q water. This solution was passed through a Sep-Pak C-18 cartridge (Waters) pre-rinsed with EtOH, followed by another 10 ml of Milli-Q water. After that, the labeled tracer was drop-wise eluted from the cartridge with EtOH into the reaction tube followed by vigorous vortexing. The volume of this eluate was reduced to 10 µl by evaporation of ethanol. The radiochemical purity of the final product ^{99m}Tc-Cy5-MAS_3 was analyzed by radio-thin layer chromatography (radio-TLC; Supelco) using acetonitrile as mobile phase.

Rodent experiments

All animal experiments were granted a license by the Competent Authority after advice by the Animal Experiments Committee Leiden (AVD1160020173304). All experiments were performed in accordance with the Experiments on Animals Act (Wod, 2014), the applicable legislation in the Netherlands, and in accordance with the European guidelines (EU directive no. 2010/63/EU) regarding the protection of animals used for scientific purposes. All experiments were performed in a licensed establishment for the use of experimental animals (LUMC). For this study we used female Swiss OF1 mice (6-7 weeks old; Charles River) that were housed in individually ventilated cages furnished with autoclaved aspen woodchip, fun tunnel, wood chew block and nestlets at 21 ± 2°C under a 12:12 hr light-dark cycle at a relative humidity of 55 ± 10%.

Plasmodium sporozoite production

Naive mice were infected with the rodent malaria species *Plasmodium berghei* as described previously[27]. The transgenic line 1868cl1 expressing mCherry and luciferase under the constitutive HSP70 and eef1a promotors respectively (*Pb*ANKA-$\text{mCherry}_{\text{hsp70}}$+$\text{Luc}_{\text{eef1}\alpha}$; line RMgm-1320, www.pberghei.eu) was used. The infected mice were anesthetized and *Anopheles stephensi* female mosquitoes were infected by feeding on the gametocytemic mice. The mosquitoes were kept at a temperature of 21 °C and 80% humidity until dissection. SPZ were obtained by manual dissection of the salivary glands of the infected mosquitoes 20-24 days post infection. The salivary glands were collected and homogenized to release SPZ in Roswell Park Memorial Institute medium (RPMI; Thermo Fisher Scientific) enriched with 10% fetal bovine serum (FBS; Life Technologies Inc.). The free SPZ were counted in a Bürker counting chamber using phase-contrast microscopy and thereafter, within 1 hr, the labeling of the SPZ was initiated. To obtain salivary gland material (SGM), the salivary glands of uninfected mosquitoes were collected and homogenized in RPMI + 10%FBS.

Labeling of sporozoites

To label isolated SPZ with Cy5-MAS_3 or ^{99m}Tc-Cy5-MAS_3, 0.5 nmol tracer in 10 µl EtOH was added to $1.0*10^6$ SPZ in 990 µl RPMI + 10% FBS. The mixture was gently stirred at room temperature for 30 minutes. The SPZ were then purified by 3 consecutive wash steps; 5 minutes centrifugation at 7,200 x g, followed by decanting and adding 1.5 ml RPMI + 10% FBS. Critical in this process was to reduce the amount of unbound tracer by >99.99% while preserving SPZ viability. After the labeling, the SPZ were recounted. To obtain non-viable labeled SPZ, the viable radiolabeled SPZ were fixed for 20 minutes with 4% paraformaldehyde (Thermo Fisher Scientific). This was done in between the first and the second wash step. The viability of the live/non-viable SPZ was validated by measuring the bioluminescent signal by a GloMax plate reader (Promega) after adding cell culture lysis reagent and luciferase assay reagent (Promega) following the manufacturer's instruction.

Sporozoite labeling stability and dissociation

To study the labeling stability, SPZ labeled with Cy5-MAS_3 were pipetted on the coverslip of a confocal dish without any precoating (ø14mm; MatTek Corporation), covered and microscopically analyzed. Images of the SPZ were taken using an Andor Dragonfly 500 spinning disk confocal on a Leica DMi8 microscope (Oxford Instruments) combined with the Andor imaging software Fusion (Oxford Instruments). The mCherry expressed by SPZ was excited with the 561 nm laser and the Cy5-MAS_3 tracer was excited with the 637 nm laser. The fluorescent intensity of SPZ labeled with Cy5-MAS_3 was also evaluated using a flow cytometer (BD LSR Fortessa 4L; BD Bioscience and Cytek Aurora; Cytek Biosciences). The data was analyzed using the FlowJo software (FlowJo LLC). SPZ were selected by gating on mCherry-positive events, and per SPZ, the mean fluorescent intensity of the Cy5-MAS_3 labeling was quantified. To determine the dissociation of the ^{99m}Tc-Cy5-MAS_3 from SPZ over time, at various intervals up to 24 hr after labeling, SPZ labeled with ^{99m}Tc-Cy5-MAS_3 were filtered (Millex-HV syringe filter unit, 0.2 µm; Millipore), the radioactivity in the filtrate was measured with a gamma counter (Wizard2 2470 automatic gamma scintillation counter; PerkinElmer) and the percentage decrease of SPZ-bound tracer was calculated by comparing the amount of radioactivity in the filtrate with the amount of radioactivity in a non-filtered sample. As a control, SGM was labeled and the stability of the labeling was determined according to the same protocol.

Sporozoite motility assessment

The motility of the SPZ labeled with Cy5-MAS_3 was assessed *in vitro* as described previously[28] and was compared to the motility of non-labeled SPZ. The SPZ were pipetted on the coverslip of a confocal dish and covered. Movies of their circular movement pattern were recorded on a Leica TCS (true confocal scanning) SP5 microscope (Leica Microsystems, Wetzlar) combined with Leica imaging software (Leica Microsystems, Wetzlar). The mCherry expressed by SPZ was excited with the 561 nm laser and the emission signal was collected between 600-650 nm. The movies were recorded with a frame rate of 35 frames per minute, 200 frames per movie. Maximum projections of the recorded microscopy movies were generated using Fiji software[29]. The movies were further processed using SMOOT$_{in\ vitro}$, an in-house developed graphical user interface (GUI), written in the MATLAB programming environment (The MathWorks Inc.)[28]. The movement pattern of the SPZ was classified as floating, stationary or circling and the velocity of the circling SPZ was determined. In total, the motility of 379 SPZ was analyzed, distributed over the labeled (n=178) and control (n=201) condition.

Infectivity labeled sporozoites

The infectivity of the SPZ labeled with Cy5-MAS$_3$ was assessed *in vitro* and *in vivo* and compared to the infectivity of non-labeled SPZ. For *in vitro* assessment, Huh-7 cells (immortal human hepatoma cell line) were seeded into a 24-well plate at $5*10^4$ cells/well and kept overnight in RPMI + 10% FBS at 37°C in a humidified atmosphere with 5% CO_2. SPZ were added to the hepatocytes in a 1:1 ratio. Live imaging of liver-stage parasite development (presence of liver schizonts) was performed 44 hr after the addition of the SPZ using a conventional fluorescent microscope (Leica AF6000LX, Oxford Instruments). The nuclei of the cells were stained using Hoechst 33342 (1:200; 1 mg/ml; Sigma-Aldrich). The mCherry expressed by the schizonts was excited with the 561 nm laser and Hoechst was excited with the 405 nm UV laser. After imaging, the medium was removed and the cells were incubated for 5 minutes with cell culture lysis reagent. Subsequently, luciferase assay reagent was added to the lysed cells and the bioluminescence signal was measured by a GloMax plate reader.

To assess the infectivity of the labeled SPZ *in vivo*, $5*10^4$ SPZ in 200 µl medium were injected intravenously into the tail vein of mice (n=6 for labeled SPZ, n=6 for non-labeled SPZ) using an insulin syringe (Micro-Fine+, 0.5 ml, 0.30 x 8.0 mm, 30G; Becton Dickinson). The parasite liver load was visualized and quantified by measuring the luciferase activity in the liver at 44 hr after the challenge with SPZ using the IVIS Lumina II (Perkin Elmer Life Sciences). Animals were kept anesthetized during the measurements using the isoflurane-anesthesia system (XGI-8, Caliper Life Sciences). IVIS measurements (exposure time: 60 seconds, binning factor: 8, aperture: f/1) were performed 8 minutes after subcutaneously injection of D-luciferin in the neck (100 mg/kg in PBS; Caliper Life Sciences). The liver load was quantified by measuring the total flux (p/s) of an ROI covering the liver (same ROI for all mice). Image analysis was performed using the Living Image® 4.4 software (Perkin Elmer Life Sciences). Infected mice were monitored for blood-stage infections by Giemsa-stained blood smear at day 5 to 14 post infection. The prepatent period (measured in days after SPZ injection) was defined as the first day at which blood-stage infection with a parasitemia of >0.5% was observed.

Biodistribution of ^{99m}Tc-Cy5-MAS$_3$

The biodistribution of the free tracer ^{99m}Tc-Cy5-MAS$_3$ was determined 2 hr after intravenous (IV) administration. For IV injection, 200 µl medium containing 0.5 nmol of ^{99m}Tc-Cy5-MAS$_3$ (45±8 MBq) was injected into the tail vein of the mice (n=6) using an insulin syringe. Animals were kept anesthetized during the injections using the isoflurane-anesthesia system. The total injected dose was determined by counting full and empty syringes in a gamma counter (2470 automatic gamma counter, Perkin–Elmer) or by counting the whole mouse in the gamma counter directly post injection. To obtain a total body SPECT scan at 2 hr post injection, the mice were placed onto a dedicated positioning bed of a three-headed U-SPECT-2 (MILabs) under continuous isoflurane anesthesia and radioactivity counts from total body scans were acquired for 18 min on the 140-keV photopeak with a 20% symmetrical window. The projections were reconstructed as described before[30]. Reconstructed images were generated using MATLAB software (The MathWorks Inc.). After imaging, blood was collected by heart puncture and the mice were euthanized by cervical dislocation. The organs of the mice were harvested and weighed. To determine the biodistribution of the tracer, the organs were scanned for fluorescence by IVIS and counted for radioactivity in a gamma counter (Wizard2 2470 automatic gamma scintillation counter, Perkin Elmer). After excision of the tissues, the total amount of remaining radioactivity in the animal carcass was counted. Radioactive counts in tissues were expressed as the percentage of the total injected dose of radioactivity (%ID, corrected for radioisotope decay) or %ID per gram of tissue (%ID/g).

Biodistribution of sporozoites

The biodistribution of SPZ labeled with ^{99m}Tc-Cy5-MAS$_3$ was determined 2 hr post injection under 2 different conditions: 1) 200 µl medium containing $0.5*10^6$ live SPZ was IV injected into the tail vein of the mice using an insulin syringe (n=6), 2) 200 µl medium containing $0.5*10^6$ non-viable SPZ was IV injected into the tail vein of the mice using an insulin syringe (n=6). As a control, 200 µl medium containing the estimated amount of radiolabeled SGM present in a sample containing $0.5*10^6$ SPZ was IV injected into the tail vein of the mice using an insulin syringe (n=9). Animals were kept anesthetized during the injections using the isoflurane-anesthesia system. The total injected dose was determined by counting full and empty syringes in a gamma counter. At 2 hr post injection, blood was collected by heart puncture and the mice were euthanized by cervical dislocation. The organs of the mice were harvested, weighed and counted in a gamma counter (Wizard2 2470 automatic gamma scintillation counter, Perkin Elmer). After excision of the tissues, the remaining radioactivity in the animal carcass was determined. Radioactive counts in tissues were expressed as the percentage of the total injected dose of radioactivity (%ID, corrected for decay) or %ID per gram of tissue (%ID/g). An overview of the biodistribution results of the different conditions which includes the %ID and %ID/g determined for 16 different tissues has been attached as Sup. Figure S1. Based on the %ID per organ, the ratio of radioactivity retrieved from the liver to the clearance organs (intestines + gall bladder) and the ratio of radioactivity retrieved from the lungs to the clearance organs were calculated (liver:clearance ratio, lungs:clearance ratio).

Statistics

The average and variability of the data were summarized using the mean and standard deviation (SD) for parametric data or the median and interquartile range (IQR) for nonparametric data. For the comparison of groups, the difference between means or medians was assessed using respectively the independent sample T-test and the Mann-Whitney U test. For the comparison of a group with a set value, the one-sample T-test was used. P-values < 0.05 were considered significant. All statistical tests were performed by SPSS Statistics (IBM Nederland BV).

RESULTS

Sporozoite radiotracer development

A radiotracer suitable to label SPZ was developed by coupling the previous synthesized fluorescent tracer Cy5-Methyl-Methyl[24] to a MAS_3 chelate followed by ^{99m}Tc radiolabeling, yielding the hybrid tracer ^{99m}Tc-Cy5-MAS_3 (Figure 1A). The brightness of the tracer, its most valuable photophysical trait, was $3.45 \cdot 10^3\ M^{-1} \cdot cm^{-1}$ (the product of its quantum yield $\phi_{F,\ PBS} = 13\%$ and molar extinction coefficient $\varepsilon_{PBS} = 2.65 \cdot 10^4\ M^{-1} \cdot cm^{-1}$). *In vitro* confocal microscopy of SPZ labeled with Cy5-MAS_3 revealed a similar staining pattern as previously reported for Cy5-Methyl-Methyl[24]; a single fluorescent spot adjacent to the nucleus where the single parasite mitochondrion is located (Figure 1B). Cy5-MAS_3 uptake by SPZ was also quantified by flow cytometry which showed a 8.9-fold increase in mean fluorescence intensity of Cy5-MAS_3 labeled SPZ compared to non-labeled controls (Figure 1C). Microscopic and flow cytometric analyses showed that the tracer accumulated in SPZ and in the residual salivary gland material (SGM) resulting from the isolation of SPZ (Figure 1B, Sup. Figure S2).

Tracer dissociation over time

The radiolabeling of SPZ with ^{99m}Tc-Cy5-MAS_3 yielded an average of 1.4 MBq bound activity per $1*10^6$ SPZ. Directly after washing, the supernatant contained <2% of background signal originating from non-bound tracer. After 2 hr, 10 ± 2% of the bound tracer was released from the SPZ (and the SGM present) versus 24 ± 4% in case of the SGM control (Figure 2). This indicated that the tracer was mainly released from SGM and that the SPZ were stably labeled, which was confirmed by flow cytometry (Sup. Figure S2).

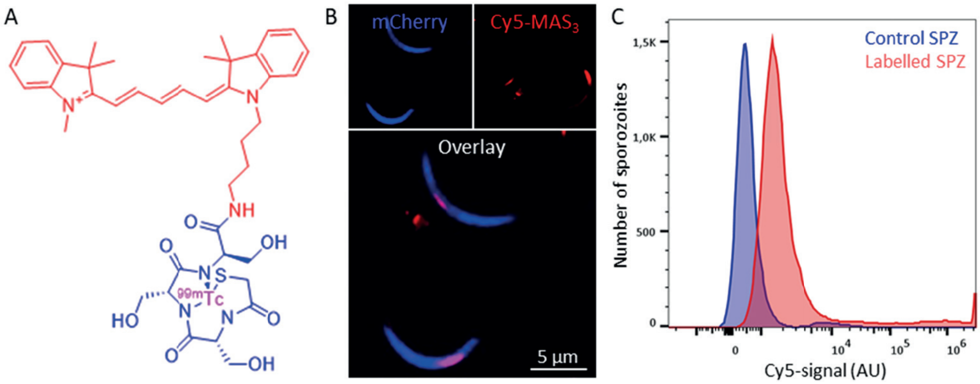

Figure 1 Molecular structure and sporozoite labeling. A) The chemical structure of the hybrid tracer ^{99m}Tc-Cy5-Methyl-AmineC4.MAS$_3$ which contains a Cy5 dye (depicted in red) and a MAS$_3$ chelate (depicted in blue) containing ^{99m}Tc (depicted in pink). B) Microscopic analysis of SPZ expressing mCherry (top left, depicted in blue) labeled with the Cy5-MAS$_3$ tracer (top right, depicted in red), the bottom panel shows the overlay. C) Representative graph of the flow cytometric analysis of the SPZ labeling. Blue lines represent background signal in non-labeled control SPZ, red lines show Cy5 signal in the SPZ labeled with the Cy5-MAS$_3$ tracer.

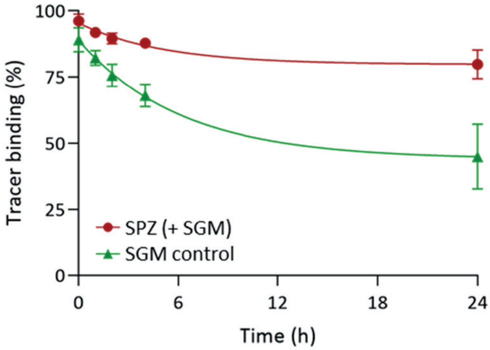

Figure 2 Tracer dissociation. Over time bound tracer was released. The dissociation dynamics are estimated by non-linear fitting using the one phase exponential decay equation and plotted for SPZ (with SGM present) and the SGM control.

Motility and infectivity of labeled sporozoites

The motility of the Cy5-MAS$_3$ labeled SPZ was compared to the motility of non-labeled SPZ using SMOOT$_{in\ vitro}$[28], which is to our knowledge the most sensitive motility analysis tool to detect differences in viability. A representative example of SPZ tracks is shown in Figure 3A. 58% of both labeled and non-labeled SPZ were moving during recording, a third was floating (labeled: 35%, non-labeled: 34%) and a small part was stationary (labeled: 7%, non-labeled: 8%) (p=0.89; Chi-square test) (Figure 3B). The circular movements of both groups had a similar mean velocity (labeled: 2.1 ± 0.8 µm/s, non-labeled: 2.2 ± 0.6 µm/s;

p=0.292, independent sample T test) (Figure 3C). Besides SPZ motility, also their infectivity was assessed both *in vitro* (infection of hepatocytes) and *in vivo* (infection of mice) (Figure 3D-F). 44 hr post infection with labeled SPZ, fully mature liver stages were detected in *in vitro* hepatocytes (Figure 3D) and the livers of mice (Figure 3E). The infectivity of labeled SPZ *in vitro* in hepatocytes was not statistically significantly different, although this assay is known to display high variability (76 ± 44%, 7 independent experiments; p=0.198, one sample T-test). Also *in vivo* there was little difference between infectivity of labeled vs unlabeled SPZ (86 ± 3%, 2 independent experiments; p=0.098, one sample T-test) (Figure 3F). The prepatency of the mice infected with the labeled SPZ was comparable to that of mice infected with non-labeled SPZ, both at 5-6 days after infection. Overall, we concluded that Cy5-MAS_3 labeled SPZ were equally capable of migrating, infecting hepatocytes and propagating to blood stage parasites.

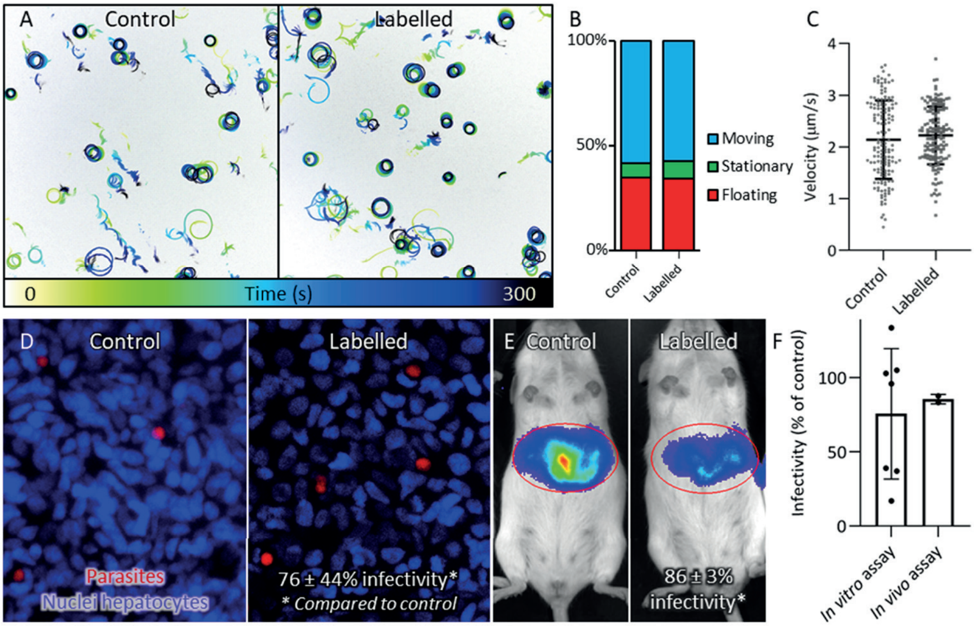

Figure 3 Sporozoite motility and infectivity. A) Overview of the tracks of non-labeled control SPZ and SPZ labeled with Cy5-MAS_3. The tracks are color-coded for time. B) The movement pattern distribution of control and labeled SPZ, classified as floating, stationary or moving. C) The mean velocity of the moving control and labeled SPZ. D) The infectivity of control and labeled SPZ is shown as the *in vitro* infection of hepatocytes (parasites are depicted in red, nuclei of hepatocytes in blue). E) The infectivity of control and labeled SPZ is shown as the parasite liver load in mice after 44 hr (bioluminescence signal – median total flux). F) The infectivity of the labeled SPZ is calculated and plotted as a percentage of the infectivity of the control SPZ (middle; the dots represent individual experiments and the error bars represent the SD).

Biodistribution of free tracer and SGM

To be able to investigate the biodistribution results of the labeled SPZ, we first assessed the biodistribution of the free tracer and labeled SGM (Figure 4). Both SPECT imaging and radioactivity biodistribution revealed that, 2 hr after intravenous injection, the free tracer ^{99m}Tc-Cy5-MAS$_3$ mainly accumulated in the gall bladder and the intestines and to a lesser extent in the liver (Figure 4AB). This clearly pointed towards a biliary clearance pathway and subsequent intestinal uptake. Using SGM (particles of varying size around an average of ~2 µm (Sup. Figure S5)), radioactivity was mainly retrieved from the clearance organs (intestines and gall bladder), similar to the free tracer distribution (Figure 4). These results corroborated with prior findings that the tracer rapidly dissociated from SGM (Figure 2). In addition to that, uptake was detected in the liver and the lungs. The signal obtained from the lungs seemed specific for SGM, since the lungs were not a site of accumulation for the free tracer. The signal obtained from the liver may, in part, be attributed to SGM and in part due to free tracer which has been released. This assumption was supported by the notion that the ratio of the clearance organs (intestines + gall bladder) to the liver was larger for SGM (0.41) as compared to the free tracer (0.23). Indicating that roughly half of the signal in the liver came from the labeled SGM (Figure 4B).

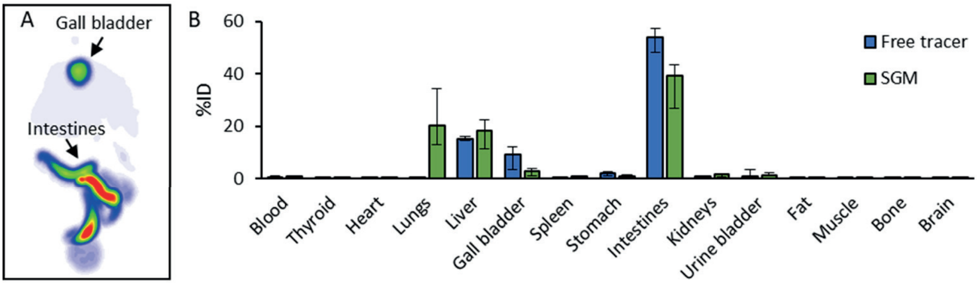

Figure 4 Biodistribution of free tracer and SGM. A) At 2 hr after injection of ^{99m}Tc-Cy5-MAS$_3$, a total body SPECT scan was obtained. B) The biodistribution of the tracer (depicted in light blue) and the biodistribution of SGM labeled with ^{99m}Tc-Cy5-MAS$_3$ (depicted in dark blue) measured 2 hr after injection, plotted as the median percentage of injected dose (%ID) per organ including error bars representing the inter quartile range.

Biodistribution of sporozoites

Radiolabeled SPZ were injected intravenously into the mouse tail vein as depicted in Figure 5A. The biodistribution results (%ID) revealed that 2 hr after intravenous injection, accumulation occurred in the lungs, liver and intestines + gall bladder (Figure 5B). Since SPZ cannot migrate to the bile, this signal and that in the intestines reflected the presence of free tracer (which was cleared via the bile and intestines), which was confirmed by qRT-PCR analysis (Sup. Figure S3). Based on these findings, we calculated the lungs:clearance ratio and the liver:clearance ratio and compared these to the ratio's obtained for the biodistribution of SGM. The lungs:clearance ratio was comparable, though slightly increased, compared to SGM (lungs:clearance ratio live SPZ: 0.52, SGM: 0.46). However, the liver:clearance ratio of live SPZ was higher compared to the ratio of SGM (liver:clearance ratio live SPZ: 0.62, SGM: 0.41). Indicating that while some SPZ had ended up in the lungs, most had reached the liver, which was confirmed by visualization of liver parasites by microscopy (Sup. Figure S4).

Effect of viability on the biodistribution of sporozoites

To assess the role of SPZ viability in their biodistribution, we compared the biodistribution results of non-viable SPZ to the biodistribution of live SPZ. Two hours after the injection of non-viable radiolabeled SPZ relatively larger amounts of radioactivity were retrieved from the lungs, which was offset by a reciprocal decrease in signal retrieved from the liver (increase in lungs:clearance ratio: +0.21, decrease in liver:clearance ratio: -0.26) (Figure 5C). As such the lack of viability induced a significant shift in radioactivity accumulation from liver to lungs (p=0.025; Mann-Whitney U test). This indicated that live SPZ were better able to pass the lungs and reach the liver than non-viable SPZ.

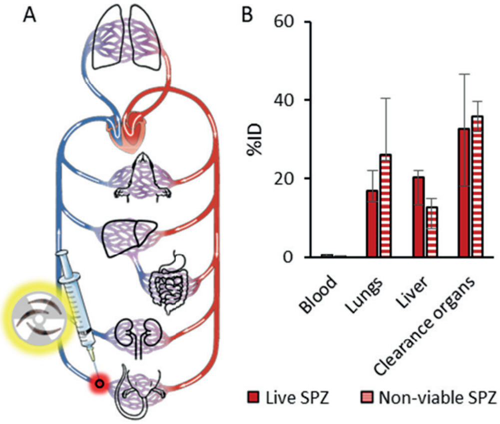

C

	Lungs:Clearance	Liver:Clearance
Free tracer	0.00	0.23
SGM	0.46	0.41
Live SPZ	0.52	0.62
Non-viable SPZ	0.73	0.36

Figure 5 Biodistribution of intravenously injected live and non-viable sporozoites. A) The intravenous injection route of labeled SPZ is annotated in a schematic overview of the circulatory system. B) The biodistribution results of live (plain red) and non-viable SPZ (striped red) measured 2 hr after injection, plotted as the median percentage of injected dose (%ID) per organ including error bars representing the inter quartile range. Clearance organs: intestines + gall bladder. C) The ratio of signal from the lungs versus the clearance organs (lungs:clearance) and from the liver versus the clearance organs (liver:clearance) was calculated.

DISCUSSION

Using ^{99m}Tc-Cy5-MAS$_3$, we labeled SPZ and assessed their motility *in vitro* and their dissemination *in vivo*. The fluorescent signature of the tracer was used to confirm the labeling of SPZ by microscopy and flow cytometry. The radioactive signature enabled the quantitative assessment of the distribution of SPZ in a murine model. This study revealed that following intravenous injection, live SPZ mainly migrate towards the liver, whereas non-viable SPZ partly relocate to the lungs. These results indicate that SPZ viability plays a role in overcoming the physical barrier of lung microvasculature.

The design of the hybrid tracer was based on the previous developed fluorescent tracer Cy5-methyl-methyl, now extended with a chelate for technetium[24]. So far, besides Cy5-methyl-methyl only CFSE (covalently couples to intracellular free amines) has been used to fluorescently label live SPZ for tracking and no radioactive tracers suitable to label SPZ have been reported[31]. The use of a hybrid tracer proved to be valuable in providing both the envisaged radiolabeling of SPZ needed for whole-body tracking and the microscopic and flow cytometric validation of the labeling. ^{99m}Tc-Cy5-MAS$_3$ was 1) able to accumulate intracellularly and had a low efflux rate, 2) nontoxic for SPZ and 3) detectable over a longer period of time. First, the tracer accumulated inside the SPZ resulting in a concentration of radioactivity which was high enough for a biodistribution study in a murine model and which was stable for at least the 2 hr measured in this study. This sensitivity needed to quantify the biodistribution of SPZ in mice has not been achieved by other techniques applied so far, such as bioluminescence-based imaging or PCR[32]. Moreover, the fitness assays did not reveal significant toxic effects of the labeling with ^{99m}Tc-Cy5-MAS$_3$ to SPZ at the dose used; although the infectivity may have been somewhat decreased (albeit non-significantly) based on infection assays *in vitro* and *in vivo*. Lastly, ^{99m}Technetium, the most commonly utilized radionuclide due to favorable properties such as a 6-hour half-life[33], enabled SPZ tracking 2 hr post injection and might support longitudinal tracking up to 24 hr in future studies if the initial tracer uptake is sufficiently high.

The lack of specificity of ^{99m}Tc-Cy5-MAS$_3$ for SPZ was a disadvantage, because the SPZ sample which was labeled *ex vivo* was contaminated with SGM. This resulted *in vivo* in the presence of labeled SGM and free tracer released from SGM which complicated the interpretation of the absolute SPZ biodistribution data. These findings are in line with the fact that tracer release from dead cells is commonly noted as a pitfall of *ex vivo* labeling methods[22]. Nevertheless, the fast hepatic clearance of free tracer facilitated the separation of signal from free tracer (in the gall bladder and intestine) and SPZ, which could be used for a reliable assessment of the relative SPZ biodistribution. The use of purified SPZ could in the future solve the problem of SGM contamination[34].

The biodistribution results of SGM revealed a preference of SGM to relocate to the lungs and liver. The varying SGM particle size (around an average of ~2 µm) may explain the distribution of these particles over the lungs and the liver, smaller particles tend to be cleared via the liver, while bigger particles end up in the lungs[35-37]. Interestingly, the biodistribution of the SPZ was impacted by their viability with a lower liver-to-lungs distribution for non-viable SPZ. Based on the size of SPZ (crescent-shaped, length: 8-14 µm), it is not that surprising that part of them get physically trapped in lung capillaries (typical diameter mouse capillaries: ~4 µm[38]). These results suggest that SPZ viability, and probably their motility, plays a key role in passing the lungs to reach hepatocytes to complete their life cycle[39]. Using confocal microscopy, we observed motile SPZ in rodent lung tissue; future studies should investigate how this motility facilitates lung passage.

We are the first to demonstrate the presence and passage of SPZ through the lungs. Lung passage of malaria SPZ has not been previously investigated. However, particles of similar size, such as intravenously injected albumin-based microspheres (diameter: 18 µm) are used as a clinical tool to visualize lung perfusion because of their capacity to get trapped in the lungs. Also for monocytes and dendritic cells it has been shown that they first accumulate in the lungs before getting distributed to other organs[37, 40-42]. These studies support the notion that the microvasculature of the lungs can provide a physical barrier for particles, amongst which SPZ, to passage. Interestingly, SPZ-immune cell interactions in the lungs have not yet been considered in the field of malaria vaccine development.

Further SPZ biodistribution and immunological studies are needed to provide valuable insights into the spatial and temporal dynamics of the migration of vaccine SPZ which are attenuated (e.g. genetically attenuated, radiation attenuated) or administered via different routes (e.g. intravenous, intradermal, subcutaneous)[11] and the role of the lung-trapped SPZ in the induction of the overall immune response. This would help understand what would be the most optimal means of delivering these complex vaccines, critical viability thresholds and the sites where essential immune interactions take place.

In conclusion, development of a hybrid tracer enabled the first radioactivity-based assessment of the SPZ biodistribution in mice. Despite the need for further technical improvements, these first results provided new insights into SPZ dissemination *in vivo*. Moreover, the presented method allows monitoring of the spatial and temporal dynamics of SPZ migration throughout the host post injection, providing critical information for the improvement of whole SPZ vaccine potency.

Acknowledgments: We would like to thank ing. J. Ramesar and dr. C.J. Janse for support with the mosquito infection.

REFERENCES

1. World Health, O., World malaria report 2021. 2021, Geneva: World Health Organization.
2. de Korne, C., et al., Clustering and erratic movement patterns of syringe-injected versus mosquito-inoculated malaria sporozoites underlie decreased infectivity. Msphere, 2021. 6(2): p. e00218-21.
3. Frischknecht, F. and K. Matuschewski, Plasmodium sporozoite biology. Cold Spring Harbor Perspectives in Medicine, 2017. 7(5): p. a025478.
4. Medica, D.L. and P. Sinnis, Quantitative dynamics of Plasmodium yoelii sporozoite transmission by infected anopheline mosquitoes. Infection and immunity, 2005. 73(7): p. 4363-4369.
5. Sinnis, P. and A. Coppi, A long and winding road: the Plasmodium sporozoite's journey in the mammalian host. Parasitology international, 2007. 56(3): p. 171-178.
6. Richie, T.L., et al., Progress with Plasmodium falciparum sporozoite (PfSPZ)-based malaria vaccines. Vaccine, 2015. 33(52): p. 7452-61.
7. Roestenberg, M., et al., A double-blind, placebo-controlled phase 1/2a trial of the genetically attenuated malaria vaccine PfSPZ-GA1. Sci Transl Med, 2020. 12(544).
8. Sissoko, M.S., et al., Safety and efficacy of a three-dose regimen of Plasmodium falciparum sporozoite vaccine in adults during an intense malaria transmission season in Mali: a randomised, controlled phase 1 trial. The Lancet Infectious Diseases, 2022. 22(3): p. 377-389.
9. Epstein, J.E., et al., Live attenuated malaria vaccine designed to protect through hepatic CD8(+) T cell immunity. Science, 2011. 334(6055): p. 475-80.
10. Seder, R.A., et al., Protection against malaria by intravenous immunization with a nonreplicating sporozoite vaccine. Science, 2013. 341(6152): p. 1359-65.
11. Itsara, L.S., et al., The development of whole sporozoite vaccines for Plasmodium falciparum malaria. Frontiers in immunology, 2018. 9: p. 2748.
12. Phillips, M.A., et al., Malaria. Nature Reviews Disease Primers, 2017. 3(1): p. 17050.
13. Amino, R., et al., Quantitative imaging of Plasmodium transmission from mosquito to mammal. Nat Med, 2006. 12(2): p. 220-4.
14. Yamauchi, L.M., et al., Plasmodium sporozoites trickle out of the injection site. Cellular microbiology, 2007. 9(5): p. 1215-1222.
15. Hopp, C.S., et al., Longitudinal analysis of Plasmodium sporozoite motility in the dermis reveals component of blood vessel recognition. Elife, 2015. 4.
16. Vanderberg, J.P. and U. Frevert, Intravital microscopy demonstrating antibody-mediated immobilisation of Plasmodium berghei sporozoites injected into skin by mosquitoes. Int J Parasitol, 2004. 34(9): p. 991-6.
17. Winkel, B.M.F., et al., Quantification of wild-type and radiation attenuated Plasmodium falciparum sporozoite motility in human skin. Scientific Reports, 2019. 9.
18. Ploemen, I.H., et al., Plasmodium liver load following parenteral sporozoite administration in rodents. Vaccine, 2013. 31(34): p. 3410-3416.
19. Vaughan, A.M., et al., A Plasmodium parasite with complete late liver stage arrest protects against preerythrocytic and erythrocytic stage infection in mice. Infection and immunity, 2018. 86(5): p. e00088-18.
20. Perrin, J., et al., Cell tracking in cancer immunotherapy. Frontiers in Medicine, 2020. 7: p. 34.
21. Rodriguez-Porcel, M., et al., Cell tracking and the development of cell-based therapies: a view from the Cardiovascular Cell Therapy Research Network. JACC: Cardiovascular Imaging, 2012. 5(5): p. 559-565.
22. Kurebayashi, Y., P.L. Choyke, and N. Sato, Imaging of cell-based therapy using 89Zr-oxine ex vivo cell labeling for positron emission tomography. Nanotheranostics, 2021. 5(1): p. 27.
23. Roca, M., et al., Guidelines for the labelling of leucocytes with 111In-oxine. European journal of nuclear medicine and molecular imaging, 2010. 37(4): p. 835-841.
24. Winkel, B.M.F., et al., A tracer-based method enables tracking of Plasmodium falciparum malaria parasites during human skin infection Theranostics, 2019. 9(10): p. 2768-2778.
25. Hensbergen, A.W., et al., Evaluation of asymmetric orthogonal cyanine fluorophores. Dyes and Pigments, 2020. 183: p. 108712.
26. Robu, S., et al., Preclinical evaluation and first patient application of 99mTc-PSMA-I&S for SPECT imaging and radioguided surgery in prostate cancer. Journal of Nuclear Medicine, 2017. 58(2): p.

235-242.
27. Haeberlein, S., et al., Protective immunity differs between routes of administration of attenuated malaria parasites independent of parasite liver load. Sci Rep, 2017. 7(1): p. 10372.
28. de Korne, C.M., et al., Regulation of Plasmodium sporozoite motility by formulation components. Malaria Journal, 2019. 18.
29. Schindelin, J., et al., Fiji: an open-source platform for biological-image analysis. Nature Methods, 2012. 9(7): p. 676-682.
30. Welling, M., et al., Interventional nuclear medicine:"click" chemistry as an in vivo targeting strategy for imaging microspheres and bacteria. Biomaterials Science, 2021. 9(5): p. 1683-1690.
31. Zhou, C., et al., Laser mimicking mosquito bites for skin delivery of malaria sporozoite vaccines. Journal of Controlled Release, 2015. 204: p. 30-37.
32. Ploemen, I.H.J., et al., Visualisation and Quantitative Analysis of the Rodent Malaria Liver Stage by Real Time Imaging. Plos One, 2009. 4(11).
33. Moreira, M.L., et al., In vivo tracking of cell therapies for cardiac diseases with nuclear medicine. Stem cells international, 2016. 2016.
34. Hoffman, S.L. and T.C. Luke, Apparatuses and methods for the production of haematophagous organisms and parasites suitable for vaccine production. 2014, Google Patents.
35. He, Q., et al., In vivo biodistribution and urinary excretion of mesoporous silica nanoparticles: effects of particle size and PEGylation. small, 2011. 7(2): p. 271-280.
36. Ogawara, K.-i., et al., Hepatic uptake of polystyrene microspheres in rats: effect of particle size on intrahepatic distribution. Journal of Controlled Release, 1999. 59(1): p. 15-22.
37. Stephens, R.W., et al., 99mTc-radiolabeled composites enabling in vivo imaging of arterial dispersal and retention of microspheres in the vascular network of rabbit lungs, liver, and liver tumors. International Journal of Nanomedicine, 2019. 14: p. 889.
38. Müller, B., et al. High-resolution tomographic imaging of microvessels. in Developments in X-ray Tomography VI. 2008. SPIE.
39. Ejigiri, I. and P. Sinnis, Plasmodium sporozoite–host interactions from the dermis to the hepatocyte. Current opinion in microbiology, 2009. 12(4): p. 401-407.
40. Ritchie, D., et al., In vivo tracking of macrophage activated killer cells to sites of metastatic ovarian carcinoma. Cancer Immunology, Immunotherapy, 2007. 56(2): p. 155-163.
41. Spa, S.J., et al., A supramolecular approach for liver radioembolization. Theranostics, 2018. 8(9): p. 2377.
42. Van Hemert, F.J., et al., Labeling of autologous monocytes with 99mTc–HMPAO at very high specific radioactivity. Nuclear medicine and biology, 2007. 34(8): p. 933-938.

SUPPLEMENTARY INFORMATION

1. Tracer synthesis
2. Overview biodistribution results (Sup. Figure S1)
3. Labeling of and tracer release from salivary gland material (Sup. Figure S2)
4. Validation of SPZ presence in organs by PCR (Sup. Figure S3)
5. Validation of SPZ presence in organs by confocal microscopy (Sup. Figure S4)
6. Estimation of SGM particle size (Sup. Figure S5)

1. Tracer synthesis

General

All chemicals and solvents were obtained from commercial sources and used without further purification. Dimethylformamide (DMF), dichloromethane (DCM) and dimethylsulfoxide (DMSO) were dried with 4 Å molecular sieves, unless stated otherwise. Column chromatography was performed with 40–63 µm silica from Screening Devices. Dry column vacuum chromatography (DCVC) was performed as published by Pedersen *et al*. [1] with 15–40 µm silica and Hyflo Supercell Celite from Fisher Scientific. High-performance liquid chromatography (HPLC) was performed with a Waters HPLC system using either a 1525EF or 2545 pump and a 2489 UV/VIS detector. For preparative HPLC either a Dr. Maisch GmbH Reprosil-Pur 120 C18-AQ 10 µm (250 × 20 mm) column or a XBridge Prep C8 10 µm OBD 250 × 30 mm column was used with a gradient of 0.1% trifluoro acetic acid (TFA) in H_2O/acetonitrile (CH_3CN) 95:5 to 0.1% TFA in H_2O/CH_3CN 5:95 in 40 min (12 or 25 ml/min, respectively) was employed. For semi-preparative HPLC a Dr. Maisch GmbH Reprosil-Pur C18-AQ 10 µm (250 × 10 mm) column was used and a gradient of 0.1% TFA in H_2O/CH_3CN 95:5 to 0.1% TFA in H_2O/CH_3CN 5:95 in 40 min (5 ml/min) was employed. For analytical HPLC a Dr. Maisch GmbH Reprosil-Pur C18-AQ 5 µm (250 × 4.6 mm) column was used and a gradient of 0.1% TFA in H_2O/CH_3CN 95:5 to 0.1% TFA in H_2O/CH_3CN 5:95 in 40 min (1 ml/min) was employed. High-resolution mass spectrometry (HRMS) was performed on a Waters Acquity H-class UPLC using a Acquity UPLC BEH C18 1.7 µm (2.1 × 50 mm) column with a gradient of 0.1% FA in H_2O/CH_3CN 98:2 to 0.1% FA in H_2O/CH_3CN 60:40 in 1.8 min (0.6 ml/min) coupled to a high-resolution Waters XEVO G2S-XTOF Mass Spectrometer. Low-resolution mass spectrometry (LRMS) was performed using a Bruker Microflex matrix-assisted laser desorption ionization time-of-flight (MALDI-TOF) mass spectrometer. ^1H and ^{13}C NMR were performed on a Bruker Ascend 850 (850 MHz) equipped with a CryoProbe in deuterated solvents. Absorbance spectra were recorded using an Ultrospec 2100 pro from Amersham Biosciences. Fluorescence spectra were recorded using a PerkinElmer LS-55 fluorescence spectrometer.

Synthesis mercaptoacetyltriserine (mas$_3$)

D-Ser(tBu)-WANG (3.0 g, 720 µmol) was swollen in DCM (20 ml) and washed 4 times with

DCM (20 ml). mas$_3$ was synthesized using standard Fmoc-based SPPS procedures using two cycles of Fmoc-D-(Ser(tBu)-OH (4 eq), PyBOP (4 eq) and N-methylmorpholine (5 eq) at RT for 2 hr and one cycle of s-acetylthioacetic acid (4 eq), PyBOP (4 eq) and N-methylmorpholine (5 eq) at RT for 2 hr. The resin was cleaved by shaking with TFA/H_2O (95:5; 20 ml) for 90 minutes and precipitating in ice cold MTBE/Et_2O (300 ml). The precipitate was washed with ice cold MTBE/Et_2O twice before drying *in vacuo*. The crude compound was purified using prep-HPLC. Lyophilization then yielded the title compound as a white fluffy solid (145 mg, 51%). 1H NMR (850 MHz, D_2O) δ 4.52 (t, J = 5.1 Hz, 1H), 4.50 (t, J = 4.4 Hz, 1H), 4.47 (t, J = 5.4 Hz, 1H), 3.74 (dd, J = 5.2, 11.6 Hz, 1 H), 3.76 (dd, J = 4.3, 12.1 Hz, 1 H), 3.78 (dd, J = 6.6, 11.8 Hz, 1 H), 3.79 (dd, J = 6.0, 11.9 Hz, 1 H), 3.80 (dd, J = 5.8, 11.8 Hz, 1 H), (dd, J = 4.9, 11.8 Hz, 1 H), 3.72 (q, J = 15.6 Hz, 2H), 2.37 (s, 3H). ^{13}C NMR (214 MHz, D_2O) δ 200.72, 174.08, 172.77, 172.47, 172.32, 62.03, 62.00, 61.93, 61.85, 56.84, 56.38, 55.93, 33.72, 30.41. HRMS m/z calculated for $C_{13}H_{21}N_3O_9S$ 396.1077, measured 396.1092 (3.79 ppm).

Synthesis Cy5-AmineC4Phth-Methyl

Indole-AmineC4Phth (1479 mg, 3.35 mmol; [2]) and malonaldehyde dianilide HCl (954 mg, 3.69 mmol) were dissolved in Ac2O/AcOH (1:1; 40 ml) and stirred at 60 °C overnight. The mixture was subsequently heated to 120 °C for 60 min and then cooled down to RT. Precipitation in and washing with Et_2O yielded the crude hemicyanine which was dissolved in DMF/DCM (1:1, 40 mL) and added to swollen WANG resin (1065 mg, 1.78 mmol). After coupling for 60 minutes, the resin was washed with DMF/DCM mixtures. Indole-methyl (213 mg, 0.84 mmol; [3]) was dissolved in pyridine/Ac2O (3:1, 40 ml) and added to the resin. The mixture was shaken overnight at RT before collecting the filtrate. The obtained crude was purified by DCVC and prep-HPLC. Lyophilization yielded the title compound as a blue solid. ^{1}H NMR (850 MHz, DMSO) δ 8.30 (q, J = 14.0 Hz, 2H), 7.87 (dd, J = 5.4, 3.0 Hz, 2H), 7.82 (dd, J = 5.4, 3.0 Hz, 2H), 7.62 (d, J = 7.3 Hz, 1H), 7.60 (d, J = 7.2 Hz, 1H), 7.43 – 7.38 (m, 3H), 7.36 (td, J = 3.6, 0.4 Hz, 1H), 7.26 (ddd, J = 7.4, 5.9, 2.3 Hz, 1H), 7.21 (td, J = 7.3, 0.7 Hz, 1H), 6.52 (t, J = 12.3 Hz, 1H), 6.28 (t, J = 13.0 Hz, 2H), 4.11 (m, 2H), 3.62 (s, 5H), 1.71 (br. s, 4H), 1.68 (s, 6H), 1.66 (s, 6H). ^{13}C NMR (214 MHz, DMSO) δ 173.45, 172.37, 168.11, 158.11, 157.95, 154.18, 154.00, 142.79, 142.09, 141.10, 141.02, 134.47, 134.39, 131.57, 128.40, 125.33, 124.83, 124.56, 123.10, 123.03, 122.44, 122.36, 111.15, 111.03, 103.49, 102.99, 48.93, 48.81, 42.85, 39.88, 39.78, 37.04, 31.15, 27.19, 26.99, 25.13, 24.21. HRMS m/z calculated for $C_{38}H_{40}N_3O_2^+$ 570.3121, measured 570.3107 (2.45 ppm).

Synthesis Cy5-AmineC4-Methyl

Cy5-Methyl-AmineC4Phth (60 mg, 105 µmol) was dissolved in methylamine (33 wt% in EtOH, 25 ml) and stirred at RT. After 3 hours, the reaction was complete and volatiles were removed *in vacuo*. The crude product was purified by prep-HPLC. Lyophilization yielded the title compound as a blue solid (40.9 mg, 88%). ^{1}H NMR (850 MHz, MeOD) δ 8.27 (q, J = 13.6

Hz, 2H), 7.51 (d, J = 7.3 Hz, 1H), 7.49 (d, J = 7.0 Hz, 1H), 7.43 (td, J = 7.9, 1.1 Hz, 1H), 7.40 (td, J = 7.9, 1.1 Hz, 1H), 7.33 (d, J = 7.9 Hz, 1H), 7.30 (d, J=8.0 Hz, 1 H), 7.29 (td, J=7.4, 0.7 Hz, 1 H), 7.25 (td, J = 7.4, 0.5 Hz, 1H), 6.64 (t, J = 12.4 Hz, 1H), 6.30 (t, J = 12.5, 2H), 4.16 (t, J = 7.4 Hz, 2H), 3.65 (s, 3H), 2.99 (t, J = 7.6 Hz, 2H), 1.94 – 1.85 (m, 2H), 1.84 – 1.77 (m, 2H), 1.74 (s, 6H), 1.73 (s, 6H). ^{13}C NMR (214 MHz, MeOD) δ 176.01, 174.16, 174.13, 155.99, 155.93, 155.35, 155.30, 144.16, 143.57, 142.65, 142.50, 129.78, 129.75, 126.75, 126.71, 126.55, 126.06, 123.47, 123.32, 112.08, 111.74, 104.87, 103.91, 50.70, 50.67, 50.41, 44.14, 40.38, 31.61, 28.01, 27.70, 26.02, 25.53. HRMS m/z calculated for $C_{30}H_{48}N_3^+$ 440.3066, measured 440.3087 (4.77 ppm).

Synthesis Cy5-AmineC4.mas$_3$-Methyl

mas$_3$ (27 mg, 68 µmol), 1-[bis(dimethylamino)methylene]-1H-1,2,3-triazolo[4,5-b] pyridinium 3-oxide hexafluorophosphate (26 mg, 68 µmol) and N-methylmorpholine (34 mg, 340 µmol) were dissolved in DMSO (2 ml), and the solution immediately turned yellow. This solution was then added to Cy5-AmineC4-Methyl (30 mg, 68 µmol) and the reaction mixture was stirred at RT for 25 min. A mixture of H_2O/MeCN (85/15, 8 ml) with 0.1% TFA was added and the crude product was purified by prep-HPLC. Lyophilization yielded the product as a blue solid (30 mg, 54%). ^{1}H NMR (850 MHz, DMSO) δ 8.37 – 8.29 (m, 3H), 8.15 (dd, J = 13.0, 7.2 Hz, 1H), 7.90 (d, J = 7.9 Hz, 1H), 7.87 (d, J = 7.9 Hz, 1H), 7.62 (d, J = 7.4 Hz, 1H), 7.61 (d, J = 7.4 Hz, 1H), 7.43 – 7.36 (m, 4H), 7.25 (t, J = 7.6 Hz, 1H), 7.24 (t, J = 7.4 Hz, 1H), 6.56 (t, J = 12.0 Hz, 1H), 6.26 (d, J = 13.8 Hz, 1H), 5.19 (t, J = 4.9 Hz, 1H), 5.14 (t, J = 4.9 Hz, 1H), 4.88 (t, J = 4.7 Hz, 1H), 4.36 (dt, J = 7.6, 6.0 Hz, 1H), 4.30 (q, J = 6.36 Hz, 1H), 4.20 (dt, J = 8.0, 5.5 Hz, 1H), 4.07 (t, J = 7.1 Hz, 2H), 3.68 (s, 2H), 3.60 (br. s, 5H), 3.57 – 3.49 (m, 2H), 3.16 (sextet, J = 7.0 Hz, 1H), 3.08 (sextet, J = 6.4 Hz, 1H), 2.33 (d, J = 4.8 Hz, 3H), 1.73 – 1.62 (m, 14H), 1.53 (p, J = 6.5 Hz, 2H). ^{13}C NMR (214 MHz, DMSO) δ 194.57, 194.56, 173.25, 172.49, 172.47, 170.38, 170.20, 170.02, 169.99, 169.69, 169.67, 167.23, 167.20, 154.12, 154.04, 142.81, 142.01, 141.09, 141.05, 128.48, 128.39, 125.45, 124.75, 124.64, 122.44, 122.35, 111.15, 111.07, 103.35, 103.33, 103.11, 61.70, 61.46, 61.42, 61.36, 61.34, 55.76, 55.66, 55.54, 55.39, 55.33, 55.24, 48.87, 43.16, 39.98, 39.88, 39.78, 38.04, 37.99, 32.52, 32.50, 31.34, 31.08, 30.13, 27.21, 27.02, 26.25, 26.18, 24.14. HRMS m/z calculated for $C_{43}H_{57}N_6O_8S^+$ 817.3959, measured 817.3946 (1.59 ppm).

References

1. D.S. Pedersen *et al*. Synthesis 2001. DOI: 10.1055/s-2001-18722
2. A.W.H. Hensbergen *et al*. J. Nucl. Med. 2020. DOI: 10.2967/jnumed.119.233064
3. A. Bunschoten *et al*. Bioconjug. Chem. 2016 DOI: 10.1021/acs.bioconjchem.6b00093

2. Overview biodistribution results

In this study the biodistribution was determined of: 1) the free tracer ^{99m}Tc-Cy5 -AmineC4.

MAS$_3$-Methyl (abbreviated as ^{99m}Tc-Cy5-MAS$_3$), 2) SGM labeled with ^{99m}Tc-Cy5-MAS$_3$, 3) live SPZ labeled with ^{99m}Tc-Cy5-MAS$_3$ and 4) non-viable SPZ ^{99m}Tc-Cy5-MAS$_3$. An overview of the results is shown in Sup. Figure S1, which includes the %ID and %ID/g determined for 16 different tissues.

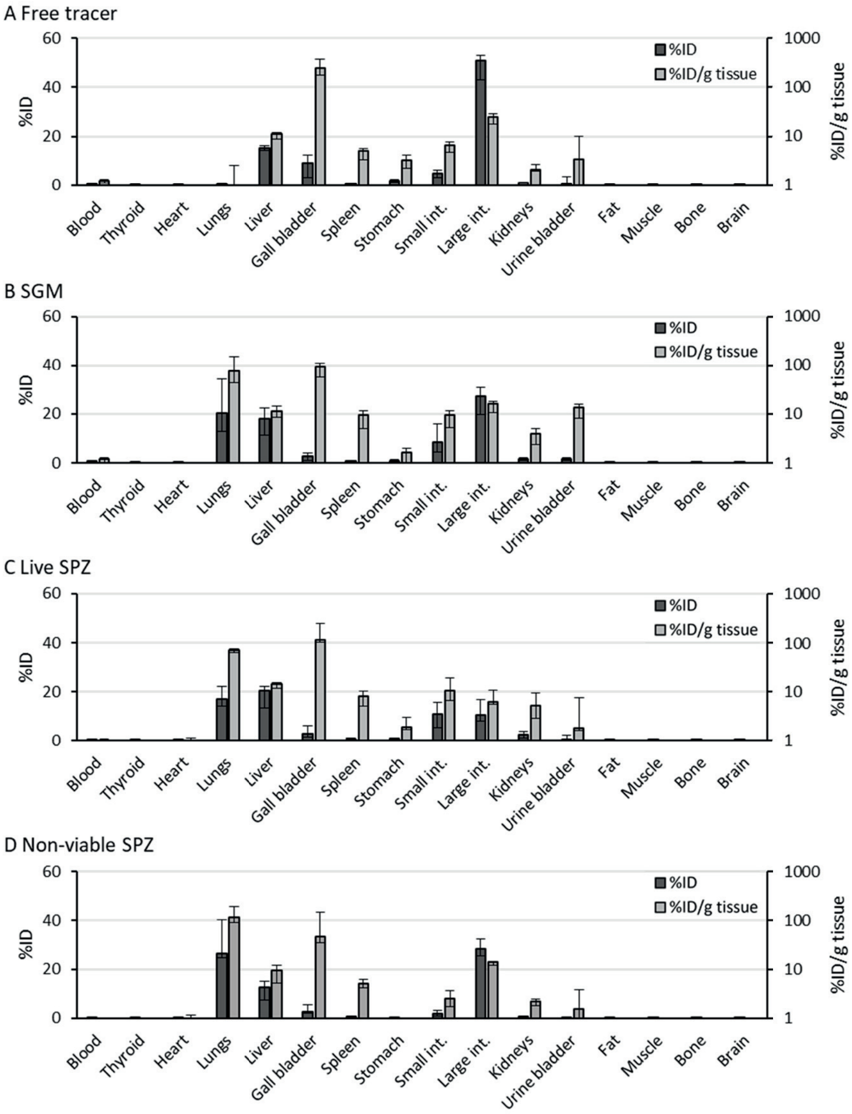

Sup. Figure S1 Biodistribution results. A-D) The biodistribution of the free tracer ^{99m}Tc-Cy5-MAS$_3$ (A), SGM labeled with ^{99m}Tc-Cy5-MAS$_3$ (B), live SPZ labeled with ^{99m}Tc-Cy5-MAS$_3$ (C) and non-viable SPZ labeled with ^{99m}Tc-Cy5-MAS$_3$ (D) measured 2 hr post injection, plotted as the median percentage of injected dose (%ID; depicted in dark grey) and the %ID per gram tissue (&ID/g tissue; depicted in light gray) per organ including error bars representing the inter quartile range.

3. Labeling of and tracer release from SGM

Flow cytometric analysis of the labeled SPZ sample revealed that besides the SPZ (42 ± 9 % of the detected particles) also the present SGM was labeled, on average the mean fluorescent intensity of the SGM was 1.9 fold higher compared to the SPZ (Sup. Figure S2). Over time, tracer was released from SGM which led to a 1.6 fold decrease in mean fluorescent intensity in 2 hr time (Sup. Figure S2).

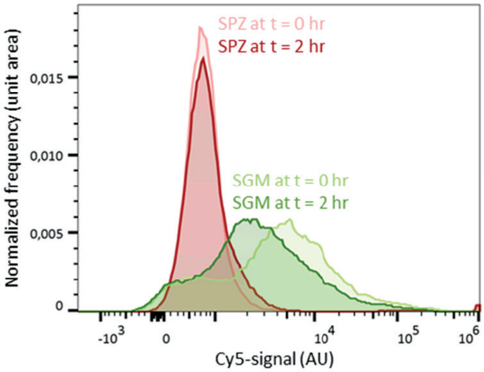

Sup. Figure S2 Labeling of sporozoites and SGM.
The Cy5-signal in labeled SPZ (depicted in red) and labeled SGM (depicted in green) was measured at t = 0 hr (depicted in light color) and at t = 2hr (depicted in dark color). The fold change in mean fluorescence intensity over time was 1.0 for SPZ and 1.6 for SGM.

4. Validation of SPZ presence in organs by PCR

To interpret the biodistribution results, more specifically to estimate the share of SPZ in the mixed distribution of SPZ, SGM and free tracer, the assumption was made that the radioactive signal found back in the tracer clearance organs (intestines + gall bladder) came from free tracer released from the SGM. This assumption was supported by qRT-PCR analysis of the different organs from mice used for the biodistribution study whereby no clearance organs positive for *Plasmodium* DNA were found, whereas occasional positive signals in liver and lungs were found (Sup. Figure S3).

Methods

Parasite burden in lungs, liver, skin and clearance organs (intestines and gall bladder) was measured by quantitative real-time reverse transcription-polymerase chain reactions (qRT-PCR). The DNA was extracted from the frozen tissues using the QIAamp DNA Micro Kit (Qiagen) following the manufacturer's instruction. Amplification reactions of each DNA sample were performed in PCR plates (hard-shell PCR plate, #HSP9645; Bio-Rad), in a volume of 25 µl containing 12.5 µl PCR buffer (HotstarTaq mastermix; Qiagen), 0.5 µl MgCl2 (25mM), Plasmodium-specific forward and reverse primer (12.5 pmol; Plas-7F 5'-GTTAAGGGAGTGAAGACGATCAGA-3' and Plas-171R 5'-AACCCAAAGACTTTGATTTCTCATAA-3'; Sigma-Aldrich), PhHV-specific forward and reverse primer (15 pmol; PhHV-267S 5'-GGGCGAATCACAGATTGAATC -3' and PhHV-337AS

5’-GCGGTTCCAAACGTACCAA -3’; Biolegio), Plasmodium-specific FAM10 labeled detection probe (2.5 pmol; PP FAM 5’-ACCGTCGTAATCTTAACC-3’; Biolegio), PhHV-specific Cy5 double-labeled detection probe (1.25 pmol; PhHV-305TQ Cy5 5’-TTTTTATGTGTCCGCCACCATCTGGATC-3’-BHQ2; Biolegio) and 5 µl of the DNA sample (20 ng/µl, dilution factor: 10x). Amplification consisted of 15 min at 95°C followed by 50 cycles of 15 s at 95°C, 30 s at 60°C, and 30 s at 72°C. Amplification, detection, and analysis were performed with the CFX96TM real-time PCR detection system (Bio-Rad).

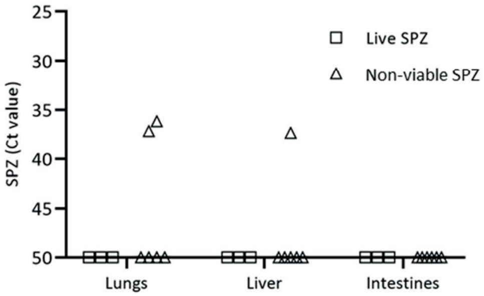

Sup. Figure S3 PCR on organs to assess the presence of sporozoites.
The Ct (cycle threshold) value obtained by qRT-PCR for the lungs, livers and intestines of the mice used for the biodistribution study was plotted. A Ct-value of 50 meant that no *Plasmodium* DNA was detected.

5. Validation of sporozoite presence in organs by confocal microscopy

To validate the presence of SPZ in the lungs and the liver, these organs were microscopically examined 2 hr after intravenous injection of SPZ labeled with Cy5-MAS$_3$. Following injection of live SPZ, a few SPZ were found back in the lungs and the majority was found back in the liver (Sup. Figure S4A). Following injection of non-viable SPZ, we could not find back SPZ in neither the lungs and the liver, which suggested that the fluorescent signal had disappeared probably due to disintegration of the SPZ. Video recording of live SPZ in lung tissue showed that the SPZ were able to move in this environment (Sup. Figure S4B).

Methods

To validate the SPZ presence in different organs by confocal microscopy, 1.0*10^6 live or non-viable SPZ labeled with Cy5-MAS$_3$ were intravenously injected into the tail vein of mice. At 2 hr post-injection the mice were euthanized, lungs and liver were sliced and mounted in a confocal dish. To assess SPZ motility in lung tissue, 1.0*10^6 live SPZ were injected via the heart into the lung circulation directly after euthanization and subsequently the lungs were sliced and mounted in a confocal dish. Images and movies (2 min) were recorded as a Z-stack covering a total depth of 30 µm. An Andor Dragonfly 500 spinning disk confocal on a Leica DMi8 microscope (Oxford Instruments) with a 40x objective (HCX PL APO 40x/1.30 OIL) was used. The mCherry expressed by the SPZ was excited with the 561 nm laser and the 637 nm laser was used to excite Cy5. Maximum projections of the Z-stacks were generated using Fiji software.

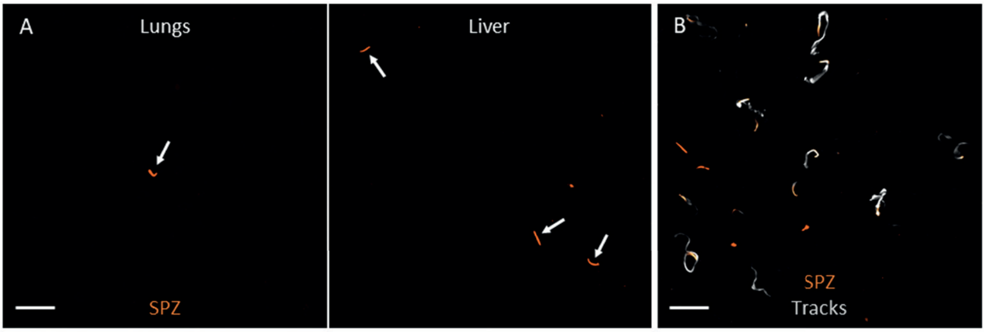

Sup. Figure S4 Sporozoite presence in lungs and liver. A) Confocal images of SPZ in lung tissue (left) and liver tissue (right) (depicted in orange and annotated with a white arrow). B) A maximum projection of a movie (2 min) of SPZ in lung tissue. The SPZ at t= 0 min are shown in orange and the tracks of the moving SPZ are shown in grey. Scale bar: 30 µm.

6. Estimation of SGM particle size

To estimate the size of the SGM particles, flow cytometric analysis was used whereby SGM was compared to 2, 3 and 10 µm beads based on FSC intensity which is proportional to particle size. The median FSC intensities of the beads were: $8.5*10^4$ (IQR: $7.5*10^4$-$9.7*10^4$) for the 2 µm beads, $7.3*10^5$ (IQR: $7.1*10^5$-$7.5*10^5$) for the 3 µm beads and $2.4*10^6$ (IQR: $2.4*10^6$-$2.4*10^6$) for the 10 µm beads (Fig. S5). The median FSC intensity of the SGM came closest to the 2 µm beads, however the IQR was much larger compared to the beads (median FSC intensity SGM: $1.2*10^5$ (IQR: $8.0*10^4$-$2.1*10^5$)) (Fig. S5). So, the SGM particle size varied substantially, but was on average ~2 µm.

Methods

To estimate the SGM particle size, the forward scatter (FSC) intensity of SGM was assessed using a flow cytometer (Cytek Aurora; Cytek Biosciences) and compared to the FSC intensity of 2 µm and 3 µm CS&T research beads (BD Biosciences) and 10 µm FITC labeled micro particles based on melamine resin (Merck). The data was analyzed using the FlowJo software (FlowJo LLC). SGM and the CS&T beads were selected by gating based on a forward versus sideward scatterplot and the 10 µm beads were selected by gating on FITC-positive events.

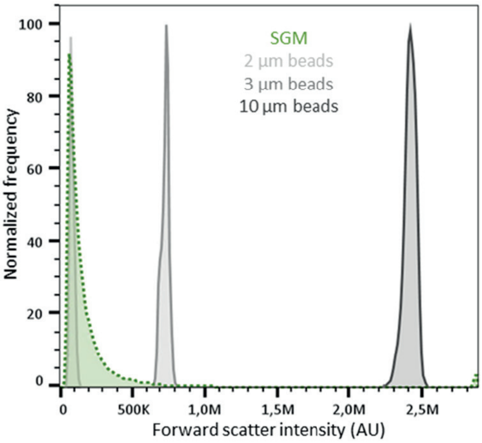

Sup. Figure S5 SGM particle size.
Flowcytometric analysis of the mean FSC intensity of SGM (depicted in green) which was compared to the mean FSC intensity of 2 µm, 3 µm and 10 µm beads (depicted in grey). The frequency of the events was normalized to the mode.

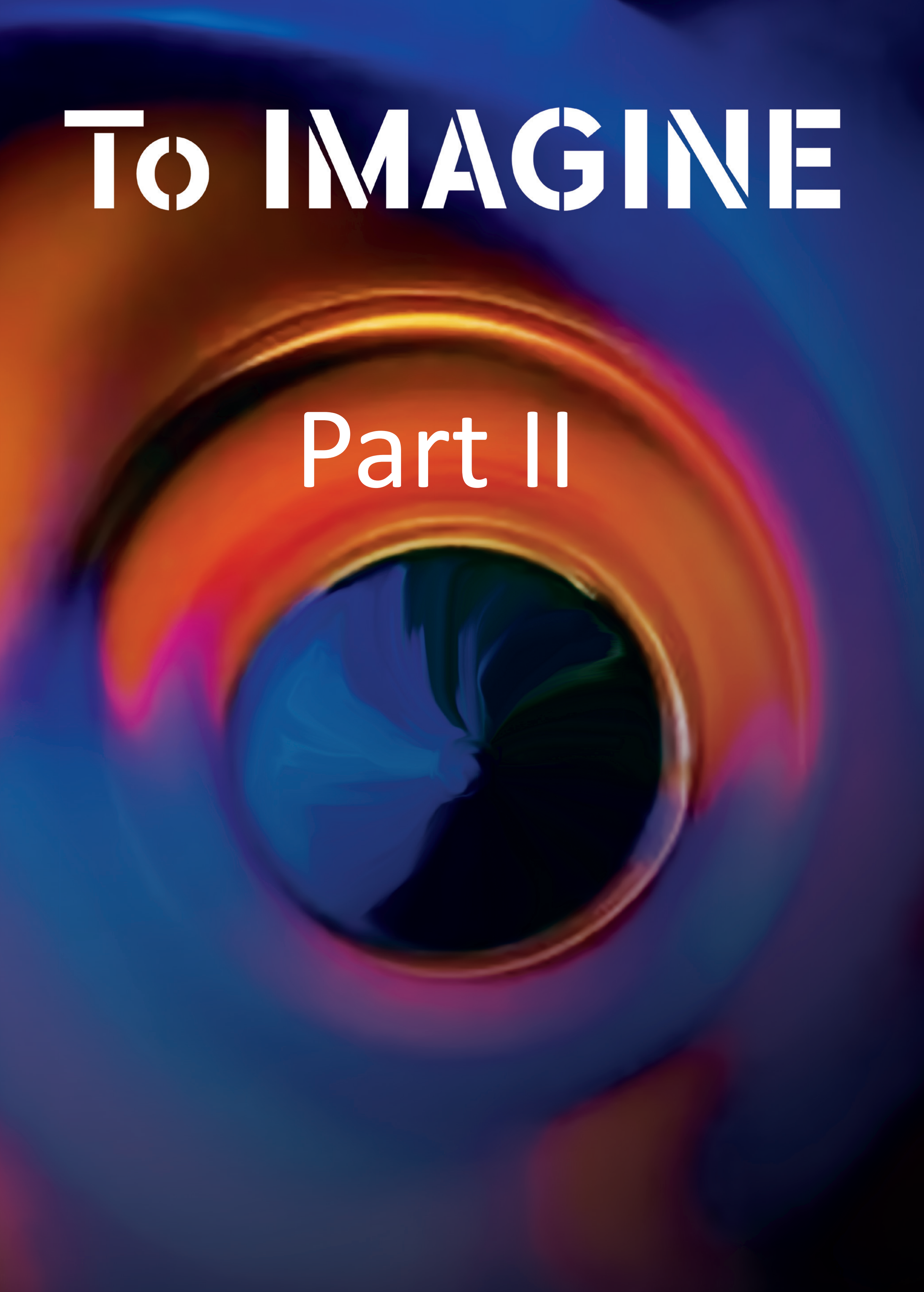

To IMAGINE

Part II

“

What is now proved was once only imagined.

- William Blake

6

Development of a multimodal imaging setup to study human skin invasion by helminths

Clarize M. de Korne, Mick M. Welling, Danny M. van Willigen,
Fabian W. Hensbergen, Meta Roestenberg, Fijs W.B. van Leeuwen

Unpublished

ABSTRACT

In light of the continued global health threat posed by neglected tropical diseases such as helminths, there is a need for tools that can assist in the development of effective anthelminthic strategies. The aim of this study was to address this need by developing a multimodal imaging setup capable of visualizing and quantifying the invasion of human skin by *Schistosoma mansoni* and *Necator americanus* larvae. The hybrid tracer ^{99m}Tc-Cy5-Methyl-AmineC4.MAS$_3$ was used, enabling the simultaneous fluorescent and radioactive labeling of the larvae and thereby facilitating the monitoring of their invasion patterns and the quantification of invasion events. This setup demonstrated the feasibility of a comprehensive and quantitative evaluation of helminthic invasion, offering opportunities for interventions aiming at obtaining a deeper understanding of the invasion process and serving as a useful readout for assessing the efficacy of future invasion-blocking strategies.

INTRODUCTION

Schistosomiasis and hookworms are two of the most common neglected tropical diseases, currently affecting more than 10% of the world population. These parasitic infections cause chronic disease which a gradual decline in health (0.4 million life years and 2.2 million years of healthy life are lost annually) and eventually cause great economic impact[1]. Global control mainly relies on mass drug administration which has reduced overall disease morbidity, but due to drug-failure and high re-infection rates in endemic areas, schistosomiasis and hookworm infection have remained a global health threat[2].

Schistosomes and hookworms are skin-invading helminths; an infection starts when the infective larval stages of these helminths, which are free-living in water or soil, actively penetrate intact skin of their human host upon contact. Thereafter, the larvae migrate through the human body to the location suitable to mature into adult worms and to release eggs which are passed into the environment via the stool[3, 4]. Since the life cycles of these helminths depend amongst other things on the ability of the larvae to invade the skin, blocking skin invasion is one of the possible approaches to reduce disease transmission.

Despite being a crucial part of the life cycle and thereby a potential target for anthelminthic strategies, skin invasion by helminths has only rarely been studied. To date, only few studies using *in* vitro, rodent, canine or non-human primate models have provided some knowledge about the temporal dynamics of skin invasion and the key regulators, e.g. chemical cues, of the process[5-7]. These models have also been used to test several potential anti-penetrants, such as creams that act as a repellent/physical/larvicidal barrier or drugs that can kill larvae during the invasion process[8]. However, since the structure and composition of non-human skin differs significantly from that of human skin in terms of thickness, hairiness, and chemical properties[9-11] and the availability of large animal models for research is restricted, utilizing a human skin model would facilitate further investigation of helminthic skin invasion and assessment of potential invasion blocking strategies.

The limited use of a human skin model to study helminthic skin invasion can be attributed to the absence of an appropriate method to visualize and quantify invasion in human skin. Brightfield microscopy has been used to count and observe the behavior of helminths *in vitro*[3, 12, 13], however cannot be used to visualize helminths during skin invasion. On the other hand, molecular imaging techniques using fluorescent and radioactive labeling approaches have been successfully employed for *in vivo* studies of other pathogens (e.g. malaria parasites and *S. aureus* bacteria[14, 15]) as well as non-pathogenic cells (e.g. immune cells and stem cells[16, 17]). Thus, we reasoned that the development of a multimodal imaging setup for helminths would pave the way towards studying helminthic invasion in a human skin model.

We recently reported the preliminary results of monitoring skin invasion by schistosomes labeled with a fluorescent mitochondrial tracer[18]. In this study, we use the radiolabeled analogue ^{99m}Tc-Cy5-Methyl-AmineC4.MAS$_3$ to label the larval stages of the helminths *Schistosoma mansoni* and *Necator americanus*. The fluorescent signature of the tracer was used to microscopically assess human skin invasion to deepen our understanding of that process. The radioactive signature was applied to establish a quantitative readout for helminthic skin invasion which may be useful in the future to assess the efficacy of potential parasite invasion blocking strategies.

METHODS

Parasite production

The Puerto Rican strain of *Schistosoma mansoni* (*Sm*) has been maintained in laboratory culture in the LUMC by means of its natural cycle between *B. glabrata* snails as the intermediate host and hamsters (RjHan:AURA strain; Janvier labs) as the definitive host as previously described[19]. To obtain larvae, infected snails were transferred to a 6-well plate filled with Bar-le-Duc water in a water bath at 30 °C. Subsequently, the snails were exposed to light and were allowed to shed larvae for 1 hr. Thereafter, the shed larvae were collected and kept at 30 °C until further use. Experiments were started within 1 hr after the collection of larvae. To count the larvae, 0.5 ml of the larvae solution was stained with Lugol's iodine and the stained larvae were counted using a stereomicroscope.

Third-stage larvae of *Necator americanus* (*Na*) were obtained from fecal samples collected from a healthy donor carrying a chronic hookworm infection (infected in the context of a controlled human hookworm infection trial[20]). The presence of *Na* eggs in the donor feces was confirmed by brightfield microscopy of Kato smears as described before[21]. Subsequently, 5 g feces was mixed with gentamicin (38 µl, stock: 40 mg/ml), amphotericin B (1 ml; stock: 750 µg/ml) and charcoal (1.5 g), placed on moist filter paper on a plastic platform in a petri dish and cultured for 7 days at 25 °C. Larvae migrated from the feces to the clean water surrounding the filter paper, were collected, washed and kept in Bar-le-Duc water at 25 °C until further use. The larvae were used up to 7 weeks after collection. The larvae were counted per 0.5 ml using a Leica M80 stereomicroscope (Leica Microsystems).

Hybrid tracer synthesis

Cy5-AmineC4.MAS$_3$-Methyl was synthesized and characterized as described (see Chapter 6 from this thesis). In brief, the chelate mercaptoacetyltriserine (MAS$_3$) was coupled to Cy5-Methyl-AmineC4 by forming an amide bond, yielding the tracer Cy5- AmineC4.MAS$_3$-Methyl (from now abbreviated as Cy5-MAS$_3$). The crude compound was purified using preparative-scale prep-HPLC (high-performance liquid chromatography) and the product structure was confirmed by NMR (nuclear magnetic resonance) spectroscopy. Subsequently, the (photo) physical properties of the tracer were assessed; the molar extinction coefficient (ε) and quantum yield (ΦF) were assessed to calculate the brightness (ε*ΦF) and the lipophilicity (log P) and serum binding were determined using methods previously described[22].

Radiolabeling of Cy5-MAS$_3$

Radiolabeling of Cy5-MAS$_3$ with technetium-99m was performed according to a previously described protocol (see Chapter 6 from this thesis) with some minor amendments. To Cy5-MAS$_3$, 1 GBq technetium-99m freshly eluted from a generator (~1 GBq/ml; Ultra-Technekow™, Mallinckrodt Medical B.V.) was added to a mixture containing 2.5 nmol of the tracer (992 µM stock in H_2O) and the following buffer solutions: 47.5 µl of phosphate buffer (0.5 M, pH 8), 50 µl of phosphate buffer (0.25 M, pH 8), 40 µl disodium tartrate dihydrate (50 mg/mL in phosphate buffer (0.5 M, pH 8)) and 10 µl of Tin(II) chloride dihydrate (4 mg/ml in L-ascorbic acid solution (3 mg/ml in 0.1 M HCl)) (Sigma-Aldrich). The Tin(II) chloride dihydrate solution was freshly prepared and N_2 degassed for 20 min, all other buffers were prepared and stored at 4°C for maximally 1 month. After heating the reaction mixture to 100°C for 20 min, the reaction mixture was cooled down to room temperature and diluted with 10 ml Milli-Q water. This solution was passed through a Sep-Pak C-18 cartridge (Waters) pre-rinsed with EtOH, followed by another 10 ml of Milli-Q water. After that, the labeled tracer was drop-wise eluted from the cartridge with EtOH into the reaction tube followed by vigorous vortexing. The volume of this eluate was reduced to 5 µl by evaporation of ethanol. The radiochemical purity of the final product ^{99m}Tc-Cy5-MAS$_3$ was analyzed by radio-thin layer chromatography (radio-TLC; Supelco) using acetonitrile as mobile phase and the identity of the final product was confirmed using a HPLC system (high-performance liquid chromatography; Waters).

Parasite labeling

To label the *Sm* larvae with Cy5-MAS$_3$ (for fluorescent-based read-out) or ^{99m}Tc-Cy5-MAS$_3$ (for radioactivity-based readout), 2.5 nmol tracer in 5 µl EtOH was added to 495 µl of the larvae in Bar-le-Duc water. The larvae were incubated for 1 hr at 31 °C and subsequently washed. To wash the larvae, 4.5 ml of Bar-le-Duc water was added to the labeling solution and the 5 ml larvae solution was added to the reservoir of an überStrainer (filter mesh size 10 µm; Pluriselect). The strainer was connected to a valve which allowed to control the filter flow rate and to prevent the filter from running dry during the wash steps. The larvae were washed twice by draining and refilling the reservoir with Bar-le-Duc water and subsequently the reservoir was connected to a peristaltic pump (flow rate 1.3 l/hr; Gilson) for 30 minutes.

To label the *Na* larvae with Cy5-MAS$_3$ (for fluorescent-based read-out) or ^{99m}Tc-Cy5-MAS$_3$ (for radioactivity-based readout), 2.5 nmol tracer in 5 µl EtOH was added to 1245 µl of the larvae in Bar-le-Duc water. The larvae were incubated for 3 hr at 25 °C and subsequently washed. To wash the larvae, the larvae solution was poured through a pluriStrainer (filter mesh size 10 µm; Pluriselect) followed by 500 ml Bar-le-Duc water. Subsequently, the larvae were collected from the filter and the wash step was repeated.

Parasite labeling stability

To determine the stability of the labeling of *Sm* and *Na* larvae over time, at various intervals up to 24 hr after labeling, larvae labeled with ^{99m}Tc-Cy5-MAS$_3$ were filtered (Millex-HV syringe filter unit, 0.2 µm; Millipore). Subsequently, the radioactivity in the filtrate was measured with a gamma counter (Wizard2 2470 automatic gamma scintillation counter; PerkinElmer) and compared to the amount of radioactivity in a non-filtered sample to calculate the percentage decrease of parasite-bound tracer.

Parasite viability and labeling toxicity

The viability of the *Sm* larvae was assessed by brightfield microscopy; the number of whole larvae and separated larval bodies and tails were counted as well as moving and non-moving larvae. The viability of the *Na* larvae was also assessed by brightfield microscopy; moving and non-moving larvae were counted after stimulation with water of 50°C. After labeling of the *Sm* and *Na* larvae with ^{99m}Tc-Cy5-MAS$_3$, their viability was confirmed before further use. To determine possible toxic effects of ^{99m}Tc-Cy5-MAS$_3$, the viability of labeled and non-labeled *Sm* and *Na* larvae was assessed over time, at various intervals up to 48 hr after labeling. Brightfield movies of the *Sm* and *Na* larvae in solution were captured using a Leica AF6000 inverted widefield microscope with a 1.25x objective (Leica Microsystems). Using the Fiji package for the open-source software ImageJ[23] the movies were compressed into a single image using minimum-intensity projection (retrieves the level of minimum intensity over time for each x,y position).

Fluorescence-based imaging of skin invasion

Human skin explants were obtained from collaborating surgery centers immediately after cosmetic mastectomy. The use of human skin explants for this research was approved by the Commission Medical Ethics (CME) of the LUMC (CME: B18-009). The methods were carried out in accordance with the relevant guidelines and regulations, and informed consent was obtained from all participants. Pieces of human skin (5 x 10 mm) were placed into a confocal dish (Ø35mm; MatTek Corporation). The fluorescently labeled *Sm* larvae were added to the epidermal side of the skin piece and invasion was imaged using a Leica TCS (true confocal scanning) SP8X WLL (white light laser) microscope with a 10x objective (Leica Microsystems). Cy5-MAS$_3$ was excited at 633 nm and the emission was collected between 650 and 700 nm. The UV-laser (excitation: 405 nm, emission: 420–470 nm) was used to visualize the skin structures based on its autofluorescence. The movies were recorded with a frame rate of 70 frames per minute. The fluorescently labeled *Na* larvae were added to a piece of gauze (Ø 10 mm; Cutisoft) which was placed in a confocal dish. A piece of skin (10 x 10 mm) was, with the epidermal side down, put on top of the gauze. Movies of the *Na* larvae were captured using a Leica AF6000 inverted widefield microscope with a 10x objective (Leica Microsystems). Cy5-MAS$_3$ was excited at 633 nm and the movies were recorded with a frame rate of 240 frames per minute. Images with a higher resolution of the empty sheaths of the *Na* larvae were taken with a Leica TCS SP8X WLL microscope with a 40x objective (Leica Microsystems).

Radioactivity-based assessment of skin invasion

Pieces of human skin explant (~2x2 cm) were pre-heated to 37 °C before exposing them to *Sm* or *Na* larvae. The skin was exposed for 30 min to *Sm* larvae by putting a piece of skin on top of a well (24-well plate; Greiner Bio-One) filled with Bar-le-Duc water containing different numbers of radiolabeled larvae depending on the larval batch. Dose was normalized per experiment as a percentage of the highest dose. A plastic insert was used to allow the skin to be in contact with the solution without falling into it. The skin was exposed for 1 hr to 20, 40 or 60 *Na* larvae by putting a piece of skin on top of a piece of gauze (3x3 cm) containing radiolabeled larvae. To control for the radioactivity counts resulting from the presence of unbound tracer, control skin pieces were exposed to the last flow-through obtained during the washing of the *Sm* or *Na* larvae. During exposure, the skin was kept warm by putting a heating element at 37 °C on top of the skin. After exposure, the skin was rinsed with Bar-le-Duc water and counted using a gamma counter (Wizard2 2470 automatic gamma scintillation counter, Perkin Elmer).

Statistical analysis

The average and variability of the data were summarized using the mean and standard deviation (SD). The correlation between two numeric variables was assessed using the Pearson's correlation coefficient. p-values of <0.05 were considered significant. All statistical tests were performed by SPSS Statistics (IBM Nederland BV).

RESULTS

Development of a hybrid tracer labeling approach

A hybrid tracer suitable to label the helminth larval stages was developed by coupling a previously synthesized fluorescent mitochondrial tracer Cy5-Methyl-Methyl[24] to a MAS$_3$ chelate followed by ^{99m}Tc radiolabeling. The resulting hybrid tracer ^{99m}Tc-Cy5-MAS$_3$ was used to label *Sm* larvae freshly shed by their snail intermediate host and *Na* larvae cultured from donated feces from a controlled hookworm infection trial participant (Figure 1AB). The radiolabeling of Cy5-MAS$_3$ with ^{99m}Tc yielded 78 ± 9% binding of the total added radioactivity. The brightness of the tracer was $3.45 \cdot 10^3$ $M^{-1} \cdot cm^{-1}$ (the product of its quantum yield $\phi_{F,\ PBS}$ = 13% and molar extinction coefficient $\varepsilon_{PBS} = 2.65 \cdot 10^4$ $M^{-1} \cdot cm^{-1}$). A filter set-up was developed to purify the labeled larvae from the unbound tracer while preserving their viability (Figure

1C). Since *Sm* larvae are known to transform when exposed to high water turbulence or die when taken out of the water, this was prevented by controlling the flowrate in the filter set-up to allow for slow continuous washing. By filtering, >99.99% of the unbound tracer could be removed, reducing the background signal from the solution to <3% for *Sm* larvae and <1% for *Na* larvae (Figure 1D). Microscopical examination of the labeled *Sm* and *Na* larvae revealed that the larvae were wholly labeled; their outer membrane as well as their internal organs were labeled (Figure 1E-F).

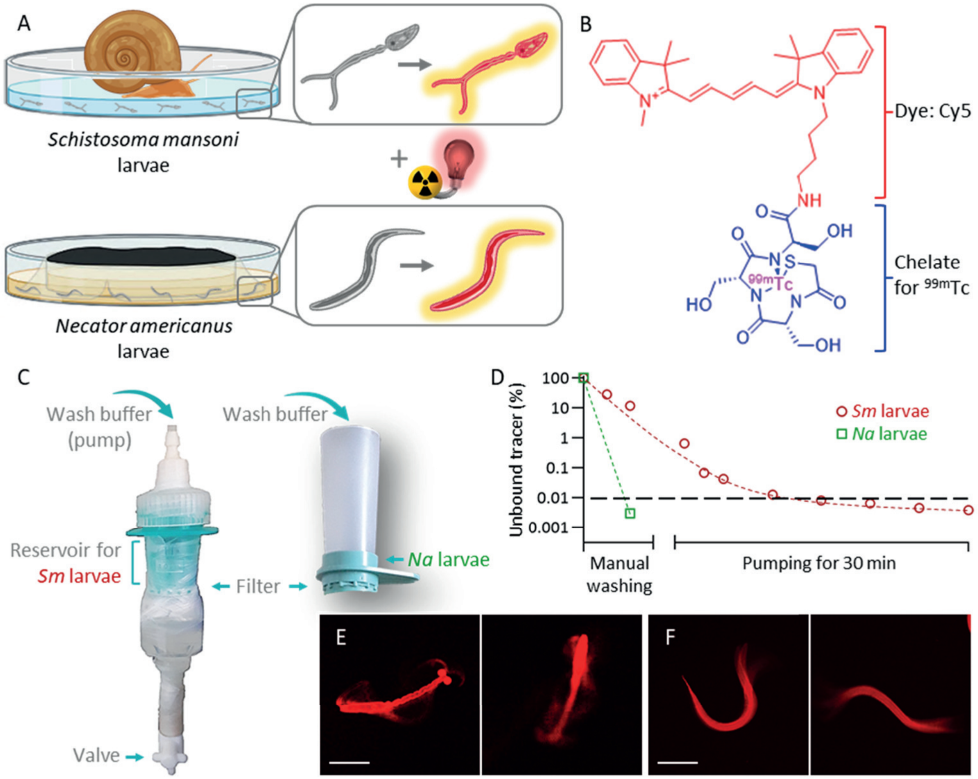

Figure 1 Hybrid tracer labeling approach for helminthic larvae. A) The *Schistosoma mansoni* (*Sm*) larvae were shed by their intermediate snail host and the *Necator americanus* (*Na*) larvae were cultured from feces containing eggs. The larvae were labeled with a hybrid tracer. B) The chemical structure of the hybrid tracer ^{99m}Tc-Cy5-Methyl-AmineC4.MAS$_3$ which contains a Cy5 dye (depicted in red) and a MAS$_3$ chelate (depicted in blue) containing ^{99m}Tc (depicted in pink). C) The filter set-up for *Sm* and *Na* larvae based on the use of a filter with a mesh size of 10 µm. D) Quantification of the reduction of the percentage of unbound tracer by filtering. E-F) Microscopic analysis of *Sm* (E) and *Na* larvae (F) labeled with the Cy5-MAS$_3$ tracer (shown in red). Scale bar: 150 µm.

Labeling stability and parasite viability over time

The stability of the labeling was assessed by measuring the reduction in the percentage bound tracer *in vitro*. Four hours after labeling, the time frame in which the labeled larvae were used for experiments, still >80% of the tracer was bound to the larvae (Figure 2A). The viability of the larvae was assessed by counting the percentage of motile larvae (Figure 2CD). In solution, the *Sm* larvae displayed intermittent backward (tail-first) locomotion by beating their tails (Figure 2C). The *Na* larvae propagated sinusoidal waves along their bodies, but this movement did not result in forward or backward locomotion (Figure 2D). The viability of the labeled larvae directly after the labeling procedure was comparable to unlabeled larvae; 99 ±1 % of the *Sm* larvae were viable and 93 ± 3% of the *Na* larvae (Figure 2B-D). Over time, the viability of the *Sm* larvae decreased which was independent of the labeling (viability at t=24 hr: 69 ± 8 %) (Figure 2B). The viability of the *Na* larvae did not decrease over the measured period of time (viability at t=48 hr: 93 ± 5%) (Figure 2B).

Microscopic assessment of skin invasion behavior

The labeling method was subsequently used to assess the skin invasion behavior of helminth larvae. The larvae were exposed to human skin explants in a set-up suited for confocal microscopic analysis (Figure 3A). The *Sm* larvae approached the skin in a body-first swimming mode (Figure 3B). Within minutes, the larvae were able to penetrate the skin. Three different ways of skin invasion were observed: 1) larvae penetrated the skin with their head, the head got separated from the tail and continued migration through the skin while the tail was left behind, 2) larvae penetrated the skin completely and whether or not shed their tail while migrating through the skin (some larvae disappeared from the field of view before they had shed their tail), 3) larvae penetrated the skin with their head but no further migration was observed during the observed period of time (Figure 3B).

The *Na* larvae were not able to propel forward in an aqueous environment (Figure 2D), however a structured environment better mimicking their natural soil environment, enabled 3-dimensional locomotion (Figure 3C). Therefore, the *Na* larvae were exposed to human skin while present in gauze. Unlike the *Sm* larvae, the gauze limited the visualization of *Na* larvae while penetrating. However, upon skin exposure, exsheathment could be observed (Figure 3C).

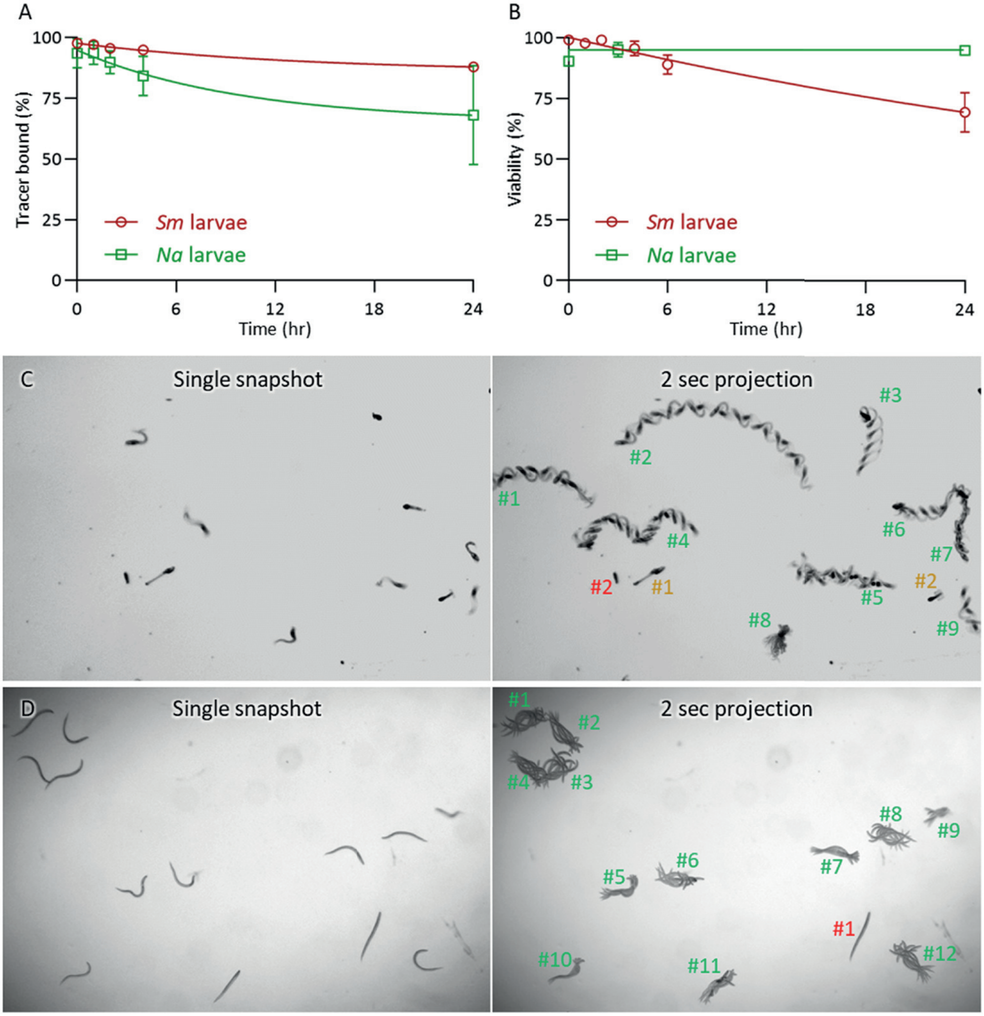

Figure 2 Labeling stability and parasite viability. A) The stability of the labeling plotted as the percentage of tracer bound to *Sm* and *Na* larvae over time. B) The viability of labeled *Sm* and *Na* larvae plotted as the percentage of motile larvae over time. C) A single brightfield image of *Sm* larvae (left) and a minimum intensity projection of the single brightfield image including the 19 consecutive frames captured in 2 s (right). The moving larvae are annotated in green, the stationary larvae are annotated in orange, the fallen apart larvae are annotated in red. D) A single brightfield image of *Na* larvae (left) and a minimum intensity projection of the single brightfield image including the 9 consecutive frames captured in 2 s (right). The moving larvae are annotated in green, the stationary larvae are annotated red.

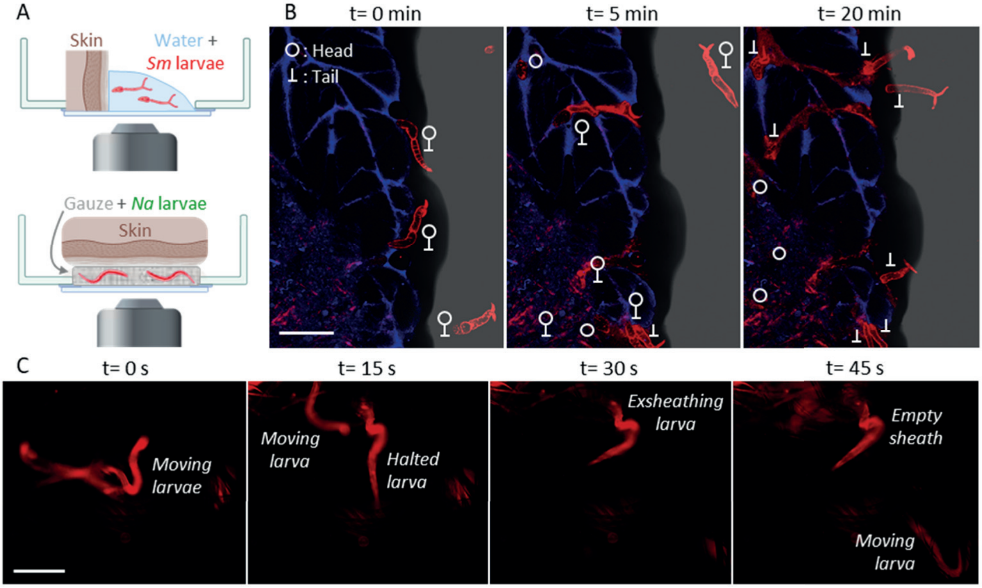

Figure 3 Microscopic assessment of skin invasion behavior. A) Schematic overview of the imaging set-up to monitor skin invasion behavior of *Sm* and *Na* larvae. B) Three screenshots from a movie (t=0, 5, 20 min) of skin-invading *Sm* larvae are shown; the brightfield signal is shown in grey, labeled larvae are shown in red and autofluorescence signal from the skin is shown in blue. The (separated) heads (O) and tails (⊥) of the larvae are annotated. Scale bar: 250 µm. C) Four screenshots from a movie (t=0, 15, 30, 45 s) of skin-exposed *Na* larvae in gauze are shown; labeled larvae are shown in red. Scale bar: 200 µm.

Radioactivity-based quantification of skin invasion

The radioactivity signature of the hybrid tracer was used to quantify skin invasion by *Sm* and *Na* larvae. Human skin was exposed to radiolabeled *Sm* larvae in solution or *Na* larvae in gauze (Figure 4A). Subsequently, the radioactivity signal in the skin was quantified. For both exposure to *Sm* and *Na* larvae, the radioactivity retrieved from the skin was linearly correlated with the amount of larval exposure (Pearson's correlation coefficient *Sm* larvae: 0.951, *Na* larvae: 0.958; p<0.001) (Figure 4DE). Skin invasion was confirmed by microscopic assessment of the remaining larval solution and gauze. Mainly separated tails from the *Sm* larvae and empty sheaths from the *Na* larvae were found back (Figure 4B-C).

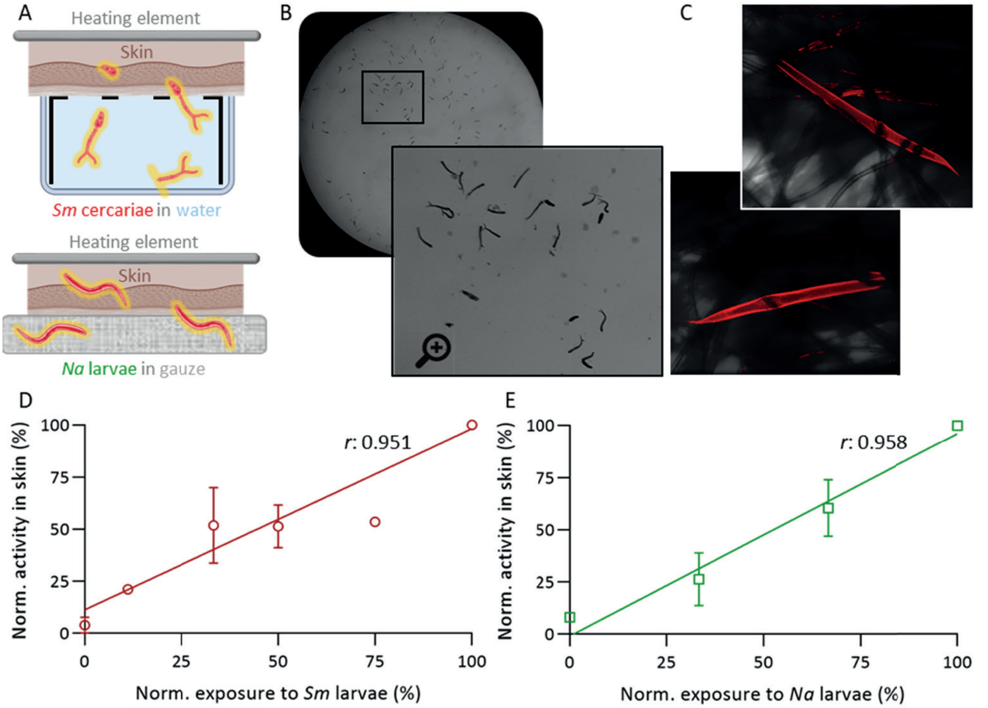

Figure 4 Radioactivity-based quantification of skin invasion. A) Schematic overview of the set-up to quantify skin invasion by *Sm* and *Na* larvae. B) The *Sm* larvae solution after skin exposure, mainly containing separated tails. C) Empty sheaths of *Na* larvae (depicted in red) in gauze after skin exposure. D) Quantification of skin invasion by *Sm* larvae. The radioactivity retrieved from the skin is plotted against the exposure to *Sm* larvae, normalized to the maximum dose. Pearson's correlation coefficient: 0.951; p<0.001. E) Quantification of skin invasion by *Na* larvae. The radioactivity retrieved from the skin is plotted against the exposure to *Na* larvae, normalized to the maximum dose. Pearson's correlation coefficient: 0.958; p<0.001.

DISCUSSION

In this study we present a multimodal imaging setup to study human skin invasion of helminths using the hybrid tracer ^{99m}Tc-Cy5-MAS$_3$. The fluorescent signature of the tracer allowed for real-time microscopical assessment of *Schistosoma mansoni* (*Sm*) and *Necator americanus* (*Na*) larvae invading human skin explant. The radioactive signature provided a quantitative measurement of the extent of skin invasion by *Sm* and *Na* larvae; we found that the radioactivity retrieved from the skin was directly proportional to the number of larvae in the exposure solution. This assay can aid investigating skin invasion by helminths and evaluating potential anti-invasion strategies aimed at preventing the neglected tropical diseases caused by these parasites.

Labeled *Sm* and *Na* larvae formed the basis of this study. Uniquely, we had both human helminth species at our disposal, since the *Sm* life cycle has been maintained in laboratory culture in the LUMC and *Na* larvae could be obtained from a donor participating in a controlled human hookworm infection trial[19, 20]. The limited availability of larvae for research in non-endemic areas, as well as the limited options for labeling them endogenously (expression of reporter proteins) or exogenously (use of imaging agents), have resulted in a paucity of imaging studies focused on helminths[25-28]. The use of the hybrid tracer ^{99m}Tc-Cy5-MAS$_3$ was successful in labeling both *Sm* and *Na* larvae for *ex vivo* imaging, while preserving their viability. This offers the prospect of a widely applicable exogenous labeling strategy for helminths that can advance further imaging-based research.

This study and our recent study using the precursor of the hybrid tracer used here (Cy5-Methyl-Methyl[18]) are the first to report real-time monitoring of human skin invasion by schistosomes. Prior studies on helminth behavior 1) have limited real-time monitoring to *in vitro* setups[13, 29-31], 2) mainly relied on animal models for *in/ex vivo* invasion studies[32-34] and 3) were based on retrospective assessment to estimate (human skin) invasion[35, 36]. The integration of these aspects in a single setup enhances the comprehensive study of host-seeking and invasion behavior, leading to the acquisition of complementary information. For instance, previous studies have reported both tail-first and head-first swimming patterns of schistosomes[12]. However, our integrated setup emphasized the role of skin in regulating these swimming patterns, as head-first swimming was observed during invasion and tail-first swimming occurred in the absence of skin. Moreover, as a follow-up to the discovery of delayed tail loss by Whitfield *et al.* that challenged the widely accepted notion that larvae immediately lose their tails upon skin penetration[37], our assay enables further exploration of this process by real-time monitoring of its temporal and spatial dynamics which may have immunological consequences. In case of the *Na* larvae, incorporating a transparent material that allows for movement, rather than the non-transparent gauze used in this study, would facilitate real-time monitoring of their complete human skin invasion. Incorporating a motility analysis tools into the setup may add value by providing detailed information about the motility patterns of these larvae[15, 38-40].

The radiolabeling approach provided a quantitative evaluation of the invasion of *Sm* and *Na* larvae. The need for a quantitative readout to assess the anthelminthic properties of potential new drugs and invasion blockers has been acknowledged in the field, as several screening assays have been recently developed[41-45]. Our radiolabeling approach offered a more direct and quantitative measurement of the efficacy of invasion blockers as opposed to the more indirect measures utilized thus far such as the effect on *in vitro* motility of larvae and adult worms or, in the case of *Sm* larvae, the count of released tails as a proxy for transformation. In the past, metabolic radiolabeling has been applied to study the distribution and migration patterns of schistosomes within rodent host tissue[46, 47]. However, up to now there were no radiotracers available suitable for tracking of live helminths[26]. To improve the accuracy of the quantification, a filtering setup was developed that reduced the background signal while maintaining the larvae viability, resulting in a sufficient signal-to-background ratio. Further standardization of the setup is required to progress from the relative quantification of invasion applied in this study to a quantification of the absolute number of invaded larvae.

In conclusion, our study introduced a novel multimodal imaging approach that combined fluorescent and radioactive imaging to assess helminth skin invasion in real-time using a human skin explant model. This setup enables a more comprehensive and quantitative evaluation of helminthic invasion, providing possibilities for gaining deeper insights into this process as well as serving as a useful readout for assessing the efficacy of future helminth invasion-blocking strategies.

Acknowledgments: We are grateful to our colleagues Jacqueline Janse, Yvonne Kruize and Jan Pieter Koopman and the anonymous donor, for their assistance in obtaining the *Necator americanus* larvae through fecal donation. We also extend our gratitude to Jan de Best, Arifa Ozir-Fazalalikhan and Jeroen Sijtsma for their support in maintaining the life cycle of *Schistosoma mansoni* and providing the larvae. Furthermore, we would like to thank Leon Slof for providing building blocks used in the invasion assay. We acknowledge ChatGPT for providing assistance in generating written content during the preparation of this chapter.

REFERENCES

1. Organization, W.H., Schistosomiasis and soil-transmitted helminthiases: progress report, 2020. Weekly Epidemiological Record= Relevé épidémiologique hebdomadaire, 2021. 96(48): p. 585-595.
2. Tsuji, N., Schistosomiasis and hookworm infection in humans: Disease burden, pathobiology and anthelmintic vaccines. Parasitology international, 2020. 75: p. 102051.
3. Chauhan, V.M., et al., The physicochemical fingerprint of Necator americanus. PLoS neglected tropical diseases, 2017. 11(12): p. e0005971.
4. Nation, C.S., et al., Schistosome migration in the definitive host. PLoS neglected tropical diseases, 2020. 14(4): p. e0007951.
5. Gang, S.S. and E.A. Hallem, Mechanisms of host seeking by parasitic nematodes. Molecular and biochemical parasitology, 2016. 208(1): p. 23-32.
6. McKerrow, J. and J. Salter, Invasion of skin by Schistosoma cercariae. Trends in parasitology, 2002. 18(5): p. 193-195.
7. Wheeler, N.J., E.A. Hallem, and M. Zamanian, Making sense of sensory behaviors in vector-borne helminths. Trends in Parasitology, 2022.
8. Downs, P.W., et al., New tools for the schistosomiasis elimination toolbox: Barriers and opportunities for the development of a topical cercarial anti-penetrant. 2017.
9. Jung, E.C. and H.I. Maibach, Animal models for percutaneous absorption. Topical drug bioavailability, bioequivalence, and penetration, 2014: p. 21-40.
10. Souci, L. and C. Denesvre, 3D skin models in domestic animals. Veterinary research, 2021. 52(1): p. 1-15.
11. Treuting, P.M., S.M. Dintzis, and K.S. Montine, Comparative Anatomy and Histology: A Mouse and Human Atlas. Academic Press, Elsevier, 2017. Chapter 24: p. 433-441.
12. Krishnamurthy, D., et al., Schistosoma mansoni cercariae swim efficiently by exploiting an elastohydrodynamic coupling. Nature Physics, 2017. 13(3): p. 266-271.
13. Nguyen, K., B. Gemmell, and J. Rohr, Effects of temperature and viscosity on miracidial and cercarial movement of Schistosoma mansoni: ramifications for disease transmission. International journal for parasitology, 2020. 50(2): p. 153-159.
14. Welling, M.M., et al., Multimodal Tracking of Controlled Staphylococcus aureus Infections in Mice. Acs Infectious Diseases, 2019. 5(7): p. 1160-1168.
15. Winkel, B.M.F., et al., Quantification of wild-type and radiation attenuated Plasmodium falciparum sporozoite motility in human skin. Scientific Reports, 2019. 9.
16. Perrin, J., et al., Cell tracking in cancer immunotherapy. Frontiers in Medicine, 2020. 7: p. 34.
17. Roca, M., et al., Guidelines for the labelling of leucocytes with 111In-oxine. European journal of nuclear medicine and molecular imaging, 2010. 37(4): p. 835-841.
18. Winkel, B.M.F., et al., Early Induction of Human Regulatory Dermal Antigen Presenting Cells by Skin-Penetrating Schistosoma Mansoni Cercariae. Frontiers in Immunology, 2018. 9.
19. Janse, J.J., et al., Establishing the production of male Schistosoma mansoni cercariae for a controlled human infection model. The Journal of infectious diseases, 2018. 218(7): p. 1142-1146.
20. Hoogerwerf, M.-A., et al., New insights into the kinetics and variability of egg excretion in controlled human hookworm infections. The Journal of infectious diseases, 2019. 220(6): p. 1044-1048.
21. Meurs, L., et al., Diagnosing polyparasitism in a high-prevalence setting in Beira, Mozambique: detection of intestinal parasites in fecal samples by microscopy and real-time PCR. PLoS neglected tropical diseases, 2017. 11(1): p. e0005310.
22. Hensbergen, A.W., et al., Evaluation of asymmetric orthogonal cyanine fluorophores. Dyes and Pigments, 2020. 183: p. 108712.
23. Schindelin, J., et al., Fiji: an open-source platform for biological-image analysis. Nat Methods, 2012. 9(7): p. 676-82.
24. Winkel, B.M.F., et al., A tracer-based method enables tracking of Plasmodium falciparum malaria parasites during human skin infection Theranostics, 2019. 9(10): p. 2768-2778.
25. Beckmann, S. and C. Grevelding, Paving the way for transgenic schistosomes. Parasitology, 2012. 139(5): p. 651-668.
26. de Korne, C.M., et al., Imaging as a (pre) clinical tool in parasitology. Trends in Parasitology, 2023.

27. Novobilsky, A. and J. Hoglund, Small animal in vivo imaging of parasitic infections: A systematic review. Experimental Parasitology, 2020. 214.
28. Pearce, E. and J. Lok, Imaging trematode and nematode parasites. Parasite Immunology, 2013. 35(9-10): p. 248-255.
29. Bryant, A.S., et al., A critical role for thermosensation in host seeking by skin-penetrating nematodes. Current Biology, 2018. 28(14): p. 2338-2347. e6.
30. Santos, M.J., et al., Qualitative and quantitative behavioral traits in a community of furcocercariae trematodes: tools for species separation? Journal of Parasitology, 2007. 93(6): p. 1319-1323.
31. Selbach, C. and R. Poulin, Parasites in space and time: a novel method to assess and illustrate host-searching behaviour of trematode cercariae. Parasitology, 2018. 145(11): p. 1469-1474.
32. Krautz-Peterson, G., et al., Imaging schistosomes in vivo. The FASEB Journal, 2009. 23(8): p. 2673.
33. Paveley, R.A., et al., Fluorescent imaging of antigen released by a skin-invading helminth reveals differential uptake and activation profiles by antigen presenting cells. PLoS neglected tropical diseases, 2009. 3(10): p. e528.
34. Pellegrino, J., Protection against human schistosome cercariae. Experimental Parasitology, 1967. 21(1): p. 112-131.
35. Cooper, E., et al., A comparison of topical formulations for the prevention of human schistosomiasis. Journal of pharmacy and pharmacology, 2004. 56(8): p. 957-962.
36. Ingram, R., et al., Dimethicone barrier cream prevents infection of human skin by schistosome cercariae: evidence from Franz cell studies. Journal of Parasitology, 2002. 88(2): p. 399-402.
37. Whitfield, P., et al., Delayed tail loss during the invasion of human skin by schistosome cercariae. Parasitology, 2003. 126(2): p. 135-140.
38. Ramot, D., et al., The Parallel Worm Tracker: a platform for measuring average speed and drug-induced paralysis in nematodes. PloS one, 2008. 3(5): p. e2208.
39. Storey, B., et al., Utilization of computer processed high definition video imaging for measuring motility of microscopic nematode stages on a quantitative scale:“The Worminator”. International Journal for Parasitology: Drugs and Drug Resistance, 2014. 4(3): p. 233-243.
40. de Korne, C., et al., Clustering and erratic movement patterns of syringe-injected versus mosquito-inoculated malaria sporozoites underlie decreased infectivity. Msphere, 2021. 6(2): p. e00218-21.
41. Bartlett, A., et al., The infection of human skin by schistosome cercariae: studies using Franz cells. Parasitology, 2000. 121(1): p. 49-54.
42. Duguet, T.B., et al., Identification of annotated bioactive molecules that impair motility of the blood fluke Schistosoma mansoni. International Journal for Parasitology: Drugs and Drug Resistance, 2020. 13: p. 73-88.
43. Kotze, A., et al., An in vitro larval motility assay to determine anthelmintic sensitivity for human hookworm and Strongyloides species. The American journal of tropical medicine and hygiene, 2004. 71(5): p. 608-616.
44. Tritten, L., O. Braissant, and J. Keiser, Comparison of novel and existing tools for studying drug sensitivity against the hookworm Ancylostoma ceylanicum in vitro. Parasitology, 2012. 139(3): p. 348-357.
45. Wangchuk, P., et al., Identification of lead chemotherapeutic agents from medicinal plants against blood flukes and whipworms. Scientific reports, 2016. 6(1): p. 32101.
46. Li, J.-W., et al., Tran35S-labeling of cercariae of Schistosoma mansoni: a less expensive tool for tracing in vivo migration of schistosomula in mice. Parasitology International, 1997. 46(1): p. 55-65.
47. Salafsky, B., et al., Evaluation of N, N-diethyl-m-toluamide (DEET) as a topical agent for preventing skin penetration by cercariae of Schistosoma mansoni. The American journal of tropical medicine and hygiene, 1998. 58(6): p. 828-834.

7

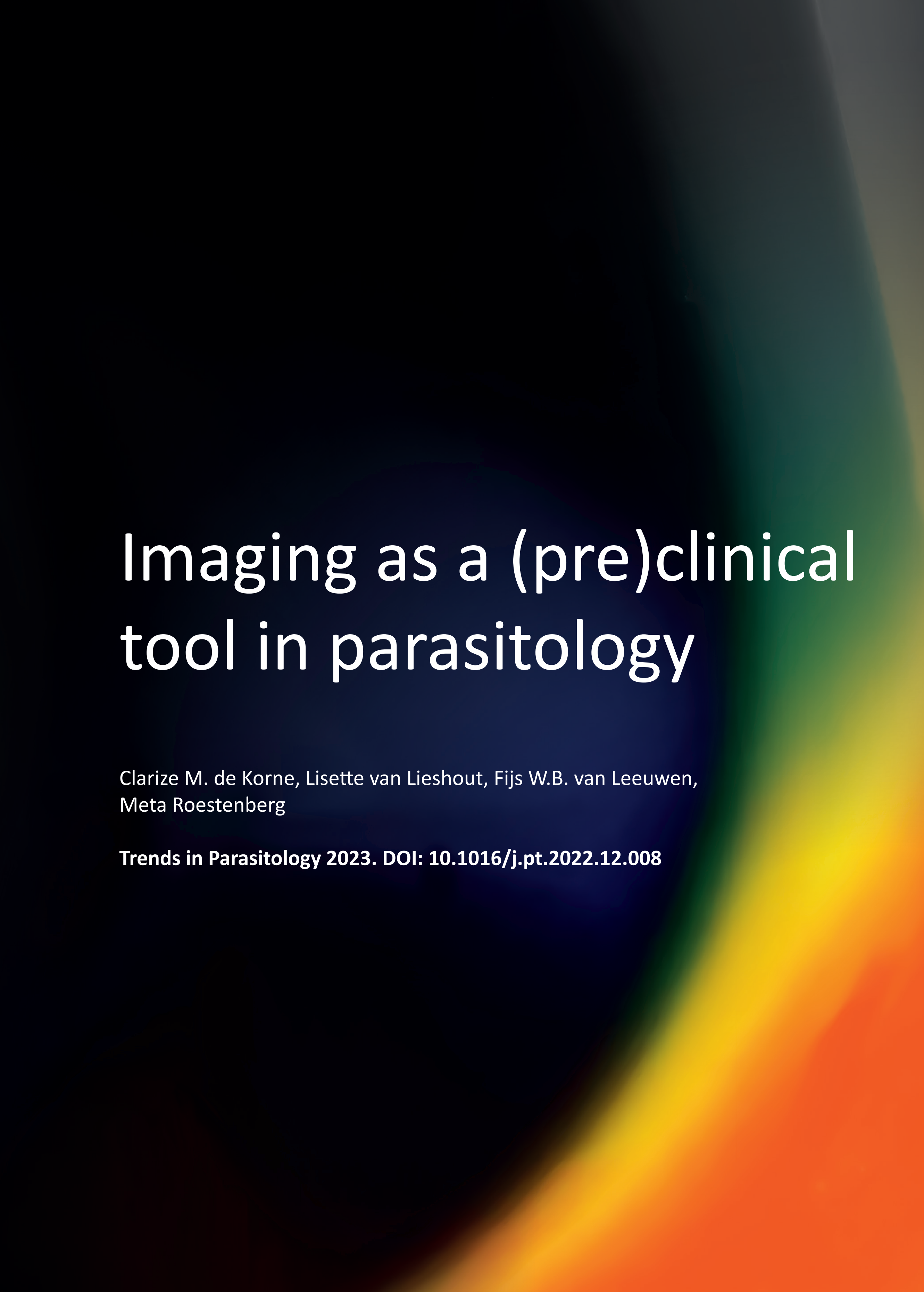

Imaging as a (pre)clinical tool in parasitology

Clarize M. de Korne, Lisette van Lieshout, Fijs W.B. van Leeuwen,
Meta Roestenberg

Trends in Parasitology 2023. DOI: 10.1016/j.pt.2022.12.008

ABSTRACT

Imaging of parasites is central to diagnosis of many parasitic diseases and has thus far played an important role in the development of antiparasitic strategies. The development of novel imaging technologies has revolutionized medicine in fields other than parasitology and has also opened up new avenues for the visualization of parasites. Here we review the role imaging technology has played so far in parasitology and how it may spur further advancement. We point out possibilities to improve current microscopy-based diagnostic methods and how to extend them with radiological imaging modalities. We also highlight *in vivo* tracking of parasites as a readout for efficacy of new antiparasitic strategies and as a source of fundamental insights for rational design.

HIGHLIGHTS

- Implementation of immunohistochemistry and computer vision can improve the specificity/sensitivity of microscopy-based diagnostics for parasitic infections and decrease their labor intensity.
- For accurate diagnosis of parasitic infections, the right body sites need to be assessed. Non-invasive radiological imaging techniques provide a means to assess body sites that are not (easily) accessible for specimen collection.
- Because of the relatively high prevalence of parasitic infections in low-resource settings, innovation of diagnostics includes reducing the costs of the hardware needed.
- Quantitative imaging of parasite behavior provides a functional readout of antiparasitic strategies and has enhanced the throughput of drug screens.
- Real-time tracking of parasites in the host can provide fundamental insights needed for the rational design of antiparasitic strategies.

INTRODUCTION

Preventive measures such as clean water, sanitation and vector control have reduced morbidity due to parasitic diseases substantially, but they have not led to eradication. Because R&D investments into novel tools to help control parasite disease and transmission have suffered from neglect, only a relatively small number of drugs and no vaccines are available to confront a plethora of parasites. Also, the development of diagnostic tools for parasitic diseases has received little attention. Consequently, bright-field microscopy has been (and still is) the cornerstone for diagnosis of parasitic diseases for decades[1]. In other biomedical fields, such as bacteriology and oncology, imaging technologies have been instrumental in advancing diagnostics and spurring development of novel drugs and vaccines[2, 3]. Also in the field of parasitology, novel imaging tools have the potential to greatly enhance the sensitivity and ease with which parasites can be detected and particularly imaging-based tracking of parasites can be instrumental to identify potential targets for novel interventions.

Because of the scale of many parasites (1-100 µm diameter for protozoa and helminthic eggs to a length of millimeters or even meters for helminthic adult worms), these microorganisms are highly amenable to imaging (Figure 1). Recent advances in microscopy, clinical imaging modalities, (fluorescent/luciferase) gene tagging and computer vision have increased 1) the detectability of live parasites in host tissue (both *in vivo* and *ex vivo)* by generating contrast between the parasites and their environment using endogenous/exogenous labeling approaches, and 2) the detection capacity of imaging modalities, which have led to a higher sensitivity and spatial/temporal resolution[4]. In this review we will discuss how (novel) imaging technologies have helped and may help advance the field of parasitology and, more specifically, which role they can play in innovating diagnostic approaches (first part) and supporting the development of drugs, vaccines and other preventives (second part). The first part points out the possibilities to improve and automate the current microscopy-based diagnostic methods and how to extend them with the use of radiological imaging modalities. In the second part, we will mainly focus on imaging technologies that may enable tracking of live parasites in a 3D environment and highlight how their implementation can lead to target discovery, fundamental insights for rational design and a readout for testing the efficacy of new antiparasitic strategies.

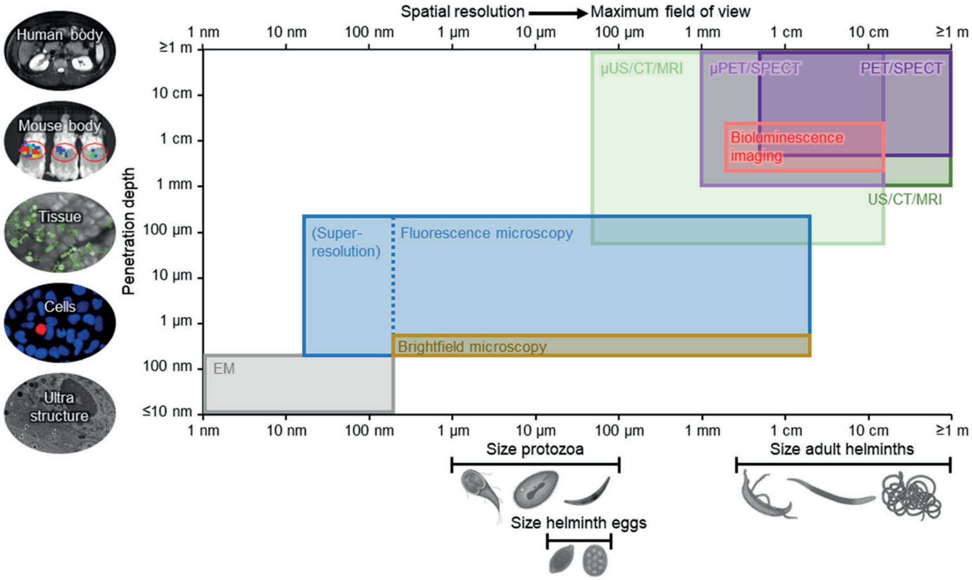

Imaging modality	Parasite visibility	Sensitivity* (M)	Temporal resolution
Brightfield microscopy	Label-free (& exogenous labels)	N/A	ms – s
Electron microscopy	Label-free (& exogenous labels)	N/A	N/A
Fluorescence microscopy	Endogenous & exogenous labels	$10^{-15} – 10^{-17}$	ms – s
Bioluminescence imaging	Endogenous labels	$10^{-15} – 10^{-17}$	s – min
(micro-) US/CT/MRI	Label-free (& exogenous labels)	N/A (MRI: $10^{-3} – 10^{-5}$)	min (US: s – min)
(micro-) PET/SPECT	Exogenous labels	$10^{-10} – 10^{-12}$	min

*Minimum concentration of imaging agent that can be detected

Figure 1 Characteristics of molecular imaging modalities. A broad range of imaging techniques are available for biomedical applications; this graph and table summarize the most important characteristics of the different (widely applied) imaging modalities. The spatial resolution combined with the maximum field of view (x-axis) of different imaging modalities (depicted as differently colored boxes) are plotted against their penetration depth (y-axis). The spatial resolution describes how detailed the parasites can be represented in the image (ranging from ultrastructural to whole-organ resolution), the maximum field of view determines the area of the sample that can be seen (ranging from squared micrometers to a whole-body field of view) and the penetration depth defines how deeply radiation can penetrate tissue (ranging from thin tissue slides to the whole human body). For the same imaging modalities, the temporal resolution is listed in the table, which defines the amount of time needed to reacquire data for the exact same location (ranging from milliseconds to minutes). In the table, it is also annotated if labeling (endogenous or exogenous) is a prerequisite for the visualization of parasites. This determines the sensitivity of the imaging modality (detection limits range from millimolar to femtomolar concentrations of the imaging agent). Some images used were adapted from: [5, 6]. Abbreviations: CT, computed tomography; EM, electron microscopy; MRI, magnetic resonance imaging; PET, positron emission tomography; SPECT, single-photon emission computed tomography; US, ultrasound.

THE ROLE OF IMAGING TECHNOLOGY IN INNOVATING DIAGNOSTIC APPROACHES FOR PARASITIC INFECTIONS

Correct diagnosis of parasitic infections (detection of parasites and identification of their species) is crucial to provide effective treatment. Particularly in low-income settings, the use of brightfield microscopy to examine patient specimens has remained the most important diagnostic tool for parasitic disease. For this purpose, non- or minimal-invasively obtained patient specimens are mostly assessed using light microscopy to detect the presence of parasites. For example, blood is examined to detect blood protozoa and microfilariae released by parasitic worms and feces is examined to detect cysts, eggs or larvae shed by intestinal protozoa and helminths[7]. Two of the limitations of the use of bright field microscopy for diagnostics that can be (partly) addressed by (novel) imaging technologies are 1) the low sensitivity and labor-intensity of the diagnostic procedures that require highly trained microscopists and 2) the restricted number of bodily locations at which parasites can be detected due to the need for patient specimens. In this section, we discuss the potential of immunohistochemistry (IHC), automated imaging and computer-aided image analysis to improve the sensitivity and laboriousness of microscopy-based methods (first part) and the potential of affordable medical imaging modalities to assess hard-to-reach body sites (second part). Together, these approaches can revolutionize the diagnostic workflow that is schematically depicted in Figure 2.

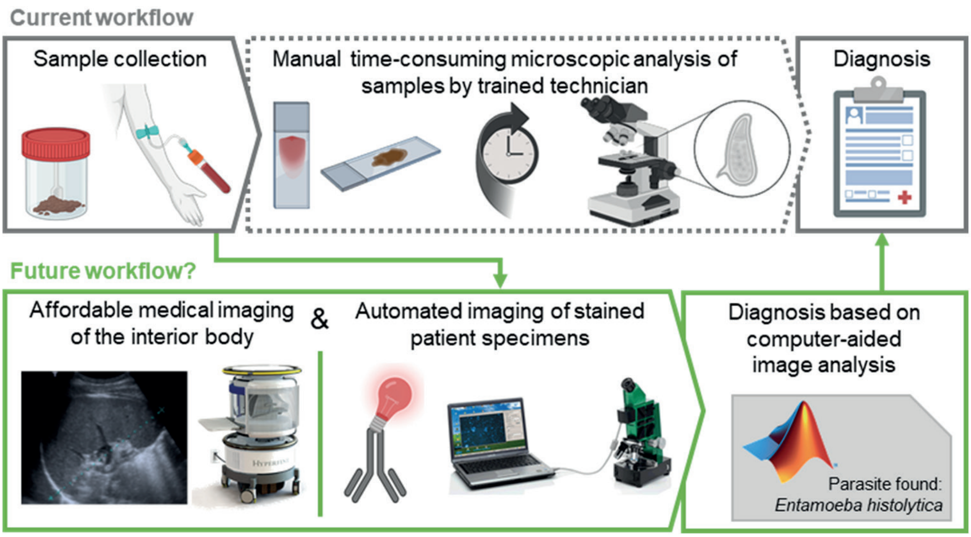

Figure 2 Innovating diagnostic approaches for parasitic infections. The traditional workflow for parasitic diagnostic methods (grey) and the potential for imaging-based technologies to accelerate this workflow (green). For the creation of this figure content form BioRender.com has been used and the ultrasound scan and Cyscope set-up have been reprinted from: [8, 9].

Low hanging fruits: innovation of microscopical methods for assessment of patient specimens

Low levels of parasites can easily be missed when microscopically analyzing patient specimens, either by overlooking parasites that are present in the sample or by accidentally examining a part of the sample that does not contain parasites. For example, for malaria diagnosis, the WHO recommends to screen 100 oil immersion visual fields before calling a thick blood smear negative, which in practice will yield a detection limit of 10–50 parasites/µl[10]. To assess the prevalence and infection intensity of intestinal helminths (e.g. the genera *Schistosoma, Ascaris, Necator*) the WHO recommends the use of Kato-Katz. This method is based on the microscopical analysis of the presence of eggs in a standard quantity of feces (most commonly used: 41 mg), which limits sensitivity of this tool to >20 eggs per gram feces[11]. To increase this sensitivity, different concentration methods have been developed and implemented. For example, the FLOTAC apparatus has been designed, based on the concept of centrifugal flotation of a fecal sample suspension and allows for quantitative copromicroscopic analysis[12]. To enable faster and more sensitive examination of patient specimens, and food samples in the case of screening for foodborne parasites[13], histological stains and to a lesser extent fluorescent dyes that enhance contrast between the parasites and the rest of the specimen can be used (Box 1). Enhancing contrast between parasites and the rest of the specimen aids the detection of parasites, since it improves the sensitivity by enabling the faster screening of higher volumes of sample. The advancement of enhancing contrast can be further exploited by the implementation of parasite-specific stains.

In addition, specific staining such as IHC can be used to identify parasites. IHC relies on antibodies that bind to a specific antigen, which results in highly specific staining methods that allow for identification and speciation of microorganisms beyond morphology seen with simple light microscopy. For example, IHC on patient specimens is routinely used in certain laboratories to diagnose *Toxoplasma gondii*. However, in general, remarkably, IHC barely plays a role in parasite diagnostics, whereas it has dramatically transformed the approach to histopathologic diagnosis in oncology[17]. Recently, several reports were published using IHC in parasitology. For example, Saïdi *et al*., amongst others, have reported the development of an immunofluorescent method suitable to stain *Leishmania* parasites in dermal scrapings, which improved the sensitivity of microscopy-based assessment of patient specimens[18]. In addition, Reinehr *et al.* re-examined metacestode material, which was archived as formalin-fixed, paraffin-embedded specimens in a biobank, for echinococcosis using IHC; their results show that IHC can contribute to diagnosing echinococcosis with greater certainty and can robustly discriminate between cystic and alveolar echinococcosis[19]. Beside its potential, IHC has also limitations since, despite the use of specific antibodies, nonspecific staining or cross-reactivity can occur which limit its specificity. Overall, development of immunohistochemical methods for parasites provides a relatively easy and cheap way to increase the sensitivity and specificity of microscopy-based diagnostics of parasitic infections and can also aid the identification of parasite species needed to decide the right treatment.

Box 1. Current staining methods for patient specimens

The most commonly used histological stains for parasites[7]:

- Mixtures of polychromed methylene blue and eosin (e.g. Giemsa staining) for microfilariae and protozoa in blood.
- Iodine which makes several parasitic worms appear brown while the rest of the stool specimen remains clear.
- Red acid-fast stains whereby coccidian species stand out clearly against a blue or green background.

Examples of successful implementation of fluorescent stains:

- Fluorescent acid-fast stains (e.g. auramine-rhodamine) have improved the diagnostic procedures for coccidian species by further increasing contrast between the parasites and their surroundings, which led to a higher sensitivity and a shorter observation time needed[14].
- The fluorescent nucleic acid binding dye acridine orange enables rapid identification of the nucleated blood parasites within a blood sample. Based on this fluorescent staining, the quantitative buffy coat test has been developed, which allows for more sensitive and rapid diagnosis compared with the traditional fix-and-stain techniques[15, 16].

Another simple method to improve the diagnostic workflow is to bypass the laborious process of preparing microscope slides of patient specimens to manually screening and interpreting these slides, which relies on the experience of trained technicians. Automated microscopy imaging and image analysis have the potential to reduce hands-on time, can standardize image interpretation (omitting the need for highly trained personnel) and can reduce the number of false negatives by screening larger samples. Current advances in the field of oncology exemplify what can be achieved when it comes to automation of histopathologic diagnosis; automated whole-slide imaging combined with computer-aided diagnosis are becoming the core of modern histopathology[20]. These concepts also have potential to innovate parasite diagnostics. For example, recent studies have shown that images of feces can automatically be generated and subsequently analyzed with learning software good enough for accurate diagnosis of multiple intestinal helminths with high accuracy[21, 22]. Other examples are the automated analyses of trichrome stained slides for the presence of protozoa in feces (both cyst and trophozoites) and the automated classification of stained malaria parasites in blood smears[23, 24]. These examples also suggest that implementation of more parasite-specific staining methods, as described in the previous paragraph, would increase the applicability of automated image interpretation. In the future, automated detection and classification can potentially be extended with artificial intelligence-based reasoning to provide a treatment proposal based on the findings.

To enable implementation of new diagnostic methods in low-income countries, tools need to be affordable. Thus, innovation of imaging-based diagnostic methods for parasitic infections also means reducing the costs of equipment such as microscopes. In this respect, two promising lines of research are the development of LED microscopy that offers the benefits of fluorescence microscopy without the associated costs and the development of smartphone-based imaging devices. For example, the portable LED microscope CyScope has achieved a sensitivity and specificity of up to 90% regarding the detection of malaria parasites in blood[25, 26]. Moreover, although presently moderate, the accuracy of smartphone-based imaging devices is constantly improving and has, for example, been used to quantify *Loa* microfilariae in blood and *Schistosoma haematobium* eggs in urine[27, 28]. Such technical innovations at the hardware site may boost the accessibility of imaging devices in low-income countries.

The next level: molecular imaging technology for the detection of parasites inside the body

With brightfield microscopy as the most important diagnostic tool, parasites are commonly detected in specimens that can be easily and non- or minimal-invasively obtained, such as feces, blood and sputum. However, parasites migrate through the human body (Figure 3), which means that diagnosis of parasitic disease at any organ level can be time-sensitive. Thus, for accurate diagnosis of parasitic infections, it is important to assess both enough and the right body sites. This is exemplified by the fact that only recently two other reservoirs in the host for trypanosomes besides the blood were discovered, namely the interstitial fluid of adipose tissue and skin[29, 30]. These reservoirs were even identified in individuals without trypanosomes in their blood, highlighting the limitations of only blood slides to diagnose trypanosomiasis[31]. A step in the right direction, is the recent translation of confocal laser scanning microscopy in combination with standard cystoscopy to the clinic. This technique permits non-invasive cell imaging *in vivo* in order to obtain images with a microscopic resolution. As an example, this technique enabled the non-invasive visualization of *Schistosoma* eggs in the urothelium of patients with urinary schistosomiasis without the need of a patient specimen[32].

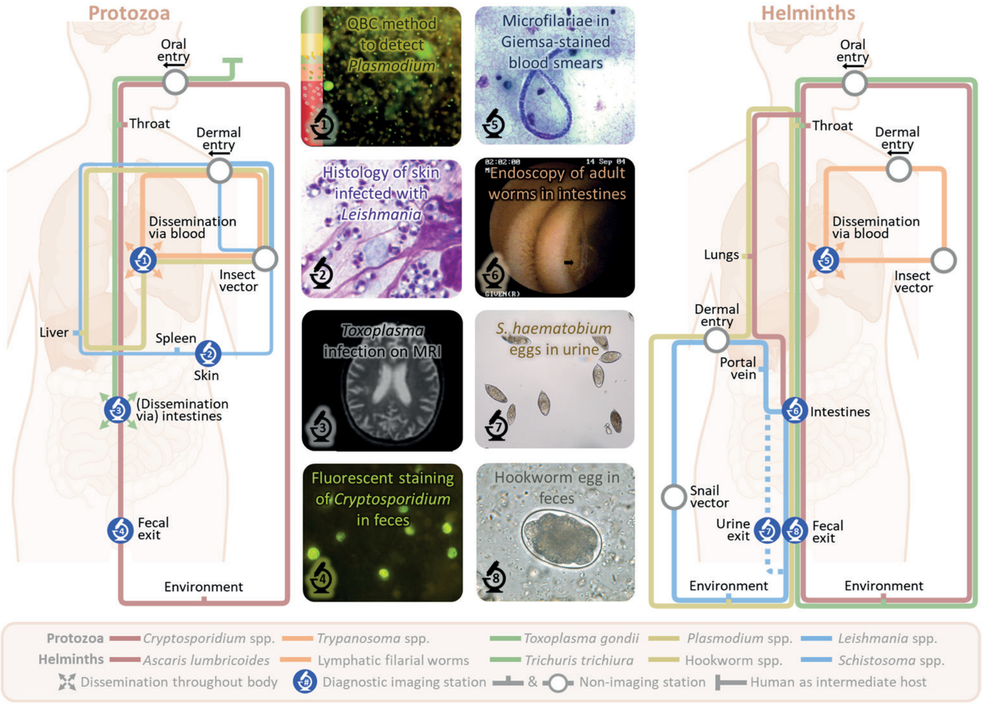

Figure 3 The role of imaging technology in diagnostics. The life cycles of the ten most clinically relevant protozoa and helminths are schematically depicted (five protozoa species in the left figure panel and five helminth species in the right figure panel), showing the different 'stations' these parasites pass while migrating through the human body. The 'stations' at which parasites can be detected for diagnosing an infection are annotated. Examples of images that can be obtained at the different diagnostic 'stations' are shown, which were kindly provided by Eric Brienen (1, 2, 4, 5, 7, 8) or adapted from: [33, 34]. Abbreviations: MRI, magnetic resonance imaging; QBC, quantitative buffy coat.

For detection of parasites at different body sites (e.g. brain, lungs, liver and intestines) without the need to obtain diagnostic material through puncture or biopsy, non-invasive radiological imaging techniques can provide a solution. Radiological imaging modalities (ultrasound (US), computed tomography (CT) and magnetic resonance imaging (MRI)) are macroscopic, noninvasive imaging modalities that allow the visualization of tissue morphology deep inside the body. Over the past years, the soft tissue contrast of US, CT and MRI has improved enough to allow for visualization of large adult worms. However, in the field of parasitology, these medical imaging modalities are mainly used to visualize how a parasitic infection has altered pathology. Especially in cystic diseases, such as neurocysticercosis caused by the *Taenia* tapeworm and cerebral toxoplasmosis caused by the protozoa *Toxoplasma gondii*, radiological imaging techniques are already applied to aid identification of disease stage (e.g. active/inactive disease) and thus guide the choice of treatment[9]. More recent advances are morphological MRI imaging to visualize and quantify liver tissue alterations resulting from an infection with *Schistosoma* parasites in a rodent model[35]. It is, however, important to note that high costs are associated with most of these radiological imaging procedures which results in low availability of equipment in low-income countries with a high prevalence of parasitic infections (Uganda: <0.5 MRI and CT units per million people versus the Netherlands: >10 MRI and CT units per million people[36]). Nevertheless, US especially has become more and more accessible and affordable (price drop >10x, hand-held scanners available) and different studies have shown its potential to diagnose a broad range of parasitic infections by detecting the parasites or the tissue alterations they induce[37].

A second category of imaging modalities that allows the detection of cells inside the body are nuclear imaging modalities (positron emission tomography (PET) and single-photon emission computed tomography (SPECT)) which are based on the principle of detecting gamma rays emitted from exogenous radiotracers present in target tissue. The advantage of using gamma rays is that they easily penetrate tissue allowing the non-invasive visualization of signal coming from deep within a patient, which have proven to be of great value in diagnosing cancer and subsequently monitoring the effect of treatment[38]. The success of these approaches fully relies on the ability to target cells with an exogenous radiotracer. While radiotracers are increasingly developed and used for specific types of cancer, there are no radiotracers available that target parasites yet. As a proof of concept, the nonspecific metabolic tracer 2-deoxy-2[^{18}F]fluoro-D-glucose (FDG) has once been successfully used to visualize the helminth burden in mice[39]. Although these techniques have shown great potential for diagnostic innovation in other fields, the benefits of increased sensitivity might not outweigh the high costs (development of an imaging agent is estimated to cost 50 to 100 million dollars and also their use within diagnostics is expensive[40]), especially not in the context of low-income countries.

THE ROLE OF IMAGING TECHNOLOGY IN DEVELOPING DRUGS, VACCINES AND PREVENTIVE MEASURES

A characteristic of parasites is that they migrate throughout their host and transition from one life cycle stage to the other. Recent advances in imaging technology have enabled real-time tracking of parasites, both *in vitro* and *in vivo*; individual parasites can be tracked using microscopy and the total parasite load can be monitored using bioluminescence-based imaging. These technologies are the result of developments in 1) the generation of transgenic parasite lines that express reporter proteins which has largely increased the detectability of parasites in tissue[41], 2) advanced microscopes with increased imaging resolution (e.g. development of laser scanning confocal), imaging speed (e.g. development of spinning disk confocal) and signal penetration depth (e.g. development of multiphoton laser excitation) which have improved their capacity to detect parasites[4] and 3) the availability of software tools for spatio-temporal cell tracking which are capable of automatically identifying parasites in images and following them over time[42, 43]. In this section the application of these technical advances is discussed. Tracking of parasites during their journey through the body helps to unravel mechanisms that can serve as potential targets for drugs, vaccines and preventive measures, as the feature of migration is essential to the survival of the parasite (first part). In addition, during development of new drugs, vaccines and preventive measures, monitoring parasite migratory behavior can serve as a readout for testing their efficacy (second part).

Imaging of parasite migration to generate fundamental insights needed for rational design of antiparasitic strategies

Historically, it was through imaging technology (bright field microscopy) that parasite transmission routes were discovered, which provided the basis for many of the preventive measures that are available nowadays (Box 2). Whilst these initial studies were instrumental to uncovering fundamental preventive measures, more advanced imaging tools were subsequently applied to understand the fundamental mechanisms that play a role when parasites enter the human host. These imaging studies can provide insights needed for the rational design of new antiparasitic strategies (such as preventive measures, vaccines, drugs).

Box 2. From microscopical findings to preventive measures

Bright field microscopy has played a pivotal role in the discovery of parasite transmission from one host to the other, shifting the initial paradigm that parasites were capable of ‘spontaneous generation’.

- The oral route of parasite transmission was unraveled by amongst other things feeding humans with larvae of the *Taenia* tapeworm or eggs of the *Enterobius* roundworm whereafter the adult worms could be visualized respectively in the intestines and the feces. Friedrich Küchenmeister published in 1855 his findings that *Taenia* larvae fed to a man under death sentence (currently considered unethical) had transformed into *Taenia* worms within the human intestinal tract and in 1865, Rudolf Leuckart and some of his students swallowed *Enterobius* eggs and found *Enterobius* worms in their feces around 2 weeks later[44].
- Microscopical analysis of skin previously exposed to hookworm larvae, revealed that hookworm larvae were able to penetrate intact skin and uncovered the transdermal route of parasite transmission. In 1898 Arthur Looss noted reddening of his skin and a burning sensation after a drop of water containing a high number of *Ancylostoma* larvae had fallen on his hand. He scraped of the last moisture residue from the epidermis and found numerous empty worm skins and just a few larvae. He was the first to report dermal penetration of any

worm[44].

- The role of vectors in parasite transmission was discovered using microscopy, starting with the discovery, made by Patrick Manson in 1877, that filarial parasites metamorphosed in the mosquito' abdomen. Subsequently the uptake and development of several parasite species in arthropod vectors was visualized (e.g. *Babesia* parasites in ticks, *Plasmodium* parasites in mosquitoes, *Trypanosoma* parasites in tsetse flies and blood-sucking bugs and *Leishmania* parasites in sand flies)[45].

The knowledge gained by detecting parasite transmission has formed the basis for many of the preventive measures that are available nowadays (Figure I). For example:

- Safe water, sanitation and hygiene (WASH) activities to prevent the release of parasitic eggs into the environment[46].
- Promoting awareness of how to handle potentially infected food to prevent food-borne parasite transmission[47].
- Increasing access to footwear to prevent soil-borne parasite transmission[48].
- Using insect repellants and nets to reduce vector exposure[49].

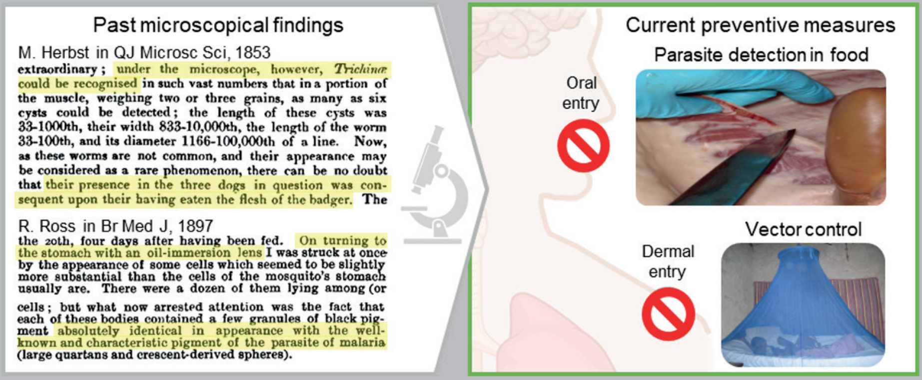

M. Herbst in QJ Microsc Sci, 1853

extraordinary; under the microscope, however, *Trichinæ* could be recognised in such vast numbers that in a portion of the muscle, weighing two or three grains, as many as six cysts could be detected; the length of these cysts was 33-1000th, their width 833-10,000th, the length of the worm 33-100th, and its diameter 1166-100,000th of a line. Now, as these worms are not common, and their appearance may be considered as a rare phenomenon, there can be no doubt that their presence in the three dogs in question was consequent upon their having eaten the flesh of the badger. The

R. Ross in Br Med J, 1897

the 20th, four days after having been fed. On turning to the stomach with an oil-immersion lens I was struck at once by the appearance of some cells which seemed to be slightly more substantial than the cells of the mosquito's stomach usually are. There were a dozen of them lying among (or

cells; but what now arrested attention was the fact that each of these bodies contained a few granules of black pigment absolutely identical in appearance with the well-known and characteristic pigment of the parasite of malaria (large quartans and crescent-derived spheres).

Figure I Past microscopical findings have formed the basis for the current preventive measures.

Because multiple parasites enter the human body via the skin, which can be easily imaged, thus far many *in vivo* imaging studies that involved real-time tracking of parasites have focused on the skin stage of parasitic infections (Figure 3, 4). These studies have uncovered important invasion mechanisms. For example, it was initially assumed that most *Plasmodium* parasites were directly inoculated into the capillaries present in the skin, while imaging studies revealed that significant numbers of them reside in avascular tissue[50-52]. Also, *Leishmania* parasites were found to be phagocytosed by immune cells infiltrating the bite site because of the bite of the vector[53-55]. Microscopic tracking of helminths that use the transdermal route to enter their host, revealed that infective larvae can respond to stimuli like chemical cues, water turbulence and temperature to increase their chances for successful host skin penetration[56-58]. These studies have also enabled assessment of time taken to invade and investigation of invasion which uncovered the process by which schistosomes lose their tail and surface glycocalyx and release excretory/secretory molecules (which are potent stimulants of innate immune cells) as they enter the skin [59, 60]. Together, these imaging studies focusing on the host entrance of parasites have revealed that the skin is an important anatomical reservoir and immune sentinel site for these parasitic infections, which are valuable insights for vaccine design.

Next to the skin, tracking of individual parasites in other organs has also led to an increased understanding of organ-specific parasitism and development. For example, intravital imaging of the liver revealed that *Plasmodium* sporozoites use several pathways to reach hepatocytes, rather than only passing through the Kupffer cells as the earlier accepted model proposed [61]. Also, *Trypanosoma* parasites have been found inside the brain parenchyma within hours after entering the bloodstream, which was assumed only to happen at the final stages of the disease[62, 63]. For schistosomes, imaging revealed that schistosomula migration in the lungs and liver is restricted to the vascular system, solving the question of whether or not extravascular routes exist and that eggs lodge in the venule part of the intestinal vasculature (and dependent on the species, also the urogenital vasculature) and can subsequently pass through the vessel wall[64]. The mechanisms behind the processes described in this paragraph serve as a potential target for drugs and vaccines[65], because blocking these essential mechanisms may prevent the establishment of a full-blown infection.

Despite successes in imaging of parasites in specific organs, real-time imaging of parasites during their dissemination throughout the human body has not been performed yet, due to technical challenges (except recently in the transparent zebrafish model[66]). However, bioluminescence imaging of the total parasite load in animal models such as mice has aided our understanding of parasite dissemination (Figure 4AB). For example, bioluminescence-based imaging of the total parasite load has played a key role in understanding the differential spread of parasites in cutaneous leishmaniasis versus visceral leishmaniasis[67, 68]. Another example of insight into parasite dissemination is the testis tropism of *Trypanosoma brucei* parasites, which might be of importance considering the role of the blood-testis barrier in determining drug efficacy[69]. More importantly, the presence of parasitized red blood cells in the brain of mice was identified as crucial for the onset of experimental cerebral malaria, the most severe complication of infection with *Plasmodium* parasites[70]. Together, these imaging studies have brought parasite migration into the limelight as a potential target for new drugs and vaccines. For *Plasmodium falciparum* malaria, these findings were translated to potential novel therapeutics with the visualization of a direct inhibitory effect of circulating antibodies targeting parasite motility[71].

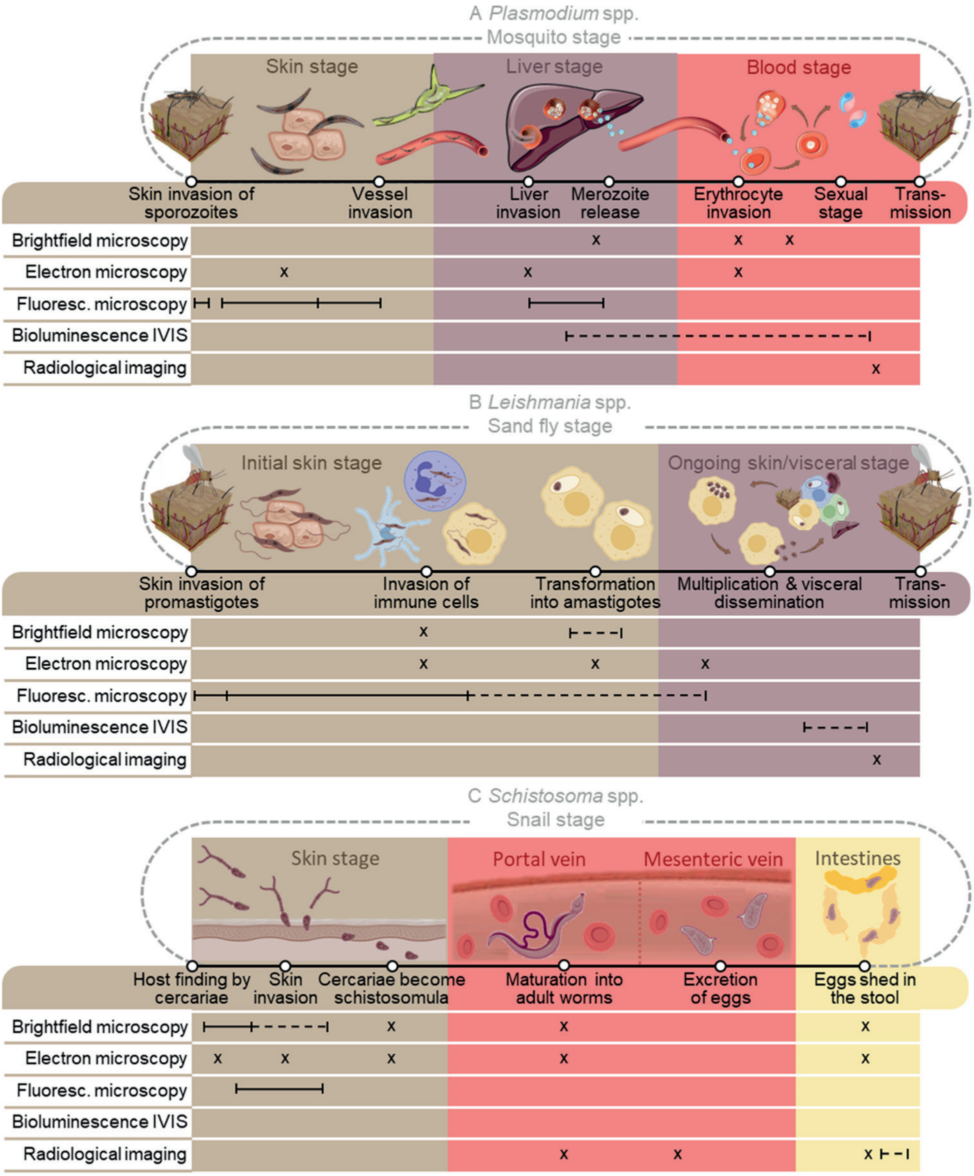

Figure 4 Imaging of parasitic life cycles. The life cycles of *Plasmodium* spp. (A), *Leishmania* spp. (B) and *Schistosoma* spp. (C) are schematically depicted (top). Imaging modalities used to visualize parasites are indicated (left) and their particular role within visualizing the parasite life cycle is highlighted for a single timepoint (x), for recording a time-lapse (- -) or for real-time tracking (—). For the creation of this figure content form BioRender.com has been used.

The majority of *in vivo* imaging studies regarding parasites make use of transgenic protozoa lines that express fluorophores or luciferase[72]. Unfortunately, the difficulties with transfecting multicellular organisms to obtain stable reporter lines have slowed down the progress made in intravital imaging of helminths. The first transgenic helminths expressing reporter proteins have been documented; however, stable transgenic lines suitable for *in vivo* tracking are not available yet[73, 74]). Thus, most of the recent *in vivo* imaging studies regarding helminths make use of larvae that are labeled *ex vivo* with fluorescent dyes and subsequently detected in specific organs of their (intermediate) host[60, 75, 76]. To study their dissemination through the host the development of radiotracers could provide a solution. Although not applied in the field of parasitology yet, tracking of low numbers of cells migrating throughout the body is achieved in other research fields using the sensitivity, quantifiability and tissue penetration capacity of radioactivity[77, 78]. A suitable radiolabeling method would facilitate *in vivo* study of migration and development of helminths (and protozoa) without the need for transgenic lines.

Collectively, different imaging modalities have been applied to track protozoa such as *Plasmodium* and *Leishmania* species (Figure 4AB) and a few helminths such as schistosomes (Figure 4C) during their journey through the body. These studies can provide insights needed for the development of new drugs, vaccines and preventive measures. Unfortunately, there are only a few imaging studies investigating other parasite species beyond those listed. The progress made so far demonstrates the potential of what can be achieved for other parasite species in the future.

Imaging of parasite migration to test the efficacy of potential antiparasitic strategies

Over the past years, imaging-based approaches have played an increasingly important role in the screening of novel antiparasitic compounds. For example, imaging-based models that enable monitoring of schistosome skin invasion have been used to test compounds potentially having schistosome cercariae anti-penetrant properties (repellent, barrier or cercaricide); for example DEET formulations, dimethicone-based barrier creams and topical applied chemicals such as niclosamide[79]. Several of these compounds have now shown to prevent schistosomiasis in clinical (field) trials[80]. Similarly, transmission of vector-borne protozoa such as *Plasmodium* and *Leishmania* parasites has been visualized in rodent models using confocal imaging of transgenic parasites expressing a fluorophore. *Plasmodium* sporozoites have been followed from the mosquito salivary cavities, through the salivary ducts, into the skin, pointing out that motility is crucial within the vector and thereby a potential target for transmission-blocking compounds[81]. To assess the transmission reducing activity of new antimalarial drug candidates, a standard membrane feeding assay is used; mosquitoes are fed with infected blood including the compound of interest and subsequently imaged by brightfield/fluorescence microscopy or by a bioluminescence-based imaging system to check for transmission events[82]. Similar assays for other vector-borne parasites do not exist yet, but may have applications for parasites such as trypanosomes. Together, these imaging-based setups to study parasite transmission offer a platform that supports the discovery of transmission blocking compounds needed as part of a strategy to prevent parasitic infections (Figure 5A).

To screen compound libraries for the identification of compounds with antiparasitic properties *in vitro* imaging-based screening platforms have been developed (Figure 5B). Screening of already approved drugs, aiming at repurposing them (while avoiding expensive approval procedures) seems an especially promising strategy given the low commercial attractiveness of developing new drugs for most parasitic diseases. The effect of compounds has commonly been assessed by manual scoring of viability using brightfield microscopy[83, 84]. This has recently been replaced by automated image analysis based on video recordings of parasite motility and the uptake of fluorescent viability dyes to generate more high-throughput screening assays[85-87]. For example, using an imaging-based screening assay, the compound tolfenpyrad, which nearly completely reduced the motility of third-stage *Haemonchus contortus* larvae (ruminant helminth), was identified[88]. Several reviews have provided an overview of the compounds with anthelmintic or antiprotozoal properties identified by imaging-based screening of compound libraries[89-91].

Following *in vitro* identification of antiparasitic drug and vaccine candidates, imaging also plays a role in the *in vivo* characterization of their effect (Figure 5B). Regarding helminths, testing new drug or vaccine candidates involves microscopical assessment of the worm burden after sacrificing the animal. For instance, this approach was used to validate the *in vitro* anti-schistosomal activity of hydroxyquinoline derivatives in a mouse model and to evaluate recombinant hookworm antigens as vaccine candidates in a hamster model[95, 96]. In contrast, the availability of transgenic reporter lines of protozoa has facilitated the *in vivo* monitoring of the temporal dynamics of the effect of, for example anti-trypanosomal compounds and anti-leishmanial compounds[92, 97-99]. Moreover, bioluminescence-based monitoring in mice has been applied to assess the protective efficacy of immunization with genetically attenuated *Plasmodium* parasites with complete late liver stage arrest, which are currently in clinical trial[100, 101]. Taken together, imaging technology can play an indispensable role in the preclinical phase of the development of drugs, vaccines and preventive measures.

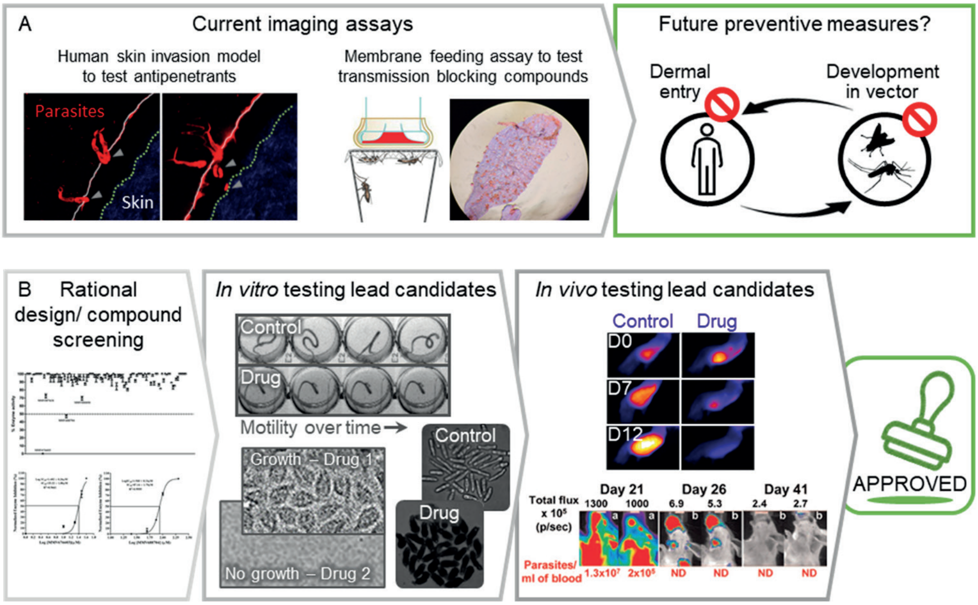

Figure 5 Preclinical testing the efficacy of antiparasitic strategies. A) The currently available imaging assays (grey panel) to study parasite transmission and the effect of potential transmission blockers aimed at the development of new preventive measures (green panel). B) A workflow diagram summarizing the drug/vaccine discovery process. After rational design or compound screening, the second and third panel give examples of how imaging technologies can be used for the *in vitro* and *in vivo* testing of lead compounds, respectively. The images used as examples were adapted from: [39, 85, 92-94].

CONCLUDING REMARKS

Implementation of IHC and automated image acquisition/interpretation are potential approaches to improve microscopy-based parasitological diagnostics. We envisage that further implementation can be boosted by leveraging the experience available in other biomedical fields, while keeping in mind the importance of cost reduction. When innovation in divergent areas (imaging hardware, staining methods, computer vision etc.) occurs in alignment, it may be mutually reinforcing and lead towards the widespread availability of improved affordable diagnostic approaches.

A growing number of *in vitro* and *in vivo* screening approaches relying on imaging of parasites has become available, suitable for identifying antiparasitic compounds and validating the efficacy of potential drug/vaccine candidates. We expect that *in vivo* tracking of parasites can also point towards targets for rational design of antiparasitic strategies by unraveling mechanisms essential for parasite survival that can be translated into suitable targets. The development of radiotracers for *in vivo* tracking of parasites might even pave the way towards obtaining such insights in controlled human infection studies (see Outstanding Questions).

OUTSTANDING QUESTIONS

- The low-cost widespread availability of brightfield microscopy often outweighs the application of novel molecular (imaging) tools in low- and middle-income countries. Can technical innovations at the hardware site aimed at improved accessibility tip the scale?
- How can the experience available in the field of oncology regarding the use of immunohistochemistry and computer vision be leveraged for application in diagnostics for parasitic infections?
- How can innovation in divergent areas (imaging hardware, staining methods, computer vision etc.) be coordinated to assure a better linkage that makes advances in different areas mutually reinforcing?
- Which so far unknown parasite reservoirs would we encounter in the human body if we could follow individual parasites on all potential paths through the host?
- How can we ensure that fundamental insights in parasite migration obtained by imaging translate into the identification of a suitable target for antiparasitic strategies?
- Can the development of radiotracers suitable to label helminths provide a means to study their dissemination bypassing the difficulties with the generation of transgenic lines that are used so far to study the dissemination of protozoa?

Acknowledgments: We would like to thank Eric Brienen for contributing to Figure 3.

REFERENCES

1. Van Lieshout, L. and M. Roestenberg, Clinical consequences of new diagnostic tools for intestinal parasites. Clinical Microbiology and Infection, 2015. 21(6): p. 520-528.
2. Ordonez, A.A., et al., Molecular imaging of bacterial infections: Overcoming the barriers to clinical translation. Science translational medicine, 2019. 11(508): p. eaax8251.
3. Rowe, S.P. and M.G. Pomper, Molecular imaging in oncology: Current impact and future directions. CA: a cancer journal for clinicians, 2022. 72(4): p. 333-352.
4. De Niz, M., et al., Toolbox for in vivo imaging of host–parasite interactions at multiple scales. Trends in parasitology, 2019. 35(3): p. 193-212.
5. Greani, S., Y. Quilichini, and B. Marchand, Ultrastructural study of vitellogenesis and oogenesis of Crepidostomum metoecus (Digenea, Allocreadiidae), intestinal parasite of Salmo trutta (Pisces, Teleostei). Parasite, 2016. 23.
6. Vendiš, T. Axial slice of abdomen, image was acquired by 3T NMR. 2011; Available from: https://commons.wikimedia.org/w/index.php?curid=13303937.
7. Mahmud, R., Y.A.L. Lim, and A. Amir, Medical parasitology. Cham, Switzerland: Springer International Publishing. doi: 0.1007/978-3-319-68795-7, 2017.
8. Gwanzura, L., et al., Evaluation of "Cyscope", a novel fluorescence-based microscopy technique for the detection of malaria. The Journal of Infection in Developing Countries, 2012. 6(02): p. 212-215.
9. Carnero, P.R., et al., Unexpected hosts: imaging parasitic diseases. Insights into Imaging, 2017. 8(1): p. 101-125.
10. Trampuz, A., et al., Clinical review: Severe malaria. Critical Care, 2003. 7(4): p. 315-323.
11. Ngwese, M.M., et al., Diagnostic Techniques of Soil-Transmitted Helminths: Impact on Control Measures. Tropical Medicine and Infectious Disease, 2020. 5(2).
12. Cringoli, G., et al., FLOTAC: new multivalent techniques for qualitative and quantitative copromicroscopic diagnosis of parasites in animals and humans. Nature Protocols, 2010. 5(3): p. 503-515.
13. Chalmers, R.M., et al., Parasite detection in food: Current status and future needs for validation. Trends in Food Science & Technology, 2020. 99: p. 337-350.
14. Hanscheid, T., J.M. Cristino, and M. Salgado, Screening of auramine-stained smears of all fecal samples is a rapid and inexpensive way to increase the detection of coccidial infections. International journal of infectious diseases, 2008. 12(1): p. 47-50.
15. Chagas, C.R.F., et al., The buffy coat method: a tool for detection of blood parasites without staining procedures. Parasites & Vectors, 2020. 13(1).
16. Kochareka, M., et al., A preliminary comparative report of quantitative buffy coat and modified quantitative buffy coat with peripheral blood smear in malaria diagnosis. Pathogens and Global Health, 2012. 106(6): p. 335-339.
17. Mungenast, F., et al., Next-generation digital histopathology of the tumor microenvironment. Genes, 2021. 12(4): p. 538.
18. Saïdi, N., et al., Imaging Leishmania major Antigens in Experimentally Infected Macrophages and Dermal Scrapings from Cutaneous Leishmaniasis Lesions in Tunisia. Microorganisms, 2022. 10(6): p. 1157.
19. Reinehr, M., et al., Pathology of echinococcosis: a morphologic and immunohistochemical study on 138 specimens with focus on the differential diagnosis between cystic and alveolar echinococcosis. The American Journal of Surgical Pathology, 2020. 44(1): p. 43-54.
20. Li, X., et al., A comprehensive review of computer-aided whole-slide image analysis: from datasets to feature extraction, segmentation, classification and detection approaches. Artificial Intelligence Review, 2022: p. 1-70.
21. Fernández-Rivas, G., et al., Automated parasitological diagnosis in clinical microbiology laboratories. Scientific Reports, 2021. 11(1): p. 1-6.
22. Nkamgang, O.T., et al., Automating the clinical stools exam using image processing integrated in an expert system. informatics in Medicine Unlocked, 2019. 15: p. 100165.
23. Mathison, B.A., et al., Detection of Intestinal Protozoa in Trichrome-Stained Stool Specimens by Use of a Deep Convolutional Neural Network. Journal of Clinical Microbiology, 2020. 58(6).
24. Poostchi, M., et al., Image analysis and machine learning for detecting malaria. Translational

Research, 2018. 194: p. 36-55.
25. Birhanie, M., Comparison of Partec rapid malaria test with conventional light microscopy for diagnosis of malaria in Northwest Ethiopia. Journal of parasitology research, 2016.
26. Mbohou Nchetnkou, C., et al., Comparison of the fluorescence microscopy Cyscope® with light microscopy for malaria diagnosis in a small and active surveillance in Cameroon. Tropical Medicine and Health, 2020. 48(1): p. 1-10.
27. Kamgno, J., et al., A test-and-not-treat strategy for onchocerciasis in Loa loa–endemic areas. New England Journal of Medicine, 2017. 377(21): p. 2044-2052.
28. Meulah, B., et al., Performance Evaluation of the Schistoscope 5.0 for (Semi-) automated Digital Detection and Quantification of Schistosoma haematobium Eggs in Urine: A Field-based Study in Nigeria. The American Journal of Tropical Medicine and Hygiene, 2022: p. tpmd220276-tpmd220276.
29. Capewell, P., et al., The skin is a significant but overlooked anatomical reservoir for vector-borne African trypanosomes. Elife, 2016. 5.
30. Trindade, S., et al., Trypanosoma brucei Parasites Occupy and Functionally Adapt to the Adipose Tissue in Mice. Cell Host & Microbe, 2016. 19(6): p. 837-848.
31. Camara, M., et al., Extravascular dermal trypanosomes in suspected and confirmed cases of gambiense human African trypanosomiasis. Clinical Infectious Diseases, 2021. 73(1): p. 12-20.
32. Fritzsche, C., et al., Confocal Laser Scanning Microscopy, a New In Vivo Diagnostic Tool for Schistosomiasis. Plos One, 2012. 7(4).
33. Croese, J. and R. Speare, Intestinal allergy expels hookworms: seeing is believing. Trends in Parasitology, 2006. 22(12): p. 547-550.
34. Siddiqui, M.F., A.W. Reza, and J. Kanesan, An automated and intelligent medical decision support system for brain MRI scans classification. PloS one, 2015. 10(8): p. e0135875.
35. Lindner, T., et al., Anatomical MRI and [18F] FDG PET/CT imaging of Schistosoma mansoni in a NMRI mouse model. Scientific Reports, 2020. 10(1): p. 1-11.
36. WHO, Global atlas of medical devices. 2017.
37. Belard, S., et al., Review Article: Point-of-Care Ultrasound Assessment of Tropical Infectious Diseases-A Review of Applications and Perspectives. American Journal of Tropical Medicine and Hygiene, 2016. 94(1): p. 8-21.
38. Mankoff, D.A., et al., Making molecular imaging a clinical tool for precision oncology: a review. JAMA oncology, 2017. 3(5): p. 695-701.
39. Salem, N., et al., In Vivo Imaging of Schistosomes to Assess Disease Burden Using Positron Emission Tomography (PET). Plos Neglected Tropical Diseases, 2010. 4(9).
40. Weissleder, R., Molecular imaging in cancer. Science, 2006. 312(5777): p. 1168-1171.
41. Othman, A.S., et al., The use of transgenic parasites in malaria vaccine research. Expert review of vaccines, 2017. 16(7): p. 685-697.
42. Husson, S.J., et al., Keeping track of worm trackers. WormBook: The Online Review of C. elegans Biology [Internet], 2018.
43. Winkel, B.M.F., et al., A tracer-based method enables tracking of Plasmodium falciparum malaria parasites during human skin infection. Theranostics, 2019. 9(10): p. 2768-2778.
44. Grove, D.I., History of human helminthology. 1990: CAB International.
45. Cox, F.E.G., History of the discovery of the malaria parasites and their vectors. Parasites & Vectors, 2010. 3.
46. Nery, S.V., et al., The role of water, sanitation and hygiene interventions in reducing soil-transmitted helminths: interpreting the evidence and identifying next steps. Parasites & Vectors, 2019. 12.
47. FAO, Parasites in Foods: An Invisible Threat. 2021, Food and Agriculture Organization of the United Nations Bangkok, Thailand.
48. Tomczyk, S., et al., Association between Footwear Use and Neglected Tropical Diseases: A Systematic Review and Meta-Analysis. Plos Neglected Tropical Diseases, 2014. 8(11).
49. Chan, E.Y.Y., et al., Narrative Review on Health-EDRM Primary Prevention Measures for Vector-Borne Diseases. International Journal of Environmental Research and Public Health, 2020. 17(16).
50. Amino, R., et al., Quantitative imaging of Plasmodium transmission from mosquito to mammal. Nature medicine, 2006. 12(2): p. 220-224.
51. de Korne, C., et al., Clustering and erratic movement patterns of syringe-injected versus

mosquito-inoculated malaria sporozoites underlie decreased infectivity. Msphere, 2021. 6(2): p. e00218-21.
52. Hopp, C.S., et al., Longitudinal analysis of Plasmodium sporozoite motility in the dermis reveals component of blood vessel recognition. Elife, 2015. 4.
53. Beattie, L. and P.M. Kaye, Leishmania-host interactions: what has imaging taught us? Cellular Microbiology, 2011. 13(11): p. 1659-1667.
54. Forestier, C.L., et al., Imaging Host Cell-Leishmania Interaction Dynamics Implicates Parasite Motility, Lysosome Recruitment, and Host Cell Wounding in the Infection Process. Cell Host & Microbe, 2011. 9(4): p. 319-330.
55. Peters, N.C., et al., In vivo imaging reveals an essential role for neutrophils in leishmaniasis transmitted by sand flies. Science, 2008. 321(5891): p. 970-974.
56. Bryant, A.S., et al., A Critical Role for Thermosensation in Host Seeking by Skin-Penetrating Nematodes. Current Biology, 2018. 28(14): p. 2338-+.
57. Haas, W., Parasitic worms: strategies of host finding, recognition and invasion. Zoology, 2003. 106(4): p. 349-364.
58. Nguyen, K., B. Gemmell, and J. Rohr, Effects of temperature and viscosity on miracidial and cercarial movement of Schistosoma mansoni: ramifications for disease transmission. International journal for parasitology, 2020. 50(2): p. 153-159.
59. Paveley, R.A., et al., Fluorescent Imaging of Antigen Released by a Skin-Invading Helminth Reveals Differential Uptake and Activation Profiles by Antigen Presenting Cells. Plos Neglected Tropical Diseases, 2009. 3(10).
60. Winkel, B.M.F., et al., Early Induction of Human Regulatory Dermal Antigen Presenting Cells by Skin-Penetrating Schistosoma Mansoni Cercariae. Frontiers in Immunology, 2018. 9.
61. Tavares, J., et al., Role of host cell traversal by the malaria sporozoite during liver infection. Journal of Experimental Medicine, 2013. 210(5): p. 905-915.
62. Caljon, G., et al., The Dermis as a Delivery Site of Trypanosoma brucei for Tsetse Flies. Plos Pathogens, 2016. 12(7).
63. Frevert, U., et al., Early Invasion of Brain Parenchyma by African Trypanosomes. Plos One, 2012. 7(8).
64. Nation, C.S., et al., Schistosome migration in the definitive host. Plos Neglected Tropical Diseases, 2020. 14(4).
65. Aliprandini, E., et al., Cytotoxic anti-circumsporozoite antibodies target malaria sporozoites in the host skin. Nature Microbiology, 2018. 3(11): p. 1224-1233.
66. Doro, E., et al., Visualizing trypanosomes in a vertebrate host reveals novel swimming behaviours, adaptations and attachment mechanisms. Elife, 2019. 8.
67. Calvo-Alvarez, E., et al., A new chimeric triple reporter fusion protein as a tool for in vitro and in vivo multimodal imaging to monitor the development of African trypanosomes and Leishmania parasites. Infection, Genetics and Evolution, 2018. 63: p. 391-403.
68. Melo, G.D., et al., New insights into experimental visceral leishmaniasis: Real-time in vivo imaging of Leishmania donovani virulence. PLoS neglected tropical diseases, 2017. 11(9): p. e0005924.
69. Claes, F., et al., Bioluminescent Imaging of Trypanosoma brucei Shows Preferential Testis Dissemination Which May Hamper Drug Efficacy in Sleeping Sickness. Plos Neglected Tropical Diseases, 2009. 3(7).
70. Baptista, F.G., et al., Accumulation of Plasmodium berghei-Infected Red Blood Cells in the Brain Is Crucial for the Development of Cerebral Malaria in Mice. Infection and Immunity, 2010. 78(9): p. 4033-4039.
71. Gaudinski, M.R., et al., A Monoclonal Antibody for Malaria Prevention. New England Journal of Medicine, 2021. 385(9): p. 803-814.
72. Novobilsky, A. and J. Hoglund, Small animal in vivo imaging of parasitic infections: A systematic review. Experimental Parasitology, 2020. 214.
73. Kines, K.J., et al., Integration of reporter transgenes into Schistosoma mansoni chromosomes mediated by pseudotyped murine leukemia virus. The FASEB Journal, 2008. 22(8): p. 2936-2948.
74. Shao, H., et al., Transposon-mediated chromosomal integration of transgenes in the parasitic nematode Strongyloides ratti and establishment of stable transgenic lines. 2012.
75. Kolbekova, P., et al., Imaging of Toxocara canis larvae labelled by CFSE in BALB/c mice.

Parasitology Research, 2011. 108(4): p. 1007-1014.
76. Wang, S., et al., Construction of in vivo fluorescent imaging of Echinococcus granulosus in a mouse model. The Korean Journal of Parasitology, 2016. 54(3): p. 291.
77. Perrin, J., et al., Cell tracking in cancer immunotherapy. Frontiers in Medicine, 2020. 7: p. 34.
78. Rodriguez-Porcel, M., et al., Cell tracking and the development of cell-based therapies: a view from the Cardiovascular Cell Therapy Research Network. JACC: Cardiovascular Imaging, 2012. 5(5): p. 559-565.
79. Downs, P.W., et al., New tools for the schistosomiasis elimination toolbox: Barriers and opportunities for the development of a topical cercarial anti-penetrant. 2017.
80. Ramaswamy, K., et al., Topical application of DEET for schistosomiasis. Trends in Parasitology, 2003. 19(12): p. 551-555.
81. Frischknecht, F., et al., Imaging movement of malaria parasites during transmission by Anopheles mosquitoes. Cellular Microbiology, 2004. 6(7): p. 687-694.
82. Wadi, I., et al., Malaria transmission-blocking drugs: implications and future perspectives. Future Medicinal Chemistry, 2020. 12(11): p. 1071-1101.
83. Douglas, R.G., et al., Screening for potential prophylactics targeting sporozoite motility through the skin. Malaria Journal, 2018. 17.
84. Paveley, R.A. and Q.D. Bickle, Automated Imaging and other developments in whole-organism anthelmintic screening. Parasite Immunology, 2013. 35(9-10): p. 302-313.
85. Chen, S., et al., A multi-dimensional, time-lapse, high content screening platform applied to schistosomiasis drug discovery. Communications Biology, 2020. 3(1).
86. Storey, B., et al., Utilization of computer processed high definition video imaging for measuring motility of microscopic nematode stages on a quantitative scale: “The Worminator’’. International Journal for Parasitology-Drugs and Drug Resistance, 2014. 4(3): p. 233-243.
87. Kanatani, S., et al., Screening the pathogen box for inhibition of Plasmodium falciparum sporozoite motility reveals a critical role for kinases in transmission stages. Antimicrobial agents and chemotherapy, 2022. 66(9): p. e00418-22.
88. Preston, S., et al., Screening of the ‘Pathogen Box’ identifies an approved pesticide with major anthelmintic activity against the barber’s pole worm. International Journal for Parasitology-Drugs and Drug Resistance, 2016. 6(3): p. 329-334.
89. Muller, J. and A. Hemphill, Drug target identification in protozoan parasites. Expert Opinion on Drug Discovery, 2016. 11(8): p. 815-824.
90. Partridge, F.A., et al., Anthelmintic drug discovery: target identification, screening methods and the role of open science. Beilstein Journal of Organic Chemistry, 2020. 16: p. 1203-1224.
91. Rana, A.K. and S. Misra-Bhattacharya, Current drug targets for helminthic diseases. Parasitology Research, 2013. 112(5): p. 1819-1831.
92. Myburgh, E., et al., In Vivo Imaging of Trypanosome-Brain Interactions and Development of a Rapid Screening Test for Drugs against CNS Stage Trypanosomiasis. Plos Neglected Tropical Diseases, 2013. 7(8).
93. Partridge, F.A., et al., Dihydrobenz [e][1, 4] oxazepin-2 (3 H)-ones, a new anthelmintic chemotype immobilising whipworm and reducing infectivity in vivo. PLoS neglected tropical diseases, 2017. 11(2): p. e0005359.
94. Bharti, H., et al., Repurposing the Pathogen Box compounds for identification of potent antimalarials against blood stages of Plasmodium falciparum with PfUCHL3 inhibitory activity. Scientific reports, 2022. 12(1): p. 1-16.
95. Allam, G., A.F. Eweas, and A.S.A. Abuelsaad, In vivo schistosomicidal activity of three novels 8-hydroxyquinoline derivatives against adult and immature worms of Schistosoma mansoni. Parasitology Research, 2013. 112(9): p. 3137-3149.
96. Xiao, S., et al., The evaluation of recombinant hookworm antigens as vaccines in hamsters (Mesocricetus auratus) challenged with human hookworm, Necator americanus. Experimental Parasitology, 2008. 118(1): p. 32-40.
97. Canavaci, A.M.C., et al., In Vitro and In Vivo High-Throughput Assays for the Testing of Anti-Trypanosoma cruzi Compounds. Plos Neglected Tropical Diseases, 2010. 4(7).
98. Caridha, D., et al., Use of Optical Imaging Technology in the Validation of a New, Rapid, Cost-Effective Drug Screen as Part of a Tiered In Vivo Screening Paradigm for Development of Drugs To

Treat Cutaneous Leishmaniasis. Antimicrobial Agents and Chemotherapy, 2017. 61(4).
99. Rice, D.R., et al., Zinc(II)-Dipicolylamine Coordination Complexes as Targeting and Chemotherapeutic Agents for Leishmania major. Antimicrobial Agents and Chemotherapy, 2016. 60(5): p. 2932-2940.
100. Franke-Fayard, B., et al., Creation and preclinical evaluation of genetically attenuated malaria parasites arresting growth late in the liver. NPJ vaccines, 2022. 7(1): p. 1-17.
101. Vaughan, A.M., et al., A Plasmodium parasite with complete late liver stage arrest protects against preerythrocytic and erythrocytic stage infection in mice. Infection and immunity, 2018. 86(5): p. e00088-18.

8

Summarizing discussion and future perspectives

INTRODUCTION

In this thesis the development and application of quantitative imaging-based assays suitable to study parasite migration have been described that aimed to support the development of antiparasitic vaccines needed to reduce the global disease burden caused by parasitic infections (Figure 1). In this final chapter key concepts from this thesis will be discussed:

1. SMOOT (Sporozoite Motility Orienting and Organizing Tool) was developed and established as a quantitative software analysis tool for tracking the migration of malaria sporozoites *in vitro* and in human skin explant. This tool provided a readout with high kinematic detail, enabling the quantitative characterization of novel factors influencing the migration capability of malaria sporozoites (**chapter 1-4**).
2. A hybrid tracer labeling approach for parasites was developed which yielded viable parasites that were both fluorescently and radioactively labeled. With this approach the *in vivo* dissemination of malaria sporozoites could be revealed and human skin invasion behavior of helminths was monitored in both a qualitative and quantitative way (**chapter 5-6**).
3. By imaging the migration of parasites, insights were gained into questions that have arisen during the development of malaria vaccines, and the broader potential for imaging technology to advance the development of new diagnostic methods, therapeutic interventions and vaccines for combating parasitic infections was discussed. (**chapter 1-7**).

In this chapter, the development of new building blocks for quantitative imaging-based assays suitable to study parasite migration will be discussed, covering the first two novel concepts. The second part of this chapter will focus on the application of quantitative imaging-based assays in exploring questions related to malaria vaccine development, covering the third concept.

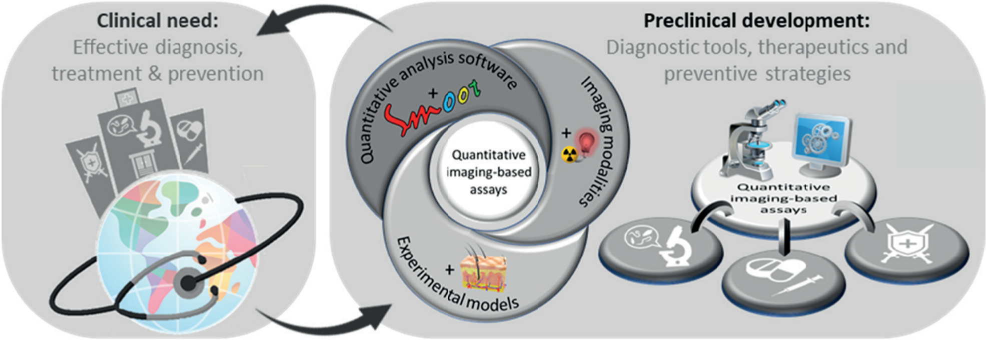

Figure 1 Schematic representation of the interaction between clinical need and preclinical development. The interaction is shown between the clinical need (left panel) for diagnostic methods, therapeutics and preventive measures to combat parasitic infections and the preclinical use of quantitative imaging-based assays (right panel) to help fulfil this need. The three elements of quantitative imaging-based assays are shown on the right panel: quantitative analysis software, imaging modalities and experimental models. In this thesis three building blocks were added; the software analysis tool SMOOT to quantitatively analyze parasite migration, a radiolabeling suitable for parasites and human skin explant as an experimental model.

DEVELOPMENT OF QUANTITATIVE IMAGING-BASED ASSAYS

Towards quantitative microscopical analysis of parasite migration

Optical microscopy is the most commonly used imaging technique for visualizing parasites and also the imaging technique most used in this thesis (**chapter 1-6**). Historically, optical microscopy has been considered a qualitative observational technique. However, advances in camera technology and imaging analysis software have increasingly enabled the extraction of quantitative data from images[1]. At the interface of software engineering and biomedical imaging, optical microscopy can be transformed into a quantitative observational technique. Our interdisciplinary environment enabled us to develop SMOOT (Sporozoite Motility Orienting and Organizing Tool), a software analysis tool for automatically tracking sporozoites by fluorescence microscopy. This tool provided a quantitative assessment of malaria sporozoite migration *in vitro* and in (human) skin tissue (**chapter 1-2**). Previous studies on sporozoite motility were mainly *in vitro* studies using qualitative or semi-quantitative readouts[2-4]. Only recently, the use of projections of time-lapse videos of moving sporozoites has been used to replace the post hoc staining of sporozoite trails[5, 6]. SMOOT increased the level of kinematic detail, revealing that a complex interplay of different (macro) molecules balances strong attachment and fast detachment needed for forward locomotion (**chapter 1**). The few studies that have assessed sporozoite migration *in vivo* (in a murine model), described sporozoite migration in terms borrowed from diffusion physics (e.g. velocity and mean squared displacement)[7, 8]. However, as sporozoites purposely migrate through tissue, we included measures of directional movement such as path tortuosity measures (e.g. straightness index and angular dispersion[9]) to describe the movement patterns of sporozoites. This increased level of detail proved to be valuable to reveal for example the impact of radiation attenuation on sporozoite directionality (**chapter 2**).

> At the interface of software engineering and biomedical imaging, optical microscopy can be transformed into a quantitative observational technique

Various aspects of sporozoite migration can be assessed independently, however together they can provide a multidimensional comprehension of sporozoite migration under different conditions. In **chapter 3**, we took the first steps in presenting a multidimensional view of sporozoite migration to describe the movement exhibited by sporozoites inoculated into the skin by mosquitoes versus sporozoites intradermally injected by needle. With the growing use of quantitative imaging assays to study sporozoite behavior, the volume and complexity of the data acquired will increase, which will in turn increase the need for comprehensive multidimensional data visualization. The recent advances in other biomedical fields (e.g. genomics and immunology) in exploring and visualizing large high-dimensional data sets may offer computational methods that can be adapted for the assessment of parasite behavior[10-12]. Taken together, quantitative microscopical imaging of parasite migration appeared at the interface of software engineering and biomedical imaging and needs an interdisciplinary environment for further development.

Expanding the imaging toolkit to enable visualization of *in vivo* parasite dissemination

Over the past years, a broad range of imaging modalities have become available for biomedical applications. Their characteristics determine their suitability and purpose within parasitology[13, 14]. For instance, in this thesis, fluorescent microscopy enabled real-time monitoring of individual sporozoites with a small field of view and subcellular resolution in skin tissue (**chapter 1-5**), while bioluminescence-based imaging enabled whole-body imaging of the total parasite load at a whole-organ resolution in mice two days post injection of sporozoites (**chapter 3**, **5**). In **chapter 5** and **6**, we aimed to develop the first radiotracer for parasites. It is remarkable that radiotracers suitable for parasites have not been developed yet, given the fact that they have proven to be of great value in other biomedical fields by virtue of the sensitivity, quantifiability and tissue penetration capacity of radioactivity[15]. In **chapter 5**, we developed the tracer ^{99m}Tc-Cy5-AmineC4.MAS$_3$-Methyl, which is suitable to radiolabel sporozoites and quantitatively assessing their biodistribution. The traditional methods to study sporozoite distribution (e.g. PCR or bioluminescence-based imaging) can be used to detect the large numbers of parasites which are obtained once the malaria parasite has replicated in the liver. However, these methods are not sensitive enough to monitor the distribution of the relative low number of malaria sporozoites towards different organs directly after infection[16, 17]. In **chapter 6**, we applied the radiotracer to radiolabel schistosomal and hookworm larvae and quantify their human skin invasion. So far, the human skin invasion rate of schistosomal larvae has only been indirectly estimated by counting the tails of the cercariae that were left behind during invasion, and for hookworm larvae it has not been assessed at all[18]. Further optimization of the radiolabeling approach is needed to obtain parasites containing larger amounts of radioactivity, which would pave the way towards whole-body longitudinal SPECT imaging of the dissemination of parasites in live animal models and potentially also in humans in the context of controlled human infection studies. Overall, with the development of a radiolabeling approach for parasites, we have expanded the imaging toolkit available for imaging parasite migration.

Although a broad range of imaging modalities is available, parasite samples are typically examined using only one imaging modality. Nevertheless, combining different imaging modalities and correlating their results would provide a more comprehensive (both structural and functional information) and multi-scale view (with high spatial/temporal resolution as well as a large field/depth of view) on parasite behavior. The tracer that we developed and used in **chapter 5** and **6** was a radiolabeled analogue of a fluorescent tracer. It contained both a radioisotope and a fluorophore, making it suitable for bimodal imaging. Especially in **chapter 6** the bimodal imaging approach was applied to its full advantage and allowed for detailed real-time monitoring of human skin invasion behavior of individual larvae as well as quantitative assessment of the total amount of invasion. So far, different multimodal imaging approaches have been developed for biomedical applications[14, 19, 20]. For example, correlative light and electron microscopy (CLEM), which combines optical and electron microscopy, has been developed. This approach can put the functional results obtained by optical microscopy in an ultrastructural context[21]. Adapting this approach to the imaging of sporozoite migration in skin could reveal the cellular context of the migrating sporozoites, which so far has remained a ‘black box’ in our studies. For *in vivo* studies, the most widely used multimodal approaches are PET/CT and SPECT/CT which offer integrated functional and anatomic whole-body imaging[22]. Taken together, both adding imaging modalities to the toolkit for parasite imaging and using them in a correlated multimodal imaging approach are means to support comprehensive assessment of parasite migration *in vivo*.

> Combining different imaging modalities can provide a more holistic and multiscale view of parasite behavior

Diversifying experimental models to better approach the human situation

We studied parasite migration in different experimental models, each of which has its own possibilities and limitations. In **chapter 2** and **4**, we have implemented the use of human skin explant to investigate the migration of malaria sporozoites in their natural human host environment. Until now, *in vivo* studies of sporozoite migration have been performed in animal, mainly mouse, models. Because of the differences between animal and human skin regarding physical and chemical properties, a human skin model is a valuable contribution to the available experimental models[23]. Comparing our data regarding the tortuosity of malaria sporozoite tracks obtained in mouse abdominal skin (**chapter 3**) and human abdominal skin (**chapter 2**), suggested that the differences between mouse and human skin induced differential movement patterns; sporozoites in human skin travelled along more straight lines compared to their counterparts in mouse skin. A human skin explant model represents part of the human environment, but since the skin is no longer connected to a living organism, sporozoites cannot leave the skin via the bloodstream as they normally would. Therefore, in **chapter 3** and **5**, we used a mouse model to be able to correlate findings from the skin and liver stage of infection and to track malaria sporozoites beyond the skin to other organs. To dissect the role of different factors which influence parasite migration inside their host separately, more simplified imaging-based *in vitro* models can be of value. In **chapter 1** and **4**, we have used an *in vitro* assay to specifically assess the effects of chemical stimuli and anti-CSP antibodies on sporozoite motility. Together, these examples illustrate how a variety of experimental models can complement each other since each of them is suited to answer different research questions.

> Experimental models can complement each other since each of them is suited to answer different research questions

The lack of coherence between the results of our *in vitro* and human skin explant models in **chapter 4** raises the question to which extent the results obtained with our different experimental models are representative for the human *in vivo* situation. While anti-CSP antibodies were able to completely block the motility of malaria sporozoite *in vitro*, they could not completely stop their migration in human skin. This question about coherence is linked to a broader challenge, generally acknowledged within the biomedical field; how to develop and validate experimental pre-clinical models with a high clinical predictive value[24, 25]. There are different criteria proposed according to which an experimental model can be validated[25]. An example is predictive validity; the criterium that the effects of an intervention in the human situation and in the experimental model should be comparable. We used that criterium in **chapter 3** where we first validated that the difference in infectivity between mosquito-inoculated and intradermal syringe-injected malaria sporozoites, which had been observed in humans[26, 27], also occurred in our mouse model. A second criterium is face validity; the closer the species used as a model is to humans, the better[28]. Besides the *ex vivo* use of human tissue as we describe in this thesis (**chapter 2**, **4**, **6**), recently, humanized mouse models have been developed for *in vivo* assessment of human malaria species[29, 30]. These models, although costly, combine the advantages of the use of an animal model and human tissue. Ideally, a preclinical assay can be validated using data from clinical studies. For example, when in addition to CIS43LS[31], more anti-CSP antibodies will be tested in future controlled human infection studies, their protective efficacy against a malaria infection can be compared to their IC_{50} value obtained with our assay, to assess the predictive value of the latter. Nonetheless, despite shortcomings, experimental models have been invaluable for parasitological research. A diverse range of experimental models can help to investigate different aspects of the human situation and together approach the clinical reality as good as possible.

APPLICATION OF QUANTITATIVE IMAGING OF PARASITE MIGRATION

Investigating questions raised during malaria vaccine development

In **chapter 1-3**, we gained insights into three aspects of live attenuated malaria sporozoite vaccination strategies that influence their efficacy: 1) the vaccine formulation (**chapter 1**), 2) radiation-attenuation of the sporozoites (**chapter 2**) and 3) the route of administration (**chapter 3**). We observed that after intradermal administration the injected liquid spreads through the skin and fills the interstitial space (**chapter 3**), impacting the chemical properties of the environment in which the sporozoites need to migrate. Combined with the *in vitro* findings described in **chapter 1** that different (macro) molecules regulate sporozoite motility, these findings suggest that it would be worthwhile to further investigate the *in vivo* effects of formulation on sporozoite migration. Adjusting the attenuated whole sporozoite vaccine formulation, which is currently only enriched with the motility-regulatory protein albumin[32], may provide a means to support attenuated sporozoites in reaching the liver after intradermal administration. In **chapter 2**, we showed that radiation-attenuation impairs the sporozoite's capability to migrate through human skin. Ideally, an optimal balance should be struck between sufficient attenuation to ensure safety and minimal impairment to support continuation of the first part of the life cycle needed to induce protective immunity. Besides radiation-attenuated, genetically attenuated sporozoites are also under clinical investigation[33]. This type of attenuation is likely to be better suited to generate sporozoites that can safely be used while still capable to completely accomplishing the intended part

> Quantitative imaging-based assays to study parasite migration can be used to investigate questions raised during clinical trials

of their life cycle in the host. In **chapter 3**, we examined the dermal site after sporozoite administration by syringe compared to mosquito inoculation. The differences found suggest that investigating engineering solutions that better mimic mosquito inoculation with regard to the volume and distribution of the sporozoite sample (e.g. a micro needle patch[34]) may provide a means to increase the efficacy of intradermally delivered attenuated whole sporozoite vaccines. Together, these examples reveal how quantitative imaging-based assays to study parasite migration can be used to investigate questions raised during clinical testing of vaccine candidates and can offer possibilities for further optimization of vaccine strategies.

Sporozoite migration plays a major role in the performance of the current malaria vaccine candidates

Since migration is crucial for sporozoites to continue their life cycle within the host, it not only influences the efficacy of live attenuated sporozoite vaccines, but also provides a potential target for malaria vaccines. In **chapter 4**, we showed that anti-CSP antibodies directly impact sporozoite motility both *in vitro* and in human skin. In the future, our quantitative imaging-based assay can be used as an additional tool to comprehensively assess the parasite inhibitory capacity of anti-CSP antibodies and potentially other antibodies targeting sporozoite motility. These antibodies become available in the context of clinical trials testing malaria vaccine candidates[35-37], and selecting the most efficacious ones can support optimization of subunit and passive immunization strategies.

In **chapter 1-4**, the migration capacity of sporozoites during the skin stage of the infection has been used as a readout to investigate factors that (may) impact the efficacy of attenuated whole sporozoite vaccine strategies, such as the vaccine formulation and the route of administration. In the future, this readout can be expanded with the assessment of the dissemination of sporozoites through the body, an approach developed in **chapter 5**. This would provide more information on how different vaccine strategies impact the spatial and temporal dynamics of sporozoite dissemination, which in turn would give insights into the parasite-host interactions that may take place and contribute to the overall immune response. Also, in this thesis and in most other imaging-based studies on *in vivo* parasite behavior, parasites are monitored without simultaneously visualizing their host environment (in high detail). This makes it challenging to explain observed parasite migration behavior in terms of parasite-host interactions. As a step in the right direction, brightfield imaging was used in **chapter 3** to visualize the cellular environment, revealing structural differences that correlated with differences in sporozoite migration patterns. However, interactions of sporozoites with host cells, such as dermal antigen-presenting cells like macrophages and dendritic cells, have only been studied *in vitro*[38]. Nevertheless, real-time *in vivo* imaging of the immune system is a rapidly emerging field and the first findings at the interface of *in vivo* immuno-imaging and parasitology have been reported[39, 40]. Combining real-time *in vivo* monitoring of parasites and immune cells would provide a means to deepen our understanding of where, when and how migrating (vaccine) parasites can interact with specific parts of the immune system. In conclusion, sporozoite migration throughout the human host is a key characteristic that plays a major role in the performance of current malaria vaccine candidates; both whole sporozoite vaccine candidates and subunit vaccine candidates. This underlines the importance of visualizing sporozoite migration in the context of understanding and optimizing malaria vaccine performance.

Applying quantitative imaging of parasite migration beyond malaria vaccine development
In most chapters of this thesis (**chapter 1-5**), quantitative imaging assays have been used to study the migratory behavior of malaria sporozoites in the context of vaccine development. However, **chapter 6** investigates the migratory behavior of schistosomal and hookworm larvae, while **chapter 7** explores the applications of imaging of parasite migration beyond vaccine development. First of all, the distribution of chapters in this thesis between malaria and other parasitic diseases reflects the imbalance in research efforts; most imaging studies have focused on malaria parasites and a few other protozoa, while other harmful parasites such as schistosomes and hookworms remain neglected[41]. The gained insights so far because of the imaging of malaria parasites should inspire for more research regarding other parasite species.

Vaccines are considered a promising strategy to combat parasitic infections, but there are other important strategies. For example, accurate diagnosis of parasitic infections followed by effective treatment is crucial to avoid morbidity and mortality. In **chapter 7** the role preclinical development of imaging technology can play in fulfilling this clinical need has been extensively reviewed. **Chapter 6** provides an example of this potential role; a readout for helminthic skin invasion was established, which is needed to assess the efficacy of potential parasite invasion blocking strategies aiming at selecting an efficacious one. Another example is the screening of already approved drugs and aiming at repurposing them (while avoiding expensive approval procedures) which is highlighted in **chapter 7** as a promising strategy for antiparasitic drug discovery. Imaging-based whole-organism screening tools have been developed to enable screening of large compound libraries to identify compounds with

> The translational value of the quantitative imaging of parasite migration goes beyond supporting parasite vaccine development

antiparasitic effects[42, 43]. The imaging-based *in vitro* assay developed and used in **chapter 1** and **4** to investigate the effects of formulation components and anti-CSP antibodies on sporozoite migration is an example of such a screening tool and can potentially be applied to identify a new malaria prophylaxis that targets sporozoite motility. Taken together, the translational value of the quantitative imaging of parasite migration can go beyond supporting parasite vaccine development.

CONCLUDING REMARKS

Parasitic infections have a major impact on the global disease burden and molecular imaging technology can play a role in the development of strategies to reduce this burden. This thesis highlights the role that quantitative imaging of parasite migration can play in supporting the development of parasite vaccines. To fully realize the potential of imaging technology in parasitology, investment is needed 1) to translate the use of imaging technology already successfully applied in biomedical fields such as oncology and immunology to the field of parasitology and 2) to foster interdisciplinary research teams which form the ideal environment for the development of quantitative imaging-based assays with translational potential. Quantitative imaging-based research is most effective when there is room for exploration; first and foremost, imaging of parasite migration is an invitation to explore and observe uncharted territory, only thereafter quantitative data should be collected to transform observations into interpretable charts. This will help us uncover the behavior of parasites and how to combat them driven by, but not limited to, our imagination.

First and foremost, imaging of parasite migration is an invitation to explore and observe uncharted territory

REFERENCES

1. Waters, J. and T. Wittmann, Quantitative imaging in cell biology. 2014: Academic Press.
2. Behet, M.C., et al., Sporozoite immunization of human volunteers under chemoprophylaxis induces functional antibodies against pre-erythrocytic stages of Plasmodium falciparum. Malaria Journal, 2014. 13.
3. Carey, A.F., R. Menard, and D.Y. Bargieri, Scoring sporozoite motility. Methods Mol Biol, 2013. 923: p. 371-83.
4. Stewart, M.J. and J.P. Vanderberg, Malaria sporozoites leave behind trails of circumsporozoite protein during gliding motility. J Protozool, 1988. 35(3): p. 389-93.
5. Hegge, S., et al., Automated classification of Plasmodium sporozoite movement patterns reveals a shift towards productive motility during salivary gland infection. Biotechnol J, 2009. 4(6): p. 903-13.
6. Kebaier, C. and J.P. Vanderberg, Initiation of Plasmodium sporozoite motility by albumin is associated with induction of intracellular signalling. Int J Parasitol, 2010. 40(1): p. 25-33.
7. Hellmann, J.K., et al., Environmental constraints guide migration of malaria parasites during transmission. PLoS pathogens, 2011. 7(6): p. e1002080.
8. Hopp, C.S., et al., Longitudinal analysis of Plasmodium sporozoite motility in the dermis reveals component of blood vessel recognition. Elife, 2015. 4.
9. Benhamou, S., How to reliably estimate the tortuosity of an animal's path:: straightness, sinuosity, or fractal dimension? Journal of theoretical biology, 2004. 229(2): p. 209-220.
10. Dunn Jr, W., et al., Exploring and visualizing multidimensional data in translational research platforms. Briefings in bioinformatics, 2017. 18(6): p. 1044-1056.
11. O'Donoghue, S.I., et al., Visualization of biomedical data. Annual Review of Biomedical Data Science, 2018. 1: p. 275-304.
12. Saeys, Y., S. Van Gassen, and B.N. Lambrecht, Computational flow cytometry: helping to make sense of high-dimensional immunology data. Nature Reviews Immunology, 2016. 16(7): p. 449-462.
13. De Niz, M., et al., Toolbox for in vivo imaging of host–parasite interactions at multiple scales. Trends in parasitology, 2019. 35(3): p. 193-212.
14. Walter, A., et al., Correlated multimodal imaging in life sciences: expanding the biomedical horizon. Frontiers in Physics, 2020: p. 47.
15. Mankoff, D.A., et al., Making molecular imaging a clinical tool for precision oncology: a review. JAMA oncology, 2017. 3(5): p. 695-701.
16. Pichugin, A. and U. Krzych, Detection of Plasmodium berghei and Plasmodium yoelii liver-stage parasite burden by quantitative real-time PCR. Malaria Vaccines: Methods and Protocols, 2015: p. 81-89.
17. Ploemen, I.H.J., et al., Visualisation and Quantitative Analysis of the Rodent Malaria Liver Stage by Real Time Imaging. Plos One, 2009. 4(11).
18. Bartlett, A., et al., The infection of human skin by schistosome cercariae: studies using Franz cells. Parasitology, 2000. 121(1): p. 49-54.
19. van Leeuwen, F.W.B., et al., Trending: Radioactive and Fluorescent Bimodal/Hybrid Tracers as Multiplexing Solutions for Surgical Guidance. Journal of Nuclear Medicine, 2020. 61(1): p. 13-19.
20. Welling, M.M., et al., Multimodal Tracking of Controlled Staphylococcus aureus Infections in Mice. Acs Infectious Diseases, 2019. 5(7): p. 1160-1168.
21. De Boer, P., J.P. Hoogenboom, and B.N. Giepmans, Correlated light and electron microscopy: ultrastructure lights up! Nature methods, 2015. 12(6): p. 503-513.
22. Martí-Bonmatí, L., et al., Multimodality imaging techniques. Contrast media & molecular imaging, 2010. 5(4): p. 180-189.
23. Treuting, P.M., S.M. Dintzis, and K.S. Montine, Comparative Anatomy and Histology: A Mouse and Human Atlas. Academic Press, Elsevier, 2017. Chapter 24: p. 433-441.
24. de Oliveira, I.S., et al., Research models in biomedical sciences: Advantages and limitations. 2020.
25. Denayer, T., T. Stöhr, and M. Van Roy, Animal models in translational medicine: Validation and prediction. New Horizons in Translational Medicine, 2014. 2(1): p. 5-11.
26. Roestenberg, M., et al., Controlled human malaria infections by intradermal injection of cryopreserved Plasmodium falciparum sporozoites. Am J Trop Med Hyg, 2013. 88(1): p. 5-13.
27. Verhage, D., et al., Clinical outcome of experimental human malaria induced by Plasmodium

falciparum-infected mosquitoes. 2005.
28. Harding, J.D., Nonhuman primates and translational research: progress, opportunities, and challenges. ILAR journal, 2017. 58(2): p. 141-150.
29. Hopp, C.S., et al., Comparative intravital imaging of human and rodent malaria sporozoites reveals the skin is not a species-specific barrier. Embo Molecular Medicine, 2021. 13(4).
30. Minkah, N.K., C. Schafer, and S.H. Kappe, Humanized mouse models for the study of human malaria parasite biology, pathogenesis, and immunity. Frontiers in immunology, 2018. 9: p. 807.
31. Gaudinski, M.R., et al., A Monoclonal Antibody for Malaria Prevention. New England Journal of Medicine, 2021. 385(9): p. 803-814.
32. Lyke, K.E., et al., Attenuated PfSPZ Vaccine induces strain-transcending T cells and durable protection against heterologous controlled human malaria infection. Proc Natl Acad Sci U S A, 2017. 114(10): p. 2711-2716.
33. Roestenberg, M., et al., A double-blind, placebo-controlled phase 1/2a trial of the genetically attenuated malaria vaccine PfSPZ-GA1. Sci Transl Med, 2020. 12(544).
34. Quinn, H.L., et al., The role of microneedles for drug and vaccine delivery. Expert Opinion on Drug Delivery, 2014. 11(11): p. 1769-1780.
35. Livingstone, M.C., et al., In vitro and in vivo inhibition of malaria parasite infection by monoclonal antibodies against Plasmodium falciparum circumsporozoite protein (CSP). Scientific Reports, 2021. 11(1).
36. Murugan, R., et al., Evolution of protective human antibodies against Plasmodium falciparum circumsporozoite protein repeat motifs. Nature Medicine, 2020. 26(7): p. 1135-+.
37. Tan, J., et al., A public antibody lineage that potently inhibits malaria infection through dual binding to the circumsporozoite protein. Nature Medicine, 2018. 24(4): p. 401-+.
38. Winkel, B.M., et al., Plasmodium sporozoites induce regulatory macrophages. PLoS Pathogens, 2020. 16(9): p. e1008799.
39. Germain, R.N., E.A. Robey, and M.D. Cahalan, A decade of imaging cellular motility and interaction dynamics in the immune system. Science, 2012. 336(6089): p. 1676-1681.
40. Peters, N.C., In vivo imaging reveals an essential role for neutrophils in leishmaniasis transmitted by sand flies (vol 321, pg 970, 2008). Science, 2008. 322(5908): p. 1634-1634.
41. Novobilsky, A. and J. Hoglund, Small animal in vivo imaging of parasitic infections: A systematic review. Experimental Parasitology, 2020. 214.
42. Muller, J. and A. Hemphill, Drug target identification in protozoan parasites. Expert Opinion on Drug Discovery, 2016. 11(8): p. 815-824.
43. Partridge, F.A., et al., Anthelmintic drug discovery: target identification, screening methods and the role of open science. Beilstein Journal of Organic Chemistry, 2020. 16: p. 1203-1224.


A

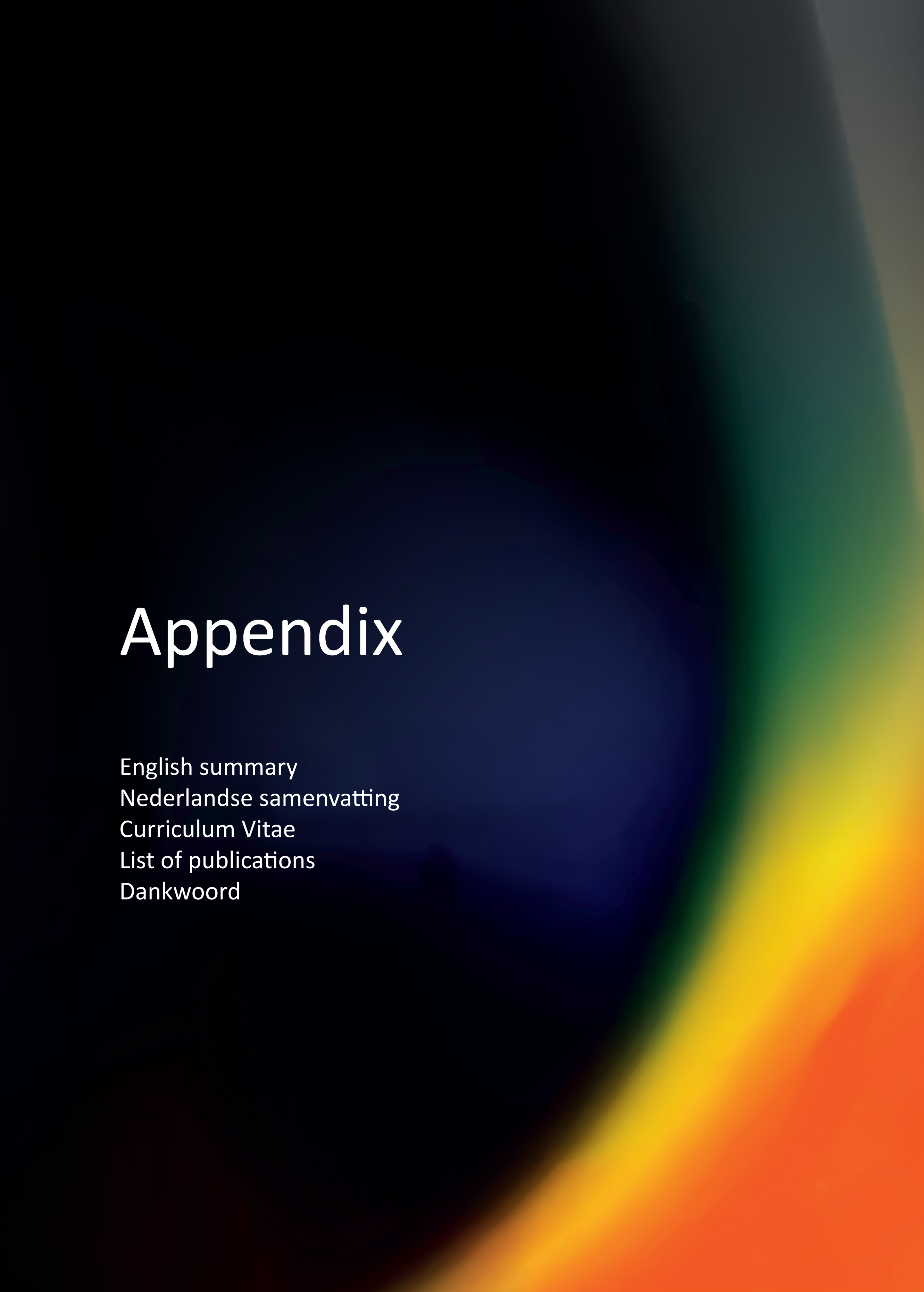

Appendix

English summary
Nederlandse samenvatting
Curriculum Vitae
List of publications
Dankwoord

ENGLISH SUMMARY

Summary of this thesis entitled: 'To image or to imagine - Visualization of parasite migration as a means to support (malaria) parasite vaccine development'.

This thesis describes the development of quantitative imaging-based tools to study parasite migration under different conditions aiming to support the development of antiparasitic vaccines needed to reduce the global disease burden caused by parasitic infections.

Development of SMOOT

SMOOT (Sporozoite Motility Orienting and Organizing Tool) was developed and established as a quantitative software analysis tool for tracking the migration of malaria sporozoites *in vitro* and in human skin explant. This tool provided a readout with high kinematic detail, enabling the quantitative characterization of novel factors influencing the migration capability of malaria sporozoites:

- A complex interplay of different (macro)molecules act as regulators of sporozoite motility (chapter 1).
- Radiation attenuation impairs the capacity of sporozoites to vary their turn angle, velocity and direction, resulting in a loss of movement variability (chapter 2).
- The administration route of sporozoites, whether via mosquito inoculation or intradermal syringe injection, cause differences in the sporozoite distribution through the skin, the presence of hematomas, tissue structure and (possibly as an indirect consequence of the other differences) sporozoite migration patterns (chapter 3).
- Anti-CSP antibody concentrations far above the theoretical saturating binding concentration are needed to inhibit sporozoite motility *in vitro,* these values increase even further in human skin explant and subsets of sporozoites seem to be refractory to the effect of anti-CSP antibodies (chapter 4).

Development of a hybrid tracer for sporozoites

In chapter 5 we expanded the study of sporozoite migration beyond *in vitro* and *ex vivo* models. A hybrid tracer labeling approach for malaria sporozoites was developed which yielded viable sporozoites that were both fluorescently and radioactively labeled. With this approach the *in vivo* dissemination of malaria sporozoites could be revealed in a murine model showing that live sporozoites are able to migrate from the lungs to the liver more efficiently than non-viable sporozoites.

Relevance for vaccine development

Since migration is crucial for sporozoites to continue their life cycle within the host, factors influencing their migration capability may be important targets for (vaccine-induced) immunity.

In this thesis, imaging of parasite migration was used to gain insights that can support the development of antiparasitic vaccines. The findings from chapter 1, which demonstrate that different (macro)molecules regulate sporozoite motility, and the observations from chapter 3, which show the impact of the administration route on sporozoite migration patterns, suggest that optimizing the vaccine formulation and developing an administration method that mimics mosquito inoculation may enhance the ability of vaccine sporozoites to reach the liver after intradermal delivery and thereby improve their efficacy to induce immunity. Additionally, the results from chapter 2, that radiation attenuation impairs the sporozoite's migration capability and from chapter 5, that live sporozoites are more efficient in migrating from the lungs to the liver than non-viable sporozoites, suggest that there needs to be an optimal balance between the degree of attenuation that ensures safety of the vaccine and minimal impairment to allow sufficient antigenic exposure required for inducing protective immunity. Furthermore, quantitative assessment of the parasite inhibitory capacity of anti-CSP antibodies, as described in chapter 4, can aid in selecting the most efficacious antibodies to support optimization of subunit and passive immunization strategies.

Broader potential for imaging technology in parasitology

In chapter 6 we used the concepts developed for studying the migration of malaria sporozoites (as described in chapter 1-5) to investigate skin invasion by *Schistosoma mansoni* and *Necator americanus* larvae. We introduced a multimodal imaging approach that combined fluorescent and radioactive imaging to assess helminth skin invasion in real-time using a human skin explant model. This setup enables a comprehensive and quantitative evaluation of helminthic invasion, providing possibilities for gaining deeper insights into this process as well as serving as a useful readout for assessing the efficacy of future helminth invasion-blocking strategies. This thesis concludes with a review of the broader potential for imaging technology to advance the development of new diagnostic methods, therapeutic interventions and vaccines for combating parasitic infections (chapter 7). This review emphasizes the possibilities to improve current microscopy-based diagnostic methods and extend them with radiological imaging modalities. Additionally, *in vivo* tracking of parasites is highlighted as a potential readout for the efficacy of new antiparasitic strategies and as a source of fundamental insights for rational design.

NEDERLANDSE SAMENVATTING

Samenvatting van dit proefschrift getiteld: 'Afbeelden of inbeelden - Visualisatie van de bewegingspatronen van parasieten als manier om de ontwikkeling van anti-parasitaire (malaria) vaccins te ondersteunen'.

Dit proefschrift beschrijft de ontwikkeling van kwantitatieve, op beeldvorming gebaseerde instrumenten om de beweging van parasieten onder verschillende omstandigheden te kunnen bestuderen. Het doel van dit soort beeldvorming is om de ontwikkeling van anti-parasitaire vaccins te ondersteunen. Deze vaccins zijn hard nodig om de wereldwijde ziektelast die veroorzaakt wordt door parasitaire infecties te verminderen.

Ontwikkeling van het analyse-instrument SMOOT

Als kwantitatief analyse-instrument voor het bestuderen van de bewegingspatronen van malaria parasieten (genaamd sporozoïeten) op een glasoppervlak en in menselijke huid hebben we het softwareprogramma SMOOT (*Sporozoite Motility Orienting and Organizing Tool*) ontwikkeld. Met behulp van SMOOT kon de motiliteit ('beweeglijkheid') van sporozoïeten gedetailleerd en op een kwantitatieve manier in kaart gebracht worden, waarmee nieuwe factoren geïdentificeerd konden worden die de motiliteit van sporozoïeten beïnvloeden. Dat leverde de volgende resultaten op:

- Er is een complex samenspel tussen verschillende (macro)moleculen die de motiliteit van sporozoïeten reguleert (hoofdstuk 1).
- Verzwakking van sporozoïeten door middel van bestraling belemmert het vermogen van sporozoïeten om hun draaiingshoek, snelheid en richting te variëren; er gaat bewegingsvariabiliteit verloren (hoofdstuk 2).
- De toedieningsroute van sporozoïeten, via een muggenbeet (de natuurlijke manier) of via een injectie in de huid met een injectiespuit, veroorzaakt verschillen in de huid. Die verschillen zijn zichtbaar in de verspreiding van sporozoïeten door de huid, in het aantal hematomen, in de weefselstructuur van de huid en (mogelijk als indirect gevolg van de andere verschillen) in de migratiepatronen van de sporozoïeten (hoofdstuk 3).
- Het was al bekend dat antistoffen tegen het meest voorkomende eiwit op de buitenkant van sporozoïeten (CSP) de motiliteit van sporozoïeten kunnen remmen. Echter, de hoeveelheid antistoffen die nodig is om de motiliteit van sporozoïeten op een glasoppervlak te remmen, is veel hoger dan verwacht op basis van de maximale hoeveelheid antistoffen die theoretisch gezien kan binden aan CSP. In een humaan huidmodel is de benodigde hoeveelheid antistoffen nog hoger. Daar komt nog bij dat een subgroep van sporozoïeten ongevoelig lijkt te zijn voor het effect van de antistoffen tegen CSP (hoofdstuk 4).

Ontwikkeling van een hybride tracer voor sporozoïeten

In hoofdstuk 5 hebben we de migratiepatronen van sporozoïeten onderzocht in een muismodel. We hebben hiervoor een hybride *tracer* ontwikkeld waarmee levende sporozoïeten tegelijkertijd zowel fluorescent als radioactief gelabeld kunnen worden. Op deze manier konden we traceren hoe sporozoïeten zich na injectie door de muis verspreidden. De resultaten lieten onder andere zien dat levende sporozoïeten beter in staat zijn om van de longen naar de lever te migreren dan dode sporozoïeten.

Belang voor het malariavaccinonderzoek

Het is voor sporozoïeten van levensbelang dat ze in staat zijn om zich voort te bewegen door het lichaam van hun gastheer. Daardoor zijn factoren die het vermogen van sporozoïeten om te bewegen beïnvloeden een mogelijk doelwit voor (vaccin-geïnduceerde) immuniteit. In dit proefschrift is het zichtbaar maken van bewegingspatronen van parasieten ingezet om inzichten te verwerven die de ontwikkeling van anti-parasitaire vaccins kunnen ondersteunen. De bevindingen uit hoofdstuk 1, die aantonen dat verschillende (macro) moleculen de motiliteit van sporozoïeten reguleren, en de observaties uit hoofdstuk 3, die de invloed van de toedieningsroute op de migratiepatronen van sporozoïeten laten zien, suggereren bijvoorbeeld dat het vermogen van vaccin-sporozoïeten om de lever te bereiken verbeterd kan worden door het optimaliseren van de vaccinformulering en het ontwikkelen van een toedieningsmethode die toediening door de mug nabootst. Op deze manier zou de werkzaamheid van vaccinkandidaten tegen malaria die gebaseerd zijn op het gebruik van verzwakte sporozoïeten verbeterd kunnen worden. De resultaten uit hoofdstuk 2, die aantonen dat verzwakking door middel van bestraling de motiliteit van sporozoïeten aantast, en uit hoofdstuk 5, die laten zien dat levende sporozoïeten beter in staat zijn om zich van de longen naar de lever te verplaatsen dan dode sporozoïeten, geven aan dat er een optimaal evenwicht gevonden moet worden tussen enerzijds voldoende verzwakking van de vaccin-sporozoïeten om de veiligheid van het vaccin te waarborgen en anderzijds zo min mogelijk verzwakking zodat de sporozoïeten hun levenscyclus ver genoeg kunnen doorlopen om immuniteit op te wekken. Verder kan de kwantitatieve analyse van de antistofconcentraties die nodig zijn om de motiliteit van sporozoïeten te remmen (hoofdstuk 4), helpen om de meest effectieve antistoffen te selecteren voor verder klinisch onderzoek naar malariavaccinkandidaten die gebaseerd zijn op de werking van specifieke antistoffen tegen sporozoïeten.

Bredere toepasbaarheid van beeldvormingstechnologie binnen de parasitologie

Hoofdstuk 6 laat zien dat de concepten die in hoofdstuk 1-5 gebruikt zijn om de bewegingspatronen van malaria parasieten te bestuderen ook breder inzetbaar zijn binnen de parasitologie. In dat hoofdstuk hebben we een hybride tracer gebruikt om huidinvasie door de parasitaire wormen *Schistosoma mansoni* en *Necator americanus* te onderzoeken. We hebben dus deze parasitaire wormen zowel fluorescent als radioactief gelabeld, zodat we ze vervolgens konden volgen terwijl ze menselijke huid binnendrongen. Deze opzet maakt het mogelijk om huidinvasie door parasitaire wormen in real-time en op een kwantitatieve manier te onderzoeken en zo tot nieuwe inzichten te komen in de mechanismen achter huidinvasie. Daarnaast kan deze methode ook gebruikt worden om de effectiviteit van nieuwe interventies te testen die als doel hebben om parasitaire huidinvasie te blokkeren. Dit proefschrift sluit af met een overzicht van de mogelijkheden die nieuwe beeldvormingstechnologie biedt om de ontwikkeling van nieuwe diagnostische methoden, medicijnen, vaccins en voorzorgsmaatregelen voor de bestrijding van parasitaire infecties te versnellen (hoofdstuk 7). Dit overzicht benadrukt de mogelijkheden die er zijn om de huidige diagnostische methoden, die gebaseerd zijn op het gebruik van microscopie, te verbeteren en uit te breiden met radiologische beeldvorming. Daarnaast wordt de analyse van migratiepatronen van parasieten in het lichaam van hun gastheer belicht als een mogelijke manier om de effectiviteit van nieuwe anti-parasitaire strategieën te meten en om inzichten te verwerven voor het ontwikkelen van nieuwe medicijnen.

CURRICULUM VITAE

Clarize de Korne was born on July 12, 1995, in Rilland, the Netherlands. After completing her secondary education in 2012 (Calvijn College, Goes), she moved to Leiden to study Biomedical Sciences. She obtained her Bachelor's degree in Biomedical Sciences from Leiden University in 2015, followed by a Master's degree in the same field from the same institution in 2018. During her academic studies, she completed a Minor in Education Biology at ICLON, Leiden, which provided her with certification as a high school biology teacher. During her Master's degree, she completed two scientific internships, both of which involved the use of molecular imaging techniques. Her first internship, conducted at the Interventional Molecular Imaging laboratory (Leiden University Medical Center (LUMC)), focused on the development of immunohistochemical staining protocols for the evaluation of membranous biomarkers in breast cancer in collaboration with the Dutch Cancer Institute in Amsterdam. Her second internship was a collaborative project between the BioNanoTechnology group (Wageningen University & Research) and the Parasitology department of the LUMC and focused on the selection of sporozoite binders using glass surface functionalization. This second internship sparked her interest in parasitology, and, combined with her passion for imaging, led to the start of her PhD project at the Radiology and Parasitology departments of the LUMC in 2018 on the fascinating intersection of imaging and parasitology. Outside of academia, Clarize has been actively involved in the community, serving as a general member of the (Supervisory) Board of IFES Nederland. After her PhD, for a year, Clarize was engaged in a traineeship in business analytics and data science to expand her data analysis skill set and broaden her horizon beyond the academic setting. Currently, she is a postdoctoral researcher in the Department of Epidemiology and Global Health of the Julius Center, a division of UMC Utrecht.

LIST OF PUBLICATIONS

Included in this thesis:

1. **C.M. de Korne**, L. van Lieshout, F.W B. van Leeuwen, M. Roestenberg (2023). "Imaging as a (pre) clinical tool in parasitology." Trends in Parasitology 39(3):212-226.
2. **C.M. de Korne**, R. van Schuijlenburg, J.C. Sijtsma, H. de Bes, E. Baalbergen, S. Azargoshasb, M.N. van Oosterom, M.B.B. McCall, F.W.B. van Leeuwen, Roestenberg (2022). "Sporozoite motility as a quantitative readout for anti-CSP antibody inhibition." Scientific Reports 12(1): 17194.
3. **C.M. de Korne**, B.M.F. Winkel, M.N. van Oosterom, S.C. Chevalley-Maurel, H.M. Houwing, J.C. Sijtsma, S. Azargoshasb, E. Baalbergen, B.M.D. Franke-Fayard, F.W.B. van Leeuwen, M. Roestenberg (2021). "Clustering and erratic movement patterns of syringe-injected versus mosquito-inoculated malaria sporozoites underlie decreased infectivity." mSphere 6(2): e00218-00221.
4. B.M.F. Winkel*, **C.M. de Korne***, M.N. van Oosterom, D. Staphorst, M. Meijhuis, E. Baalbergen, M.S. Ganesh, K.J. Dechering, M.W. Vos, S. C. Chevalley-Maurel, B.M.D. Franke-Fayard, F.W.B. van Leeuwen, M. Roestenberg (2019). "Quantification of wild-type and radiation attenuated Plasmodium falciparum sporozoite motility in human skin." Scientific Reports 9(1): 13436.
5. **C.M. de Korne**, L.T. Lageschaar, M.N. van Oosterom, E. Baalbergen, B.M.F. Winkel, S.C. Chevalley-Maurel, A.H. Velders, B.M.D. Franke-Fayard, F.W.B. Van Leeuwen, M. Roestenberg (2019). "Regulation of Plasmodium sporozoite motility by formulation components." Malaria journal 18(1): 1-11.

Imaging support for colleagues:

6. S.K. Kolli, A. Molina-Cruz, T. Araki, F.J.A. Geurten, J. Ramesar, S.C. Chevalley-Maurel, H.J. Kroeze, S. Bezemer, **C.M. de Korne**, R. Withers, N. Raytselis, A.F. El Hebieshy, R.Q. Kim, M.A. Child, S. Kakuta, H. Hisaeda, H. Kobayashi, T. Annoura, P.J. Hensbergen, B.M.D. Franke-Fayard, C. Barillas-Mury, F.A. Scheeren, C.J. Janse (2022). "Malaria parasite evades mosquito immunity by glutaminyl cyclase–mediated posttranslational protein modification." Proceedings of the National Academy of Sciences 119(35): e2209729119.
7. A. Zawistowska-Deniziak, J.M. Lambooij, A. Kalinowska, T.A. Patente, M. Łapiński, H.J. van der Zande, K. Basałaj, **C.M. de Korne**, M. A. Chayé, T.A. Gasan, L.J. Norbury, M. Giera, A. Zaldumbide, H.H. Smits, B. Guigas (2022). "Fasciola hepatica Fatty Acid Binding Protein 1 modulates T cell polarization by promoting dendritic cell thrombospondin-1 secretion without affecting metabolic homeostasis in obese mice." Frontiers in Immunology 26(13): 884663.
8. A. Zakeri, B.J. Whitehead, A. Stensballe, **C.M. de Korne**, A.R. Williams, B. Everts, P. Nejsum (2021). "Parasite worm antigens instruct macrophages to release immunoregulatory extracellular vesicles." Journal of Extracellular Vesicles 10(10): e12131.

9. B.M.F. Winkel, L.R. Pelgrom, R. van Schuijlenburg, E. Baalbergen, M.S. Ganesh, H. Gerritsma, **C.M. de Korne**, N. Duszenko, M.C.C. Langenberg, S.C. Chevalley-Maurel, H.H. Smits, E.C. de Jong, B. Everts, B.M.D. Franke-Fayard, M. Roestenberg (2020). “Plasmodium sporozoites induce regulatory macrophages.” PLoS Pathogens 16(9): e1008799.
10. N. Duszenko, D.M. van Willigen, M.M. Welling, **C.M. de Korne**, R. van Schuijlenburg, B.M.F. Winkel, F.W.B. van Leeuwen, M. Roestenberg (2020). “A supramolecular platform technology for bacterial cell surface modification.” ACS Infectious Diseases 6(7): 1734-1744.
11. M.E. Kuipers, E.N. Nolte-‘t Hoen, A.J. van der Ham, A. Ozir-Fazalalikhan, D.L. Nguyen, **C.M. de Korne**, R.I. Koning, J.J. Tomes, K.F. Hoffmann, H. H. Smits, C.H. Hokke (2020). “DC-SIGN mediated internalisation of glycosylated extracellular vesicles from Schistosoma mansoni increases activation of monocyte-derived dendritic cells.” Journal of Extracellular Vesicles 9(1): 1753420.
12. A.W. Hensbergen, D.M. van Willigen, M.M. Welling, F.A. van der Wijk, **C.M. de Korne**, M.N. van Oosterom, M. Schottelius, H.J. Wester, T. Buckle, F.W.B. van Leeuwen (2019). “Click chemistry in the design and production of hybrid tracers.” ACS omega 4(7): 12438-12448.
13. M.M. Welling, **C.M. de Korne**, S.J. Spa, D.M. van Willigen, A.W. Hensbergen, A. Bunschoten, N. Duszenko, W.K. Smits, M. Roestenberg, F.W.B. van Leeuwen (2019). “Multimodal tracking of controlled Staphylococcus aureus infections in mice.” ACS Infectious Diseases 5(7): 1160-1168.
14. B.M.F. Winkel, **C.M. de Korne**, M.N. van Oosterom, D. Staphorst, A. Bunschoten, M.C.C. Langenberg, S.C. Chevalley-Maurel, C.J. Janse, B.M.D. Franke-Fayard, F.W.B. van Leeuwen, M. Roestenberg (2019). “A tracer-based method enables tracking of Plasmodium falciparum malaria parasites during human skin infection.” Theranostics 9(10): 2768.
15. B.M.F. Winkel, M.R. Dalenberg, **C.M. de Korne**, C. Feijt, M.C.C. Langenberg, L. Pelgrom, M.S. Ganesh, M. Yazdanbakhsh, H.H. Smits, E.C. de Jong, B. Everts, F.W.B. van Leeuwen, C.H. Hokke, M. Roestenberg (2018). “Early induction of human regulatory dermal antigen presenting cells by skin-penetrating Schistosoma mansoni cercariae.” Frontiers in Immunology 9: 2510.
16. S. van der Wal, **C.M. de Korne**, L.G. Sand, D.M. van Willigen, P.C. Hogendoorn, K. Szuhai, F.W.B. van Leeuwen, T. Buckle (2018). “Bioorthogonally applicable fluorescence deactivation strategy for receptor kinetics study and theranostic pretargeting approaches.” ChemBioChem 19(16): 1758-1765.
17. T. Buckle, D.M. van Willigen, S.J. Spa, A.W. Hensbergen, S. van der Wal, **C.M. de Korne**, M.M. Welling, H.G. van der Poel, J.C. Hardwick, F.W.B. van Leeuwen (2018). “Tracers for fluorescence-guided surgery: how elongation of the polymethine chain in cyanine dyes

alters the pharmacokinetics of a dual-modality c [RGDyK] tracer." Journal of Nuclear Medicine 59(6): 986-992.

Collaboration with the Dutch Cancer Institute:

18. E.M.K. Wit, F. van Beurden, G.H. Kleinjan, N. Grivas, **C.M. de Korne**, T. Buckle, M.L. Donswijk, E.M. Bekers, F.W.B. van Leeuwen, H G. Van der Poel (2022). "The impact of drainage pathways on the detection of nodal metastases in prostate cancer: a phase II randomized comparison of intratumoral vs intraprostatic tracer injection for sentinel node detection." European Journal of Nuclear Medicine and Molecular Imaging 49(5): 1-11.
19. **C.M. de Korne***, E.M.K. Wit*, J.J. de Jong, R.A. Valdés Olmos, T. Buckle, F.W.B van Leeuwen, H.G. van der Poel (2019). "Anatomical localization of radiocolloid tracer deposition affects outcome of sentinel node procedures in prostate cancer." European Journal of Nuclear Medicine and Molecular Imaging 46: 2558-2568.
20. G.H. KleinJan, K. Sikorska, **C.M. Korne**, T. Buckle, C. Tillier, R.C. van der Roest, J.J. de Jong, F.W.B. van Leeuwen, H.G. van der Poel (2019). " A prediction model relating the extent of intraoperative fascia preservation to erectile dysfunction after nerve-sparing robot-assisted radical prostatectomy." Journal of robotic surgery 13: 455-462.
21. N. Grivas, R.C. van der Roest, **C.M. de Korne**, G.H. KleinJan, K. Sikorska, I.G. Schoots, C. Tillier, B. van der Broek, K. Jalink, S.W.T.J.P. Heijmink, T. Buckle, F.W.B. van Leeuwen, H.G. van der Poel (2019). "The value of periprostatic fascia thickness and fascia preservation as prognostic factors of erectile function after nerve-sparing robot-assisted radical prostatectomy." World Journal of Urology 37: 309-315.

**These authors contributed equally*

DANKWOORD

De afgelopen jaren voelden als bergbeklimmen, soms letterlijk, meestal figuurlijk. Ik wil mijn gidsen en teamgenoten met wie ik de afgelopen jaren mocht optrekken bedanken; de tocht heeft veel meer opgeleverd dan een proefschrift.

Mijn grootste dank gaat uit naar mijn promotores Fijs van Leeuwen en Meta Roestenberg. Ik bewonder jullie grenzeloze passie voor onderzoek, focus op impactvolle toepassingen en daadkracht waarmee bergen verzet worden. Bedankt voor de mogelijkheid om jullie dynamische samenwerking te vertalen in onderzoeksresultaten op het fascinerende snijvlak van imaging en parasieten. Fijs, bedankt voor de inspirerende omgeving (wie/wat je allemaal tegen kan komen op het chemielab is symbolisch hiervoor) en mooie kansen die je hebt gecreëerd; ze vormen een onvergetelijk onderdeel van mijn PhD. Meta, ik begon als een soort ongeleid projectiel; bedankt voor je sturing en het vergroten van mijn crashbestendigheid. Je onuitputtelijke positiviteit werkt aanstekelijk en hoopgevend.

Graag wil ik al mijn collega's met wie ik voor kortere of langere tijd heb samengewerkt bedanken. In het bijzonder:

- Mijn paranimfen; Beatrice, er waren veel personages nodig om jou te beschrijven, maar Vaiana komt nog steeds het dichtst in de buurt. Als enthousiaste, hulpvaardige, intelligente en ondernemende medeklimmer heb je een cruciale rol gespeeld in het plannen, uitvoeren en, niet te vergeten, het bespreken van onze 'beklimmingen'; ik heb genoten van ons teamwork. Roos, je hebt een mindset waarmee je Mount Everest zou kunnen beklimmen en ik bewonder het wat je daarmee ook al in je onderzoek voor elkaar hebt gebokst. Bedankt voor alle gezelligheid die ons buddyschap met zich mee heeft gebracht binnen en buiten de T-zone.
- Mijn IMI-collega's; Tessa, je hebt me wegwijs gemaakt in de ins en outs van de Biotak en Bubbelbal. Mick, met veel plezier hebben we samen het hotlab onveilig gemaakt. Matthias, Krijn en Samaneh, wat had ik zonder SMOOT-helpdesk moeten beginnen, متشکرم?! Danny, alleen jouw muziek zou mijn sporo's al kunnen laten bewegen, maar gelukkig deden ze het met je tracers ook nog. Silvia, voor de leukste samenwerking heb je geen PDMS nodig, maar Kunststof. Fabian, jouw aanwezigheid zowel binnen als buiten ons racetrap-project heb ik altijd gewaardeerd. Nina, Nina en IJsbrand, het was leerzaam om jullie te mogen begeleiden tijdens jullie stages. IMI bedankt!
- Mijn PARA-collega's; thanks everyone from the Department, led by Maria Yazdanbakhsh, for being around during joint meetings/events and for culturing millions of parasites for my experiments. Nikolas, by now 'in hetzelfde schuitje zitten' makes sense, thanks for sharing the ship. Miriam, despite good reasons, I would not describe your personality as static; thanks for your joyful and dynamic

contributions. My partners in crime, performing Das Assay was the real work. Blandine, I will never forget the dozens of time you turned in your office chair to enthusiastically greet the ‘youth’. Severine, you nearly made me cry when I left and that says a lot. Els, Jeroen, Laura, Sascha, letterlijk alle sporo-experimenten beschreven in dit proefschrift waren in meer of mindere mate afhankelijk van jullie inzet, bedankt! Jacqueline, kletsen, klussen, planten en precisiewerk hebben geleid tot mooie (en tastbare) herinneringen. Eveline, je veerkracht is nog groter dan je organisatietalent, bedankt voor al onze (telefoon)gesprekken. Cynthia, gelukkig zijn er nog heel wat ontmoetingen gevolgd op de eerste, al was die wel het origineelst. Mijn klinische mede-PhD’ers Marijke, Marie-Astrid, Jan Pieter, Vincent, Olivia en Geert, bedankt voor jullie fijne gezelschap. Ik heb diep respect (zeker sinds mijn BROK) voor wat jullie georganiseerd krijgen, ongeacht de omstandigheden. Marije, Amin, Surendra and Anna, thanks for appreciating the added value of imaging to your projects.

- Mijn overige LUMC-collega’s; Annelies, Karien, Lennard, Willem, dankzij jullie voelde de confocalruimte als een tweede thuis. Jeroen, Leon, Bram, veel proefopstellingen waren ideeën gebleven zonder jullie hulp tijdens het bouwen ervan. Een dankbare shout-out naar iedereen die heeft bijgedragen aan een schone werkomgeving met koffie, lunch en avondeten op loopafstand.

De experimenten met humane huid waren niet mogelijk geweest zonder de klinieken, chirurgen en patiënten die daaraan mee wilden werken en Nandy die het coördineerde. Dank daarvoor!

Vrienden en familie, jullie vormden de stabiele basis voor de totstandkoming van dit proefschrift. Elsbeth, samen (met C.S. Lewis) hebben we het mooie van een diepe vriendschap ontdekt. Marjolein, Mariska, jullie zijn veel meer dan mede-oud-BW’ers/Panoplieten. Huisgenoten, bedankt dat jullie er altijd waren. BSF’ers, Krabbendijkse vriendinnen, leeskringgenoten, Sollertianen, BRvT’ers, Lead-it!’cie, C1/2-buddies, bedankt voor alle waardevolle momenten van verbinding. (Schoon)familie, bedankt voor alle gezelligheid en benodigde afleiding. Ik had me geen warmer welkom op IJburg kunnen wensen. Mam, je luisterend oor en wijze raad zijn ongeëvenaard. Pap, bedankt voor je praktische zorgzaamheid. Jullie onvoorwaardelijke liefde en vertrouwen hebben mij gevormd tot wie ik nu ben; mijn dankbaarheid is met geen pen te beschrijven. Johannes, in de mooiste herinneringen van de tweede helft speel je een grote rol; zie שיר השירים א פסוק ב.

In Your light we see light.